UNIVERSITY OF LIVERPOOL

Porous Metals with Novel Structures for Optimum Heat Exchange Performance

Thesis submitted in accordance with the requirements of the

University of Liverpool for the degree of Doctor in Philosophy by

Jan Mary Baloyo

June 2016

Table of Contents

Abstract

With advancing technology, the demand for effective cooling techniques for thermal management applications has increased significantly over the last years. Open-celled porous metals are ideal and effective cooling solutions due to their superior thermal properties allied with their permeability for fluid flow. In particular, porous copper produced by the Lost Carbonate Sintering (LCS) process is an excellent candidate for thermal management applications due to its ability to transport a high amount of heat over a small volume, when allied with fluid flow.

This study aims to develop LCS porous copper with tailored, non-homogeneous structures to maximise the heat transfer performance for use in thermal management. The structural, fluid flow and heat transfer properties were studied on a number of LCS porous copper samples with different pore size, porosity and structure.

Structural analysis showed that the pore morphology within the LCS porous copper specimens closely resembled that of the potassium carbonate (space-holder) powder used in LCS. Necking between the copper particles in the matrix ensured good mechanical strength and resulted in inter-particle pores connecting the larger pores formed by the space-holder. In addition to homogeneous porous structure, non-homogeneous porous structures, such as horizontal bilayer (HB), segmented vertical bilayer (SVB), integrated vertical bilayer (IVB), multi-boundary segmented structures (SS) and structures with directional porosity (DP), were successfully produced using the LCS process.

The fluid flow properties of the LCS porous structures were measured using a purpose-built apparatus. The pressure drop fitted well with the Forchheimer's equation and the resulting air and water permeabilities were found to be independent of the sample's length. For homogeneous structures, the permeability increased with increasing porosity and decreasing pore size. For horizontal bilayer structures, the majority of the flow preferred the higher porosity layer. For both segmented vertical bilayer and integrated vertical bilayer structures, the lower porosity layer limited the overall permeability. For segmented vertical bilayer and multi-boundary segmented structures, the presence of hard boundaries had negligible effect on the overall permeability. For directional porosity structures, a greater permeability was observed due to the addition of the open tubular channels.

The heat transfer performance of the LCS porous copper structures was characterised by the heat transfer coefficient. For homogeneous structures, an optimum porosity of 60% was found to offer the highest heat transfer coefficient. For horizontal bilayer structures, a higher heat transfer performance was observed when the higher porosity layer was placed next to the heat source. For vertical bilayer structures, the layer porosity combination greatly affected the heat transfer performance. For integrated vertical bilayer structures, optimum porosity combinations had an overall porosity in the range of 55% - 65%, and having the higher porosity layer by the water inlet gave a higher heat transfer coefficient. For segmented vertical bilayer structures, the presence of the 80% layer allied with the presence of a hard boundary resulted in the best heat transfer performance. Unlike in the integrated vertical bilayer structures, having the lower porosity layer by the water inlet

offered better heat transfer performance for segmented vertical bilayer structures. For multi-boundary segmented structures, increasing the number of hard boundaries increased the overall heat transfer performance. Samples with directional porosity showed a three- to eight-fold increase in heat transfer coefficient compared to their homogeneous counterparts. Apart from the horizontal bilayer structures, the heat transfer performance of the non-homogeneous structures was greater than their homogeneous counterparts.

Declaration

This thesis is submitted for the degree of Doctor in Philosophy in the faculty of Engineering at the University of Liverpool. The research project reported herein was carried out, unless otherwise stated, by the author, in the School of Engineering at the University of Liverpool between October 2012 and September 2015.

I confirm that the thesis is my own work, that I have not presented anyone else's work as my own, and that full and appropriate acknowledgement has been given where reference has been made to the work of others.

Jan Mary Baloyo

February 2016

Acknowledgements

I would like to express my utmost gratitude to Professor Yuyuan Zhao for his supervision and invaluable support throughout the duration of the PhD programme.

I would like to thank Versarien Plc. and the Centre for Global Eco-innovation for their financial support and guidance.

I am also grateful to Dr. L. Zhang, Mr. D. Atkinson, Mr. D. Neary and Mr. J. Mathew for their assistance in the experimental aspects of this research project.

I would also like to acknowledge the support and encouragement from my friends and colleagues throughout the PhD.

To my family, I am forever grateful.

Finally, praises and thanks to the God, the Almighty, for His blessings throughout my research.

List of Publications

Baloyo, J.M. (2016). Open-Cell Porous Metals for Thermal Management Applications: Fluid Flow and Heat Transfer. Journal of Materials Science and Technology, pp. 1-12. (DOI: 10.1080/02670836.2016.1180795)

Baloyo, J. M. and Zhao, Y. Y. (2015). Heat Transfer Performance of Micro-Porous Copper Foams with Homogeneous and Hybrid Structures Manufactured by Lost Carbonate Sintering. MRS Proceedings, 1779, pp 39-44. (DOI:10.1557/opl.2015.699).

List of Tables

List of Figures

List of Symbols

A	cross sectional area to fluid flow	m^2
B	pore shape coefficient	
C	form drag coefficient	m^{-1}
c	empirical parameter in Eq. 2.10	
C_F	Forchheimer coefficient	m^{-1}
D	sample diameter	m
d	distance	m
d_i	average distance from pore to pore	m
D_p	particle diameter	m
d_p	pore diameter	m
f	thickness fraction	
h	heat transfer coefficient	$W/(m^2K)$
J	heat flux	W/m^2
K	permeability	m^2
k	thermal conductivity	W/(m.K)
L	length of the porous medium or flow length	m
l	characteristic length	m
m	mass	g
n	exponent or fitting constants	
P	pressure	Pa
p_h	partition factor	
Q	volumetric fluid flow rate	m^3/s
q	heat transfer rate	W
r	average throat radius	m

Re	Reynolds number	
s	scaling factor	
S_v	surface area per unit volume	mm^2/mm^3
T	temperature	K
t	thickness of the sample	m
u	fluid velocity in the velocity boundary layer	
V	sample volume	m^3
v	flow velocity	m/s
V_d	Darcian velocity	m/s
V_R	interstitial fluid velocity or real velocity	m/s
W	weight of the copper powder	g
w	weighting factor	
x	coordinate in the x direction	m
z	porosity variable	

Greek symbols

ϕ	porosity fraction	
μ	fluid viscosity	Pa.s
ρ	density	kg/m^3
τ	tortuosity	

Subscripts

0	initial
atm	atmosphere
B	bulk material
b	bottom region
Cu	copper
cr	percolation threshold
eff	effective
f	fluid
h	higher porosity layer
i	*i*th layer
in	inlet
k	kinematic
K_2CO_3	potassium carbonate
l	lower porosity layer
max	maximum
min	minimum
out	outlet
p	porous material
s	solid or sample
t	top region
VB	vertical bilayer
F	finite value or outer flow

Abbreviations

DP	directional porosity
H	homogeneous sample
HB	horizontal bilayer sample
IVB	integrated vertical bilayers
LCS	Lost Carbonate Sintering
SS	segmented structures
SVB	segmented vertical bilayers
VB	vertical bilayer

Chapter 1 Introduction

Porous metals are multi-functional materials that offer a combination of properties. Porous metals have proven to be highly suitable for thermal management applications, such as compact heat exchangers, due to their high surface area density and superior thermodynamic properties, together with permeability for fluid flow. The heat transfer performance of porous metals depends greatly on their structural property, which is dictated by the manufacturing process. The present study focuses on the fluid flow and heat transfer performance of porous copper produced by the Lost Carbonate Sintering (LCS) process.

1.1 Background and Motivation of the Research

As technologies become more advanced, they use more energy and hence generate a lot of heat as waste product. For example, the high demand for faster computers has led to high amounts of heat generated at chip level. This could lead to damage to the chip and decrease in the system's performance. Another example is found in a proton exchange membrane fuel cell (PEMFC) - deemed as the next generation power source for a wide range of applications like transportation and portable devices. Even though PEMFCs have very high energy conversion efficiency, they generate a significant amount of heat as waste energy. This high amount of heat could lead to membrane degradation. Therefore, it is important to remove the waste heat generated to avoid overheating, hence prevent damage to a system and increase a system's performance. As a consequence, the demand for effective cooling techniques for thermal management (i.e. more efficient heat exchangers) has increased dramatically over the recent years. Effective cooling, however, is very challenging. Porous

metals are promising effective cooling solutions due to their superior thermodynamic characteristics and good mechanical properties.

Porous metals have attracted a lot of attention in the academic field, as well as in industry due to their excellent mechanical, chemical, electrical and thermal properties (Banhart et al. 1999, Zhao et al. 2005). Porous metals are used in numerous applications such as mechanical damping, lightweight and sandwich structures, energy and sound absorption, catalyst supports and filtration. In addition, porous metals are highly valuable for thermal management applications due to their high internal surface area and high permeability for fluids. As a result, porous metals have the ability to transport large amount of heat over a small volume, making them the ideal materials for compact heat exchangers.

There have been several investigations in the past on the use of porous metals in cooling systems for electronic devices (Ogushi et al. 2006, Bourantas et al. 2014, Carpenter and da Silva 2014). The cooling system is typically made up of a liquid or gas coolant flowing through the internal pores of a porous metal medium. The coolant transports heat away from the medium by heat conduction and convection and consequently, cools the system. The ideal porous metal used for this application is porous copper due to its high thermal conductivity.

Currently, there are several methods used to manufacture porous metals. The most popular method is by powder metallurgy through sintering copper particles together without using

fillers. This method was found to produce porous copper of low and narrow porosity range (below 50%) (Zhang et al. 2009). Investment casting has also been used to produce porous metals, whereby a ceramic mould is used to cast the porous metal. The investment casting route can produce porous metals of excellent quality and with a high and narrow porosity range (above 80%) (Zhang et al. 2009). However, the cost of producing porous metals by investment casting is extremely high. Currently existing porous metals, in particular porous copper, have a porosity of either more than 80% or less than 50% (Zhang et al. 2009), limited by the manufacturing methods. There is few report on porous copper of porosity in the range of 50% to 80%.

Lost Carbonate Sintering (LCS) is a patented process used for manufacturing micro-porous metals with controlled pore size, porosity and pore shape. The LCS process was invented in the University of Liverpool (Zhao et al. 2005). LCS has provided a way in which porous copper can be produced with various pore sizes and a large range of porosity from 40% to 85% (Zhao et al. 2005, Zhang et al. 2009). LCS porous copper was found to be an excellent candidate for thermal management applications due to its unique pore morphology, excellent sintered strength and the homogeneity of its structure (Zhang et al. 2009).

So far, research on LCS has been focused mainly on process development and evaluation of the physical and mechanical properties of the structures produced. The thermal properties of the LCS structures produced have also been analysed. However, this limited research has only been confined to homogeneous porous structures. The LCS process has now matured

making it suitable for industrial scale production and the development of novel structures, maximising the potential of the LCS porous metals for various applications.

For homogeneous LCS structures, the thermal conductivity and fluid permeability are highly dependent on the porosity and pore size. The structural parameters of the porous LCS metals, therefore, dictate their thermal properties. As such, by optimising the structural parameters through changing the structure, the thermal exchange performance of the LCS porous metals can be further improved.

1.2 Research Aims and Objectives

This project aims to study and develop LCS porous copper with good thermal conductivity allied with good fluid permeability to maximise the heat exchange performance, intended for use in thermal management applications. This project explores the ways in which the heat exchange performance of LCS porous copper can be optimised by using tailored, non-homogeneous structures.

One of the project's objectives is to optimise the process conditions of the LCS process for manufacturing tailored porous copper structures. The fluid flow and heat transfer performance of the homogeneous and non-homogeneous LCS porous structures will be studied and compared. Another objective is to investigate how the structural parameters (pore size, porosity and pore distribution) affect the heat transfer coefficient of the homogeneous and non-homogeneous porous copper structures. This will allow the

formulation of a correlation between the structural parameters and the heat exchange performance in both homogeneous and non-homogeneous LCS structures.

1.3 Thesis Structure

This thesis includes seven chapters. Chapter 2 is a literature review of the work relevant to this study. A variety of open-cell or close-cell porous metals and their respective production methods are reviewed. Particular attention is given to porous metals for thermal management applications, which is highly relevant to this study. The fluid flow and heat transfer properties of porous metals are discussed in detail. Additionally, studies on porous metals produced by the LCS process are also reviewed, exploring the great potential of LCS porous copper for thermal management applications.

Chapter 3 details the experimental procedures involved in this study. The preparation conditions of the porous copper samples with homogeneous and non-homogeneous structures using the LCS process are presented. The techniques used for structural analysis and the experimental procedures for the measurement of fluid permeability and heat transfer coefficient are also described in detail.

Chapter 4 presents the results obtained from the structural analysis of the LCS porous copper with homogeneous and non-homogeneous structures. The microstructure and pore parameters of these LCS porous copper samples are discussed and analysed in detail.

Chapter 5 presents and discusses the results from the fluid permeability tests for homogenous and non-homogeneous structures. The effects of the pore structure parameters on the fluid permeability of homogeneous samples are presented and expounded. In addition, the effects of non-homogeneous structures on the fluid flow are also evaluated in this chapter. Comparative analysis of the fluid flow between the LCS porous copper samples and other existing porous metals available in literature is also presented.

Chapter 6 presents and discusses the results obtained from the heat transfer experiments. The heat transfer coefficients of both homogeneous and non-homogenous LCS porous copper samples are evaluated. The influence of the fluid flow properties on the heat transfer performance of the LCS structures is also discussed in detail. Moreover, the correlations between the fluid flow and heat transfer performance of the as-produced LCS structures are explored.

Finally, Chapter 7 concludes this study. Important results and findings are summarised in this chapter. Recommendations for future work are also presented.

Chapter 2 Literature Review

2.1 Introduction to Porous Metals

Porous metals have garnered a lot of attention in engineering research fields over the past years owing to the wide range of applications. Porous metal by definition is a porous medium consisting of a solid metal matrix and pores/voids. Porous metals are low cost and lightweight structures with distinctive mechanical, thermal, electrical and acoustical properties. With the rapid progress in the development of manufacturing processes, it is possible to tailor the structures of porous metal to produce the desired properties.

Porous metals are also multi-functional materials, and as such, they are currently being used in a very wide range of applications, including applications in aviation (e.g. sandwich parts and reinforcements for load-bearing structures), transportation (e.g. soot-loading and crash elements), civil (e.g. sound absorption materials) and biomedical engineering (e.g. dental and orthopaedic implants) (Dukhan 2013, Ashby et al. 2000, Banhart 2001). With the continued advancement of this field, many more applications of porous metals are expected.

There are two types of porous metals: closed-cell and open-cell. The voids in open-cell porous metals are interconnected, providing pathways for fluid flow and making them useful for heat exchanger applications. The voids in closed-cell porous metals are not connected and are separated by the solid metal matrix. Closed-cell porous metals are typically used for impact-absorption applications.

Since the 1990's, the research and development of porous metals has become highly popular (Dukhan 2013). Currently, there is a vast number of manufacturing processes capable of producing high quality porous metals, with the powder metallurgy routes being one of the most common production methods.

2.2 Production Methods of Porous Metals

A numerous number of production methods have been developed to produce porous metals with either open-cell or closed-cell structures. Each of these methods produces porous metals with unique characteristics, such as distinct cell morphology, cell size, porosity and/or pore distribution. This section reviews some of the most common production techniques currently used in industry.

Banhart (2001) developed a system to classify these production methods according to the initial state of the metal. The initial metal states can be in the form of a liquid, solid/powder, metal vapour/gas or metal ion solution. Table 2.1 shows some examples of the production methods that fall into these categories. The following sections compare and describe these methods.

Table 2.1: Examples of metal foam production methods (Banhart 2001, Dukhan 2013).

Classes	**Liquid Metal**	**Solid/Powdered Metal**	**Metal Vapour**	**Metal Ions**
Examples	*- direct foaming* *-solid-gas eutectic solidification* *-powder metallurgy* *-investment casting* *- space-holder casting* *-"Osprey" process*	*-sintering of metal powders/fibres* *-slurry foaming* *-pressing around space-holder fillings* *-sintering of metallic hollow spheres*	*-vapour deposition*	*-electrochemical deposition*

2.2.1 Liquid State Methods

Metals in their liquid state can be transformed to porous metals by direct foaming, solid-gas eutectic solidification, powder metallurgy, investment casting, space-holder casting and the "Osprey" process.

2.2.1.1 Direct Foaming

Direct foaming can be performed in two ways: 1) the gas is injected into the melt directly by an external force (foaming by gas injection) or 2) the gas is created in-situ by adding gas-releasing blowing agents to the liquid melt (foaming by blowing agents). Due to the high buoyancy forces, the gas bubbles created in the high density liquid melt rise to the surface. Fine ceramic powders or alloying elements (e.g. SiC, Al_2O_2 and MgO) that form stabilising particles (10-20% vol. fraction) are often added to the melt before foaming to allow the ascension of the bubbles (Jin et al. 1990, Kenny and Thomas 1994, Banhart 2001). Fig. 2.1 is an example of metal foam produced by "foaming by gas injection" technique, while Fig. 2.2 is an example of a porous metal produced using the "foaming by blowing agents" technique.

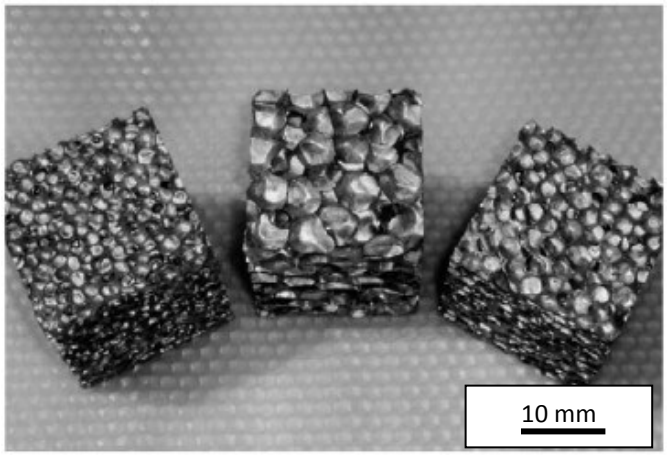

Figure 2.1: "METCOMB" aluminium foam manufactured by direct foaming (Babcsan, Leitimeier and Banhart 2005).

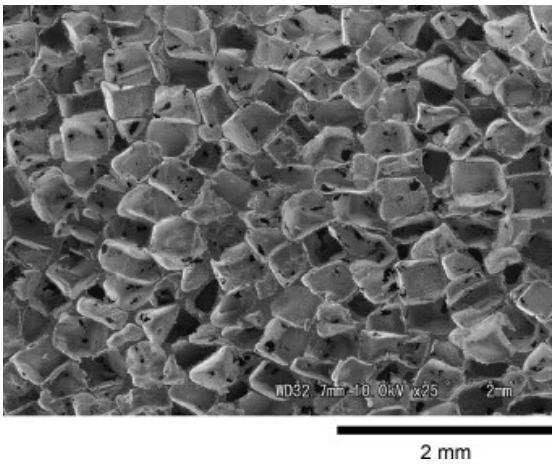

Figure 2.2: "Alporas" aluminium foam manufactured by "foaming using blowing agents" (Hakamada et al. 2007).

The resulting solid foam can be continuously produced with up to 10 cm in thickness. However, the distribution of the stabilising particles can be inhomogeneous which can lead to defects in the foam structure (Lloyd et al. 1991, Banhart 2001). The resulting foam can also be brittle due to the reinforcing particles in the cell walls.

2.2.1.2 Solid-Gas Eutectic Solidification

The solid-gas eutectic solidification process involves melting the metal (e.g. Cu, Ni, Al and Mg) in the hydrogen atmosphere (50 atm) to obtain a homogeneous melt charged with hydrogen (Banhart 2001). A eutectic transition to a solid+gas phase occurs when the temperature is lowered. This leads to directional solidification advancing through the liquid melt. The hydrogen content close to the plane of solidification is enhanced and as a consequence, gas bubbles are created. Fig. 2.3 is an image of the resultant foam, also known as "gasars" or "lotus-type" foam, which contains large directional pores with diameters of 10 µm – 10 mm and pore length of 100 µm – 30 cm (Shapovalov 1998).

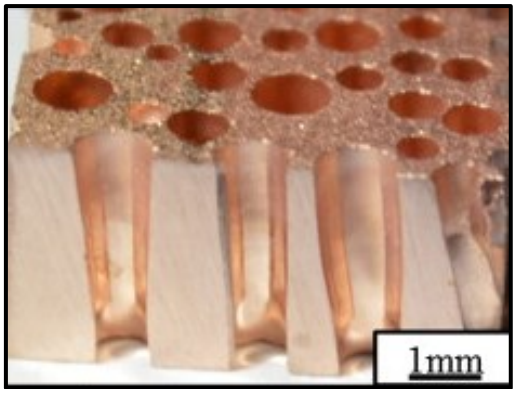

Figure 2.3: Gasar copper manufactured using the solid-gas eutectic solidification method (Du et al. 2015).

2.2.1.3 Powder Metallurgy

In the powder metallurgy, or powder-compact melting process, the blowing agents (e.g. TiH_2 or ZrH_2) are homogeneously distributed and embedded into the powdered metal matrix (e.g. Zn or Al alloys) by compaction (i.e. isostatic compression or rod extrusion), ensuring that no residual porosity remains. The green compact is then heat treated just below the matrix metal's melting point to decompose the blowing agents. The decomposition releases gas causing the matrix to expand. Fig. 2.4 shows the resulting structure, which is highly porous with fairly uniform pore morphology.

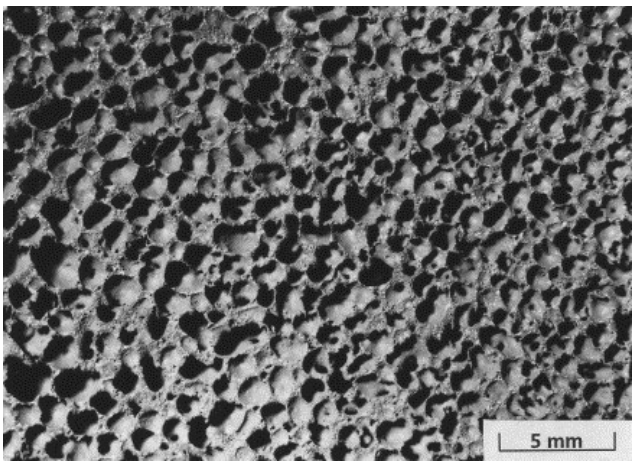

Figure 2.4: Porous lead foam made using the powder metallurgical process (Banhart 2001).

2.2.1.4 Investment Casting

In investment casting, a polyurethane foam firstly undergoes thermo-physical shock treatment (or reticulation) to remove residual closed cells. The resulting foam is then filled with a refractory moulding material and after curing, the polymer foam is burnt out. The molten metal (e.g. Al alloys, Cu and Mg) is cast into the resulting cavities, replicating the structure of the original polymer foam. Once solidified, the mould material is removed, which leaves a highly porous (80-95% porosity) and open-celled metallic structure, as shown in Fig. 2.5 (Dukhan 2013).

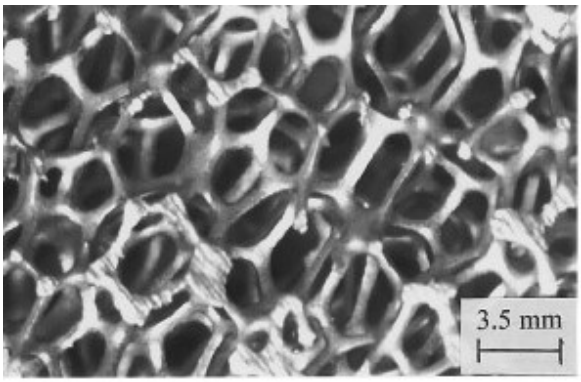

Figure 2.5: "Duocel" aluminium foam manufactured using investment casting (Harte, Fleck and Ashby 1999).

2.2.1.5 Space-Holder Casting

The space-holder casting technique can be done in two ways: 1) low density hollow spheres or inorganic/organic granules can be added into the metallic melt or 2) the molten metal is cast around the granules. The space-holders need pre-heating to prevent premature solidification of the melt. Pressurising the melt is also necessary to prevent residual porosities. The granules can then be removed either by heat treatment or leaching techniques to produce "sponge-like" foams as displayed in Fig. 2.6. Alternatively, they can remain in the metal matrix to produce syntactic foams as shown in Fig. 2.7. Currently, a wide range of metals (e.g. Al, Mg, Pb and Sn) can be processed using this method.

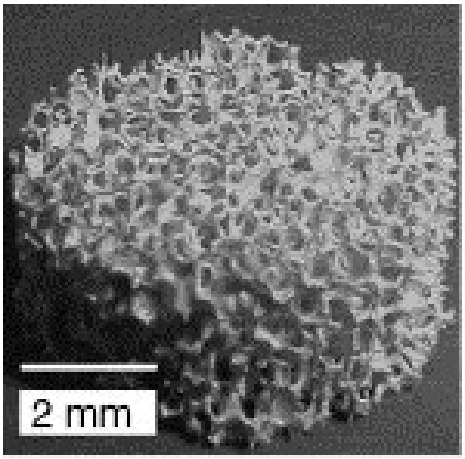

Figure 2.6: Foam produced using the space holder casting method where the space-holder is removed (Sharafat 2006).

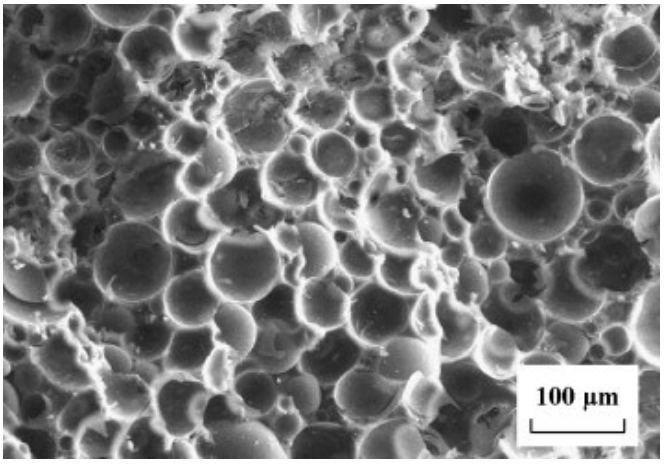

Figure 2.7: A typical micrograph of a syntactic foam produced by the space-holder casting method where the space-holder remains in the matrix (Li et al. 2009).

2.2.1.6 Osprey Process

In the Osprey process, also known as the spray forming process, the molten metal is atomised and sprayed onto a substrate. The droplets deposit and solidify. The resulting foam, as shown in Fig. 2.8, possesses fine grain size with low oxide content (Banhart 2001). In addition, the properties of the manufactured foam can be modified by injecting powders into the spray. For example, gas-releasing powders can be added into the spray to create larger pores in the deposit. However, the maximum porosity achievable through this process is only 60%. The pore morphology is also not uniform, and as such, its properties will differ throughout the structure.

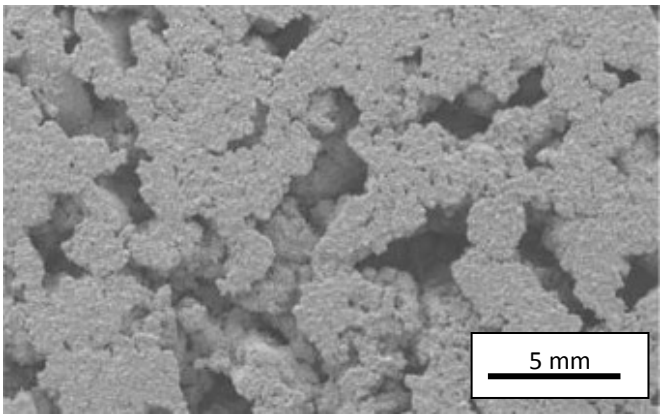

Figure 2.8: Titanium foam made using the osprey process (Fujibayashi 2004).

2.2.2 Solid State Methods

Metals in their solid state can be transformed to porous metals by metal hollow spheres/powders/fibres sintering, using space-holder fillers or slurry foaming.

2.2.2.1 Sintering of Metal Powders or Fibres

The metal powder/fibres (e.g. Ti, bronze, stainless steel) are compacted or moulded to shape then sintered at an elevated temperature. The resulting foam, as shown in Fig. 2.9,

can have a relatively low porosity, in the range of 20% to 50% (Banhart 2001). Through subsequent sintering, its comparatively low strength can be increased.

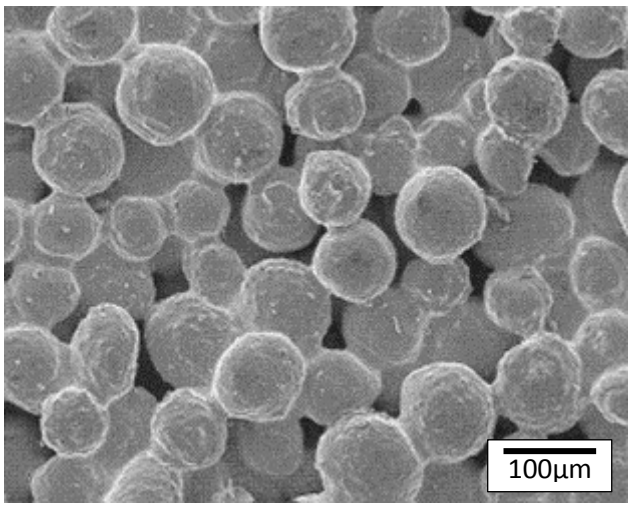

Figure 2.9: Porous sintered bronze (Eisenmann 1998).

2.2.2.2 Slurry Foaming

Slurry consisting of the metal powder, blowing agents and reactive additives is prepared and poured into a mould. It is then heated up causing the slurry to become viscous and expand. The expanded slurry is dried and the resulting metal foam is sintered to enhance the strength. A typical structure of the metal foam produced by this process is illustrated in Fig. 2.10.

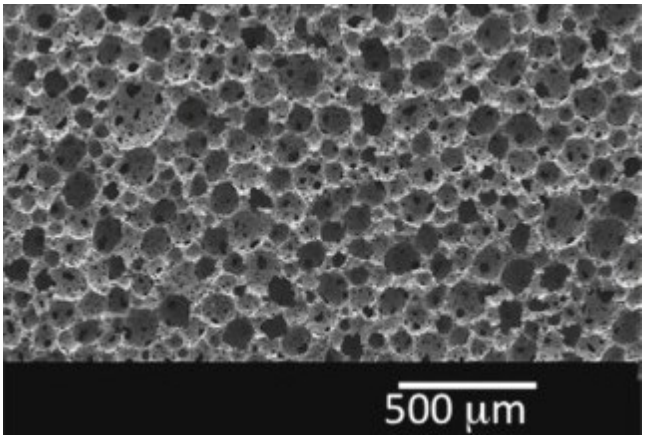

Figure 2.10: Typical structure of a foam produced by the slurry foaming technique (Gladysz and Chawla 2015).

2.2.2.3 Space-Holder Fillings

Highly porous titanium, stainless steel and nickel-based superalloys with 60-80% porosity can be produced using space-holder fillings. Ceramic particles, polymer grains, salts or hollow spheres are just some of the types of space-holders currently used. The process involves mixing the space holder with the metal powder, with the addition of a suitable solvent/binder. The mixture is then pressed and the space-holder removed by thermal treatment. The compacts are then sintered in a vacuum atmosphere to produce metal foams, as displayed in Fig. 2.11, with comparatively high strength.

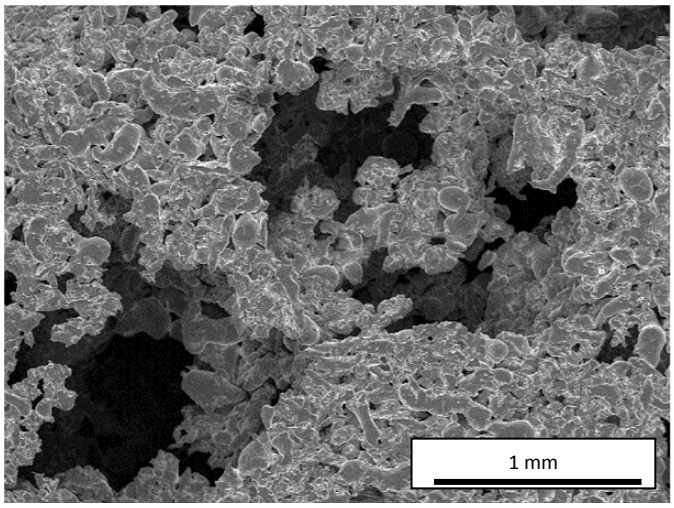

Figure 2.11: Microstructure of an Inconel 600 foam produced using carbamide space holder (Bram et al. 2000).

2.2.2.4 Metallic Hollow Spheres

Metallic hollow spheres (e.g. Cu, Ni, Ti) can be produced by electrochemical deposition of the metal onto a polymer sphere, wherein a metal+binder suspension is coated onto the polymer spheres. The coated spheres are then sintered to remove the polymer and produce a dense metal shell. The individual hollow spheres (0.8 mm to 8 mm) are then bonded together by sintering to produce the metal foam, as shown in Fig. 2.12.

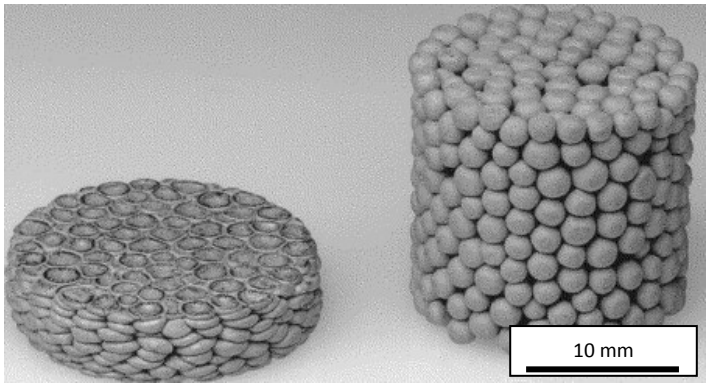

Figure 2.12: Open hollow sphere structure made from stainless steel spheres by sintering: after and before axial deformation (Banhart 2001).

2.2.3 Vapour State Method (Vapour Deposition)

Metals in their vapour state can be transformed to porous metals by the vapour deposition technique. A cold solid precursor structure (e.g. polyurethane) is placed in a vacuum chamber where the metal vapour can be produced. The metal vapour condenses onto the precursor, coating its surface. The thickness of the coating is dependent on the vapour density and time of exposure. The polymer is then removed from the metal matrix by thermal or chemical treatment. The resulting foam can have a very high porosity, as displayed in Fig. 2.13.

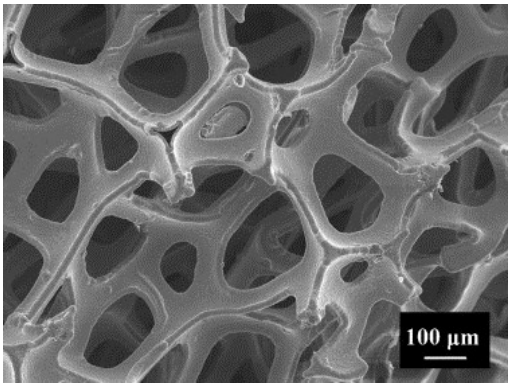

Figure 2.13: "Incofoam" produced using the "nickel carbonyl process"; a type of vapour deposition technique (Li, Yang and Zhitornirsky 2008).

2.2.4 Ionic State Method (Electro-Deposition)

Metals in their ionic state can be transformed to porous metals by electro-deposition techniques. In this process, the polymer foam precursor is coated with a conductive layer by dipping into conductive slurry or by cathode sputtering. The metal can then be electrically deposited onto the electrically conductive polymer foam. The polymer foam is removed by thermal treatment, leaving a porous metal with hollow struts, as seen in Fig. 2.14. Metal foams made of nickel, Ni-Cr alloys and copper can be produced using electro-deposition.

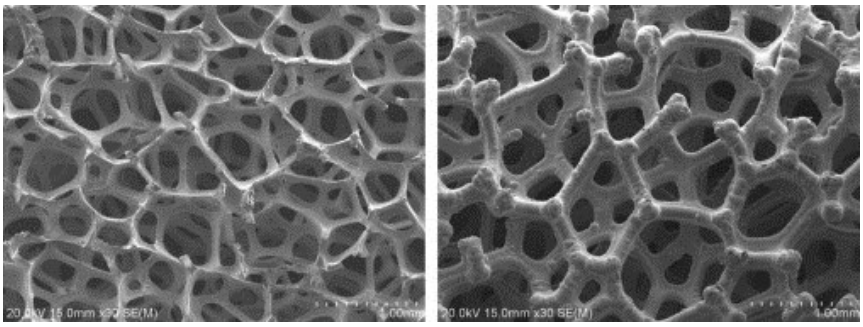

Figure 2.14: Nickel foams produced by electro-deposition process (Liu and Chen 2014).

2.2.5 Summary

Table 2.2 summarises the production methods presented in this section, including the achievable structural properties of the foam. It is evident that the structure of the resulting porous metals is unique to the production method chosen. As a consequence, the characteristics (e.g. mechanical, thermal and fluid flow properties) are also distinctive.

Table 2.2: Manufacturing processes for porous metals (Banhart 2001, Dukhan 2013).

Category	Method	Pore Type	Achievable Porosity (%)	Advantages	Disadvantages
Liquid State	Direct Foaming	Closed-cell	80-98	-foam can be produced in large volumes	-brittle foam - pore morphology prone to defects -unsuitable for use as porous heat exchanger
	Solid-gas eutectic solidification	Directional pores	5-95	-production of directional pores	-unsatisfactory homogeneity of pores -process parameters need to be carefully controlled -pores may not be interconnected, limiting its suitability for use as porous heat exchanger
	Powder metallurgy	Closed-cell or open-celled	60-90	-near-net shape can be obtained -mass production -suitable for use as porous heat exchanger	-process parameters need to be carefully controlled
	Investment casting	Open-cell	80-97	-complex shapes can be obtained by pre-forming the polymer foam -suitable for use as porous heat exchanger	-difficulties in removing the mould material from the metal matrix
	Space-holder casting	Open-cell	≤80	-close control of pore distribution -suitable for use as porous heat exchanger	-process parameters need to be carefully controlled
	"Osprey" process	Open-cell	≤60	-properties can be modified by injecting powders (oxides or gas producing powders) into the spray	-maximum porosity of 60% -non-uniformity of the pore morphology -pores may not be interconnected, limiting its suitability for use as porous heat exchanger
Solid State	Sintering of metal powders/fibres	Open-cell	20-50	-strength can be increased through subsequent sintering	-very low porosity range achievable -pores may not be interconnected, limiting its suitability for use as porous heat exchanger
	Slurry foaming	Open-cell	≤93	-large porosity range achievable -suitable for use as porous heat exchanger	-insufficient strength -cracks may exist
	Pressing around space-holder fillings	Open-cell	≤80	- large porosity range achievable suitable for use as porous heat exchanger	-size limitation for efficient removal of space-holder
	Sintering of metallic hollow spheres	Open-cell or Closed-cell	≤96	-produce open/closed porosity with ordered/disordered pore arrangement -uniform pore distribution suitable for use as porous heat exchanger	-irregular shaped pores
Vapour State	Vapour deposition	Open-cell	92-95	-pore morphology can be tailored	-only high porosity range achievable -high production costs; impractical for the production of porous heat exchangers
Ionic State	Electro-deposition	Open-cell	93-98	-pore morphology can be tailored	-only high porosity range achievable -high production costs; impractical for the production of porous heat exchangers

Open-celled porous metals are highly suitable for heat exchanger application, where a cooling fluid can flow through the interconnecting voids. The space-holder method, such as the Lost Carbonate Sintering (LCS) process, is a cost-effective technique that enables the production of open-celled porous metals with tailored pore structure (e.g. tailored porosity and pore size). This makes the LCS process highly suitable for the manufacture of open-celled porous metals for use as heat exchangers.

2.3 Porous Metals for Thermal Management Applications

Open-cell porous metals allied with fluid flow, are utilised in thermal management applications to improve the convective heat transfer of industrial processes, such as in power stations, combustion systems and for cooling turbine blades or electronic devices (Mahdi 2015). Due to their high heat transfer surface area density and superior thermodynamic characteristics, porous metals are a promising alternative for compact heat exchangers (Ghosh 2009).

Ejlali et al. (2009) numerically investigated the applicability of high-porosity metal foams as air-cooled heat exchangers for geothermal power plants and found that metal foam heat exchangers are superior compared to conventional finned surfaces at no excess cost (material weight and/or pressure drop). Boomsma, Poulikakos and Zwick (2003) proved experimentally that compressed open-cell Al metal foam heat exchangers generated thermal resistances that were 2-3 times lower than the best commercially available heat exchanger tested under similar pumping power. Similarly, Mao et al (2014) demonstrated

that the heat transfer capability of metal foam heat exchangers can supersede conventional compact heat exchangers given optimal scenario (i.e. optimal porosity and foam thickness).

Hutter et al (2011) reviewed the factors that greatly influence the heat transfer performance of porous metal-coolant heat exchangers. It was reported that the coolant properties (e.g. heat capacity or thermal conductivity) have a significant influence on the convective heat transfer of the metal-foam system. Similarly, the choice of the foam material also influences the heat transfer performance significantly. Apart from the material's thermal and mechanical properties, factors such as corrosion and its suitability in very high temperature environments also need consideration. Lastly, the foam structure considerably affects the heat transfer performance, with porosity, pore size and surface area having the greatest weightings on the effective thermal conductivity, convective heat transfer and fluid flow properties. Zhao (2012) reviewed comprehensively the previous research progress on the heat transfer in metal foams for thermal management applications.

2.4 Fluid Flow in Porous Media

Permeability is an important property of porous media. Permeability describes how easy a fluid can flow through the porous material. By definition, permeability refers to the conductivity of a porous medium with respect to fluid flow (Pal, Joyce and Fleming 2006). In addition, permeability is dependent on the nature of the porous material, i.e. its porosity, the distribution and 'connectedness' of the pores, and the pore size.

The most common theory used to evaluate fluid transport in porous media is Darcy's law:

$$\frac{\Delta P}{\Delta L} = \frac{\mu}{K}\frac{Q}{A} \tag{2.1}$$

where ΔP is the pressure drop (Pa), ΔL is the flow length (m), K is the permeability (m^2), μ is the viscosity of the fluid (Pa.s), Q is the fluid flow rate (m^3/s) and A is the cross sectional area to fluid flow (m^2) (Darcy 1856). A material is highly permeable if the permeability value is large.

Darcy's law was formulated on the late 18th century while investigating water flow through sand filters for water filtration (Tiab and Donaldson 2012); however, it was not until recently that it was applied to other porous structures. In the 19th century, Darcy's law was modified several times to fit different applications and conditions (Preziosi and Farina 2002, Gibson 1992, Davis, Olague and Goodrich 1992).

2.4.1 Modification to Darcy's Equation

Since the formulation of Darcy's law, researchers repeated the experiment using different porous media and developed equations to describe the linear flow of incompressible or slightly compressible fluids through porous media (Tiab and Donaldson 2012), assuming that:

1) there exists a steady-state flow,
2) viscosity of the fluid remains constant,
3) gravity forces are negligible,
4) permeability and porosity are constant and independent of pressure, and
5) flow is laminar and that turbulent effects are negligible.

Darcy's law can be modified to describe the flow of incompressible fluids, such that:

$$V_d = -\frac{K(P_{out}-P_{in})}{\mu L} \tag{2.2}$$

where $V_d = \frac{Q}{A}$ is the apparent velocity (also known as Darcian velocity), P_{in} is the fluid's inlet pressure and P_{out} is the outlet pressure (Pa). For compressible fluids, like air, Darcy's law can be revised to:

$$V_d = -\frac{K(P_{out}^2-P_{in}^2)}{2\mu L P_{out}} \tag{2.3}$$

Various researchers found that a deviation from Darcy's law arises when the fluid flow velocity is increased. Wright (1968) explained that this phenomenon is due to the inertial effects followed by turbulent effects.

The modified Darcy's law, commonly known as the Forchheimer's equation, describes the steady-state flow as:

$$\frac{\Delta P}{\Delta L} = \frac{\mu V_d}{K} + \rho_f C {V_d}^2 \tag{2.4}$$

where ρ_f is the fluid density (kg/m^3) and C is the form drag coefficient, also known as the turbulence factor, non-Darcy factor or Forchheimer factor.

Cornell and Katz (1953) observed that for low flow velocity, linear Darcy's law applies, whereas for high flow velocities, turbulent flow is dominant and the use of the quadratic Forchheimer equation (Eq. 2.4) is recommended to describe the turbulent flow and to determine the inertial effects. Many researchers also attempted to relate the form drag

coefficient with the permeability. Table 2.3 lists some of the correlations available in literature.

Table 2.3: Empirical *K*-*C* relations available in literature.

Author	Model	Unit of K	Unit of C	Reference
Cornell	$C = \frac{4.11 \times 10^{10}}{K^{\frac{4}{3}}}$	mD	ft^{-1}	Tiab & Donaldson 2012
Geertsma	$C = \frac{4.85 \times 10^{4}}{\phi^{5.5}\sqrt{K}}$	mD	ft^{-1}	Geertsma (1974)
Liu et al.	$C = \frac{8.91 \times 10^{4}\tau}{\phi K}$	mD	ft^{-1}	Liu et al. (1995)
Thauvin & Mohanty	$C = \frac{1.55x10^{12} \times \phi^{0.449}}{K^{1.88}}$	mD	cm^{-1}	Li & Engler (2001)
Janicek & Katz	$C = \frac{1.82 \times 10^{8}}{\phi^{0.75}K^{1.25}}$	mD	cm^{-1}	
Pascal et al.	$C = \frac{4.8 \times 10^{12}}{K^{1.176}}$	mD	m^{-1}	
Jones	$C = \frac{6.15x10^{12}}{K^{1.55}}$	mD	ft^{-1}	
Coles and Hartman	$C = \frac{1.07 \times 10^{12}\phi^{0.449}}{K^{1.88}}$	mD	ft^{-1}	
Cooper et al.	$C = \frac{\tau^{1.943}}{10^{3.25}K^{1.023}}$	cm^{-2}	cm^{-1}	

Note: where ϕ is the porosity fraction and τ is the tortuosity.

It is worth noting that the relations in Table 2.3 are only approximations obtained from curve fitting of experimental data. Hence, the constants in the relations will vary between different fluid-foam systems.

2.4.2. Reynolds Number

Reynolds number (*Re*) is used for Newtonian fluids to describe their viscous behaviour, since Re is the ratio of the inertia to viscous forces. Reynolds number is dimensionless and can be described as:

$$Re = \frac{\rho_f v l}{\mu} \tag{2.5}$$

where ρ_f is the fluid density (kg/m^3), v is the flow velocity (m/s) and l is the characteristic length (m) (White 2009). Alternatively, Reynolds number can also be expressed using kinematic viscosity, μ_k, where $\mu_k = \frac{\mu}{\rho_f}$, such that:

$$Re = \frac{v l}{\mu_k} \tag{2.6}$$

At low Re range, the flow is in the laminar region (Darcy's regime) where the fluid moves along smooth streamlines parallel to the pipe wall and the fluid velocity remains the same. At low Re, inertial effects are very small so the fluid is said to flow in a viscous creeping motion (White 2009). As the Re increases, a transition occurs where the flow is unpredictable, and both laminar and turbulent flows are present. At higher Re range on the other hand, the flow is said to be turbulent due to higher inertial effects present, and the flow is said to be in the Forchheimer's regime.

The Re number is dependent on the flow geometry and as such, the distinction between low, moderate and high Re will vary in different flow systems. In direct pipe flows, determining the characteristic length (l) is straight-forward. For porous medium, however, determining the characteristic length is more complex due to the intricate structure. Some studies described the characteristic length as equivalent to the pore size, some as the equivalent diameter of the flow channel, while others suggested that it is the square root of the permeability. As a consequence, a very wide range of Re numbers listed for porous media can be found in the literature.

A large amount of research has been conducted in the past to evaluate the Re values of different flow systems. Kececioglu and Jiang (1994) suggested that Darcy's law only applies at extremely low flow viscosities where the Reynolds number is in the range of 0.3 to 0.7. Farkas, Zhong and Guiochon (1999) investigated the validity of Darcy's flow at low flow rates using liquid chromatography and concluded that Darcy's law only applied to low flow velocities in the range of Re = $1x10^{-6}$ to $1x10^{-4}$. Cornell and Katz (1953) found that for gas flow through consolidated porous medium, the flow regime was laminar at Re < 0.08 where the pressure drop was directionally proportional to the flow rate. At 0.08 < Re < 8, the transition region occurred and at Re > 8, the flow became turbulent. Ergun (1952) observed that the critical Re = 3-10 was found for gas flow through packed beds. Hassanizadeh and Gray (1987) suggested that Re = 10 is the critical value for non-Darcy flow behaviour due to the increase of the microscopic viscous force at high velocities.

Numerical models were also used to predict the critical Re where the flow transits to turbulent flow from laminar. Blick and Civan (1988) used capillary-orifice modelling to simulate fluid flow in the porous media, and reported that the critical Re is 100 for non-Darcy behaviour. Du Plessis and Masliyah (1988) on the other hand used a representative unit cell model and calculated the critical Re = 3-17. Thauvin and Mohanty (1988) used a network model to simulate the porous media using the pore throat radius, and found the critical Re to be 0.11.

Table 2.4 summarises the Reynolds numbers listed in this section and their definitions. So far, calculations for critical Re have been inconsistent due to the varying definitions used. As

a consequence, there is currently no widely accepted criterion for non-Darcy flow in porous media (Zeng and Grigg 2006).

Table 2.4: Comparison of Reynolds numbers for Darcy flow and Forchheimer flow regimes of various porous media reported in literature.

Reference	Re Definition	Fluid	Porous media	Darcy's flow	Transition	Forchheimer's Flow
Kececioglu & Jiang (1994)	$Re = \frac{\rho_f v\sqrt{K}}{\mu}$	water	3mm beads	0.3-0.7	0.7-1.6	>1.6
			6 mm beads	0.6-1	1-3	>3
	$Re = \frac{\rho_f V_R\sqrt{K/\phi}}{\mu}$		3mm beads	0.062-0.120	0.120-0.34	>0.34
			6 mm beads	0.062-0.120	0.120-0.34	>0.34
Farkas, Zhong & Guiochon (1999)	$Re = \frac{\rho_f v D_P}{\mu}$	Ethylene glycol	Packed spheres	$1x10^{-6}$ to $1x10^{-4}$	-	-
Cornell & Katz (1953)	$Re = \frac{\rho_f v D_P}{\mu}$	gas	Packed beds	<0.08	0.08-8	>8
Ergun (1952)	$Re = \frac{\rho_f v D_P}{\mu}$	gas	Packed beds	0.1-3	3-10	>10
Hassanizadeh & Gray (1987)	$Re = \frac{\rho_f v d_p}{\mu}$	gas	Packed beds	-	10	-
Blick & Civan (1988)	$Re = \frac{\rho_f v d_p}{\mu}$	gas	Capillary tubes bundle	<100	100	>4000
Du Plessis & Masliyah (1988)	$Re = \frac{\rho_f v d_l}{\mu}$	-	Isotropic porous media	-	3-17	-
Thauvin & Mohanty (1988)	$Re = \frac{\rho_f v r}{\mu}$	gas	Porous medium	>0.11	0.11-0.17	Re>0.17
Bonnet, Topin & Tradist (2008)	$Re = \frac{\rho_f v d_p}{\mu}$	Gas and water	Metal foams	-	200	-
Despois & Mortensen (2005)	$Re = \frac{\rho_f v\sqrt{K}}{\mu}$	Water or glycerine	Polyurethane foam (75-400um)	0.5	-	-
Boomsma & Poulikakos (2001a)	$Re = \frac{\rho_f v\sqrt{K}}{\mu}$	Water	Aluminium foams (10-40PPI)	-	14.2-26.5	-
	$Re = \frac{\rho_f v d_p}{\mu}$			-	177-725	-
Dukhan, Bagci & Ozdemir (2014)	$Re = \frac{\rho_f v\sqrt{K}}{\mu}$	Water	Packed spheres	-	1-100	
Zhong et al. (2014)	$Re = \frac{\rho_f v\sqrt{K}}{\mu}$	Gas	Sintered metal powders	<0.1	0.1	>0.1
Dukhan & Ali (2012)	$Re = \frac{\rho_f v D}{\mu}$	Gas	Open-cell Al foam	-	20000-40000	-

Note: V_R= interstitial fluid velocity, D_p=particle diameter, d_p =pore diameter, d_l= average distance from pore to pore, r=average throat radius and D=sample diameter.

2.4.3 Influence of Pore Geometry on Fluid Flow

The geometry of the pores within porous metals greatly influences some of the functional properties, such as the permeability to fluid flow. Factors like porosity, pore size/characteristic length and pore distribution influence the fluid dynamics within the porous structure.

2.4.3.1 Porosity

The porosity (ϕ) of a porous medium, by definition, is a geometrical property that measures the fluid storage capacity of the porous structure (Pal, Joyce and Fleming 2006). The porosity can be described as the fraction of pores within the porous structure:

$$\phi = 1 - \frac{\rho_p}{\rho_B} \tag{2.7}$$

where ρ_p is the density of the porous material and ρ_B is the density of the bulk material. The greater the porosity, the more pores and less solid barrier are present within the structure, allowing the fluid to flow more freely. As a result, the permeability increases with porosity.

2.4.3.2 Characteristic Length

It is often difficult to accurately determine the characteristic length of a porous medium due to its complex structure. In some porous media with regular and uniformly distributed pores, the average pore size is often employed to determine the flow properties. Other studies use average pore to pore distance, average throat radius or the square-root of permeability as the porous structure's characteristic length.

Boomsma and Poulikakos (2001a) found experimentally that the permeability of open-celled metal foams increased with the characteristic length (average pore diameter), which was

similar to that found by Bhattacharya et al. (2002). Khayargoli et al. (2004) also observed increased permeability with increasing pore diameter for “Recemat” metal foams, which has a similar structure as that used by Boomsma and Poulikakos (2001a) and Bhattacharya et al. (2002), produced by the electro-deposition process. On the other hand, an opposite trend where the permeability increased when the pore diameter decreased was found for “IMI” (Industrial Materials Institute) metal foams produced by direct foaming technique (Boomsma and Poulikakos 2001a). This opposite trend was reported to be due to the decrease in tortuosity in IMI foams with smaller pores.

2.4.3.3 Tortuosity

Tortuosity characterises the fluid flow path through a porous medium. Sun, Tang and Cheng (2013) defined tortuosity simply as the ratio of the average pore length to the length of the porous medium along the major flow axis. A large tortuosity value indicates a windier channel for fluid flow, and is often linked to smaller permeability values and higher form drag coefficients. It was reported that with increased porosity, the flow becomes less tortuous since more channels are available for fluid flow (Sun, Tang and Cheng 2013, Matyka and Koza 2012).

2.4.3.4 Specific Surface Area

The specific surface area of a porous medium is defined as the interstitial surface area of pores and voids per unit volume. Several experimental methods are currently applied to determine the specific surface area of porous metals, including gas-adsorption method, fluid-permeation method and mercury method (Liu 2010). Liu et al. (2006) and Richardson et al. (2000) defined the specific surface area per unit volume of porous media (S_v) with porosity as:

$$S_v = \frac{4\phi}{d_p(1-\phi)} \tag{2.8}$$

where d_p is the pore diameter. In general, increasing the pore diameter of the metal foam leads to reduced specific surface areas.

2.4.3.5 Geometry-Permeability Models

There are many models that attempted to relate the geometrical properties (i.e. pore size and porosity) of the porous media to transport coefficients (i.e. permeability and form drag coefficient). Some of these models are discussed in this section.

The most widely accepted permeability-porosity model is the Carman-Kozeny power law model expressed as (Garboczi 1990, Ma 2015):

$$K = \frac{\phi^3}{B\tau^2 {S_v}^2} \tag{2.9}$$

where B is the pore shape coefficient, τ is the tortuosity and S_v is the surface area per unit volume. Other studies argued that the "percolation" threshold needs to be factored in the Carman-Kozeny model (Alkan 2009, Dienes 1983). It is assumed that below percolation threshold, the porosity becomes very low such that the connectivity between the pores becomes negligible. Sahimi (1994) suggested a power law model which considers the percolation threshold (ϕ_{cr}), such that:

$$K = c(\phi - \phi_{cr})^z \tag{2.10}$$

where c is an empirical parameter and z is a porosity variable. Other K-ϕ power law relationships include those proposed by Bayles et al. (1989), Costa (2006), Rodriguez et al. (2004) and Ghablezoo et al. (2009).

The relationship between permeability and porosity has also been described by exponential relationships. For example, Zhu and Wong (1997) suggested that:

$$K = K_0 \exp(n\phi) \tag{2.11}$$

where *n* is a constant. Similarly, a linear relationship between log(*K*) and porosity was proposed by Nelson (1994) and Bethke (1985), such that:

$$log_{10}K = n_1\phi + n_2 \tag{2.12}$$

where n_1 and n_2 are constants derived from the regression of the experimental data. Other exponential *K*-ϕ relationships include those proposed by Morris et al. (2003) and Yang and Alpin (2010).

In some studies, permeability was considered as a function of the geometric parameters of an equivalent channel in porous media. For example, Walsh and Brace (1984) suggested that:

$$K = \frac{(\frac{\phi}{S_v})^2}{\frac{\tau^2}{\phi}B} \tag{2.13}$$

where *B* is the pore shape coefficient, and $\frac{\tau^2}{\phi}$ is the equivalent channel in the whole porous structure.

Most of the aforementioned models are approximations from curve fitting of experimental data and can only be applied to a specific fluid-foam system. Therefore, there is a need for

these models to be tailored first or developed further to deal with fluid dynamics challenges, especially in more complex porous structures.

2.4.4 Fluid Flow in Non-Homogeneous Structures

Although a lot of research has been done to investigate the fluid dynamics in porous media and the effects that their geometry has on the fluid flow properties, most of these studies are focused on homogeneous structures where the porosity distribution and pore parameters are uniform throughout the sample. Currently, only very little research investigates the fluid flow in hybrid, non-uniform structures.

Zaragoza and Gael (2013) experimentally studied metal foams with graded pore size, as shown in Fig. 2.15, and observed similar pressure drop behaviour between the homogeneous and inhomogeneous structures. However, they observed asymmetry in the flow within the inhomogeneous structure and found increased resistance to fluid flow in smaller pore size, slowing the fluid in this region. Overall, the graded pores had negligible effects on the overall permeability. This is similar to the results obtained experimentally by Carpenter and da Silva (2014).

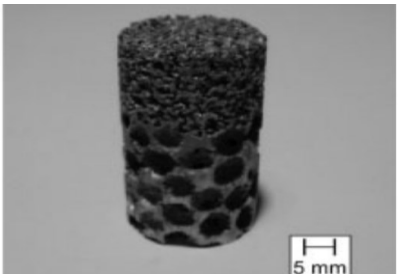

Figure 2.15: Aluminium foam with graded pore size (Zaragoza and Gael 2013).

Xiao and Zhao (2013) investigated fluid flow in LCS foams made of two vertically stacked layers of different porosities. It was found that the fluid flow chooses preferentially the layer with a higher permeability.

More recently, Oun and Kennedy (2015) explored the effects of air gaps in stacked porous layers, as displayed in Fig. 2.16. An increase in the pressure drop in stacked porous structures was reported, and was attributed to the additional entrance/exit effect developed at the additional surfaces. Their results were in agreement with that previously reported by Baril et al. (2008).

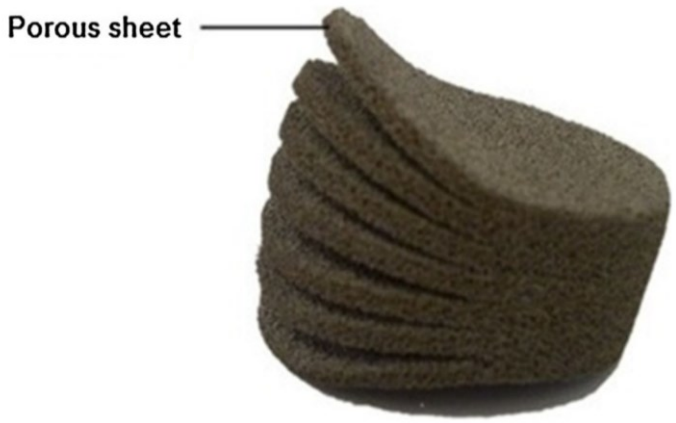

Figure 2.16: Multi-layered porous sheet (Oun and Kennedy 2015).

2.5 Heat Transfer in Porous Metals

The high surface area to volume ratio of porous metals means that a large amount of heat can be transferred over a small volume. In addition, the high porosity and open cell structure of porous metals allow the coolant to flow in the porous structure, transferring heat effectively via convection. Furthermore, the enhanced flow mixing due to turbulence and tortuosity also improves heat convection in porous metals. Therefore, porous metals are very promising materials for use as compact heat exchangers.

This section explores the heat transfer properties of metal foams currently available in the literature.

2.5.1 Introduction to Heat Transfer

Heat transfer can be defined as thermal energy in transit due to spatial temperature difference (Incropera et al. 2007). Heat transfer proceeds if there is a difference in temperature in a medium or between media. The three modes of heat transfer are:

1) conduction- heat transfer across stationary medium (solid/fluid);
2) radiation- heat transfer from surfaces of finite temperature in form of electromagnetic waves;
3) convection- heat transfer between a surface and a moving fluid.

There are two types of convection: 1) forced convection which occurs when the fluid flow is caused externally (e.g. using fans and pumps), and 2) natural convection which occurs if the flow is due to buoyancy forces.

Thermal conduction in a one dimensional conductor can be defined using Fourier's law:

$$q = -kA\frac{\Delta T}{\Delta x} \tag{2.14}$$

where q is the heat transfer rate (W), k is the thermal conductivity (W/(m.K)), T is the temperature (K), x is the coordinate in the x direction (m) and A is the area of the conductor normal to the direction of heat transfer (m^2). The minus sign is due to heat being transferred in the direction of decreasing temperature. The heat flux, J, which is the heat transfer rate per unit area, can be described as:

$$J = \frac{q}{A} = \frac{k\,\Delta T}{\Delta x} \tag{2.15}$$

Thermal conductivity, k, is a transport property and is characteristic of the material of the conductor. For an isotropic material, the thermal conductivity is independent of the heat transfer direction, i.e. remains constant regardless of the direction (Incropera et al. 2007). In general, solids have higher thermal conductivity than liquids, and liquids have higher thermal conductivity than gases due to the differences in intermolecular spacing between these phases.

A cooling fluid can be used to cool down a heated surface. Due to the temperature difference between the heated surface and the cooling fluid, heat transfer will occur by convection. A velocity boundary layer develops as a consequence of the fluid-surface interaction, displayed in Fig. 2.17, where the velocity in a region in the fluid varies from zero to a finite value (u_F). A thermal boundary layer can also develop due to the difference in the surface and flow temperatures. Hence, a region of the fluid can have temperatures of T_s at

y=0 and T_F in the outer flow, where $T_s > T_F$ (Incropera et al. 2007). As displayed in Fig. 2.17, the fluid velocity is zero at the heated surface so heat is transferred by diffusion or random molecular motion only in this region. The heat is therefore conducted at the boundary layer, then swept downstream and transferred to the fluid outside the boundary layer.

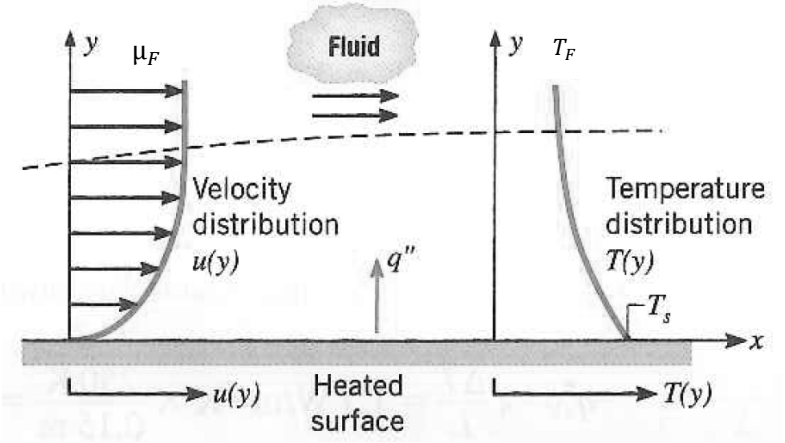

Figure 2.17: Boundary layer development in heat transfer by convection (Incropera et al. 2007).

The convective heat flux (*J*) can be expressed by Newton's law of cooling in terms of the heat transfer coefficient, *h*:

$$J = h\,(T_s - T_{F)} \tag{2.16}$$

The heat transfer coefficient is dependent on the boundary layer conditions, surface geometry, nature of fluid motion, and other fluid thermodynamic and transport properties. Therefore, the heat transfer coefficient varies between heating systems. Table 2.5 shows the typical values of heat transfer coefficients of different phases.

Table 2.5: Typical values of convection heat transfer coefficients (Incropera et al. 2007).

Process	State of Matter	Heat transfer coefficient ($W/(m^2.K)$)
Free convection	Gases Liquids	2-25 50-1000
Forced convection	Gases Liquids	25-250 100-20000

2.5.2 Mechanisms of Heat Transfer in Porous Metals

The heat transfer performance in porous metals can be explained by four mechanisms which are:

1) heat conduction through the metal cell walls;
2) heat radiation through the metal cell walls;
3) heat conduction through the pores in the sample and through the interlinked channels; and
4) convection within the pores.

Heat transfer by radiation in the porous metals is greatly affected by the porosity and pore size. If the pore size is decreased, more metal is present which acts as reflective surfaces for radiation, so heat transfer by radiation is reduced. Likewise, if porosity is reduced, more metal is present and the cell walls will act as barriers to heat radiation. Zhao et al. (2004a) reported that radiation only dominates the heat transport in porous media at very high temperatures (500-800K), and at lower temperatures (<500K), its contribution is negligible.

Solid conduction is believed to be the most dominant form of heat transfer in porous metals (Ashby and Gibson 1998). Therefore, if the density of the porous metal increases by decreasing the porosity, which in turn leads to an increase in the volume of cell walls present, the thermal conductivity of the porous medium will increase.

There are two stages involved in the transfer of heat from a heat source (heat plate) to a coolant flowing in a porous metal attached to the heat source. These are heat conduction in the metal matrix and heat convection between the metal matrix and the coolant. The flow condition in the porous media greatly affects the heat transfer by convection. The determination of whether the internal flow is laminar or turbulent is therefore very important.

2.5.3 Thermal Conductivity of Porous Metals

The effective thermal conductivity (k_{eff}) of the coolant-foam system depends on the thermal conductivity of the metal matrix (k_s) and the fluid (k_f), and the geometry of the metal matrix (Kaviany 1995). The minimum and maximum k_{eff} can be estimated using the following equations (Incropera et al. 2007, Nield and Bejan 2013).

$$k_{eff,min} = \frac{1}{\frac{1-\phi}{k_s} + \frac{\phi}{k_f}} \tag{2.17}$$

$$k_{eff,max} = \phi k_f + (1-\phi) k_s \tag{2.18}$$

Eqs. (2.17) and (2.18) were found to only have been suitable for composite systems where the solid and fluid conductivities are similar. More accurate descriptions of k_{eff} have been

derived to fit particular coolant-foam systems, especially where the thermal conductivities of the phases are significantly different, and account for the structure of the porous medium.

Calmidi and Mahajan (1999) developed a theoretical model of the effective thermal conductivity based on the two-dimensional hexagonal structure of a metal foam. Bhattacharya et al. (2002) modified the Calmidi-Mahajan model by replacing the cubic nodes (the location where ligaments or fibres join) with circular ones. The modified model was reported to be generally effective for high-porosity metals. Similar to Calmidi and Mahajan (1999), Boomsma and Poulikakos (2001b) proposed a 3D model of the metal foam structure involving geometrical parameters. The 3D model involved "tetrakaidecahedral" cells with cubic nodes at the intersection of two fibres, and was found to be in good agreement with the experimental data. Dai et al. (2010) however, found that the Boomsma–Poulikakos model contains errors, largely due to the volume-fraction-weighting of thermal conductivities. The group went on to correct the Boomsma–Poulikakos model to account for the ligament orientation. The new model was reported to provide improved predictions of the metal foam's effective thermal conductivity.

Along with analytical models, several researchers investigated experimentally how the effective thermal conductivity varied with structural parameters. Paek et al. (2000) observed that the effective thermal conductivity increased when the porosity decreased, but remained similar when the cell size of the metal foam was varied. Babcsan, Meszaros and Hegman (2003) found an increasing linear behaviour between the effective thermal

conductivity and foam density. Zhao et al. (2004a) observed that the effective thermal conductivity increased as the pore size or relative foam density increased.

2.5.4 Forced Convection

The overall thermal performance of porous metals can be substantially enhanced by forcing a fluid flow in the open-cell porous structure. However, the complexity of the morphology of porous metals limits the investigation of transport phenomena at microscopic pore level. General heat transfer equations are re-defined to accommodate the fluid and solid phases within a specific porous structure.

Several experimental and theoretical studies on the heat transfer performance with forced convections in metal foams have been reported in literature. Ding et al. (2011) reported that heat exchangers with copper metal foam allied with fluid flow showed 2.5 times greater heat transfer coefficient compared to heat exchangers without porous structures. Similarly, Hunt and Tien (1988) reported enhanced heat transfer performance with metal foams due to the intra-pore mixing that develops as the fluid moves past the solid particles, which they described as “dispersion”. They added that the dispersive transport dominates heat transfer especially at high flow rates and permeability, overpowering the solid conduction within the thin-ligament metal matrix. Kim et al. (2000) compared the heat transfer performance of louvered fins with porous fins, and concluded that both show similar performance but porous fins offered greater pressure drops. However, for applications as compact heat exchangers, porous fins were deemed more suitable. Hwang et al. (2001) experimentally studied the convective heat transfer in a duct inserted with aluminium foam and found that the volumetric heat transfer coefficient increased as the porosity of the foam decreased at a

fixed Reynolds number. An optimum porosity of 80% was reported to give the best thermal performance. Seyf and Layeghi (2010) reported that the heat transfer performance increased with increasing relative density and decreasing cell size of metal foams. Zhao et al. (2004b) experimentally studied the heat dissipation capability of metal foams with forced air convection and found that the cell size has a more significant effect on the overall heat transfer than porosity. Similar to Hwang et al. (2002), an optimal porosity was also observed by Zhao et al. (2004b), which was attributed to the balance between the pressure drop and overall heat transfer. Mancin et al. (2012) investigated forced air convection through heated copper foams and found that the heat transfer coefficient did not depend on the imposed heat flux, but increased with the air flow rate. They also reported the existence of optimal structural parameters (e.g. pore density and surface area) which gave the best heat transfer performance. Tamayol and Hooman (2011) theoretically studied the forced convection through metal foams and observed a direct relationship between the heat transfer rate and pore density and solidity, i.e. the heat transfer rate increased with pore density and decreased porosity. They also added that increasing the foam height enhanced the heat transfer rate.

It is well documented that the heat transfer performance can be significantly enhanced by utilising force-cooled metal foams. It was also observed that for metal foams, optimal structural parameters which gave the best heat transfer performance were existent. At this optimal point, a balance between the heat transfer of the fluid and solid phases is achieved. However, with the use of metal foams as heat exchangers, there is a penalty in terms of increased pressure drop which requires higher pumping power.

2.5.5 Heat Transfer in Micro-Heat Exchangers

Several studies examined forced-convection in other metal architectures. For instance, Lu (1999) designed a honeycomb metal foam structure to reduce the pressure drop and pumping power, and observed similar heat transfer performance to those of the conventional metal foams but different fluid dynamics. At low Re (<2000), the flow in honeycomb structure was laminar while in metal foams, the flow is turbulent. Heat convection in metal foams was therefore greater than in honeycomb structures due to the turbulent flow and greater mixing. The inefficiency in fluid dynamics in the honeycomb structure was however, compensated for by its greater surface area. Hence, a similar heat transfer performance was observed between the two structures.

Micro-channel heat sinks, first proposed by Tuckerman and Pease (1981), have also emerged as one of the effective cooling techniques for heat exchanger applications. The advantage of micro-channel heat sinks over porous metal foams is the reduced pressure drop due to the directional channels/pores within its structure. Zhang et al. (2005) compared the heat transfer performance of micro-channel heat sinks with metal foams and found that the metal foam heat sink with 80% porosity and 60 PPI pore density outperformed the micro-channel heat sink at large pressure drops and pumping power. At low pressure drops, however, the micro-channel heat sinks performed better than the metal foams in their study.

Recently, some attention was given in developing foam structures with “designed” architecture. Bejan (2004) proposed that the architecture of the metal foam can be designed to produce maximal heat transfer density, providing that the structure is small

enough such that the boundary layers disappear. The geometric parameters that can be optimised were the internal spacing of volumes (parallel plate or spheres), flow channel spacing and flow channel size.

Other studies focused on combining structures of different pore morphology. For example, Carpenter and da Silva (2014) investigated forced-convection in metal foams with graded pore size arranged perpendicular to the fluid flow, and found that a larger heat transfer coefficient was achieved when the layer with larger pores was placed by the fluid inlet compared to the reversed order, similar to that found by Zaragoza and Goodall (2013). This effect was attributed to the differences in the permeability and surface area of the sections. Xiao and Zhao (2013) investigated the heat transfer performance with forced convection of double-layered porous copper stacked parallel to the fluid flow. It was found that placing the higher-porosity layer next to the heat source offered a better heat transfer performance than the reverse order, which was attributed to the greater flow rate in the higher porosity region.

2.6 LCS Porous Metals

Lost Carbonate Sintering (LCS), developed by Zhao et al. (2005), is a space-holder powder metallurgy method used for the production of metal foams. Fig. 2.18 shows a graphical representation of the LCS process, which has two possible routes: dissolution or decomposition.

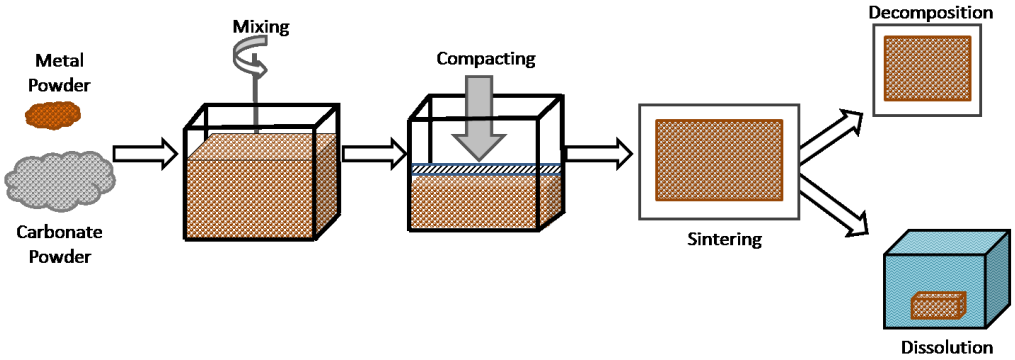

Figure 2.18: Schematic representation of the LCS process.

For both routes, the metal powder (e.g. Cu, Al, Fe, steel), carbonate powder (pore former e.g. K_2CO_3) and binder (e.g. ethanol) are mixed, compacted, and then heated to remove the binder. In the dissolution route, the compact is sintered at 850°C for four hours then placed in a water bath to dissolve the carbonate. In the decomposition route, the compact is either heated to 850°C for two hours then heated further to 950°C for 30 minutes, or heated directly to 950°C for two hours to decompose the carbonate, resulting in the porous metal as shown in Fig. 2.19. The decomposition route generally produces porous metals with higher tensile strength and higher flexural strength than those produced by the dissolution route (Zhang and Zhao 2008, Lu and Zhao 2010). A porosity range of 40% – 90% and a pore size range of 53 – 1500 µm can be achieved using the LCS process (Zhao et al. 2005).

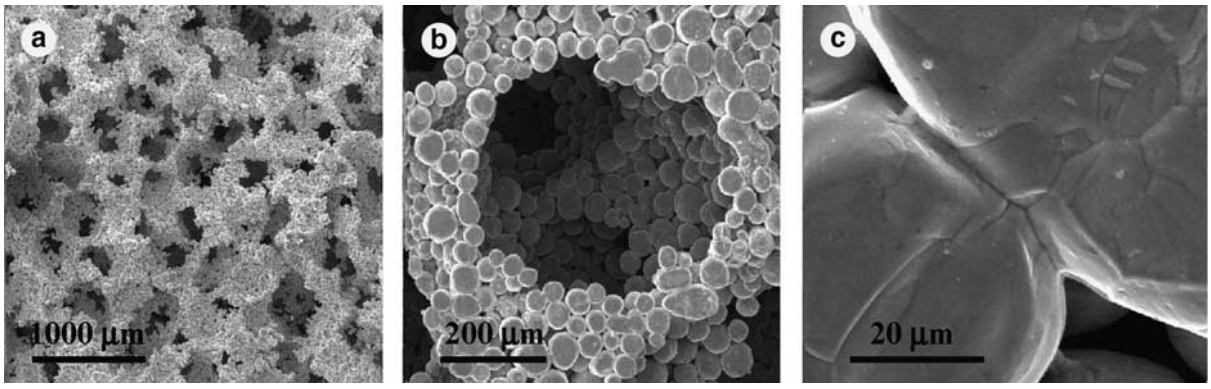

Figure 2.19: SEM micrographs showing (a) typical structure of LCS porous copper, (b) a cell and its walls, and (c) bonding between the Cu particles (Zhao et al. 2005)

Since the invention of the LCS process, the properties of the LCS porous metals have been analysed and determined by several researchers. Tao et al. (2007) found that increasing the compaction pressure and the particle size of the carbonate powder resulted in significant increase in the flexural strength and the bending energy absorption capacity, which are attributed to the reduced sintering defects. Parvanian and Panjepour (2013) analysed the mechanical behaviour of porous copper produced by the LCS process and found that the structural integrity and mechanical strength of the porous metal can be enhanced by mechanically pre-activating the copper powder. Ma et al. (2006) studied the electrical properties of LCS porous metals and found that the electrical conductivity was strongly dependent on the porosity and pore size. Lu et al. (2009), on the other hand, investigated the sound absorption characteristics of LCS porous steel and concluded that using an assembly of samples with gradient porosities gave a higher and more uniform sound absorption coefficient compared to a single-porosity assembly. Diao and Zhao (2015) recently studied the geometric, electro-active and real surface areas of LCS porous copper and found that these surface areas are due to the contributions from primary porosity, primary and secondary porosities, and surfaces of metal particles, respectively. It was also reported that the volumetric and gravimetric specific geometric surface areas increased with porosity and decreased with pore size.

The heat transfer performance of LCS porous copper was also investigated previously by Zhang et al. (2009). It was reported that the porosity has a large effect on the heat transfer performance, with 62% being the optimum porosity that gave the best heat transfer performance. The heat transfer performance of the LCS porous copper was enhanced

further when the water flow rate was increased. Thewsey and Zhao (2008) analysed the heat transfer performance of LCS porous copper, and found that the heat transfer in the porous sample was dominated by conduction in the solid phase, with convection, radiation and gaseous conduction being negligible. Xiao and Zhao (2014) studied the fluid transport and thermal properties of LCS porous copper samples with different pore structures and found that the fluid permeability increased with increasing porosity and decreasing pore size. It was also reported that the effects of porosity and pore size on the heat transfer performance of the porous copper samples were significant due to their effects on the permeability and thermal conductivity. Fig. 2.20 shows the relationship for the thermal conductivity of homogeneous LCS porous copper samples as a function of pore size and porosity established by Xiao (2013). As evident from Fig. 2.20, increasing the copper density by decreasing the sample's porosity led to greater thermal conductivities, whereas changing the pore size had a less significant effect on the thermal conductivity.

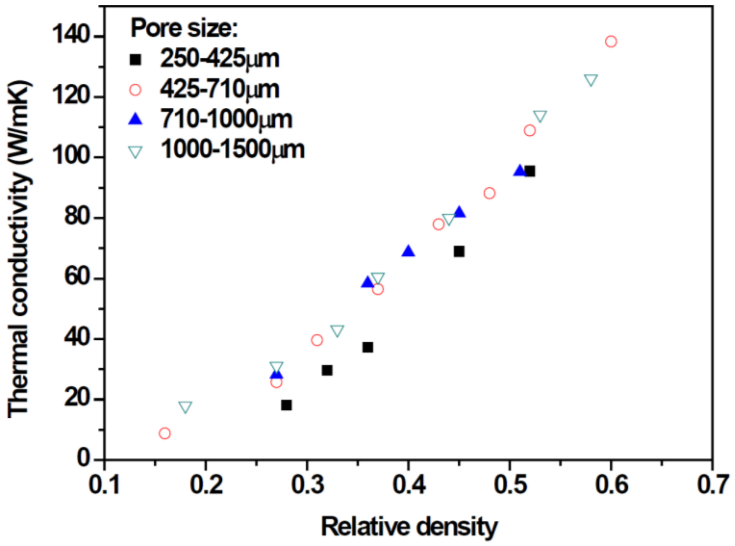

Figure 2.20: Variation of thermal conductivity with relative density for LCS porous copper samples with different pore sizes (Xiao 2013).

Recently, Xiao and Zhao (2013) investigated the heat transfer performance of double-layer LCS structures with forced convection, where the layers have different porosity and are parallel to the fluid flow. It was reported that the orientation of the layers greatly affected the heat transfer performance; having the higher-porosity layer next to the heat source offered better heat transfer than the other way round. It was also reported that compared to an empty channel (100% porosity), the heat transfer coefficient was enhanced by five to eight times when a porous copper was introduced, as displayed in Fig. 2.21. This confirms the suitability of LCS porous copper as compact heat exchangers. Versarien Technologies Ltd. (UK) currently commercialises LCS porous metals for thermal management applications.

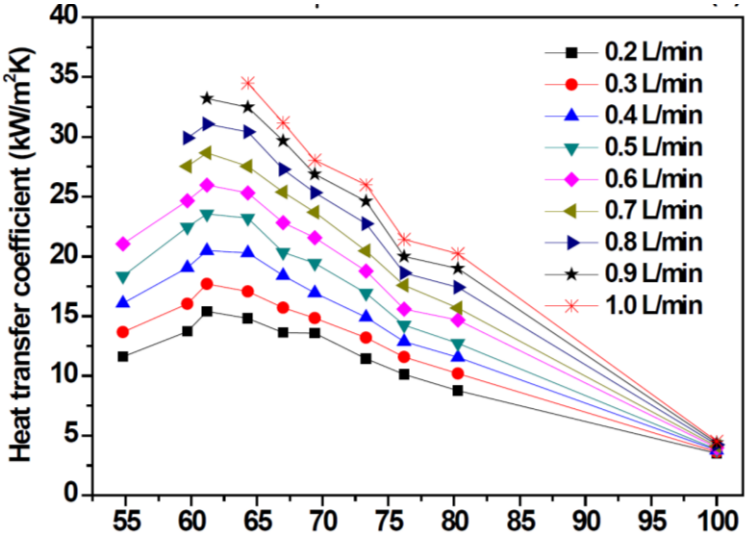

Figure 2.21: Variation of heat transfer coefficient with porosity at different water flow rates for samples with 425-710µm pore size (Xiao 2013).

Chapter 3 Experimental Procedures

The porous copper samples used in this study were manufactured using the Lost Carbonate Sintering (LCS) process developed by Zhao et al. (2005). The decomposition route was chosen instead of the dissolution route due to its simplicity and better mechanical properties of the porous metals produced. The permeability and heat transfer performance of the samples were investigated. The experimental procedures were described in the following sections in detail.

3.1 Preparation of Test Samples

Six different structures of LCS porous copper samples were manufactured in this study. These were homogeneous, horizontal bilayers, integrated vertical bilayers, segmented vertical bilayers, segmented structures and structures with directional porosity, as schematically illustrated in Fig. 3.1. Table 3.1 lists all the samples made and investigated in this study. The manufacturing procedures are described in the following sections.

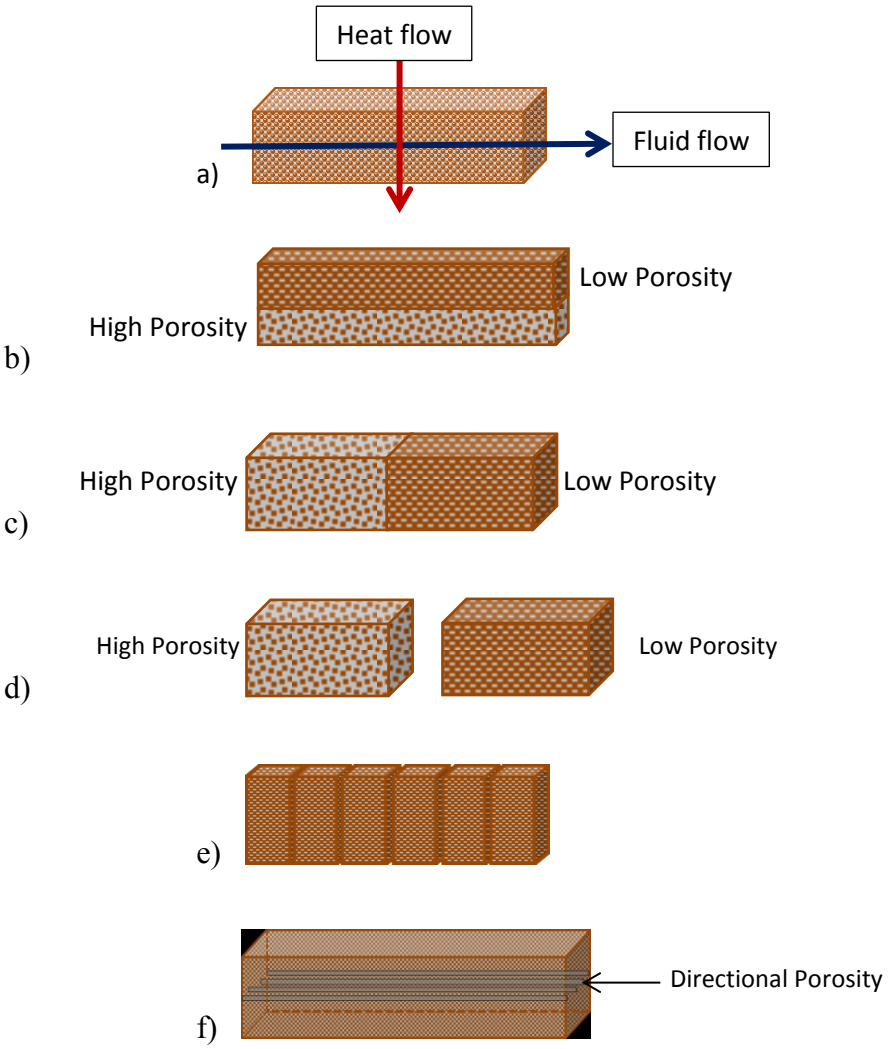

Figure 3.1: Schematic diagrams of the six different structures of LCS porous copper investigated: a) homogeneous (H), b) horizontal bilayers (HB), c) integrated vertical bilayers (IVB), d) segmented vertical bilayers (SVB), e) multi-boundary segmented structure (SS) and f) directional porosity (DP).

Table 3.1: Summary list of the LCS copper samples investigated in this study.

Sample Reference	Structure	Pore Size (μm)	Nominal Porosity (%)
H1	Homogeneous	250-425	60
H2			65
H3			70
H4			75
H5		425-710	40
H6			50
H7			60
H8			65
H9			70
H10			75
H11			80
H12		710-1000	55
H13			60
H14			65
H15			70
H16			75
H17		1000-1500	50
H18			60
H19			70
HB1	Horizontal Bilayer	425-710	40/70
HB2			40/75
HB3			40/80
HB4			50/70
HB5			50/75
HB6			50/80
IVB1	Integrated Vertical Bilayer	425-710	50/40
IVB2			40/60
IVB3			40/70
IVB4			40/80
IVB5			50/60
IVB6			50/70
IVB7			50/80
IVB8			60/70
IVB9			60/80
IVB10			70/80
SVB1	Segmented Vertical Bilayer	425-710	40/50
SVB2			40/60
SVB3			40/70
SVB4			40/80
SVB5			50/60
SVB6			50/70
SVB7			50/80
SVB8			60/70
SVB9			60/80
SVB10			70/80
SS1	Segmented Structures	425-710	40
SS2			50
SS3			60
DP1	Directional Porosity	425-710	40
DP2			50
DP3			60
DP4			70
DP5			80

3.1.1 Raw Materials

The copper powder (base metal) with particle size range of 50 µm to 150 µm and 99.9% purity was supplied by Ecka Granules UK Ltd, as seen in Fig. 3.2a. The food grade potassium carbonate powder (pore former) with particle size range of 250 µm to 1500 µm and 98-100% purity was manufactured by E&E Ltd (Fig. 3.2b). The potassium carbonate powder was sieved and categorized to four different size ranges: 250-425 µm, 425-710 µm, 710-1000 µm and 1000-1500 µm. Since the particle size of the carbonate powder determines the pore size within the porous copper sample, these four size ranges resulted in four pore sizes.

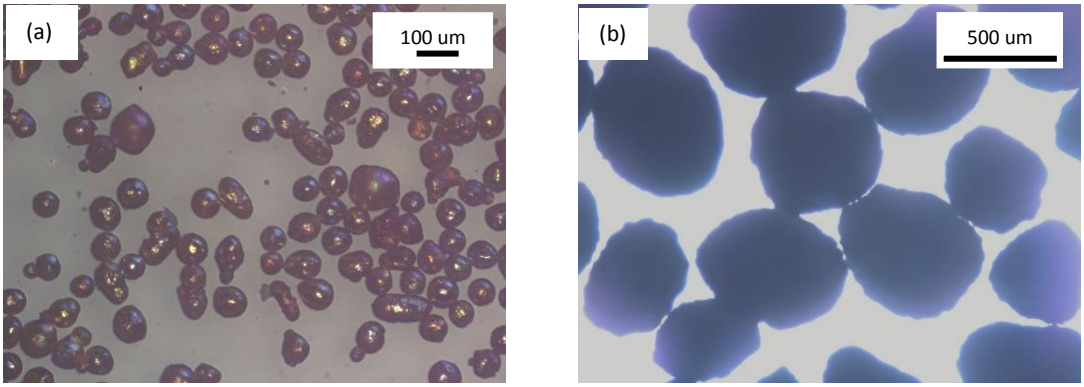

Figure 3.2: Optical micrographs of the (a) copper and (b) potassium carbonate particles used in the manufacture of the porous copper samples.

To determine the weight of the copper powder (W_{Cu}) and the weight of the potassium carbonate ($W_{K_2CO_3}$) needed for the porous copper sample fabrication, the following equations were used:

$$W_{Cu} = (1 - \phi)V\rho_{Cu} \tag{3.1}$$

$$W_{K_2CO_3} = \phi V\rho_{K_2CO_3} \tag{3.2}$$

where ϕ is the target or nominal porosity expressed as a fraction, V is the volume of the required porous copper sample, ρ_{Cu} is copper density (8.9 g/cm^3) and $\rho_{K_2CO_3}$ is the potassium carbonate density (2.3 g/cm^3).

3.1.2 Mixing and Compaction

The weighed copper and potassium carbonate powders were placed in a glass beaker. A small amount of ethanol (1% mol) was added to the mixture to act as a binder. The mixture was then mixed using a glass stirring rod until the potassium carbonate particles were covered with a layer of copper particles.

Moulds and punches made of steel were used to compress the mixed powders to shape. Samples for permeability and heat transfer tests were made using a mould with the following cavity dimensions: 30 mm in length, 20 mm in width and 30 mm in height.

Six different structures of LCS porous copper samples were fabricated, i.e. homogeneous (H), horizontal bilayers (HB), integrated vertical bilayers (IVB), segmented vertical bilayers (SVB), multi-boundary segmented structures (SS) and structures with directional porosity (DP). The modifications implemented during the fabrication process for each structure are described as follows:

a) Homogeneous Structures (H)

The mixture of the Cu and K_2CO_3 powders was placed into the mould and compacted at a pressure of 200 MPa for 10 seconds. This compaction pressure and time were chosen based on the principle laid down in the previous research (Zhao et al. 2005) The green compacts were then pressed out of the mould and placed onto a steel plate.

b) Horizontal Bilayers (HB)

The powders needed for each layer were prepared and mixed separately. The low porosity layer was first placed into the mould and lightly flattened using the punch. The second layer with the higher porosity was placed on top of the first layer. The punch was placed on top of the mixture and compacted at 200 MPa pressure for 10 seconds.

c) Integrated Vertical Bilayers (IVB)

Each powder layer were prepared and mixed separately. A partition made of thin paper was placed inside the mould to divide the cavity into two equal lengths. The layers were placed on either side of the paper partition carefully. Once the mixtures are in place, the paper partition was removed slowly causing the powder mixtures to tumble into the empty space where the paper previously was. This creates a soft boundary between the two layers. The punch was then placed on top of the mould and the mixture was compacted at 200 MPa for 10 seconds.

d) Segmented Vertical Bilayers (SVB)

The segmented vertical bilayers were made from two halves of sintered homogeneous structures and then placed next to each other during the experiments. This creates a hard boundary between the layers and often a gap exists due to poor coupling.

e) Multi-boundary Segmented Structures (SS)

The multi-boundary segmented structures were made from either two halves (15 mm in length each) or six small sections (5 mm in length each) of the same homogeneous sample. The sections are placed next to each other during experiments. A hard boundary exists between the adjacent sections.

f) Directional Porosity (DP)

The weighed copper and potassium carbonate powders were placed into the glass beaker and mixed with the addition of the ethanol binder. Half of the mixture was first placed onto the mould and slightly flattened using the punches. Four columns (30 mm in length, approx. 0.9 mm in diameter) of potassium carbonate paste were drawn on top of the first layer using a 5 mL syringe with needle (1.05 mm outside diameter). The remaining mixture of powders was spread over the first layer, covering the lines of potassium carbonate paste. The punch was then placed on top of the mixture and compacted at 200 MPa pressure for 10 seconds.

3.1.3 Sintering

The green compacts contained on a steel plate were placed inside a VTS vacuum furnace. Once the pressure of the vacuum reached below 70 Pa, the furnace was heated up to 200°C for 30 minutes to remove the ethanol binder. Considering that potassium carbonate melts at 891°C, a first sintering temperature of 800°C was chosen. The temperature of the furnace was increased to this sintering temperature for 30 min to allow the copper particles to coalesce while still having the potassium carbonate (pore former) within the compact. Finally, the furnace was heated to 950°C for 2 hours to remove the potassium carbonate by decomposition and to further sinter the copper matrix, improving its mechanical properties. The samples were then left to cool in the furnace. Fig. 3.3 shows the schematic diagram of the sintering process and Fig. 3.4 shows the typical porous copper samples produced after sintering.

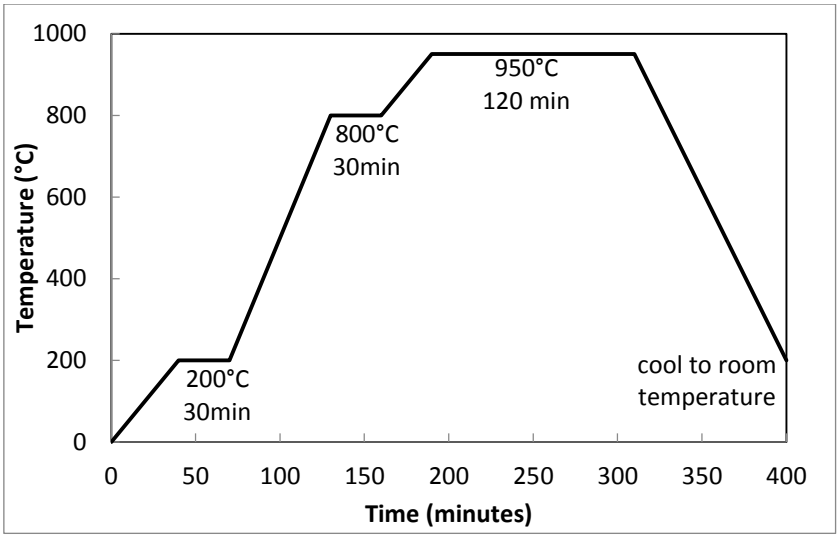

Figure 3.3: Schematic diagram of the sintering process.

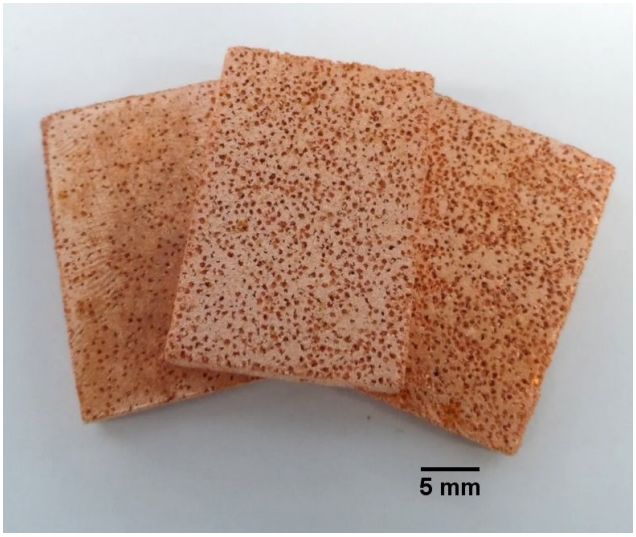

Figure 3.4: Typical porous copper samples produced after sintering using the decomposition route of the LCS process.

3.2 Structural Analysis

3.2.1 Optical Microscopy and SEM

The structure of the samples produced by the LCS process was analysed using optical microscope and scanning electron microscope (SEM). A Nikon optical microscope was used to examine the quality of the samples at low magnifications, especially for inspecting the presence of oxides and potassium carbonate. The homogeneity of the pores and their distribution throughout the samples were also investigated using optical microscopes.

A higher resolution JEOL-JSM-6610 SEM was used to analyse the pore structure in much greater detail. The pore parameters (i.e. pore size and pore shape), coalescence of the copper particles and inter-particle pores were studied using the SEM images. Both the interior and exterior microstructures were scanned for comparative analysis.

3.2.2 Measurement of Porosity

The porous copper samples were prepared by weighing the Cu and K_2CO_3 powders of a pre-specified ratio, which was determined by the target porosity (nominal porosity). However, the actual porosity of the fabricated samples is not identical to the nominal porosity because of (Zhao et al. 2005):

a) the presence of voids which add to the porosity and/or

b) shrinkage of samples during sintering which reduces porosity.

For this reason, the actual porosity of the samples needs to be measured after fabrication.

Two methods were used to determine the actual porosity of the samples: direct volume and Archimedes methods.

3.2.2.1 Direct Volume Method

The direct volume method is a relatively simple way of measuring the sample's actual porosity. This was done by measuring the mass (m) of the sample using an electronic scale (±0.05 g accuracy), and then measuring the volume (V) of the sample using a Vernier calliper (±0.01 mm accuracy). The density (ρ_s) and the porosity (ϕ) of the sample can then be determined using Eqs. (3.3) and (3.4).

$$\rho_s = \frac{m}{V} \tag{3.3}$$

$$\phi = 1 - \frac{\rho_s}{\rho_{Cu}} \tag{3.4}$$

Some samples, however, have irregular shapes or are not perfectly rectangular. This makes the calculation of the sample volume more difficult. To minimise the error, the averages of the dimensions were obtained from three measurements at three different points on the sample.

3.2.2.2 Archimedes Method

The Archimedes principle states that when a solid is submerged fully in a fluid, the apparent weight loss (buoyant force) is equivalent to the weight of the fluid displaced. By applying this principle, the volume and density of samples with irregular shapes, like that found in LCS porous samples, can be measured with a higher accuracy.

In the Archimedes method, the sample's surface was sealed with petroleum jelly to prevent water from infiltrating into the sample when submerged. The sample was then held using a thin thread and then submerged into a container filled with water on an electronic balance. The weight increase of the water container is equivalent to the buoyant force:

$$bouyant\ force = weight\ increase = V_s \times \rho_f \tag{3.5}$$

The sample's volume (V_s) was calculated, and from that, the sample's density was determined.

3.3 Permeability

The permeability of LCS porous copper samples was determined using Darcy's equation or Forchheimer's equation. Darcy's equation defines the relationship between pressure drop and flow velocity in a porous medium as:

$$\frac{\Delta P}{L} = \frac{\mu}{K}\frac{Q}{A} = \frac{\mu}{K}V_d \tag{3.6}$$

where ΔP is the pressure drop (Pa), L is the length of the porous medium (m), μ is the viscosity of the fluid (Pa.s), K is the permeability (m^2), and V_d is the Darcian velocity (m/s), which is obtained by dividing the volumetric fluid flow rate (Q) by the cross-sectional flow area (A) (Darcy 1856, Tiab and Donaldson 2012).

Darcy's law only applies to extremely low flow velocities where Reynolds number, *Re*, is in the range of 0.3 to 0.7 (Kececioglu and Jiang 1994). For high flow velocities, form drag

becomes significant and a turbulent flow occurs instead of laminar flow. For this reason, Darcy's equation has to be modified to take into consideration the effects of form drag, and the pressure drop is described by the Forchheimer's equation (Tiab and Donaldson 2012):

$$\frac{\Delta P}{L} = \frac{\mu}{K} V_d + \rho_f C {V_d}^2 \tag{3.7}$$

where ρ_f is the density of the fluid (kg/m^3) and C is a form drag coefficient (m^{-1}). The form drag coefficient, C, is sometimes replaced by $C_F/\sqrt{K}$, where C_F is often referred to as the Forchheimer coefficient.

Two fluids were used in the permeability measurements: air and water. For water flow, the pressure drop across the LCS porous copper samples was determined directly by $\Delta P = P_{in} - P_{out}$. For air flow, however, gas compressibility has to be taken into account (Dukhan 2013) and the pressure drop was modified such that:

$$\Delta P = \frac{P_{in}^2 - P_{out}^2}{2P_{atm}} \tag{3.8}$$

where P_{atm} (10 kPa) is the atmospheric pressure, P_{in} is the fluid's inlet pressure and P_{out} is the fluid's outlet pressure.

The pressure drop across the LCS porous copper sample was measured at room temperature at different fluid flow rates and was normalised against the respective length of the samples. All the data used are the averages of the values of three experimental measurements.

The pressure drop in the porous copper sample was measured using a purpose-built apparatus as shown schematically in Fig. 3.5. This apparatus consists of 1) a filter, 2) a flow meter (Omega FL50001A, ±5% full scale accuracy) at a flow rate range of 0.5 SCFM to 5 SCFM for air and 0.2 L/min to 2 L/min for water, 3) a pressure transducer (Omega PXL 219-004GI, ±0.25% accuracy, 0-4bar pressure range) to measure the inlet pressure, P_{in}, 4) the PTFE sample chamber where the LCS porous sample is placed, and finally 7) another pressure transducer (Omega PXM219-001G, ±0.25%, 0-1bar pressure range) to measure the fluid's outlet pressure, P_{out}. Inside the PTFE sample chamber is a flow channel which is 20 mm wide and 5 mm high. All the test samples were 20 mm wide and 5 mm high, fitting tightly and securely in the channel.

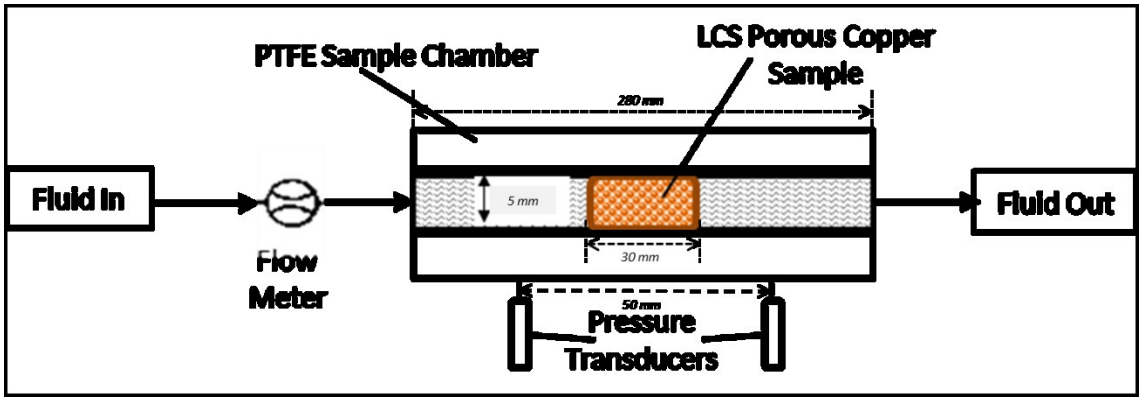

Figure 3.5: Schematic of the apparatus used to measure the pressure drop across the porous copper samples.

The permeability of the test samples was measured at different air and water flow rates at room temperature (approx. 20°C) under atmospheric conditions. The test sample was placed in the sample chamber and the chamber was tightly sealed with a PTFE lid using hexagonal bolts. The flow rate was increased gradually. The input and output pressures were recorded for each flow rate. A graph of the length-normalised pressure drop against the fluid's Darcian velocity was plotted to determine the relationship. When the trend line

was linear, Darcy's law (Eq. 3.6) was used to determine the permeability. When the trend line follows a quadratic function, Forchheimer's equation (Eq. 3.7) was used.

For structures with vertical bilayers, the orientation of the samples is an important factor in the permeability measurements. The effect of the orientation of the vertical bilayer samples on the fluid flow was analysed by flipping the sample such that either the high porosity layer or the low porosity layer was by the fluid inlet. The layer order was represented by (nominal porosity of first layer)-(nominal porosity of second layer). Pressure drop measurements were conducted in both cases, depending on which layer was by the fluid inlet.

3.4 Heat Transfer Coefficient

The purpose-built apparatus used for permeability tests was also used to measure the heat transfer coefficient of the as-fabricated LCS porous copper samples, using water as the coolant, as displayed in Fig. 3.6. Seven 100W heat cartridges were imbedded in the oxygen-free copper heat block to supply the heat flow. The heat cartridges were controlled by a variac (voltage range of 10 V - 240 V) so that a variable input voltage and heating power was generate. Attached to the heat block is another oxygen-free copper block with the same cross section as the porous copper sample (30 mm x 20 mm), and was pressed tightly against the porous copper sample to achieve good thermal contact. The temperatures at the top (T_t) and bottom (T_b) spots of the lower copper block were measured after a steady state condition was reached using T-type thermocouples ($\pm$0.1% accuracy). The heat flux (J) through the lower copper block is equivalent to the heat flux to the sample, and was calculated by:

$$J = k_{Cu}\frac{T_t - T_b}{d} \tag{3.8}$$

where d is the distance between the spots for measuring T_t and T_b (30 mm) and k_{Cu} is the thermal conductivity of the oxygen free copper block (390 W/(m.K)). The input voltage was varied using a variac between 60 V to 150 V to produce different heat fluxes.

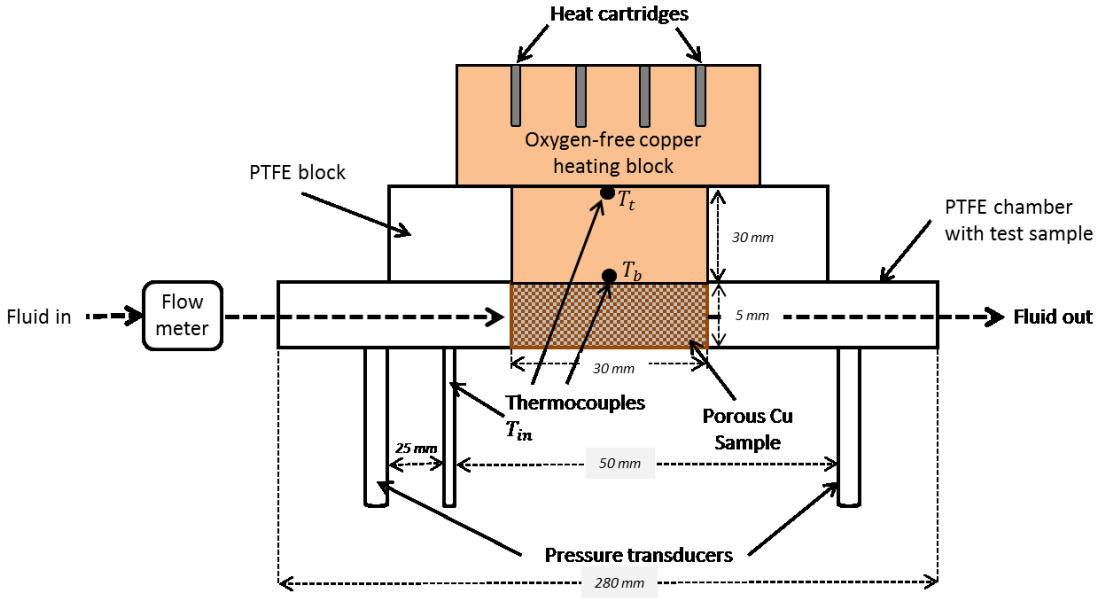

Figure 3.6: Schematic of the apparatus used to measure the permeability and heat transfer coefficient of the LCS samples.

During the experiment, the water coolant flowed through 1) a filter, 2) a flow meter (Omega FL50001A, ±5% accuracy) at a flow rate range of 0.28 L/min to 1.12 L/min, 3) a thermometer (PT 100, ±0.1°C accuracy) to measure the inlet fluid temperature (T_{in}) and 5) the porous copper in the sealed chamber. All samples were 30 mm long, 20 mm wide and 5 mm high, which tightly fit into the channel.

The overall heat transfer coefficient (h) of the cooling system, which is made of the porous copper sample and water coolant, was determined by:

$$h = \frac{J}{T_b - T_{in}} = \frac{k_{Cu}}{d}\frac{T_t - T_b}{T_b - T_{in}} \tag{3.9}$$

Temperature measurements were made at different power inputs (60 V, 80 V, 100 V, 120 V and 140 V) and five different water flow rates (0.28 L/min, 0.45 L/min, 0.68 L/min, 0.91 L/min and 1.12 L/min). A valve was used to adjust the flow rate to the desired level. It took approximately 1 hour when the input power was changed to reach steady state condition (i.e. when all the parameters no longer change), and about 20 minutes when the flow rate was altered. The temperatures were collected by a data logger and recorded by the computer. A graph of the heat flux (J) against T_b-T_{in} was plotted to determine the heat transfer coefficient of the test sample using Eq. (3.9).

For structures with horizontal bilayers, the orientation of the samples was an important factor in the overall heat transfer performance. The layer in direct contact with the heat source was called the “upper layer” and the other layer as the “lower layer”. The layer order is represented by the (nominal porosity of upper layer)/(nominal porosity of lower layer). The heat transfer performance of the horizontal bilayer samples was conducted in both cases, depending on which layer is in direct contact with the heater. The effect of the orientation of the horizontal bilayer samples on the heat transfer performance was analysed by flipping the sample such that either the high porosity layer or the low porosity layer is in direct contact with the heat block.

Similarly, for structures with vertical bilayers, the orientation of the samples was also a significant factor in the overall heat transfer performance. For vertical bilayers, the layer by the water input was named the “first layer” and the other layer as the “second layer”. The layer order is represented by the (nominal porosity of first layer)-(nominal porosity of second layer). The effect of the orientation of the vertical bilayer samples on the heat

transfer performance was analysed by flipping the sample such that either the high porosity layer or the low porosity layer is by the water inlet.

3.5 Error and Uncertainty

The error and uncertainty in the measurement are characterised by standard deviation based on the mean values and experimental uncertainty.

3.5.1 Mean Value and Standard Deviation

A finite set of values was obtained by repeating measurement under the same conditions for any physical parameters measured in this thesis. The mean value (X) for n measurements was:

$$X = \frac{1}{n}\sum_{i=1}^{n} x_i \tag{3.10}$$

and the standard deviation was calculated by:

$$\frac{\Delta x}{X} = \frac{\sqrt{\sum_i (x_i - X)^2 \,/\, (n-1)}}{X} \times 100\% \tag{3.11}$$

The length, width, height, thickness and weight of the LCS porous copper samples were measured at least three times and the standard deviation was less than 0.25%. The permeability and heat transfer coefficients were measured under the same conditions and the standard deviations were 3.5% and 4.0%, respectively.

3.5.3 Experimental Uncertainty

The uncertainty can be expressed by:

$$\frac{\Delta \emptyset}{\emptyset} = \sqrt{(a\frac{\Delta x_1}{x_1})^2 + (b\frac{\Delta x_2}{x_2})^2 + \cdots + (n\frac{\Delta x_N}{x_N})^2} \tag{3.12}$$

When several independent variables (x_1) are used in a function Ø, i.e.

$$\emptyset = x_1^a x_2^b \dots x_N^n \tag{3.13}$$

In this thesis, systematic errors of the facilities and the standard errors of measured length, width, thickness and weight were considered for uncertainties, which are summarised in Table 3.2.

Table 3.2: Uncertainty of physical parameters in this thesis.

Parameter	**Uncertainty (%)**
Porosity	<0.25
Darcian velocity	<5.1
Heat flux	<3.0
Heat transfer coefficient	<3.1

3.6 Summary

In total, 53 copper samples with different structures were produced for this study using the Lost Carbonate Sintering process. The LCS process was modified for the manufacture of non-homogeneous structures, as discussed in the previous sections. Optical microscopy and SEM were used to analyse the pore structure. Direct volume method and Archimedes method were used to measure the sample's porosity. Furthermore, purpose-built apparatuses were used to measure the pressure drop, permeability and heat transfer coefficients of the samples.

Chapter 4 Structural Analysis of LCS Porous Copper

This chapter presents the results obtained from the structural analysis of LCS porous copper with homogeneous and non-homogeneous structures.

4.1 Homogeneous LCS Porous Copper

4.1.1 Microstructure

The topography, macrostructure and microstructure of the porous copper produced by the LCS process were analysed using optical microscopes and SEM. The optical and SEM micrographs of a typical porous copper sample are shown in Figs. 4.1 and 4.2, respectively.

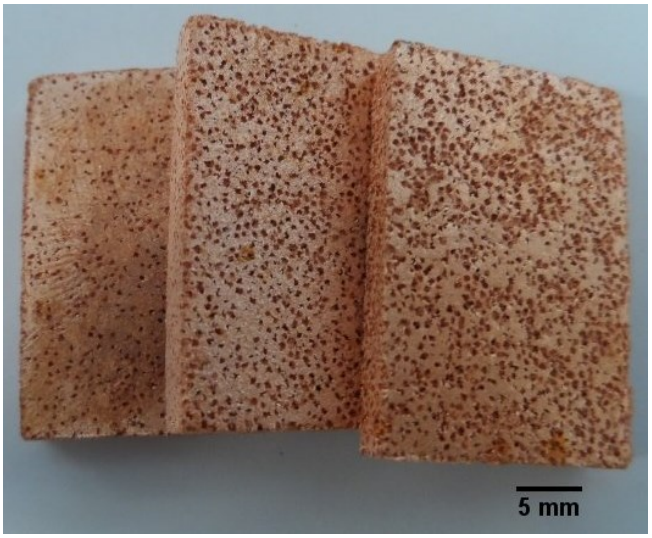

Figure 4.1: Optical micrograph of homogeneous LCS porous Cu samples with different porosities (50%, 60% and 70% from left to right; pore size: 425-710 µm) showing representative features.

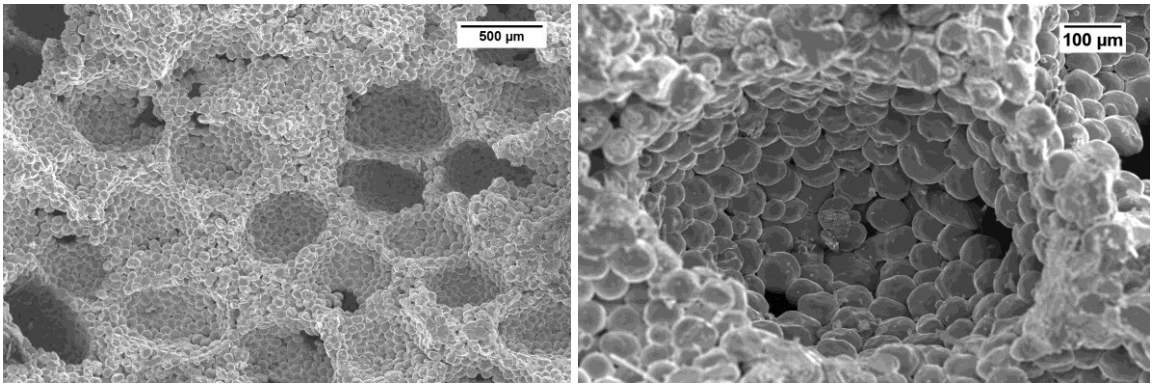

Figure 4.2: SEM micrographs of LCS porous Cu showing interconnected large pores created by K_2CO_3 particles and the solid Cu matrix formed by sintered Cu particles (Porosity: 50%; Cu particle size range: 50-150 µm; pore size: 425-710 µm).

The large pores within the samples represent the spaces previously occupied by the K_2CO_3 particles. As shown in Fig. 4.1, the pores are uniformly distributed in the samples. The samples are rectangular in shape, with similar size to the mould used (30 mm x 20 mm x 5 mm). This suggests that the samples held their shape while in the furnace during sintering. However, the edges of the samples are not as sharp as that of the mould shape. At the edges, the copper particles in these regions seperated from the rest of the sample due to insufficient binder in these regions, and so only weak mechanical binding is present in this area.

Observing these pores more closely using the SEM (Fig. 4.2) shows that some pores are spherical. The non-spherical pores are due to K_2CO_3 particles being adjacent to each other. From Fig. 4.2, the pore size ranges from 425-710 µm, which is the same particle size range as the K_2CO_3 powder used. This suggests that the pores held their original shape even until the pore former K_2CO_3 has decomposed. This contributes to the capability of the LCS process being able to produce samples of desired pore size and pore shape accurately.

Figs. 4.2 and 4.3 show the interconnection and bonding of the copper particles. Fig. 4.3 clearly shows necking between copper particles suggesting atomic diffusion of copper leading to cohesion bonds, which has occurred during sintering. This ensures good mechanical strength of the LCS porous structure. Additionally, since the pore walls are made from individual sintered copper powder particles, there is a high surface area of the matrix.

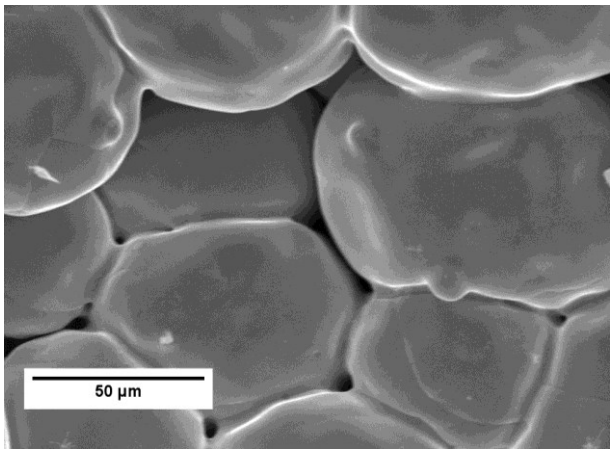

Figure 4.3: SEM micrograph of an LCS copper showing necking of Cu particles (Porosity: 50%; Cu particle size range: 50-150 µm; pore size: 425-710 µm).

Moreover, smaller cavities between the copper particles can also be seen from Figs. 4.2 and 4.3. These cavities act as small channels between pores, allowing the pores to be inteconnected. Fluid can flow through these small cavities hence increasing the fluid permeability of the LCS porous samples. In addition to the cavities, a bigger channel/hole, formed due to K_2CO_3 particles being adjacent to each other, interconnects the pores. Fluid passes through these bigger channels more readily, which can increase heat transfer by convection. As a result, the higher the porosity, the more connected the pores are since more flow channels are available. Due to this, it is expected that the higher the porosity, the more permeable the porous copper sample will be. However, since the copper density

decreases with increased porosity, it is expected that thermal conductivity will decrease as the porosity of the sample is increased.

Finally, all micrographs show no appearance of K_2CO_3 particles. This suggests that all K_2CO_3 used during sample preparation has completely decomposed during the sintering process.

4.1.2 Measurement of Porosity

The porosity of nineteen homogeneous samples was measured using both the direct volume method and the Archimedes method as described in Section 3.2.2. The LCS porous copper samples had nominal dimensions of 30 mm x 20 mm x 5 mm. The samples tested varied in pore size and porosity. The four pore size ranges studied were 250-425 µm, 425-710 µm, 710-1000 µm and 1000-1500 µm. Table 4.1 summarises the results gathered and compares the values obtained from the two methods against the nominal porosity. Fig. 4.4 displays the measured porosity values plotted against the nominal porosity values. The nominal porosity of each sample was calculated during the design and sample preparation stage (Section 3.1.1).

Table 4.1: Summary of porosity values obtained using the direct volume and Archimedes methods in comparison to the nominal porosity for different pore size ranges.

Sample Reference	Nominal Porosity (%)	Pore Size (μm)	Direct Volume Method (% ±4.2%)	Archimedes Method (% ±0.25%)
H1	60	250-425	66.9	59.7
H2	65	250-425	70.6	63.5
H3	70	250-425	72.1	68.6
H4	75	250-425	76.1	74.3
H5	40	425-710	48.5	45.8
H6	50	425-710	57.0	54.2
H7	60	425-710	65.8	59.2
H8	65	425-710	66.7	63.8
H9	70	425-710	73.3	68.7
H10	75	425-710	74.7	73.8
H11	80	425-710	80.2	77.0
H12	55	710-1000	63.0	58.2
H13	60	710-1000	67.2	63.1
H14	65	710-1000	71.3	68.2
H15	70	710-1000	73.3	73.1
H16	75	710-1000	79.8	79.5
H17	50	1000-1500	58.2	57.6
H18	60	1000-1500	69.9	69.8
H19	70	1000-1500	78.6	78.2

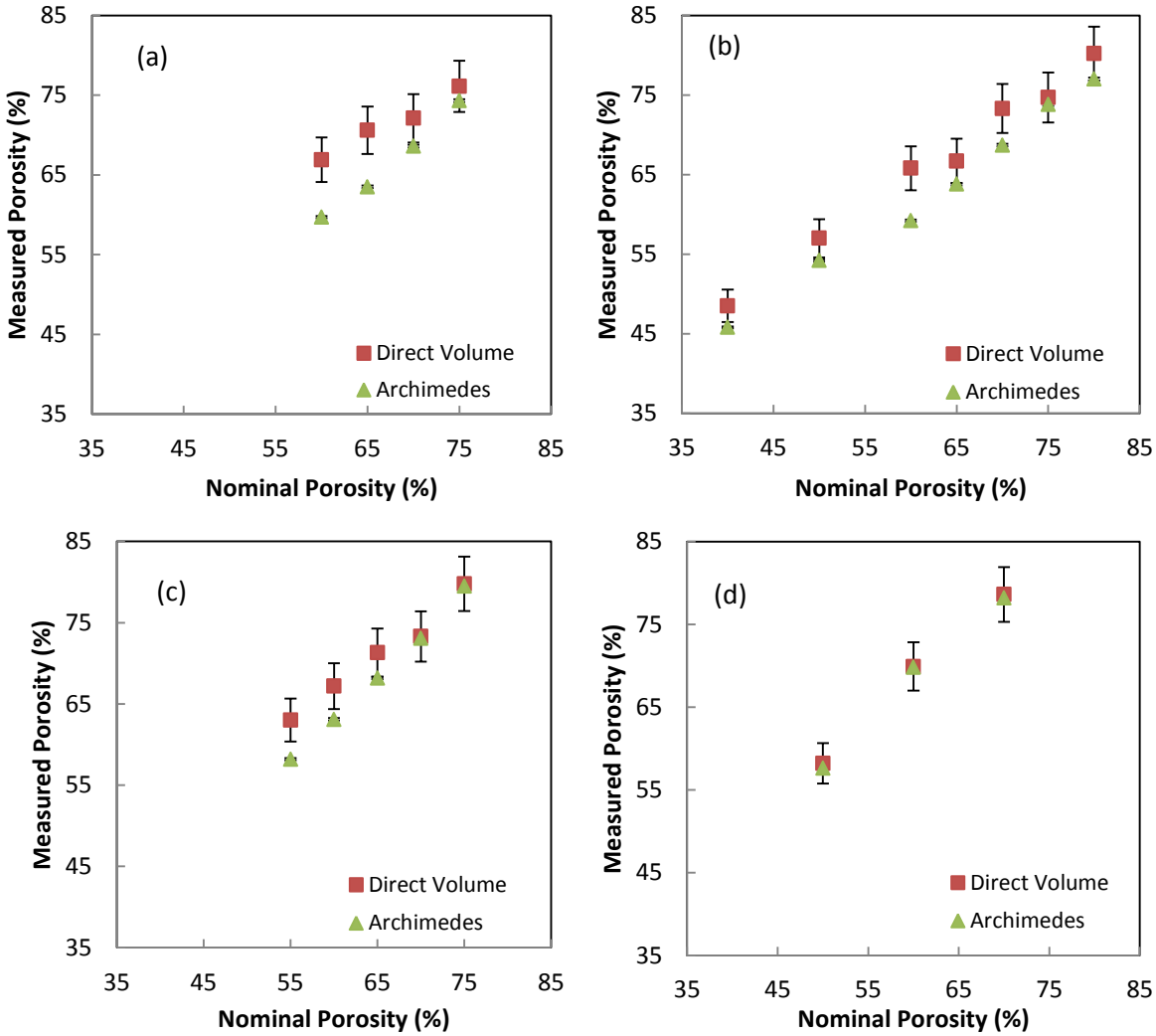

Figure 4.4: Measured porosity values obtained using the direct volume and Archimedes methods against the nominal porosity for different pore size ranges: a) 250-425 µm, b) 425-710 µm, c) 710-1000 µm and d) 1000-1500 µm.

The porosity of the samples measured by the Archimedes method is similar to the nominal porosity for pore size ranges 250-425 µm, 425-710 µm and 710-1000 µm, although the actual porosity was either slightly higher or slightly lower than the nominal porosity. In the Cu-K_2CO_3 powder mixture, there will always be porosity present due to voids between the particles even after compaction. Since the nominal porosity is calculated with the assumption that full compaction occurred and that there is no void present in the Cu-K_2CO_3 mixture, it is expected that the actual porosity will be higher than the nominal porosity. However, it is also possible to obtain a lower actual porosity due to the shrinkage of the sample during sintering, especially for samples with smaller pore size ranges. As copper particles neck during sintering, the porosity of the sintered sample will be less than that of the compacted mixture. Therefore, depending on which of these mechanisms dominates, either a higher or a lower porosity can result.

For samples with pore size range of 1000-1500 µm, however, there is a big difference between the nominal and actual porosities. The actual porosity is higher than the nominal porosity for all samples. Since the K_2CO_3 particles are bigger, more voids are present in the Cu-K_2CO_3 mixture even after compaction because the mixture is not as tightly packed as that with smaller K_2CO_3 particles. The difference suggests that the compaction pressure was not high enough to eliminate the voids and a large amount of voids remained in the sample after compaction.

In general, the direct volume method obtained higher porosity values than the nominal porosity and the values obtained by the Archimedes method. Since the LCS porous Cu

samples are not perfectly rectangular, the dimensions vary from point to point. Inaccuracy in the volume measurement using the direct volume method is inevitable. The volume measured is usually higher than the sample's true volume, making the actual porosity greater than the nominal porosity.

4.2 Non-Homogeneous LCS Porous Copper

The topography and microstructure of the non-homogenous porous copper structures produced by the LCS process were analysed using optical microscopes and SEM. For segmented vertical bilayers and segmented samples, their structures are similar to that of homogeneous samples (Section 4.1) since they originated from homogeneous structures. The following section will therefore only show the structures of horizontal bilayers, integrated vertical bilayers and samples with directional porosity.

4.2.1 Horizontal Bilayers

Fig. 4.5 shows the representative features of a typical horizontal bilayer structure containing two layers with different porosity. The top layer in the sample shown has a 40% nominal porosity while the bottom layer has 80% nominal porosity. Fig. 4.5(a) shows the side-view of the sample while Fig. 4.5(b) and Fig. 4.5(c) show the top and bottom sides of the sample.

Similar to homogeneous samples, horizontal bilayer samples kept their rectangular shape with the corners slightly rounded. This is because insufficient binder at the corners results in weak mechanical bonding in these areas. The two layers are clearly visible in Fig. 4.5. A subtle boundary between the upper and lower layers is visible from the side-view (Fig. 4.5a).

It is apparent that the two layers have different porosities. This suggests that the two layers did not mix with each other during sample preparation.

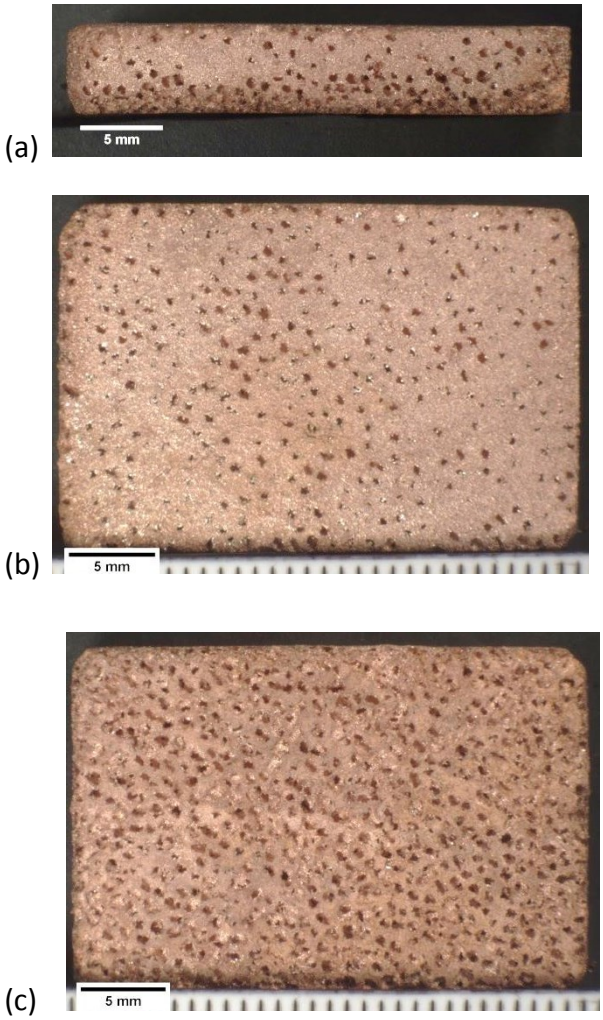

Figure 4.5: Optical micrographs of horizontal bilayer LCS porous Cu samples showing representative features: a) side-view (40/80), b) top-view (40% porosity) and c) bottom-view (80% porosity).

4.2.2 Integrated Vertical Bilayers

Fig. 4.6 shows the representative features of the LCS porous copper samples with integrated vertical bilayer structure. The samples contain two layers with different porosity. Fig. 4.6 shows that there is a clear boundary separating the higher porosity layer from the lower porosity layer suggesting that the two layers did not mix with each other during sample preparation. The two layers in each sample are also mechanically bounded to each other since the two layers were sintered together, as evident in Fig. 4.6. In addition, all the samples are rectangular in shape with similar size to the mould. However, the edges in the low porosity layer are sharper than that in the higher porosity layer. It is more likely that some copper particles fell off in the high porosity layer.

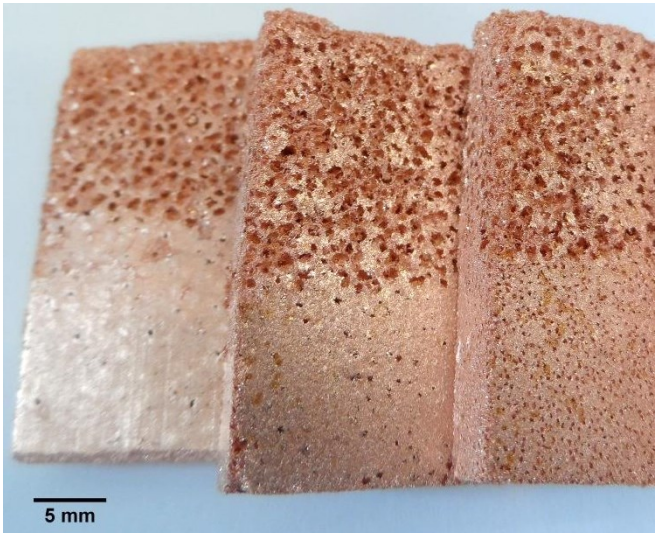

Figure 4.6: Optical micrograph of LCS porous Cu samples with integrated vertical bilayer structure showing representative features (IVB samples 40-60, 40-70 and 40-80 from left to right; 425-710 µm pore size).

4.2.3 Sample with Directional Porosity

Figs. 4.7 - 4.9 show the representative features of LCS porous copper samples with additional directional porosity (open channels). All the samples are rectangular in shape with the same dimensions as the mould.

Fig. 4.7 shows three samples of different nominal porosities, with four open channels added along the middle of each sample. For the 50% and 60% porosity samples, the four open channels are visible at the ends of the samples. However, for the 40% porosity sample, only two channels remain open. Investigating the cross section of the 40% sample on the other hand (Fig. 4.8) shows clearly the four open channels. Smearing of copper particles during the removal of green compacts from the mould could be the reason for the closure of some of the channels at the ends of the 40% porosity sample. Smearing is also visible in 50% and 60% porosity samples, where the end channels are partially closed (Fig. 4.7). Therefore, the end of the samples does not show the true representation of the channels within the sample.

Fig. 4.8 shows the four distinct open channels that were added within the LCS porous structure. The channels are oval in shape and are approximately 0.9 mm in width and 0.3 mm in height, making up 0.2% of the whole structure. The K_2CO_3 pastes in the Cu-K_2CO_3 mixture were originally circular. As the mixture was compacted, the K_2CO_3 paste flattened a little in the direction of the compaction, hence the oval shape of the channels in the sintered product.

Fig. 4.9 is an SEM micrograph of one of the pores in the 40% sample. It is visible that the channel is open. However, it does not run perfectly straight along the sample because the channels were drawn by hand during sample preparation. The channel walls are also clearly visible from Fig. 4.9, suggesting that the walls did not collapse during sintering and that the K_2CO_3 paste remained intact until decomposition.

Figure 4.7: Optical micrograph showing the LCS porous Cu samples with directional porosity (40%, 50% and 60% nominal porosity from left to right).

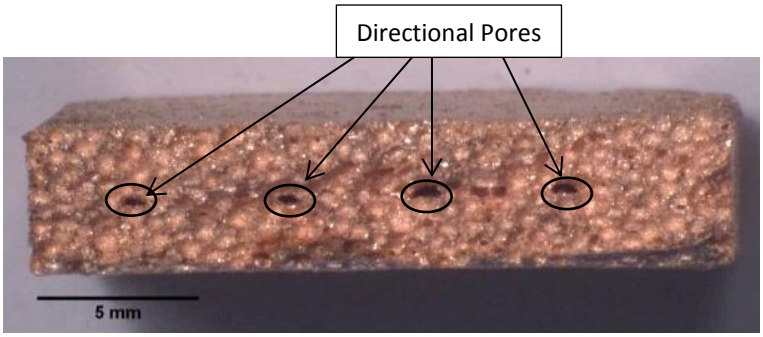

Figure 4.8: Optical micrograph showing the cross section of an LCS porous Cu sample with directional porosity (40% nominal porosity).

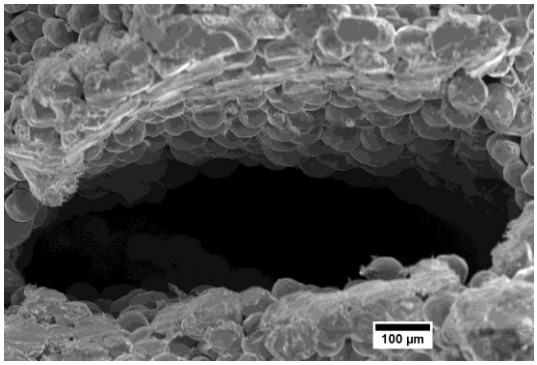

Figure 4.9: SEM micrograph showing one of the open channels at the cross section of an LCS porous Cu sample with directional porosity (40% nominal porosity).

Table 4.2 compares the actual porosities of the structures with directional porosity with homogeneous structures, obtained by the direct volume method. It is apparent that the addition of directional pores increased the overall porosity of the sample. The greatest increase contributed by the directional pores to the actual porosity was about 12% for the sample with 40% nominal porosity. As the nominal porosity increased, however, the contribution of the directional pores on the overall porosity decreased.

Table 4.2: Comparison of actual porosities between homogeneous samples and samples with directional porosity.

Nominal Porosity (%)	Actual Porosity (%)	
	Samples with Directional Porosity	Homogeneous Samples
40%	54.4	48.5
50%	63.8	57.0
60%	67.1	65.8
70%	75.3	73.3
80%	82.3	80.2

4.3 Summary

The structural analysis of the LCS samples was carried out using optical microscopes and SEM. The pore morphology within the samples replicated that of the pore former (K_2CO_3), proving the capability of the LCS process in producing samples of desired pore size and pore shape accurately. Necking between the copper particles was evident, ensuring good mechanical strength. Smaller cavities between the copper particles were also evident, which allows the larger pores to be interconnected, increasing the samples permeability to fluid flow.

The porosity of the samples was measured using direct volume and Archimedes methods. The porosity values obtained using the direct volume method was greater than the nominal porosity and Archimedes porosity. This was due to the inaccuracy in the volume measurements since the samples were not perfect rectangles. Archimedes porosities were either greater or less than to the nominal porosity. Lower actual porosities were due to the shrinkage of the sample during sintering, while greater actual porosities were due to the high presence of voids in the sintered samples. Depending on which of these mechanisms dominates, either a higher or a lower porosity can result.

The structures of the layers in the segmented vertical bilayer and segmented samples were similar to that of the homogeneous samples. For both horizontal bilayer and integrated vertical bilayer samples, a clear distinction between the high porosity and low porosity layers were evident, suggesting that the two layers did not mix during sample preparation. Finally, the directional pores in samples with directional porosity were clearly visible in the micrographs, suggesting that the K_2CO_3 paste remained intact until decomposition.

Chapter 5 Permeability and Form Drag Coefficient of LCS Porous Copper

This chapter presents the results on pressure drop, permeability and form drag coefficient for water flow in LCS porous copper with homogeneous and non-homogeneous structures. The results on pressure drop and permeability of air flow in homogeneous samples are also presented for comparison with the water results.

5.1 Water Flow in Homogeneous Samples

5.1.1 Length-Normalised Pressure Drop

The length-normalised pressure drops for LCS homogeneous samples at different water flow rates (up to 2 L/min) are shown in Fig. 5.1. The samples (Table 4.1) were categorised according to porosity and pore size. The pore size ranges were 250-425 μm, 425-710 μm, 710-1000 μm and 1000-1500 μm. For the 250-425 μm pore size range, only samples with porosity up to 74.3% were tested due to the structural integrity becoming poor at higher porosities. The actual porosity of the samples was measured using Archimedes method and the actual porosity range studied varied from 57% to 80%.

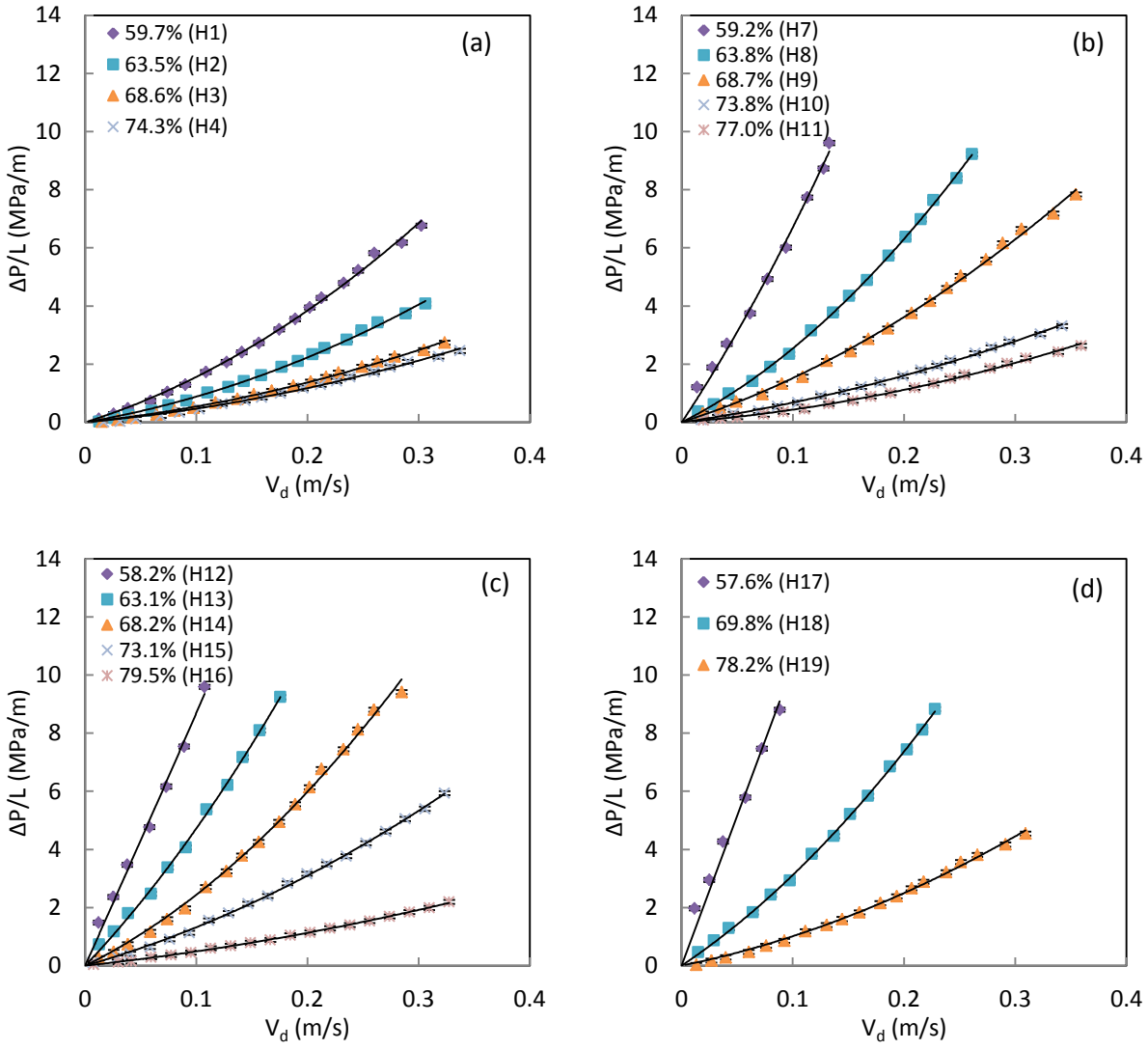

Figure 5.1: Length-normalised pressure drop (ΔP/L) versus Darcian flow velocity (V_d) for LCS homogeneous porous copper samples with different porosities (shown on graph) and pore sizes: a) 250-425 µm, b) 425-710 µm, c) 710-1000 µm and d) 1000-1500 µm.

The pressure drops for all the samples increased with increasing Darcian velocity in a quadratic fashion. This suggests that the flow may be turbulent and the inertial effects are prominent at high flow velocities. All quadratic curves fitted well with Forchheimer's equation (Eq. 3.7), with a determination coefficient R^2>99%.

The maximum water flow rates recorded for samples with nominal porosity of 50-60% ranged from 1.2 L/min to 1.5 L/min only. This was because the maximum pressure of the water pump was 3 bars and water flow rates with corresponding inlet water pressure higher than 3 bars were not permissible. As a consequence, for samples with low porosities, it was difficult to measure the water pressure drop at high velocities.

Fig. 5.1 shows that for each pore size category, the samples with the lowest porosity gave the highest pressure drop at any given water flow rate. Comparing all the samples, the sample with the lowest porosity, H17 (pore size: 1000-1500 μm), generated the greatest water pressure drop. On the other hand, the lowest water pressure drop was recorded for sample H16 (pore size: 710-1000 μm), which has the highest porosity. Overall, the porosity of the LCS porous copper samples significantly affects the pressure drop.

The pore size of the samples also affects the pressure drop. Comparing the pressure drops of samples with different pore size ranges but similar porosity (H3, H9, H14 and H18), samples with smaller pore sizes generated lower pressure drops than samples with larger pore sizes. Sample H3 with the smallest pore size range of 250-425 μm, generated the lowest pressure drop, while sample H18 with the pore size range of 1000-1500 μm gave the highest pressure drop at any given water flow rate.

Fig. 5.1 clearly shows that higher pressure drops were generated for samples with lower porosities and larger pore sizes. A lower porosity means a lower fraction of pores exists and

therefore less channels for fluid flow; or more solid fraction and therefore a greater resistance to fluid flow. Larger pores in the sample result in lower pore density per unit volume. As a consequence, there is less connectivity between the pores since the pores are farther apart. Fewer connected channels for fluid flow in samples with larger pore size result in higher pressure drops.

Past research on water flow in porous media showed that the quadratic Forchheimer relationship existed at high water flow velocities due to the inertial effects becoming more dominant (Khargyoli et al. 2004, Zhang et al. 2005, Despois and Mortensen 2005). Higher water pressure drops were observed for samples with lower porosities (Zhang et al. 2005, Despois and Mortensen 2005). In terms of pore size, some researchers observed higher pressure drops for bigger pore sizes (Despois and Mortensen 2005), while other researchers observed higher water pressure drops for samples with smaller pore sizes (Bonnet, Topin and Tadrist 2008, Boomsma and Poulikakos 2001a). This discrepancy could be due to the differences in the structures of these porous media, which will be discussed further in Section 5.1.5.

5.1.2 Transition from Darcy Regime to Forchheimer Regime

Forchheimer's equation (Eq. 3.7) is quadratic, while Darcy's equation (Eq. 3.6) is a linear correlation that does not take the inertial effects into consideration. The results displayed in Fig. 5.1 followed quadratic curves rather than linear lines, and therefore, contain a quadratic term accounting for inertial effects.

The inertial effects were investigated further by rearranging Forchheimer's equation (Eq. 3.7) to give a linear relationship as follows:

$$\frac{\Delta P}{LV_d} = \frac{\mu}{K} + \rho_f C V_d \tag{5.1}$$

Plotting $\frac{\Delta P}{LV_d}$ against V_d, $\frac{\mu}{K}$ would be the intercept of the line with the y axis and $\rho_f C$ would be the gradient of the line. In theory, if the gradient of the line is zero (i.e. $\rho_f C=0$) shown by a horizontal line, inertial effect is negligible and pressure drop is governed by Darcy's Law (Eq. 3.6). If the gradient of the line is non-zero, then the inertial effect on the pressure drop is significant. Hence, by doing this further analysis, it is possible to examine the transition between linear Darcy regime to non-linear Forchheimer regime.

Fig. 5.2 shows the relationship between $\frac{\Delta P}{LV_d}$ and V_d for samples with different pore size and porosity. It is evident that each line is composed of two segments of straight lines. The transition from one segment to another occurs at the Darcian velocity, V_d = 0.05-0.06 m/s. The trend of the first segment (V_d < 0.05 m/s) of the lines varied. A positive gradient for the first segment can be observed for samples H1-H4, H10, H11, H16 and H19, while a negative gradient for the first segment can be observed for samples H7-H9, H12-H15 and H17-H18. The second segments (Vd > 0.05m/s) of all the results are straight lines with a positive gradient. This suggests that the inertial effects became significant in the water flow in the LCS porous copper at V_d > 0.05m/s, and that the flow entered the non-linear Forchheimer regime.

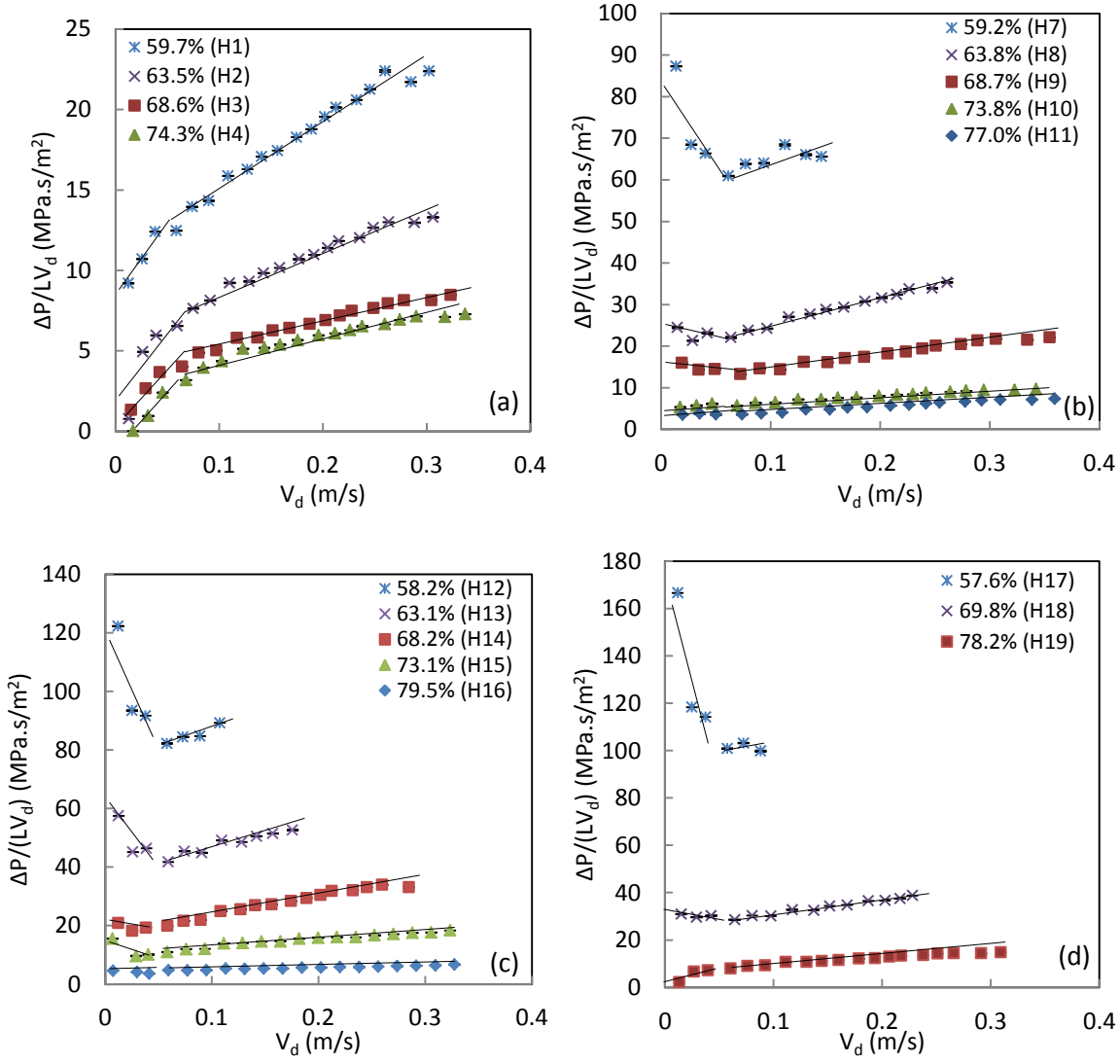

Figure 5.2: $\frac{\Delta P}{LV_d}$ versus Darcian velocity for samples with different porosities (shown on graph) and pore sizes: a) 250-425 µm, b) 425-710 µm, c) 710-1000 µm and d) 1000-1500 µm.

Boomsma and Poulikakos (2001a) observed that for open-cell aluminium foams with different pore sizes, the water pressure drop entered the Forchheimer regime at V_d = 0.074-0.101 m/s. Dukhan et al. (2014) observed that for packed spheres (1-3mm diameter), Darcy's regime was confined to even lower water flow velocities (V_d < 0.007-0.01 m/s), followed by the transition regime, and the Forchheimer regime started at V_d = 0.05-0.2 m/s. In the present study, the Forchheimer regime in all samples started at approximately V_d = 0.05 m/s, similar to that found by Boomsma and Poulikakos (2001a) and Dukhan et al. (2014). However, due to the low accuracy of the data points at very low flow velocities, defining where the Darcy and transition regimes start and end was difficult in the present study. The first segments in Fig. 5.2 showed either an increasing or a decreasing trend and no horizontal line can be determined from the points given. This suggests that the flow shown in the first segment might be within the transition regime.

The linear Darcy's regime in porous media was reported to end at 0.01 m/s (Dukhan et al. 2014), while the data points shown in Fig. 5.2 starts from V_d = 0.05 m/s. Therefore, it is possible that the velocity range investigated in the present study was too high such that the very low velocity range in which Darcy's regime occurs was not included, and that the first segments in Fig. 5.2 may indeed be in the transition region.

5.1.3 Effects of Porosity and Pore Size on Permeability and Form Drag Coefficient

Using the second segment data of the $\frac{\Delta P}{LV_d}$ against V_d graphs (Fig. 5.2) where the line has a gradient of $\rho_f C$ and an intercept of $\frac{\mu}{K}$, the permeability (K) and the form drag coefficient (C) were calculated and the results are shown in Table 5.1. The variations of water permeability with porosity and pore size are displayed in Fig. 5.3. The form drag coefficient of sample H17 is not shown because only three data points were represented (Fig. 5.2) and an accurate value cannot be obtained.

Table 5.1: Water permeability and form drag coefficient of homogeneous LCS samples

Sample Reference	Pore Size (μm)	Actual Porosity (%)	Water Permeability ($x10^{-10}$ m^2)	Form Drag Coefficient ($x10^4$ m^{-1})
H1	250-425	59.7	0.835	3.7
H2	250-425	63.5	1.523	2.3
H3	250-425	68.6	2.452	1.4
H4	250-425	74.3	2.698	1.1
H7	425-710	59.2	0.191	14.0
H8	425-710	63.8	0.538	6.5
H9	425-710	68.7	0.873	3.2
H10	425-710	73.8	1.968	1.4
H11	425-710	77.0	3.685	1.4
H12	710-1000	58.2	0.134	13.2
H13	710-1000	63.1	0.265	8.7
H14	710-1000	68.2	0.582	6.3
H15	710-1000	73.1	0.967	2.5
H16	710-1000	79.5	2.336	0.7
H17	1000-1500	57.6	0.096	-
H18	1000-1500	69.8	0.400	5.9
H19	1000-1500	78.2	1.418	2.7

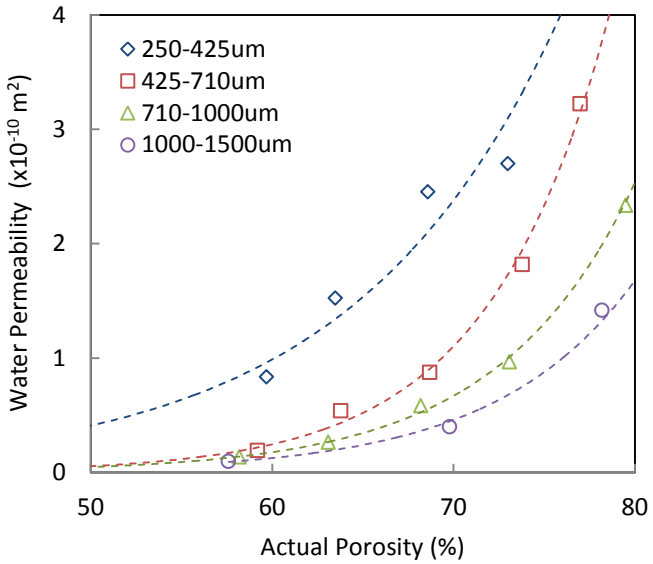

Figure 5.3: Relationship between water permeability and porosity of homogeneous LCS porous Cu with different pore sizes.

The porosity of the LCS homogeneous samples had a significant effect on the permeability. In general, there is an exponential relationship between permeability and porosity. Past research showed similar exponential relationship between water permeability and porosity (Nelson 1994, Bethke 1985). Increasing porosity leads to lower fluid resistance since there is a lower fraction of solid matrix impeding fluid flow. Furthermore, the likelihood of the pores being connected to each other is higher in samples with higher porosity than found in the lower porosity samples. Therefore, the water permeability of the samples increases with increasing porosity, as seen in Fig. 5.3.

The pore size also influences the water permeability of the LCS porous copper samples. Comparing samples with similar porosity but different pore sizes, a higher permeability was recorded for samples with smaller pore size. Ranking the samples of similar porosity (e.g. H3, H9, H14 and H18) according to their permeability, sample H3 with the smallest pore size gave the highest permeability, followed by H9 then H14, while sample H18 with the largest pore size gave the lowest permeability.

Several reports on porous media showed that smaller pore sizes led to higher water permeability (Zhang et al. 2005, Bonnet and Topin 2008, Despois and Mortensen 2005) because decreasing the pore size leads to an increase in pore density per unit volume, the pores become more connected and more channels for fluid flow are created. As a result, the resistance of the samples with smaller pores to water flow decreases, leading to lower ΔP, as observed in Fig. 5.1.

The relationship between the form drag coefficient and the structural parameters of the homogenous LCS porous copper samples was also investigated. The form drag coefficient is plotted against porosity and against permeability in Figs. 5.4 and 5.5, respectively. As shown in Fig. 5.4, the form drag coefficient decreases with increasing porosity and decreasing pore size. Additionally, the form drag coefficient decreases sharply with permeability, decaying exponentially (Fig. 5.5).

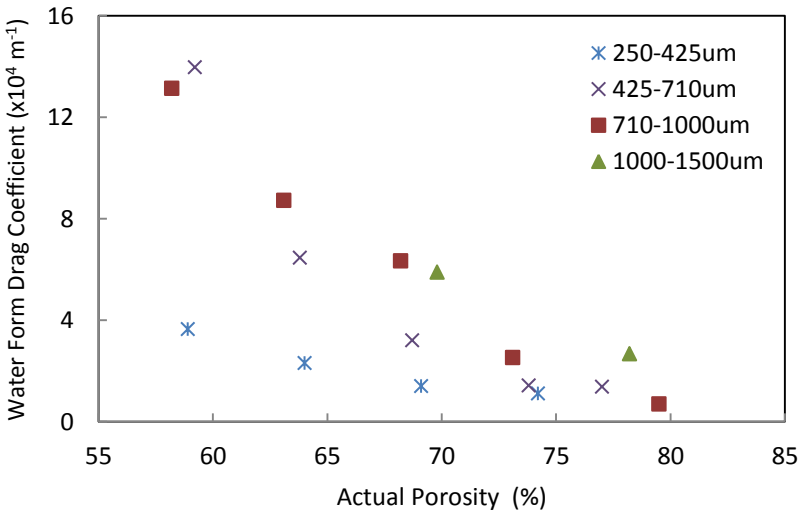

Figure 5.4: Relationship between form drag coefficient and porosity of homogeneous LCS porous Cu with different pore sizes.

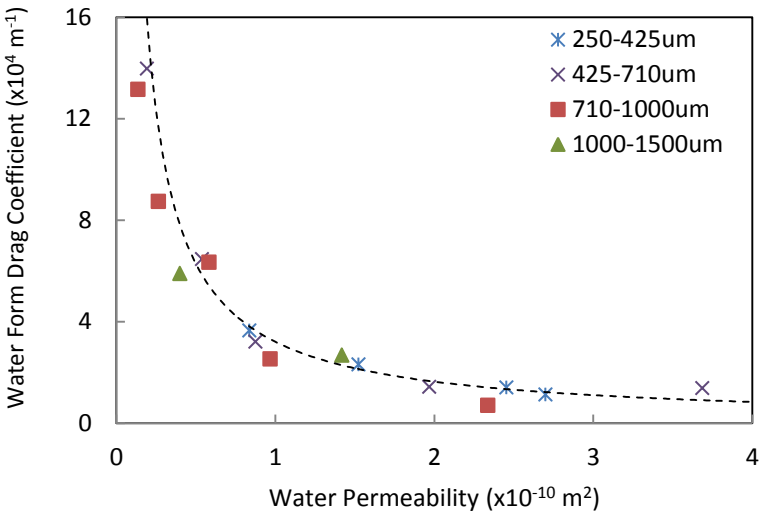

Figure 5.5: Relationship between form drag coefficient and permeability of homogeneous LCS porous Cu with different pore sizes.

Lower permeability or higher fluid resistance and higher form drag coefficient (or inertial effects) with decreasing porosity are due to a higher fraction of solid impeding the fluid flow. Samples with larger pores have more tortuous channels for fluid flow as the pore density per sample volume decreases. As a consequence, decreasing the porosity and increasing the pore size of homogeneous LCS samples led to lower permeability (Fig. 5.4) and higher form drag coefficient (Fig. 5.5). These findings are consistent with those found in literature (Bonnet and Topin 2008, Zhang et al. 2005, Cornell 1953, Geertsma 1974, Liu et al. 1995).

There exist several relationships between the form drag coefficient and the structural parameters in the literature (Section 2.4). The results for the LCS samples best fit with a relationship in the form similar to those of Cornell, Jones and Pascal (Table 2.3). Fig. 5.6 displays the relationship between *C* and *K* in comparison to literature (Section 2.4.1). The

overall relationship between *C* and *K* in all the homogeneous LCS porous copper samples can be described as:

$$C = \frac{6.1x10^{-4}}{K^{0.76}} \quad (R^2=0.82) \qquad (5.2)$$

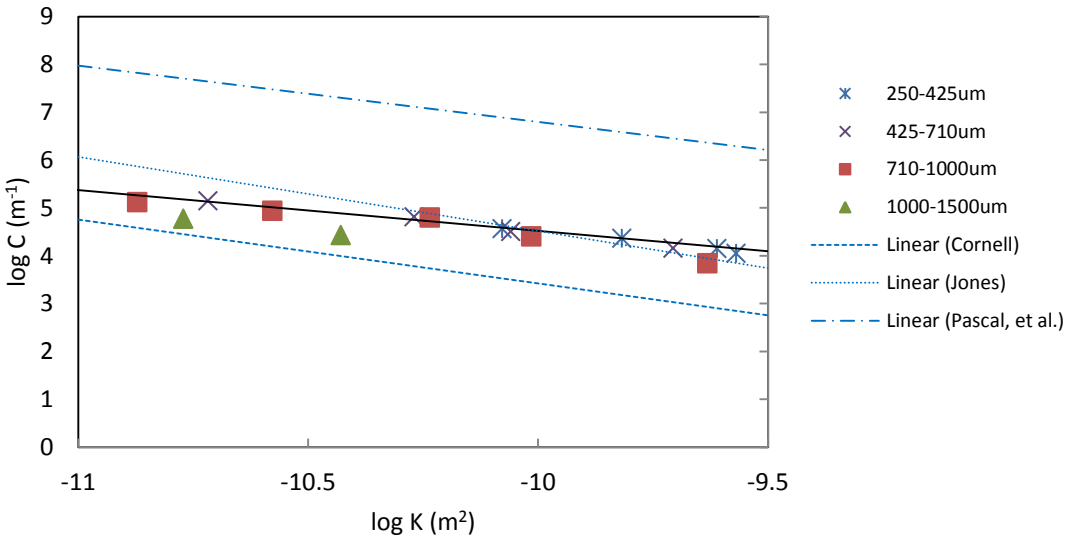

Figure 5.6: Relationship between form drag coefficient and permeability in comparison to literature.

The constants in the *K-C* relationship for the homogeneous LCS samples differ from those found in the literature. Li and Engler (2001) identified three sources of diversity in the empirical correlations, which were:

1) relativity of flow direction to pore channels, i.e. different *K-C* correlations between parallel and perpendicular flows,
2) different number of parameters considered when developing the correlations, and
3) different pore geometry.

The latter is more likely to be the reason behind the diversity in the empirical correlations displayed in Fig. 5.6, since LCS samples have a very different pore structure than those in the literature. The uniqueness of the structure of LCS porous samples will be discussed further in Section 5.1.5.

5.1.4 Transition Reynolds Number

Table 5.2 lists the Reynolds numbers (*Re*) corresponding to the transition to Forchheimer regime calculated using different length scales.

Table 5.2: Transition flow velocity and Reynolds number for water flow in homogeneous LCS samples.*

Sample Reference	Pore Size (µm)	Transition flow velocity (m/s)	$Re = \frac{\rho V_d \sqrt{K}}{\mu}$	$Re = \frac{\rho V_R \sqrt{K}}{\mu}$	$Re = \frac{\rho V_d d_P}{\mu}$	$Re = \frac{\rho V_R d_P}{\mu}$
H1	250-425	0.059	0.536	0.90	19.91	33.35
H2	250-425	0.060	0.736	1.17	20.25	31.89
H3	250-425	0.064	1.006	1.46	21.60	31.49
H4	250-425	0.068	1.116	1.50	22.95	30.89
H7	425-710	0.062	0.269	0.46	35.19	59.43
H8	425-710	0.064	0.467	0.74	36.32	56.93
H9	425-710	0.073	0.679	0.99	41.43	60.30
H10	425-710	0.069	0.972	1.31	39.16	53.06
H11	425-710	0.074	1.417	1.84	42.00	54.54
H12	710-1000	0.058	0.212	0.36	49.59	85.21
H13	710-1000	0.059	0.304	0.48	50.45	79.94
H14	710-1000	0.059	0.447	0.66	50.45	73.97
H15	710-1000	0.058	0.574	0.78	49.59	67.84
H16	710-1000	0.059	0.908	1.13	50.45	63.45
H17	1000-1500	0.057	0.178	0.31	71.25	123.70
H18	1000-1500	0.064	0.406	0.58	80.00	114.61
H19	1000-1500	0.061	0.720	0.93	76.25	97.51

*where V_R is the real velocity equivalent to $\frac{V_d}{\phi}$ and d_p is the pore diameter.

There is less variation in the resulting *Re* values when the Darcian velocity (V_d) was applied instead of the real velocity (V_R). For the *Re* numbers defined by the permeability, the transition *Re* increases with porosity and decreases with pore size. Since *Re* is proportional to $\sqrt{K}$, and *K* increases with increasing porosity and decreasing pore size, the *Re* values follow the same trend.

Utilising the average pore diameter as the length scale led to a higher variation in the resulting transition *Re* numbers. Comparing samples H1-H4 (250-425µm pore size) with samples H17-H19 (1000-1500µm pore size), the *Re* values increased by a factor of four owing to the large difference in the pore diameters. Since *Re* is directly proportional to the pore diameter, increasing the pore diameter will lead to the increase in the equivalent *Re* values.

In theory, the critical/transition *Re* number is expected to have little variations. From Table 5.2, the *Re* values defined using $\sqrt{K}$ gave a narrower range of *Re* numbers. Boomsma and Poulikakos (2001a) concluded in their paper that the best approach to calculate *Re* was using the $\sqrt{K}$ as the length scale since this method produced the narrowest range of transition *Re* numbers compared to using the average pore diameter.

From Table 5.2, there is a relatively high variation in all the *Re* numbers displayed. The variation in the transition flow velocity, however, was very small. Therefore, for LCS porous samples, the transition point to which the flow changes from laminar to turbulent is best described using the transition flow velocity instead of critical *Re* numbers.

5.1.5 Discussion on Structural Effects

The presence of inter-particle pores in LCS porous samples is one of the reasons behind the increasing permeability with decreasing pore size. The porous copper manufactured by the LCS process has a unique ability to produce narrow inter-particle pores (pores created through bonding of spherical Cu particles) in addition to the large pores created by the space-holder. Fig. 5.7 shows a typical microstructure of the LCS porous copper showing the narrow inter-particle pores. These inter-particle pores allow the pores created by the potassium carbonate (space-holder) to be connected.

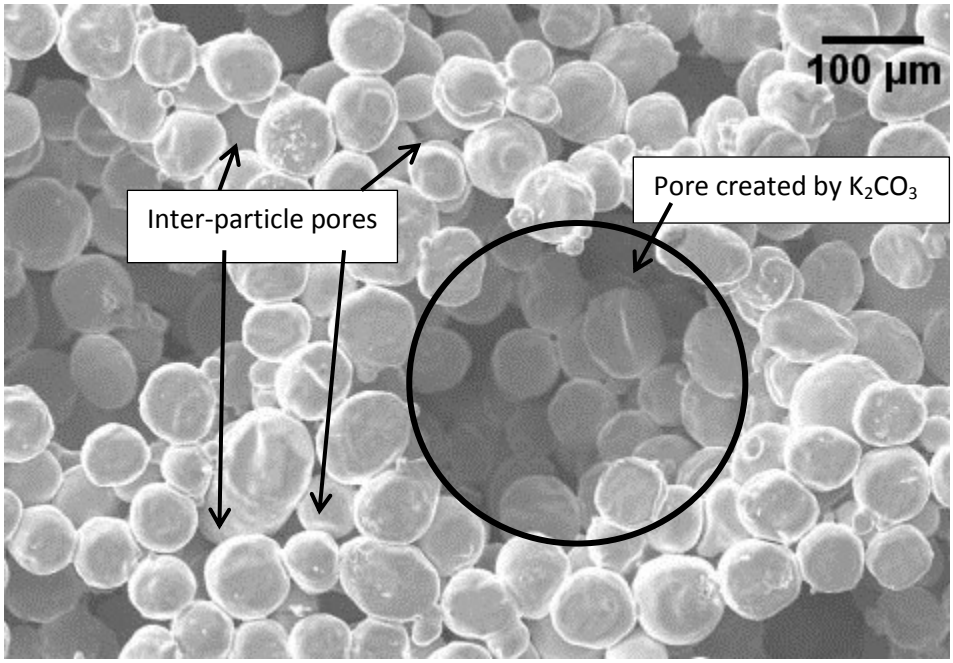

Figure 5.7: SEM micrograph of LCS porous Cu (70% porosity, 250-425um pore size) showing narrow inter-particle pores created through bonding of Cu spheres, allowing connection of the large pores created by carbonate spheres.

From the results obtained in this thesis, the permeability increased as the pore size decreased. This contradicts the results of several studies including those of Bhattacharya, Calmidi and Mahajan (2002) and Boomsma and Poulikakos (2001a). Boomsma and Poulikakos (2001a) found that holding the porosity constant and decreasing the pore diameter led to an increase in flow resistance due to the high specific surface area, hence a

decrease in permeability and an increase in form drag coefficient. Similarly, Bhattacharya, Calmidi and Mahajan (2002) reported that permeability decreased as pore diameter decreased. The difference in these results compared to the results presented in this thesis is likely due to the presence of the narrow inter-particle pores in LCS porous copper that do not exist in the other porous media. The metal foams used in the work of Bhattacharya, Calmidi and Mahajan (2002) and Boomsma and Poulikakos (2001a) only had open pores of similar diameters. In the LCS foams, the narrow inter-particle pores between the Cu spheres link the open pores created by the carbonate particles, forming channels.

As the pore diameter decreases while holding the porosity constant, the number of pores per volume increases. For example, comparing two pore sizes, 1250 µm and 338 µm, for each 1250 µm pore, there are fifty 338µm pores in the same volume. There are more small pores per volume in LCS samples with small pore sizes, so these pores are closer to each other compared to those found in samples with larger pores. The inter-particle pores interlink these small pores to form channels. The likelihood of the small pores being connected through the inter-particle pores is higher than that of the large pores, so more connecting channels are formed through which fluid can flow through.

Tortuosity is another factor contributing to the effect of pore size. According to Xiao and Zhao (2013), for the same porosity of around 62%, a tortuosity of 1.63 was found for the LCS sample with the 250-425 um pore size, while a higher tortuosity value of 2.42 was found for the LCS sample with the 1000-1500 um pore size. In other words, a more tortuous flow

occurs in samples with larger pore diameter. Furthermore, a more tortuous flow often means a more turbulent flow.

The difference in tortuosity can be illustrated in Fig. 5.8. The fluid flow between the larger pores and the connecting inter-particle pore is more tortuous than the flow between smaller pores, due to the large difference between the diameter of the large pores and the narrow inter-particle pores. In large pores, a 'bottle-neck' effect is more pronounced due to the big difference between its diameter and that of the inter-particle pores, hence limiting fluid permeability. Fluid flow between small pores is less tortuous because of the shorter distance of the flow path.

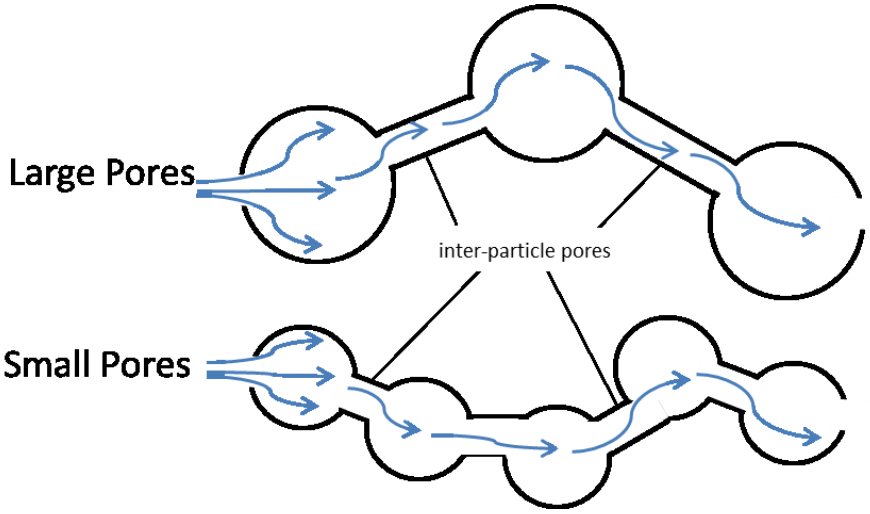

Figure 5.8: Schematic diagram to illustrate fluid flow path between small and large pores.

5.2 Air Flow in Homogeneous Samples

5.2.1 Length-Normalised Pressure Drop

The length-normalised air pressure drop $\frac{\Delta P}{L}$ for the porous copper samples listed in Table 5.1 is plotted against Darcian velocity in Fig. 5.9. The graphs were plotted separately according to the four classes of pore size. The air pressure drop for all samples increased with increasing air flow velocity in a quadratic fashion. This suggests that the inertial effects are important in the flow at high velocities. All the quadratic curves fitted well with Forchheimer's equation (Eq. 3.7) with a determination coefficient R^2>99%.

The air pressure drop results showed a similar trend to that observed when water was used as fluid (Section 5.1.1). The samples with the highest porosity gave the lowest air pressure drop for each pore size category. Likewise, samples with smaller pore size generated lower air pressure drops.

The effect of the pore size on pressure drop is greatest for samples with lower porosity. For example, comparing samples H1 and H7 with similar porosities, the pressure drop generated in sample H7 (425-710 µm pore size) is four times higher than that in H1 (250-425 µm pore size). If the pore size was further increased to 710-1000 µm (sample H12), there is a slight increase in pressure drop. Further increasing the pore size to 1000-1500 µm, a slight increase in pressure drop was observed also.

The trend of increasing pressure drop with decreasing pore size could be explained by the increase in pore density in samples with smaller pore size. As discussed in Section 5.1, increase in pore density means that the pores are more connected so resistance to air flow decreases, leading to lower pressure drop. However, this same trend is not seen for samples with very high porosities. For example, samples H4, H11, H12 and H19 have very similar pressure drops. This could be explained by the fact that for samples with very high porosity, there is already greater pore connectivity. Therefore, the increase in pore density offered by having smaller pore size has little contribution to the overall pore connectivity of the high porosity sample. Unlike in low porosity samples where there are only a small number of pores present (created by K_2CO_3), changing pore size in high porosity samples has a less significant influence on increasing the overall pore connectivity, and hence the air pressure drops in the samples.

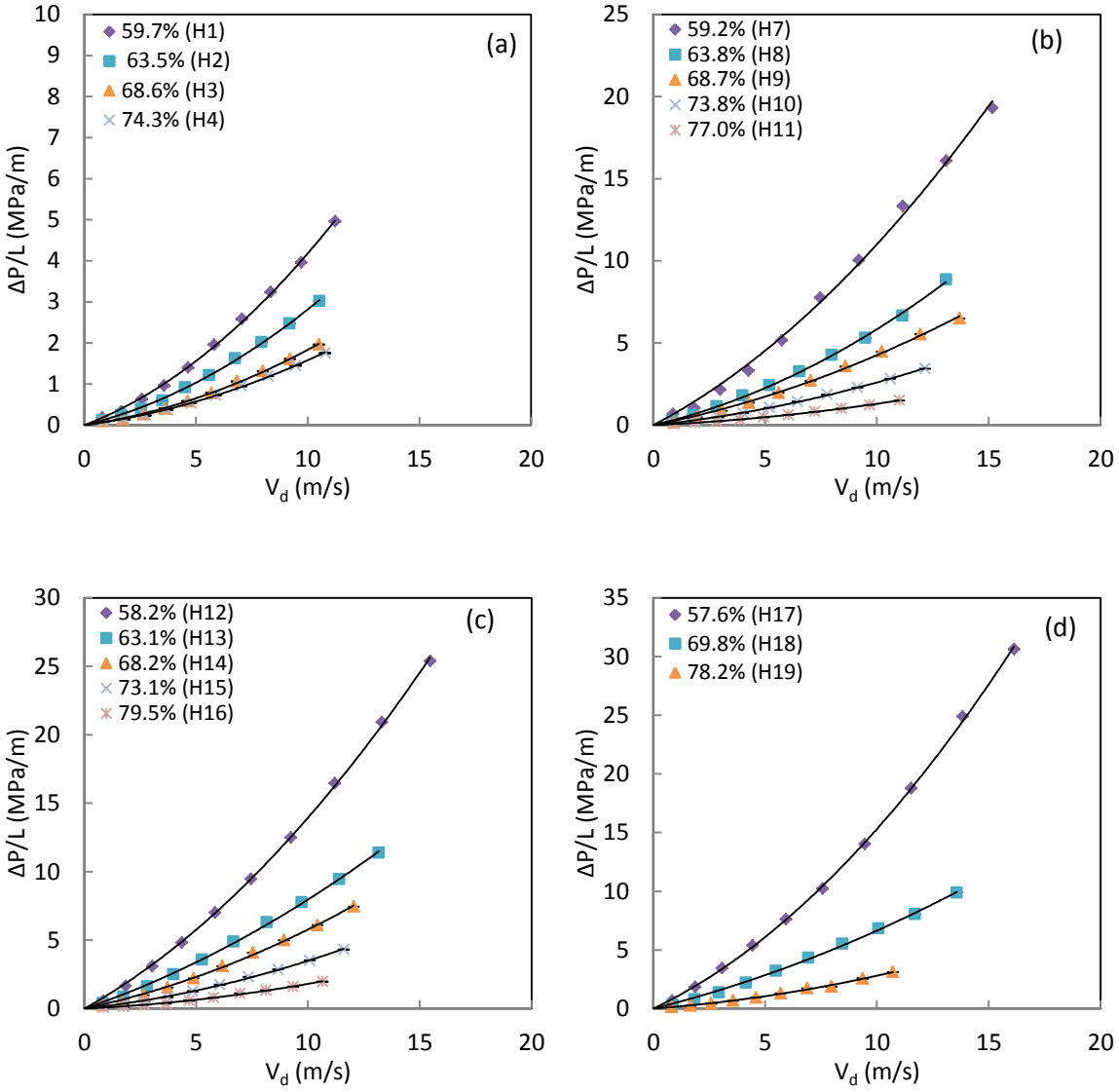

Figure 5.9: Length-normalised pressure drop (ΔP/L) versus Darcian air flow velocity for homogeneous samples with different porosities (shown on graph) and pore sizes: a) 250-425µm, b) 425-710µm, c) 710-1000µm and d) 1000-1500µm.

Past research on air flow in porous media also showed a quadratic Forchheimer relationship occurring at high air flow velocities due to inertial effects becoming dominant (Dukhan and Ali 2012, Khayargoli et al. 2004, Medraj, et al. 2007). Higher air pressure drops were observed for samples with lower porosities (Medraj et al. 2007, Dukhan and Patel 2008). In terms of pore size, higher air pressure drops were observed in samples with bigger pore size

in some studies (Xiao 2013), and in samples with smaller pore sizes in others (Medraj et al. 2007, Dukhan and Patel 2008, Khayargoli et al. 2004). This difference in the effect of pore size on the fluid's pressure drop is due to the difference in the structure/pore geometry of these porous media, as discussed in detail in Section 5.1.5.

5.2.2 Transition from Darcy Regime to Forchheimer Regime

The inertial effects in the air flow within the homogeneous samples were investigated further by plotting $\frac{\Delta P}{LV_d}$ against V_d, in order to examine the transition from linear Darcy regime to the non-linear Darcy regime (Forchheimer regime). Fig. 5.10 shows the relationship between $\frac{\Delta P}{LV_d}$ and V_d for air flow in samples with different pore size and porosity. Most trend lines are composed of two segments of straight lines. The transition from one segment to another occurs at the Darcian velocity in the range of 2.5 - 3 m/s. The gradient of the trend lines of the first segments (at V_d < 2.5 - 3 m/s) of these results varies, with an increasing gradient observed for samples H2, H8-H10, H12-H16, and a deceasing gradient for samples H1, H3-H4, H7 and H11.

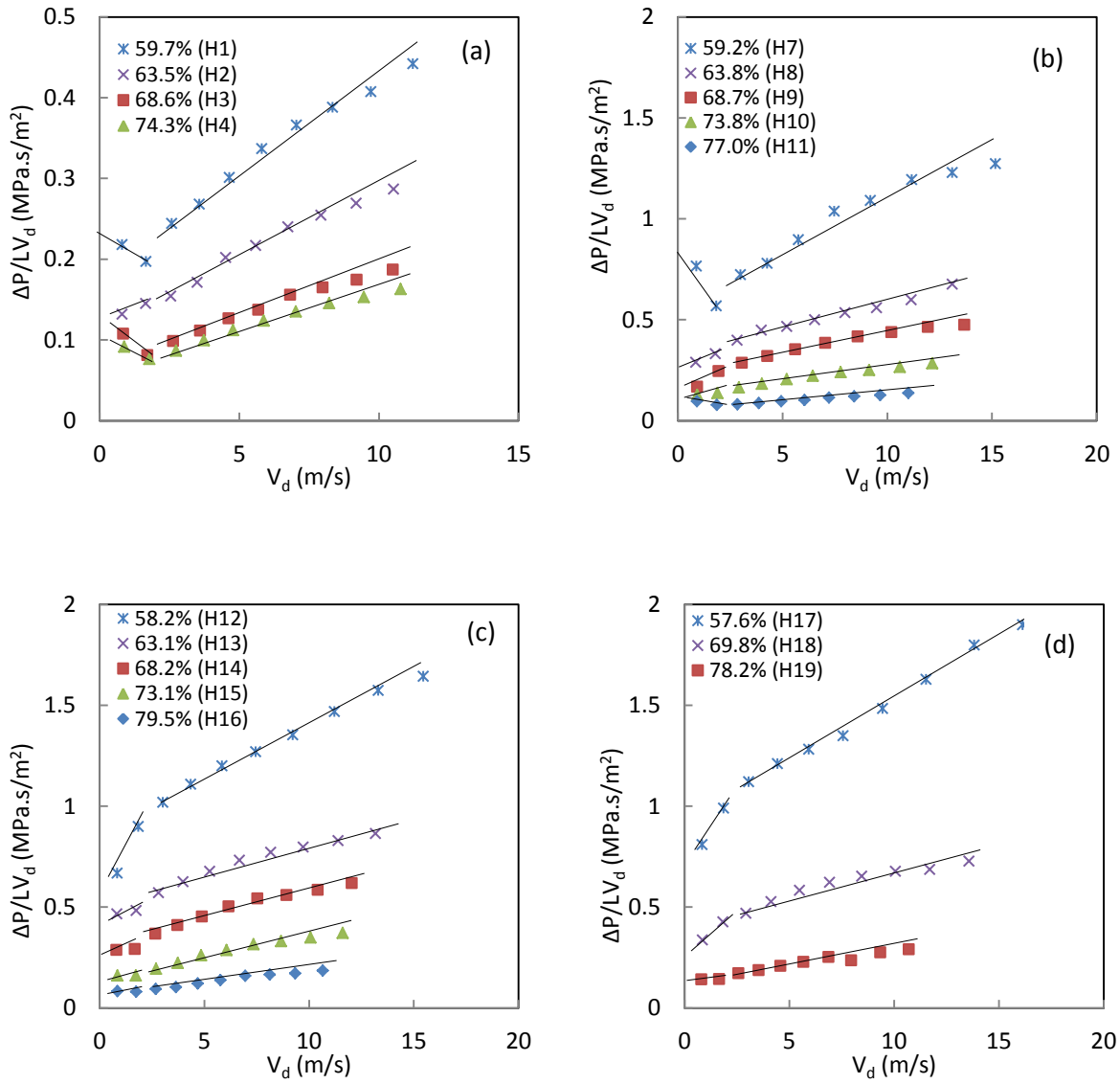

Figure 5.10: $\frac{\Delta P}{LV_d}$ versus Darcian air flow velocity for samples with different porosities (shown on graph) and pore sizes: a) 250-425 µm, b) 425-710 µm, c) 710-1000 µm and d) 1000-1500 µm.

The second segment (V_d > 2.5 - 3 m/s) for all results showed an increasing linear relationship between $\frac{\Delta P}{LV_d}$ and V_d. This suggests that inertial effects are important in the air flow within the porous copper at V_d > 2.5 m/s, and that the flow is in the non-linear Forchheimer regime.

Dukhan and Ali (2012) observed that for open-celled aluminium foams, the air pressure drop was in the Forchheimer regime for air flow velocity of 2 m/s or higher. Oun and Kennedy (2015) reported that Forchheimer regime occurred at air flow velocity in the range of 4 - 12 m/s for porous nickel. In the present study, the Forchheimer regime in all samples started at approximately V_d = 2.5-3 m/s, which is similar to those found in the previous studies.

The low accuracy of the data points at very low flow velocity makes it difficult to determine the Darcy regime and transitional region in the present study. From Fig. 5.10, no horizontal line was clearly observed; all the first segments showed only two data points which were either increasing or decreasing. This suggests that the flow shown in the first segment may be within the transition region from Darcy to Forchheimer regimes. Table 5.3 displays the transition air flow velocities for the homogeneous samples.

Table 5.3: Transition flow velocity for air flow in homogeneous LCS samples.

Sample Reference	Pore Size (μm)	Actual Porosity (%)	Translational air flow velocity (m/s)
H1	250-425	59.7	2.58
H2	250-425	63.5	2.55
H3	250-425	68.6	2.74
H4	250-425	74.3	2.64
H7	425-710	59.2	2.99
H8	425-710	63.8	2.83
H9	425-710	68.7	3.06
H10	425-710	73.8	2.88
H11	425-710	77.0	2.84
H12	710-1000	58.2	3.02
H13	710-1000	63.1	2.81
H14	710-1000	68.2	2.66
H15	710-1000	73.1	2.69
H16	710-1000	79.5	2.68
H17	1000-1500	57.6	3.07
H18	1000-1500	69.8	2.93
H19	1000-1500	78.2	2.59

5.2.3 Effects of Porosity and Pore Size on Air Permeability and Form Drag Coefficient

Using the second segment data of the $\frac{\Delta P}{LV_d}$ against V_d graphs (Fig. 5.10), the permeability and the form drag coefficient were calculated, and the results are shown in Table 5.4 and Fig. 5.11.

Table 5.4: Air permeability and form drag coefficient of homogeneous LCS samples.

Sample Reference	Pore Size (µm)	Nominal Porosity (%)	Actual Porosity (%)	Air Permeability ($x10^{-10}$ m^2)	Form Drag Coefficient ($x10^3$ m^{-1})
H1	250-425	60	59.7	0.892931	18
H2		65	63.5	1.395134	12
H3		70	68.6	2.350687	9
H4		75	74.3	2.569904	7
H7	425-710	60	59.2	0.258509	32
H8		65	63.8	0.576206	22
H9		70	68.7	0.683532	13
H10		75	73.8	1.298976	10
H11		80	77.0	2.889992	6
H12	710-1000	55	58.2	0.202161	40
H13		60	63.1	0.331318	20
H14		65	68.2	0.530596	19
H15		70	73.1	1.043167	14
H16		75	79.5	2.372051	7
H17	1000-1500	50	57.6	0.202991	52
H18		60	69.8	0.387543	16
H19		70	78.2	1.290811	11

The porosity of the LCS porous copper sample had a significant effect on the air permeability, with higher porosity resulting in greater air permeability (Fig. 5.11). Past research showed a similar exponential trend between air permeability and porosity (Moreira et al. 2004).

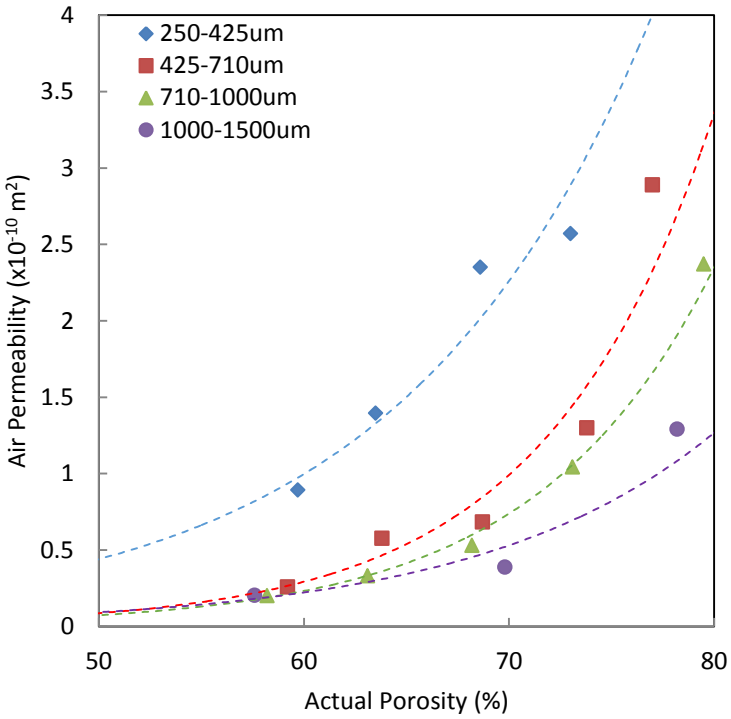

Figure 5.11: Relationship between air permeability and actual porosity of homogeneous LCS porous Cu with different pore sizes.

The pore size also influenced the air permeability of the LCS porous copper samples. Higher air permeability was observed for samples with smaller pore size. For instance, ranking samples of similar porosity (H3, H9, H14 and H18) according to their air permeability, sample H18 with the largest pore size gave the lowest permeability, followed by H14, H9, and H3. The effect of pore size was more obvious for samples in the higher porosity range (>65%). Xiao (2013) also observed that for homogeneous LCS samples, smaller pore sizes led to higher permeability coefficients.

Fig. 5.12 shows the form drag coefficient as a function of porosity for different pore size. Increasing the porosity and decreasing the pore size led to the decrease of the form drag

coefficient. The effect of pore size on the form drag coefficient is more obvious in lower porosity samples.

.

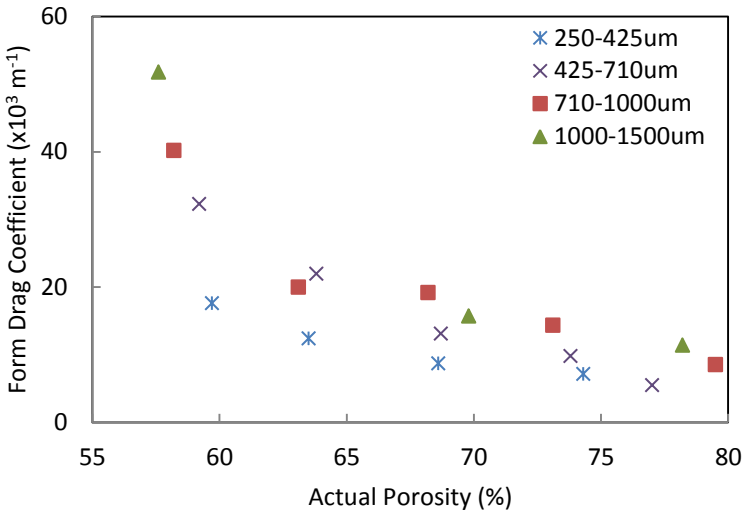

Figure 5.12: Relationship between form drag coefficient and porosity of homogeneous LCS porous Cu with different pore sizes.

Fig. 5.13 shows the relationship between the form drag coefficient and air permeability. The form drag coefficient decreased sharply into a plateau, following an "exponential decay" trend when the permeability of the sample increased. The effect of pore size is less obvious in Fig. 5.13, suggesting that the relationship between form drag and permeability was not dependent on the sample's pore size.

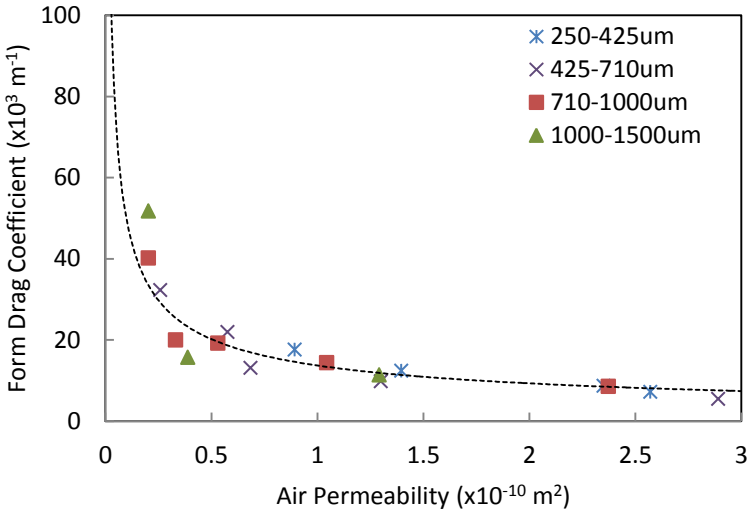

Figure 5.13: Relationship between form drag coefficient and air permeability of homogeneous LCS porous Cu with different pore sizes.

The relationship between form drag coefficient and air permeability in all the homogeneous LCS porous copper samples can be described as:

$$C = \frac{5.6\times10^{-3}}{K^{0.637}} \quad (R^2=0.89) \tag{5.3}$$

which fits well to the experimental data, as shown in Fig. 5.14.

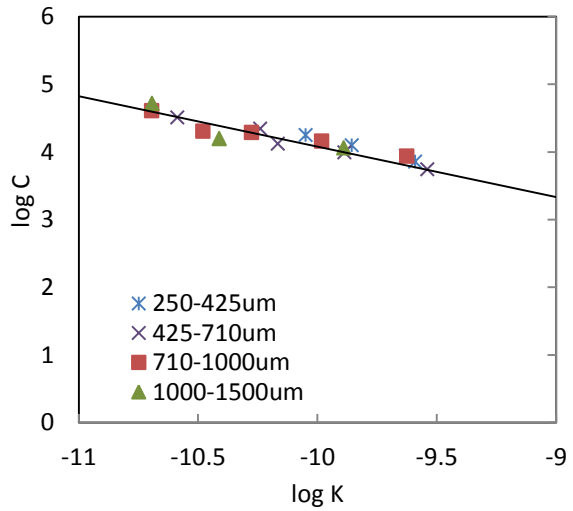

Figure 5.14: Relationship between form drag coefficient (C) and air permeability (K).

5.2.4 Comparison with Water Flow

5.2.4.1 Transition Flow Velocity

For the study of air flow, the flow velocities ranged from 0 to 20 m/s, while for liquid flow, velocities ranged between 0 and 0.4 m/s. For both cases, the pressure drop showed a quadratic relationship with Darcian velocity, suggesting that the flow regime is non-Darcy or Forchheimer where inertial effects are important. For water flow, the Forchheimer regime began at V_d = 0.05 - 0.08 m/s; while for air flow, the Forchheimer regime started at V_d = 2.5-3 m/s. The difference in the transition velocity for air and water is related to the different physical properties of the two fluids. Gas molecules can slip past the solid walls which increases the flow velocity, whereas, for water flow, this phenomenon is not experienced Jones (2013).

For both cases, the linear-Darcy flow was not observed as the velocity ranges studied were not low enough. The data points at low flow velocities may have represented the transition region between Darcy and Forchheimer regimes.

5.2.4.2 Permeability

Fig. 5.15 compares the permeability values obtained using either gas or water. The porosity of the LCS porous copper sample has a significant effect on both the water and air permeability, with higher porosity resulting in greater permeability. Smaller pore size also led to higher permeability for both air and water flows. For the same sample, the permeability values were similar for both air and water suggesting that permeability is independent of the type of fluid.

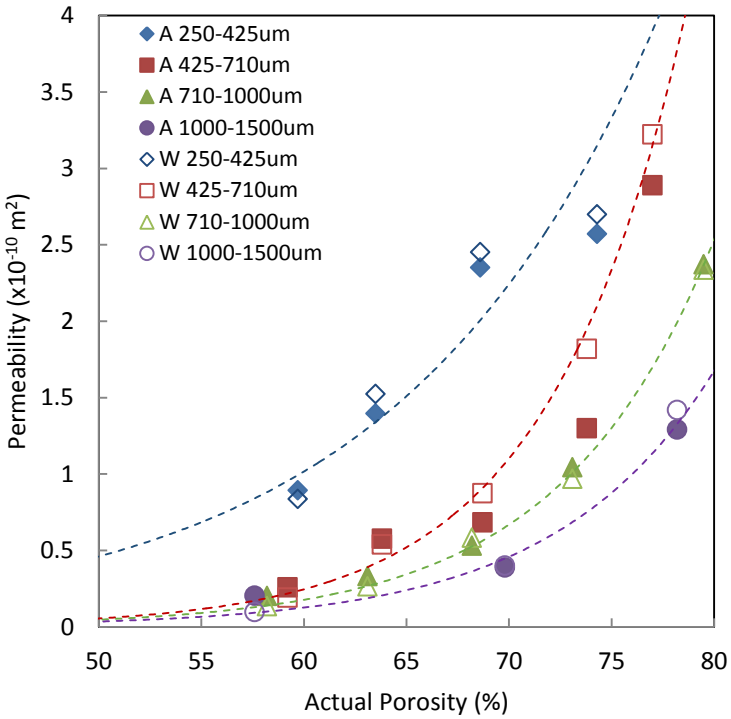

Figure 5.15: Comparison between measured air (A) and water (W) permeability for homogeneous LCS porous Cu with different porosity and pore size.

For most samples, the water and air permeability values were close to each other, with differences ranging between 0.11×10^{-10} m^2 and 0.19×10^{-10} m^2. Bigger differences between the air and water permeability values were observed for samples H10 (73.8%, 425-710 µm pore size) and H11 (77.0%, 425-710 µm pore size), with differences of 0.5×10^{-10} m^2 and 0.3×10^{-10} m^2, respectively. Nonetheless, the air and water permeability trend lines for each pore size category were very similar.

Klinkenberg (1941) and Carman (1956) observed that for the same sample, different permeabilities were obtained for gas and water fluids, due to the air compressibility. Air compressibility effects were also observed by Furbish (1997), Jones (2013), Tanikawa and Shimamoto (2006), and Zhong et al. (2014). Klinkenberg (1941) explained that when the

pore sizes are very small (0.01-0.1 µm), the slip flow of gas at pore walls enhances the gas flow. The compressibility effect is only present in air flow and not in water flow. In the present study, the compressibility effect of air was already considered in the measurement of pressure drops (Section 3.3). As a consequence, the permeabilities obtained for air and water flows are very similar.

5.2.4.3 Form Drag Coefficient

Fig. 5.16 compares the form drag coefficients obtained using the two fluids. For both fluids, the form drag coefficient deceases with increasing porosity and decreasing pore size. However, the form drag coefficients obtained from water flow was much higher than those from air flow, with greater differences in lower porosity samples. This suggests that the sensitivities of *K* and *C* to fluid properties are very different (Madani et al. 2007, Bonnet et al 2008).

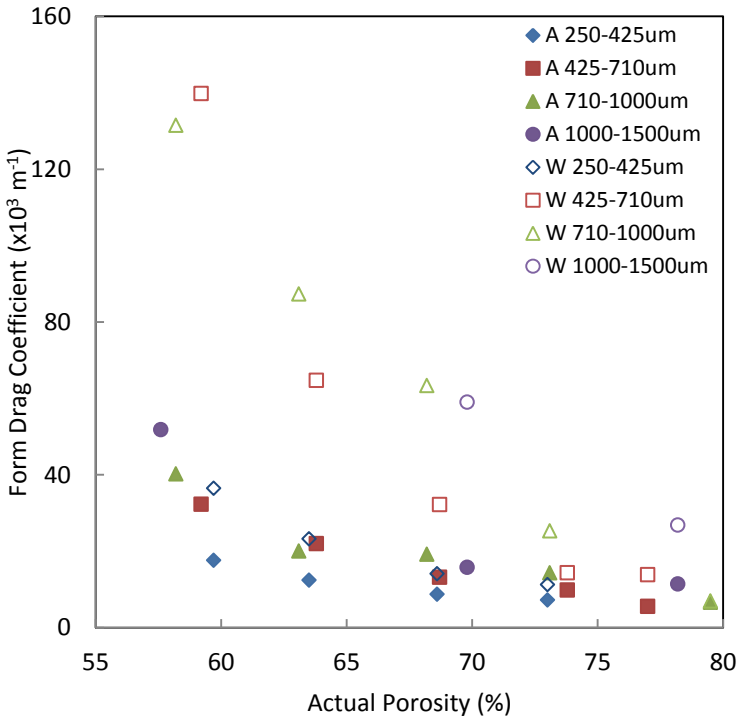

Figure 5.16: Comparison between air (A) and water (W) form drag coefficients for homogeneous LCS porous Cu with different porosity and pore size.

In the present work, the smallest difference between the form drag coefficients of air and water flows was 5% for sample H16, whose porosity is 79.5%. This result is similar to that found by Bonnet et al. (2008) who reported that form drag coefficients in water flow were approximately 10% higher than those in air for higher sample porosity. The greatest difference between air and water form drag coefficients was found for sample H7 (with a low porosity of 59.2%), where C values differ by 300%. The differences reflect the different effects of the internal pore structure on K and C. In lower porosity samples, a higher wall density results in higher flow resistance to water flow.

Several mechanisms may affect water and gas flows, with the most prominent factors depending on the internal structural properties of the porous media, i.e., pore size, pore shape or permeability. It was suggested that the difference between air and water flow is dominated by the “Klinkenberg effect” for flow resistance, such that gas slippage occurs at the walls which increases the flow velocity (Klinkenberg 1941, Furbish 1997, Jones 2013, Tanikawa and Shimamoto 2006). As a consequence, resistance to bulk air flow is reduced and inertial effects are lower. In addition, Faulkner and Rutter (2000) suggested that the adhesion of water molecules on the wall surface reduces the effective pore diameter for water flow hence higher flow resistance or inertial effects. These evidences explain the difference in water and air form drag coefficients.

5.3 Water and Air Flows in Homogeneous Samples with Different Lengths

Darcy and Forchheimer equations describe permeability as a value that is independent of sample's length. This section investigates the effect of the sample's length on the permeability and form drag coefficient, and studies the validity of Darcy and Forccheimer laws on LCS porous copper.

5.3.1 Length-Normalised Pressure Drop

A sample of known porosity (65%) and pore size (425-710 µm) was cut into different lengths and the pressure drops across these samples using air and water were measured. Fig. 5.17 displays the $\frac{\Delta P}{L}$ vs V_d graphs for air and water flows, while Fig. 5.18 displays the $\frac{\Delta P}{LV_d}$ vs V_d graphs.

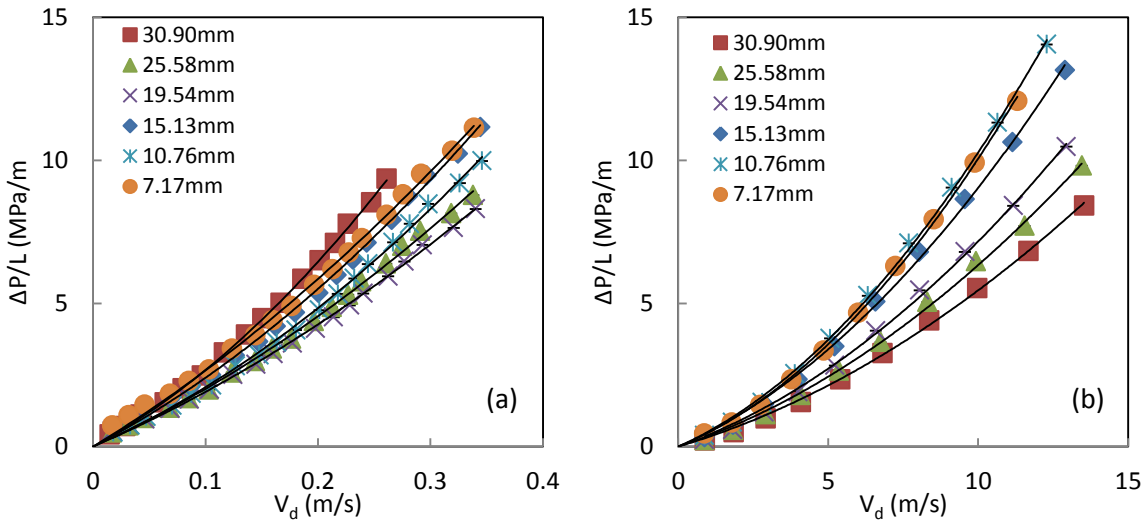

Figure 5.17: Length-normalised pressure drop versus flow velocity for homogeneous LCS porous copper samples (porosity: 65%, pore size 425-710µm) with different lengths, using either (a) water or (b) air.

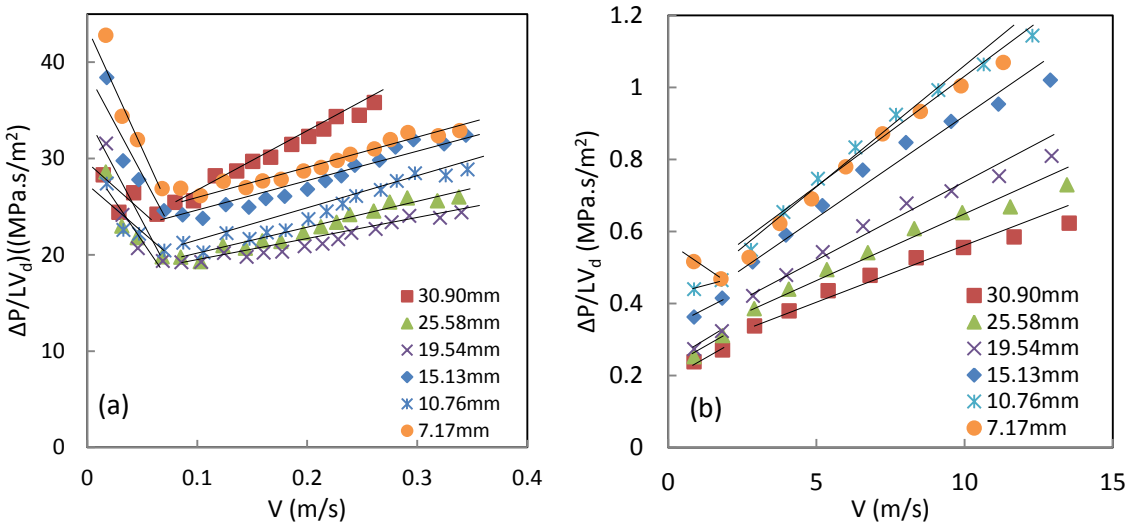

Figure 5.18: $\frac{\Delta P}{LV_d}$ versus flow velocity graphs for samples (porosity: 65%, pore size 425-710µm) with different lengths: a) water flow and b) air flow.

For all the samples of different lengths, the pressure drop increased with increasing velocity in a quadratic fashion (Fig. 5.17). All the quadratic curves fitted well with Forchheimer's equation (Eq. 3.7), with a determination coefficient R^2>99%. For water flow, there was no clear trend between the pressure drop and sample length. The normalised-water pressure drop curves differ for different sample lengths. For air flow, the samples with 7.17 mm and 10.76 mm lengths showed nearly identical curves, with the data points for each sample lying very close to each other. Increasing the sample length from 10.76 mm to 30.90 mm, however, led to the decrease in pressure drops.

From Fig. 5.18, it was apparent that the trend lines were composed of two segments of straight lines. The transition flow velocity and permeability coefficients are displayed in Table 5.5. The gradient of the trend lines of the first segments of these results varies, with an increasing gradient observed for some samples and a deceasing gradient for others. The low accuracy of the data points at very low flow velocity (first segment) makes it difficult to

determine the pressure drop trend in the present study. No horizontal line was clearly observed, suggesting that the flow in the first segment may be within the transition region from Darcy to Forchheimer regimes.

Table 5.5: Transition flow velocity and permeability of homogeneous samples with different lengths.

Sample Reference	Length (mm)	Transition water flow velocity (m/s)	Water permeability ($x10^{-10}$ m^2)	Transition air flow velocity (m/s)	Air permeability ($x10^{-10}$ m^2)
H20	7.17	0.068	0.418	2.80	0.443
H21	10.76	0.070	0.578	2.90	0.409
H22	15.13	0.070	0.483	2.95	0.415
H23	19.54	0.069	0.583	2.92	0.505
H24	25.58	0.068	0.582	2.95	0.545
H25	30.90	0.064	0.482	2.92	0.596

5.3.2 Effects of Sample Length on Pressure Drop, Permeability and Form Drag Coefficient

Fig. 5.19 plots the length-normalised pressure-drop against the sample length for different water and air flow velocities. For both flow velocities below the transition velocity, the length-normalised pressure drop is independent of the sample length. Typically, the thickness-independent behaviour is only observed in the laminar flow region, i.e. below the transition velocity (Oun and Kennedy 2015). On the other hand, increasing the flow velocity above the transitional region shows a different trend for both fluids.

For both fluid flows, the relationship between the length-normalised pressure-drops and the sample length becomes more complex at higher flow velocities. Lower pressure drops were observed for thicker samples (19.54 - 30.90 mm) than in thinner sample. Medraj, et al. (2007) explained that the difference in pressure drops in samples with varying sample lengths was due to the increasing “open area” to the fluid flow through the metallic foam

with increasing sample length. This results to lower resistance to fluid flow with sample length. However, it should be noted that the limited number of data points makes it difficult to determine precisely the transitions and subtle effects of the flow velocity, if any.

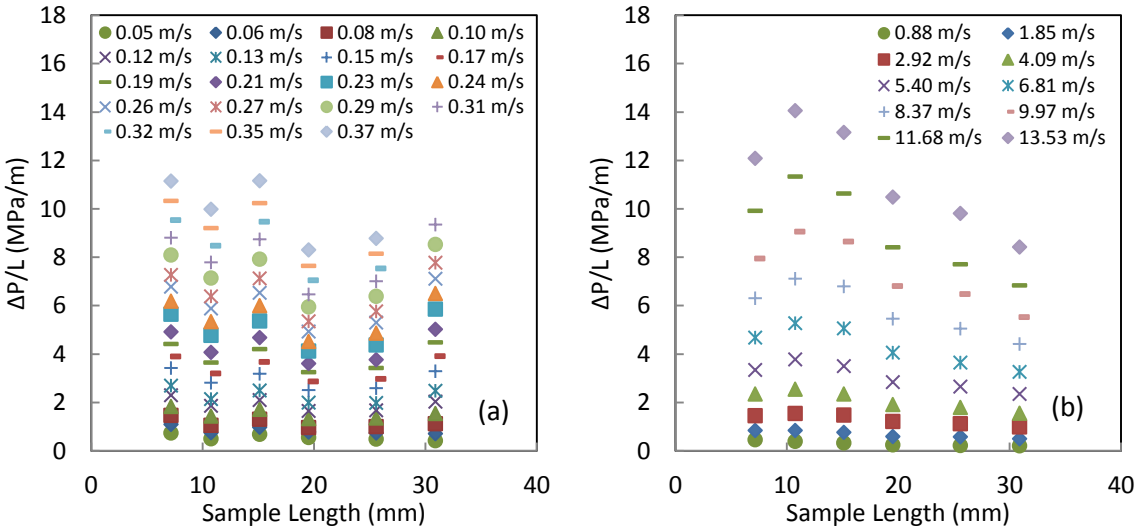

Figure 5.19: Length normalised pressure-drop versus sample length at different Darcian velocities: a) water flow and b) air flow.

Fig. 5.20 shows that varying the length of the sample had little effect on both air and water permeability. All the permeability values varied within the range of $0.4x10^{-10}$ m^2 - $0.6x10^{-10}$ m^2. Since all the data lie within the uncertainty range (±7%), the permeability values are roughly similar regardless of the sample length.

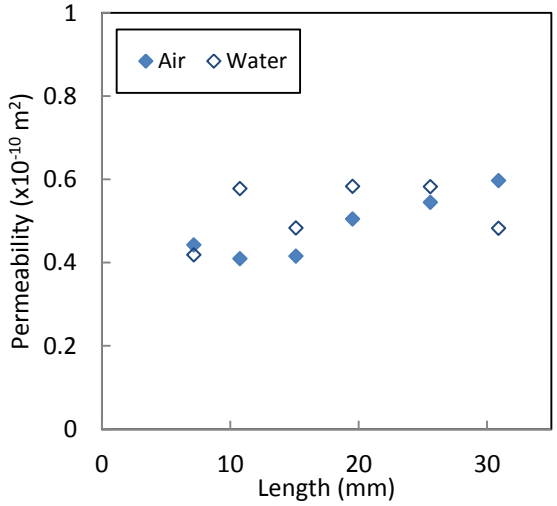

Figure 5.20: Relationship between permeability and length of the LCS porous copper samples (65% porosity, 425-710 µm pore size).

Several studies reported that a critical sample thickness/length exists beyond which the pressure drop becomes independent of the sample length. Oun and Kennedy (2015) reported a critical thickness of roughly 8mm for samples with 450 µm pore diameter. Similarly, Baril et al. (2008) reported that the critical thickness varies with pore size; the critical thicknesses were 19mm and 50mm for 400 µm and 900 µm pore sizes, respectively. The smallest sample length in the present study is 7mm, which is close to the critical thickness reported by Oun and Kennedy (2015). The results obtained from the experiments suggest that Forchheimer's equation holds true for LCS porous copper samples, and the permeability is independent of the sample's length (providing $L \geq 7$ mm).

Fig. 5.21 displays the form drag coefficients for homogenous samples of different lengths. For water flow, there is no clear trend between the form drag coefficient and sample length. For air flow however, increasing the sample length led to the decrease in form drag coefficient, suggesting that air form drag is more sensitive to the sample's length than water form drag.

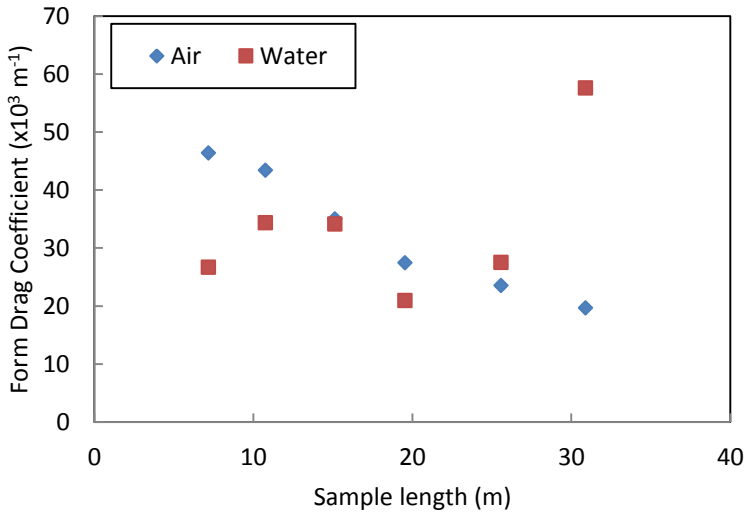

Figure 5.21: Form drag coefficients of LCS homogeneous samples with different lengths.

5.4 Water Flow in Samples with Horizontal Bilayers

The horizontal bilayer samples are composed of two layers, top (layer 1, lower porosity) and bottom (layer 2, higher porosity) layers, with each layer having a homogeneous structure. The water permeability of six horizontal bilayer samples with different porosity combinations (HB1-HB6) was investigated. All the samples were approximately 30 mm in length, 20 mm in width and 5 mm in height with pore size range of 425-710 µm. Each layer is approximately 2.5 mm in height. The structural parameters of these samples are summarised in Table 5.6.

Table 5.6: Structural parameters of LCS samples with horizontal bilayer structure.

Sample Reference	Pore Size (µm)	Layer 1 Nominal Porosity (%)	Layer 2 Nominal Porosity (%)	Overall Nominal Porosity (%)
HB1	425-710	40	70	55
HB2		40	75	57.5
HB3		40	80	60
HB4		50	70	60
HB5		50	75	62.5
HB6		50	80	65

5.4.1 Length-Normalised Pressure Drop

The length-normalised pressure drop $\frac{\Delta P}{L}$ was plotted against Darcian velocity for the LCS porous copper samples with horizontal bilayer structure for water flow, as shown in Fig. 5.22. The pressure drop for all samples increased with increasing velocity in a quadratic trend, fitting well with the quadratic function in Eq. 3.7 (determination coefficient R^2>99%).

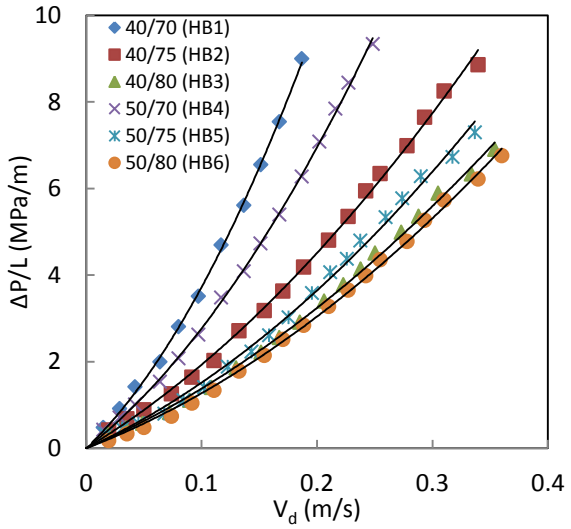

Figure 5.22: Length-normalised pressure drop versus water flow velocity for horizontal bilayer LCS porous samples.

In general, a higher pressure drop was observed for samples with the lowest overall porosity. Samples HB1 (40/70) generated the highest pressure drop while sample HB6 (50/80) generated the lowest pressure drop. In addition, increasing the porosity of the first layer from 40% to 50%, while keeping the porosity of the second layer constant, (i.e. 40/70 vs 50/70) generated a lower pressure drop. Similarly, increasing the porosity of the second layer from 70% to 80% while keeping the porosity of the first layer constant, (i.e. 40/70 vs 40/80) led to a lower pressure drop.

5.4.2 Transition from Darcy Regime to Forchheimer Regime

Fig. 5.23 shows the relationship between $\frac{\Delta P}{LV_d}$ and V_d for samples with horizontal bilayer structures. It is apparent that each curve is composed of two segments of straight lines. The transition from one segment to another occurs at V_d = 0.06-0.07 m/s (Table 5.7).

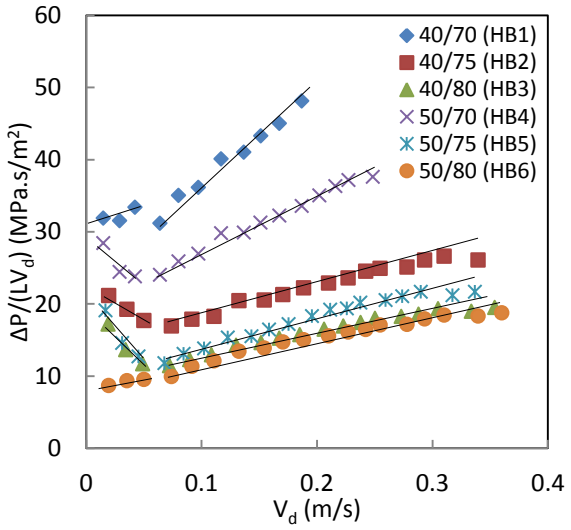

Figure 5.23: $\frac{\Delta P}{LV_d}$ versus water flow velocity for samples with horizontal bilayer structures.

Table 5.7: Transition flow velocity for water flow in LCS samples with horizontal bilayer structure.

Sample Reference	Layer 1/Layer 2 Porosity (%)	Transition flow velocity (m/s)
HB1	40/70	0.064
HB2	40/75	0.074
HB3	40/80	0.072
HB4	50/70	0.064
HB5	50/75	0.068
HB6	50/80	0.074

For the horizontal bilayer samples, the transition flow velocities (V_d = 0.06-0.07 m/s) are similar to those found in homogeneous samples with 425-710µm pore size. This suggests that, similar to homogeneous samples, the inertial effect becomes important at high flow velocity and the flow begins to enter the Forchheimer regime at V_d = 0.06-0.07 m/s for horizontal bilayer structures. The flow in this regime is said to be turbulent (Boomsma and Poulikakos 2001a, Despois and Mortensen 2005).

5.4.3 Permeability and Form Drag Coefficient

From the $\frac{\Delta P}{LV_d}$ against V_d graphs (Fig. 5.23), the permeability (*K*) and form drag coefficient (*C*) were calculated and the results are shown in Table 5.8. Figs. 5.24 and 5.25 display the variations in water permeability and form drag coefficient with the overall nominal porosity of the horizontal bilayer samples.

Table 5.8: Water permeability and form drag coefficient of LCS horizontal bilayer samples.

Sample Reference	Layer 1/Layer 2 Porosity (%)	Average overall porosity (%)	Water Permeability ($x10^{-10}$ m^2)	Form Drag Coefficient ($x10^3$ m^{-1})
HB1	40/70	55	0.420	129
HB2	40/75	57.5	0.679	37
HB3	40/80	60	0.988	29
HB4	50/70	60	0.501	74
HB5	50/75	62.5	0.973	38
HB6	50/80	65	1.106	29

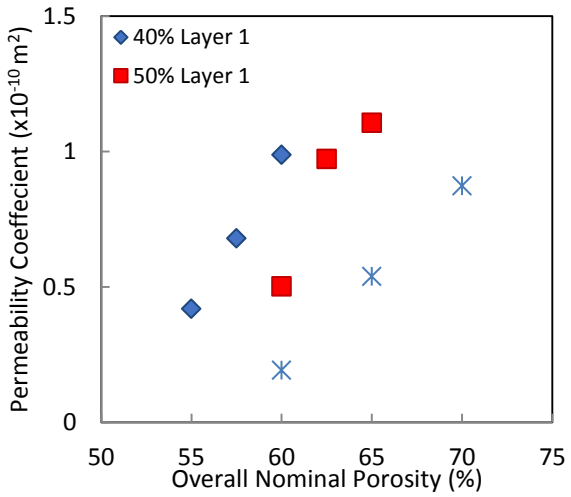

Figure 5.24: Variations in water permeability with the overall nominal porosity of the horizontal bilayer samples in comparison to homogeneous samples.

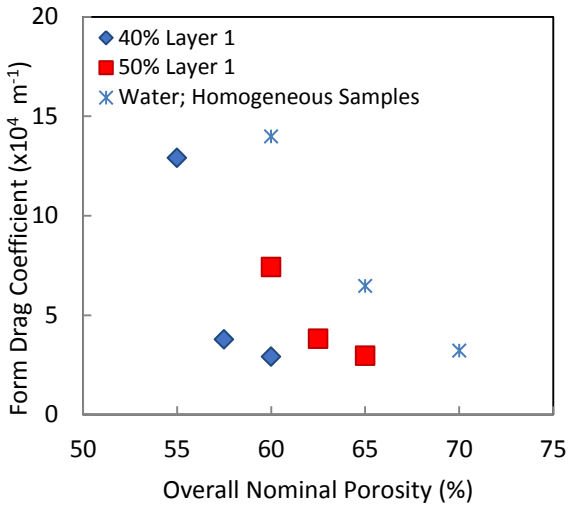

Figure 5.25: Variations in form drag coefficient with the overall nominal porosity of the horizontal bilayer samples in comparison to homogeneous samples.

The overall porosity of the sample strongly affects the permeability and form drag coefficient of the whole horizontal bilayer structure. Samples with lower overall porosity have lower permeability and higher form drag coefficient, while samples with higher overall porosity have greater permeability and lower form drag coefficient. Sample HB1 (40/70) had the lowest permeability and greatest form drag coefficient, while sample HB6 (50/80) had the highest permeability and lowest form drag coefficient.

Increasing the porosity of either of the layers led to an increase in the overall porosity of the sample and hence increased permeability and decreased form drag coefficient. Increasing the porosity of the first layer from 40% to 50% while keeping the porosity of the second layer constant (e.g. 40/70 vs 50/70), led to only a slight increase in the permeability and a slight decrease in form drag coefficient. However, increasing the second layer porosity from 70% to 80% while keeping the porosity of the first layer constant (e.g. 40/70 vs 40/80), resulted in a higher permeability and lower form drag coefficient. From Figs. 5.23 and 5.24,

changing the porosity of the second layer (i.e. 40/70 vs 40/80 and 50/70 vs 50/80) had a greater effect in permeability and form drag coefficient compared to increasing the first layer's porosity (i.e. 40/70 vs 50/70).

Comparing samples HB3 (40/80) and HB4 (50/70) with similar overall nominal porosity of 60%, HB3 showed a higher permeability and lower form drag coefficient. Although HB4 has a more porous first layer (50%) than HB3 (40%), HB3 has a more porous second layer (80%) than HB4 (70%). It appears that the high-porosity second layer has a greater effect on the water permeability and form drag coefficient of the horizontal bilayer samples.

Additionally, the permeability of the horizontal bilayer samples was greater than the homogeneous samples with similar overall porosity, while the form drag coefficient was lower than their homogeneous counterparts. The permeabilities of samples HB1 (40/70) and HB3 (40/80) with overall nominal porosities of 55% and 60%, respectively, were similar to a 65% homogeneous samples, while sample HB6 (50/80) with nominal porosity of 65%, had a permeability similar to a 70% porosity homogeneous sample. On the other hand, the form drag coefficient of sample HB1 is similar to that of a 60% porosity homogeneous sample, while the form drag coefficients of HB3 and HB6 are similar to a 70% porosity homogeneous sample.

5.4.4 Flow Stratification

Ho and Webb (2006) proposed that fluid flow often chooses preferentially the strata with higher permeability. Xiao (2013) suggested that for horizontal bilayers with large porosity difference, the equivalent porosity is larger than the sample's average porosity. This means that the permeability of a horizontal bilayer structure would be higher than its homogeneous counterpart, which is the case observed in this present study (Fig. 5.24).

Xiao and Zhao (2013) recently studied the water flow stratification in LCS porous Cu samples with horizontal bilayer structures. They concluded that the majority of the water flow passes through the higher porosity layer. Their argument is summarised as follows (Xiao and Zhao, 2013):

1) That in a horizontal bilayer structure where the layers are parallel to the flow direction, the flow velocity (*v*) of each layer is proportional to their corresponding permeability coefficient (*K*):

$$\frac{v_h}{v_l} = \frac{K_h}{K_l} \tag{5.4}$$

where subscripts *h* and *l* are labels for the high and low porosity layers, respectively.

2) That following the rule of mixture, the overall flow velocity is:

$$v = f_h v_h + f_l v_l \tag{5.5}$$

where f is the fraction of the layer's thickness relative to the overall sample's thickness.

3) That combining Eqs.(5.4) and (5.5), the scaling factors for the flow velocity in the high porosity layer, s_h, is:

$$s_h = \frac{v_h}{v} = \frac{K_h}{f_h K_h + f_l K_l} \tag{5.6}$$

4) Finally, that the partition factor, p_h, in the high porosity layer that describes the fluid flow rates in the horizontal bilayer is:

$$p_h = \frac{Q_h}{Q} = \frac{f_h v_h}{v} = f_h s_h \tag{5.7}$$

where Q_h is the flow rate through the high porosity layer and Q is the flow rate in the whole sample.

For instance, in a horizontal bilayer structure (5mm thick overall) containing 80% layer (2mm thick) and 60% layer (3mm thick), nearly 88% of the water was calculated to flow through the higher porosity layer. Even when the 80% layer's thickness was reduced to 1mm and the 60% layer was increased to 4mm thick, it was calculated that at least 72% of the water flows through the higher porosity layer.

The flow stratification model proposed by Xiao and Zhao (2013) explains why horizontal bilayer samples are more permeable than their homogeneous counterparts, as well as why increasing the porosity of the second layer (higher porosity layer) of the horizontal structures led to the increase in the permeability (Fig. 5.24). The model also explains why sample HB3 is more permeable than sample HB4. Sample HB3 has a less porous first layer (40%) but a more porous second layer (80%) than HB4 (50/70). Since majority of the water

flow will pass through the high-porosity second layer and that HB3 has a more porous second layer than HB4, the permeability of HB3 would be higher than HB4.

In addition, from Section 5.1, the form drag coefficient decreases with permeability. Therefore, higher form drag coefficients are observed in lower porosity samples/layers than in higher porosity samples/layers. Since most of the flow passes through the higher porosity layer, the overall form drag coefficient in the whole sample is dictated by the higher porosity layer. Hence, a lower form drag coefficient associated with higher porosity was observed in horizontal bilayer samples, as seen in Fig. 5.25. Since the higher porosity layer of the horizontal bilayer structures has greater porosity than their homogeneous counterparts (similar overall porosity), the form drag coefficient of the horizontal bilayer is lower than that of its homogeneous counterpart, as evident in Fig. 5.25.

These results demonstrated that the flow in horizontal bilayers is different from that found in homogeneous samples. These results will be critical to the overall convective heat transfer performance of the horizontal bilayer LCS porous samples.

5.5 Water Flow in Samples with Integrated Vertical Bilayers

The integrated vertical bilayer samples were composed of two layers, left (layer 1) and right (layer 2), with each layer having a homogeneous structure and different porosity from the other layer. The porosity of the layers ranged between 40% to 80%. These integrated vertical bilayer LCS samples were manufactured as one whole sample with two layers, such that there is a soft boundary between the layers and that the two layers are fully connected.

The effect of having two vertical layers within the sample on the water permeability was evaluated. The effect of the orientation of the sample was also analysed by flipping the sample such that either the high porosity layer or the low porosity layer was by the fluid inlet. All the samples were approximately 30mm in length, 20mm in width and 5mm in height with a pore size range of 425-710µm. Each layer within the sample is approximately 15mm in length. The structural parameters of these samples are summarised in Table 5.9. For easy comparison, the porosities displayed in this section are nominal porosities. The samples were labelled depending on the orientation of the layer in the form of (layer by water inlet)/(layer by water outlet). For example, sample “40/80” designates that the 40% porosity layer of the sample was next to the water inlet while the 80% porosity layer was next to the water outlet.

Table 5.9: Porosity and orientation of LCS porous samples with integrated vertical bilayer structures (pore size: 425-710µm).

Sample Reference	Layer 1 nominal porosity % / Layer 2 nominal porosity %
IVB1 A	40/50
IVB1 B	50/40
IVB2 A	40/60
IVB2 B	60/40
IVB3 A	40/70
IVB3 B	70/40
IVB4 A	40/80
IVB4 B	80/40
IVB5 A	50/60
IVB5 B	60/50
IVB6 A	50/70
IVB6 B	70/50
IVB7 A	50/80
IVB7 B	80/50
IVB8 A	60/70
IVB8 B	70/60
IVB9 A	60/80
IVB9 B	80/60
IVB10 A	70/80
IVB10 B	80/70

5.5.1 Length-Normalised Pressure Drop

The length-normalised pressure drop $\frac{\Delta P}{L}$ was plotted against Darcian velocity for the LCS porous copper samples with integrated vertical bilayer structures for water flow as shown in Fig. 5.26. The pressure drop for all samples increased with increasing velocity in a quadratic trend and fitted well with the quadratic function in Eq. (3.7) (determination coefficient R^2>99%).

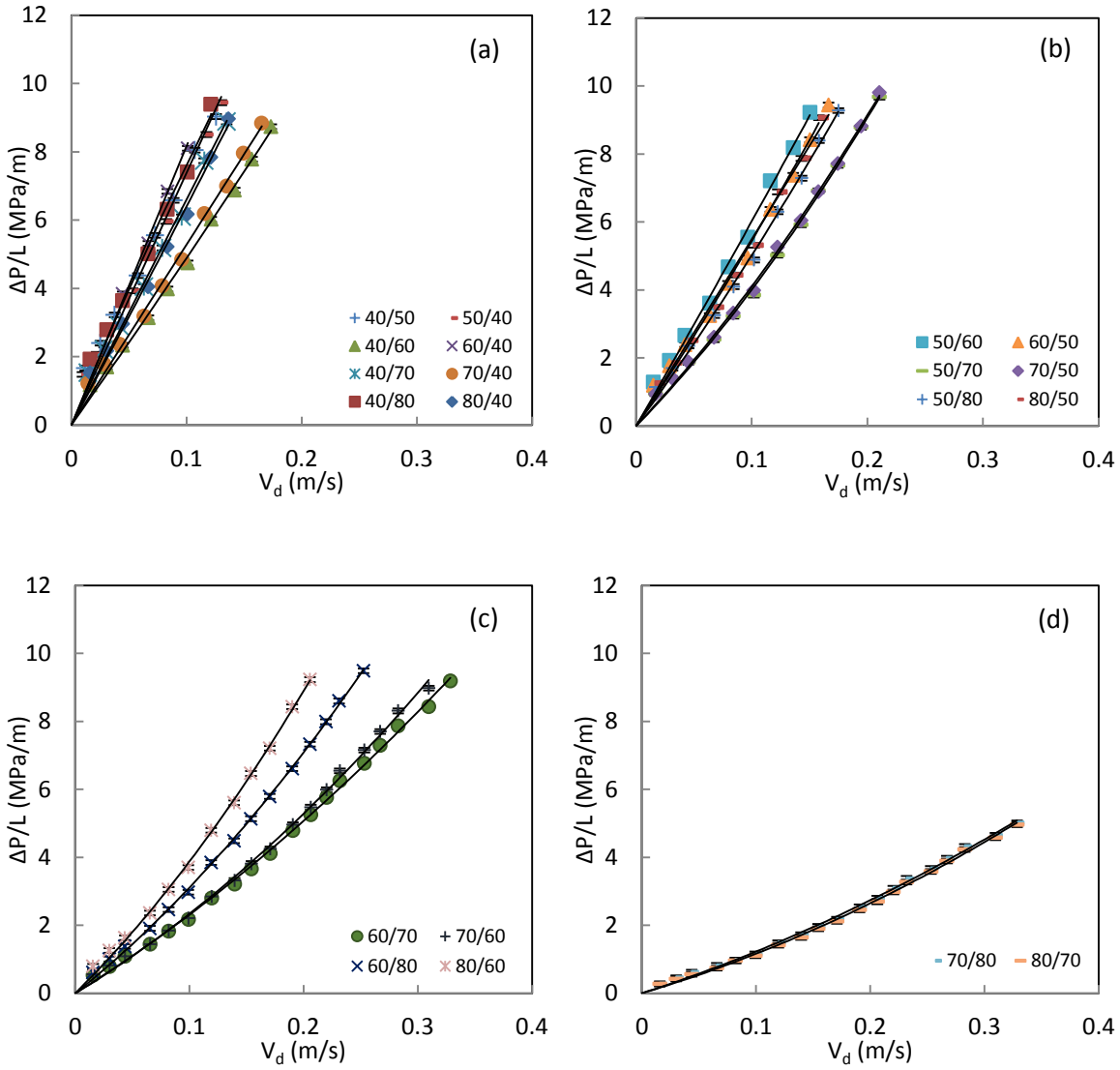

Figure 5.26: Length-normalised pressure drop versus water flow velocity for integrated vertical bilayer structures, grouped according to the porosity of the low porosity layer: (a) 40%, (b) 50%, (c) 60% and (d) 70%.

No general trend can be observed between the sample orientation and pressure drop, with some samples showing greater pressure drop when the layer with the low porosity was placed by the water inlet and other samples showing greater pressure drop when placed the other way around. Overall, however, a higher pressure drop was observed for samples containing a low porosity layer, e.g. samples with 40% porosity layer have higher pressure drops than samples whose lowest porosity is 70%.

5.5.2 Transition from Darcy Regime to Forchheimer Regime

Fig. 5.27 shows the relationship between $\frac{\Delta P}{LV_d}$ and V_d for samples with integrated vertical bilayers. It is apparent that each data trend line is composed of two segments of straight lines, where the transition from one segment to another occurs at V_d = 0.05-0.07 m/s, similar to that found in homogeneous samples. The trend lines of the first segments (at V_d < 0.05 m/s) all showed a negative gradient. However, due to the low accuracy of the data points at very low flow velocity, defining where the Darcy regime ends was difficult. Since no obvious horizontal line was observed, this suggests that the first segments are not within the linear Darcy region and are likely within the transition region from Darcy to Forchheimer's regimes.

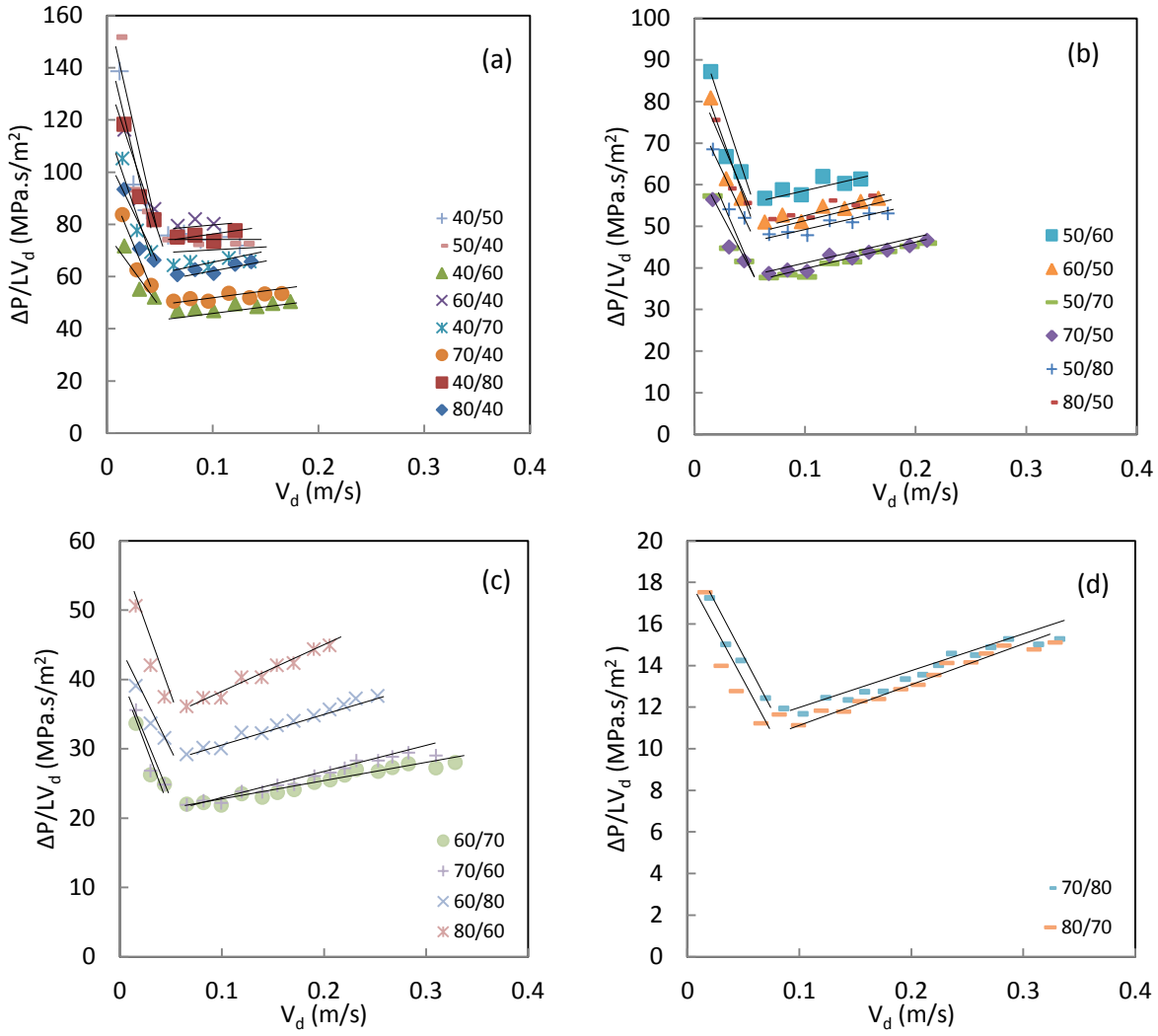

Figure 5.27: $\frac{\Delta P}{LV_d}$ versus water flow velocity graphs for samples with integrated vertical bilayer structures, grouped according to the porosity of the low porosity layer: (a) 40%, (b) 50%, (c) 60% and (d) 70%.

The second segments (V_d > 0.05-0.07 m/s) of all the curves showed an increasing, linear trend similar to that observed in homogeneous samples. This suggests that inertial effects became important in the water flow within the porous copper at V_d > 0.05-0.07 m/s. The transition flow velocities are presented in Table 5.10.

Table 5.10: Transition flow velocity for water flow in LCS samples with integrated vertical bilayer structure.

Sample Reference	Sample Porosity (%)	Transition flow velocity (m/s)
IVB1 A	40/50	0.058
IVB1 B	50/40	0.053
IVB2 A	40/60	0.067
IVB2 B	60/40	0.067
IVB3 A	40/70	0.063
IVB3 B	70/40	0.063
IVB4 A	40/80	0.067
IVB4 B	80/40	0.067
IVB5 A	50/60	0.064
IVB5 B	60/50	0.064
IVB6 A	50/70	0.067
IVB6 B	70/50	0.067
IVB7 A	50/80	0.068
IVB7 B	80/50	0.068
IVB8 A	60/70	0.066
IVB8 B	70/60	0.066
IVB9 A	60/80	0.065
IVB9 B	80/60	0.065
IVB10 A	70/80	0.066
IVB10 B	80/70	0.066

5.5.3 Permeability and Form Drag Coefficient

Using the second segment data of the $\frac{\Delta P}{LV_d}$ against V_d graphs (Fig. 5.27), the permeability coefficients and form drag coefficient were calculated and the results are shown in Table 5.11. In the case of samples IVB1 and IVB2, negative *C* values were obtained and were not used.

Table 5.11: Water permeability and form drag coefficient of LCS samples with integrated vertical bilayer structure.

Sample Reference	Layer 1 nominal porosity % / Layer 2 nominal porosity %	Water Permeability ($x10^{-10} m^2$)	Form Drag Coefficient ($x10^3\ m^{-1}$)
IVB1 A	40/50	0.126	-
IVB1 B	50/40	0.132	-
IVB2 A	40/60	0.223	312
IVB2 B	60/40	0.127	184
IVB3 A	40/70	0.159	253
IVB3 B	70/40	0.204	276
IVB4 A	40/80	0.137	288
IVB4 B	80/40	0.179	685
IVB5 A	50/60	0.185	515
IVB5 B	60/50	0.211	555
IVB6 A	50/70	0.304	632
IVB6 B	70/50	0.288	556
IVB7 A	50/80	0.227	530
IVB7 B	80/50	0.212	612
IVB8 A	60/70	0.501	261
IVB8 B	70/60	0.515	341
IVB9 A	60/80	0.383	465
IVB9 B	80/60	0.314	640
IVB10 A	70/80	0.938	147
IVB10 B	80/70	1.019	167

Figs. 5.28 and 5.29 display the variations in water permeability and form drag coefficient of samples with integrated vertical bilayer structures arranged in increasing “lower-porosity” layer. The effect of the orientation of the sample on the permeability and form drag coefficient can also be seen in Figs. 5.28 and 5.29.

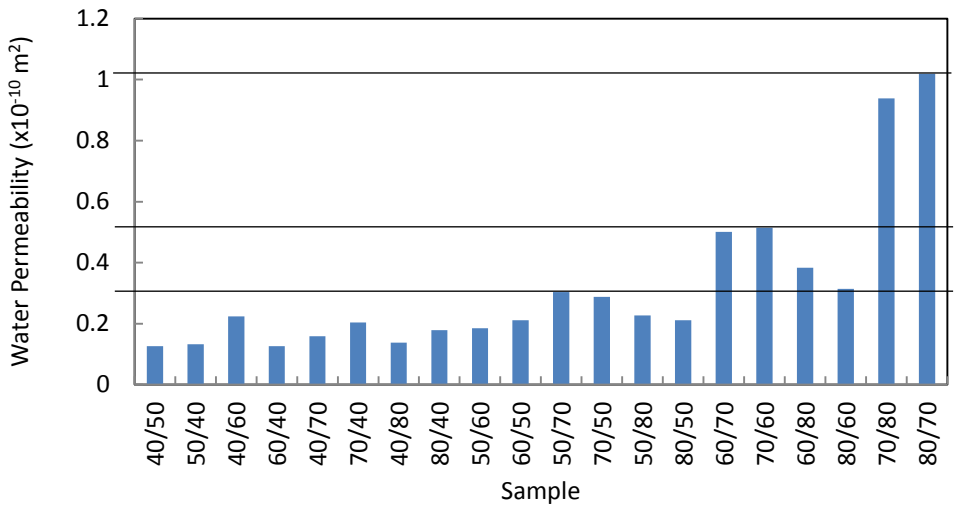

Figure 5.28: Variations in water permeability of the integrated vertical bilayer samples. The numbers in the x-axis indicate nominal porosities of the layers in the sample.

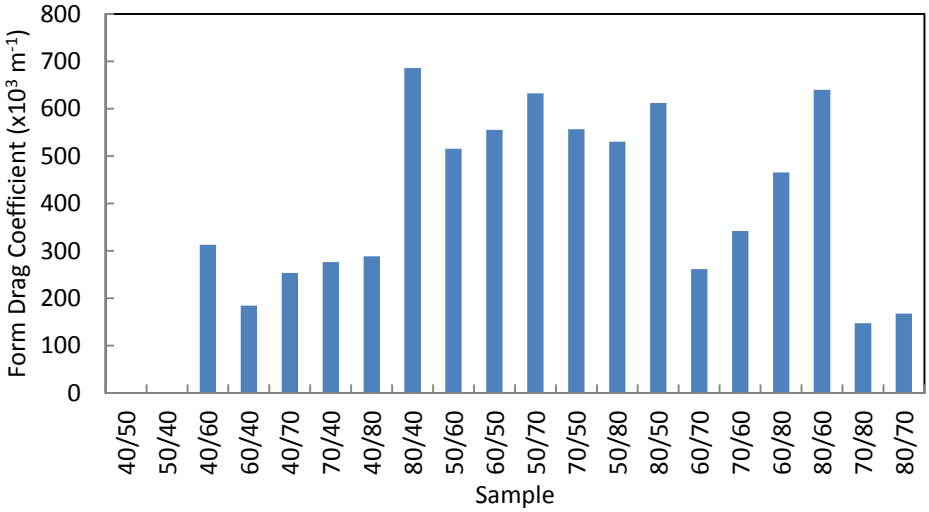

Figure 5.29: Variations in the form drag coefficient of the integrated vertical bilayer samples. The numbers in the x-axis indicate nominal porosities of the layers in the sample.

For some samples, having the "lower-porosity" layer by the water outlet gave a higher permeability (e.g. 70/40 and 80/70). For some samples, however, having the "lower-porosity" layer by the water inlet gave a higher permeability (e.g. 40/50 and 60/80). It appears that changing the orientation of the layers within the sample had little effect on the permeability. Similarly, there is no obvious trend between form drag coefficient and sample orientation.

There are three distinct levels of permeability observed in Fig. 5.28. The lowest level consists of samples whose lowest porosity is 40% or 50%. The second level, on the other hand, consists of samples whose lowest porosity is 60%. The last level consists of samples whose lowest porosity is 70%.

It was apparent that the overall porosity of the whole sample no longer dictates the permeability. For example, sample 50/60 (overall porosity of 55%) has a higher permeability than sample 40/80 (overall porosity of 60%). Similarly, for samples with similar overall porosity, the permeability differs. For example, 50/70 was more permeable than 40/80 (both with overall porosity of 60%), and 70/60 was more permeable than 50/80 (both with overall porosity of 65%).

From the results, the lower the porosity of the "lower-porosity" layer, the lower the permeability of the whole IVB structure is. In other words, the porosity of the "lower-porosity" layer limits the permeability of the whole IVB structure.

The porosity layers can be regarded as different flow control valves. The layer with a low porosity is equivalent to a valve with a higher flow resistance. If two flow control valves were placed in series, the maximum flow resistance of the two valves is mainly dependent on the higher flow resistance valve. Using this analogy, the "lower-porosity" layer acts as the critical flow control valve which limits the overall flow resistance, hence the permeability in the whole IVB structure.

From Fig. 5.29, no clear trend between the form drag coefficient and the sample's porosity can be seen. For samples with the lower porosity of 40%, 50% and 60%, the form drag coefficient was relatively high. Meanwhile, for sample 70/80 or 80/70, the permeability coefficient was very high and the form drag coefficient was relatively low. This is due to the layers in the 70/80 sample having very high porosities and therefore, less resistance to fluid flow and less inertial effect in the flow. For the samples with at least one of the layers having a low porosity, more drag/inertial effect is experienced in this low porosity layer. In addition, the transition of the fluid flow from or to the low porosity layer leads to greater turbulence in the flow, since the flow will need to slow down or speed up as it approaches or leaves the low porosity layer. In general, the form drag coefficient is mainly affected by the lower porosity layer.

5.5.4 Comparison with Homogeneous Samples

Fig. 5.30 compares the permeability of the samples with integrated vertical bilayers to the homogeneous samples. For all samples, the permeability of the samples with the integrated vertical bilayer was higher than that of the homogeneous samples when compared based on the porosity of the "lower-porosity" layer, regardless of the orientation of the sample. For example, sample 50/60 was more permeable than the homogeneous 50% porosity sample (50/50). This is due to the second layer having a higher porosity and therefore less fluid flow resistance.

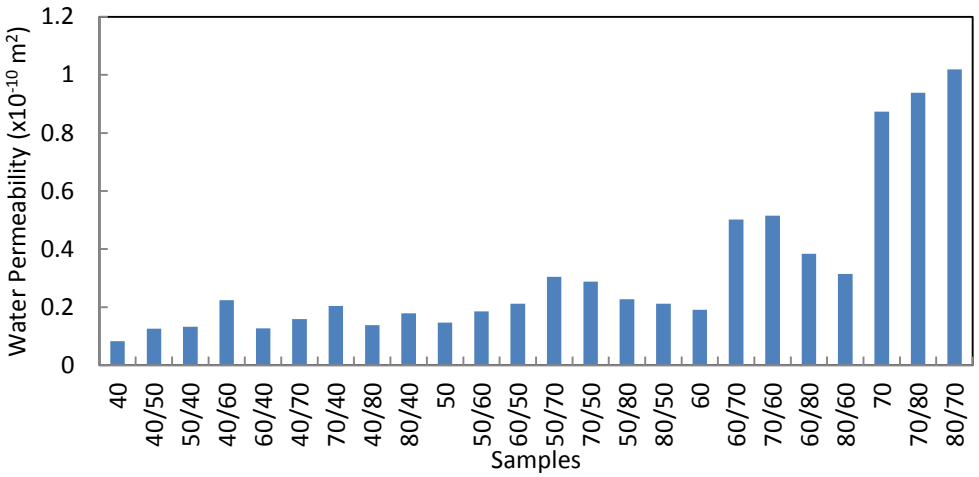

Figure 5.30: Variations in the water permeability of the integrated vertical bilayer samples and homogeneous samples. The numbers in the x-axis indicate the nominal porosities in the sample.

Fig. 5.31 compares the form drag coefficient of the samples with integrated vertical bilayers to the homogeneous samples. No general trend can be observed comparing the IVB structures and homogeneous samples with the same overall porosity. However, in general, the form drag coefficients of the samples with integrated vertical bilayers were higher than those of the homogeneous samples when compared based on the porosity of the "lower-porosity" layer or the overall sample porosity, regardless of the sample orientation. For example, sample 60/80 has a higher form drag coefficient than the homogeneous 60% and 70% porosity samples.

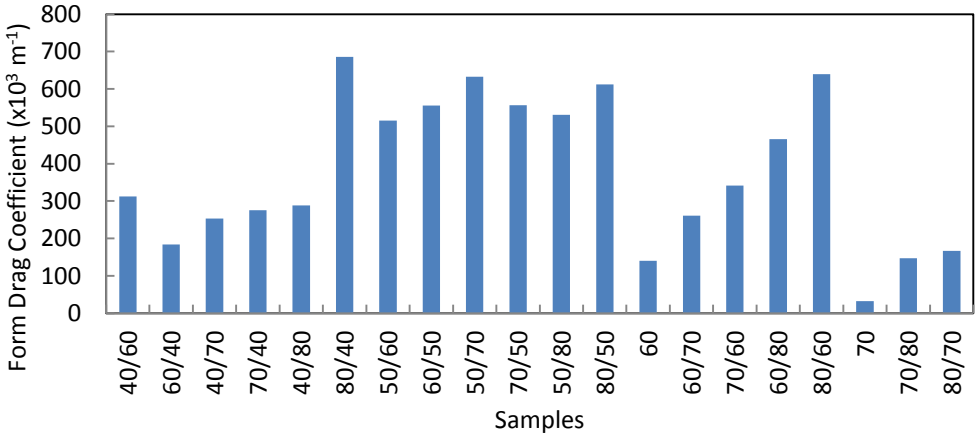

Figure 5.31: Variations in the form drag coefficients of the integrated vertical bilayer samples and homogeneous samples. The numbers in the x-axis indicates nominal porosities in the sample.

5.6 Water Flow in Samples with Segmented Vertical Bilayers

The samples labelled as “segmented vertical bilayers (SVB)” were made by cutting homogeneous samples in halves (15mm in length) and pairing them with each other to produce vertical bilayer samples 30mm in total length. This ensures that the individual layers used in the experiments were the same all the time, allowing accurate comparative analysis.

The effects of having segmented vertical bilayers on the pressure drop and water permeability were evaluated. The influence of the orientation of the layers within the sample was also analysed by flipping the sample such that either the high porosity layer or the low porosity layer was by the fluid inlet. The label of the samples indicates which layer is by the fluid inlet, e.g. “40-80” indicates that the 40% layer was by the water inlet and 80% by the water outlet. All the samples were 30mm in length (each layer was 15mm in length), 20mm in width and 5mm in height, with pore size range of 425-710µm. Table 5.12 summarises the porosities of the segmented vertical bilayers of the samples tested.

Table 5.12: Porosities of LCS porous samples with segmented vertical bilayer structures (pore size: 425-710µm).

Sample Reference	Sample Porosity (%)
SVB1 A	40-50
SVB1 B	50-40
SVB2 A	40-60
SVB2 B	60-40
SVB3 A	40-70
SVB3 B	70-40
SVB4 A	40-80
SVB4 B	80-40
SVB5 A	50-60
SVB5 B	60-50
SVB6 A	50-70
SVB6 B	70-50
SVB7 A	50-80
SVB7 B	80-50
SVB8 A	60-70
SVB8 B	70-60
SVB9 A	60-80
SVB9 B	80-60
SVB10 A	70-80
SVB10 B	80-70

5.6.1 Length-Normalised Pressure Drop

The length-normalised pressure drop $\frac{\Delta P}{L}$ was plotted against Darcian velocity for the LCS porous copper samples with segmented vertical bilayer structure, as shown in Fig. 5.32. The samples were categorised according to the lower porosity layer present within the sample. The pressure drop for all samples increased with increasing velocity in a quadratic trend and fitted well with the quadratic function in Eq. 3.7 (R^2>99%).

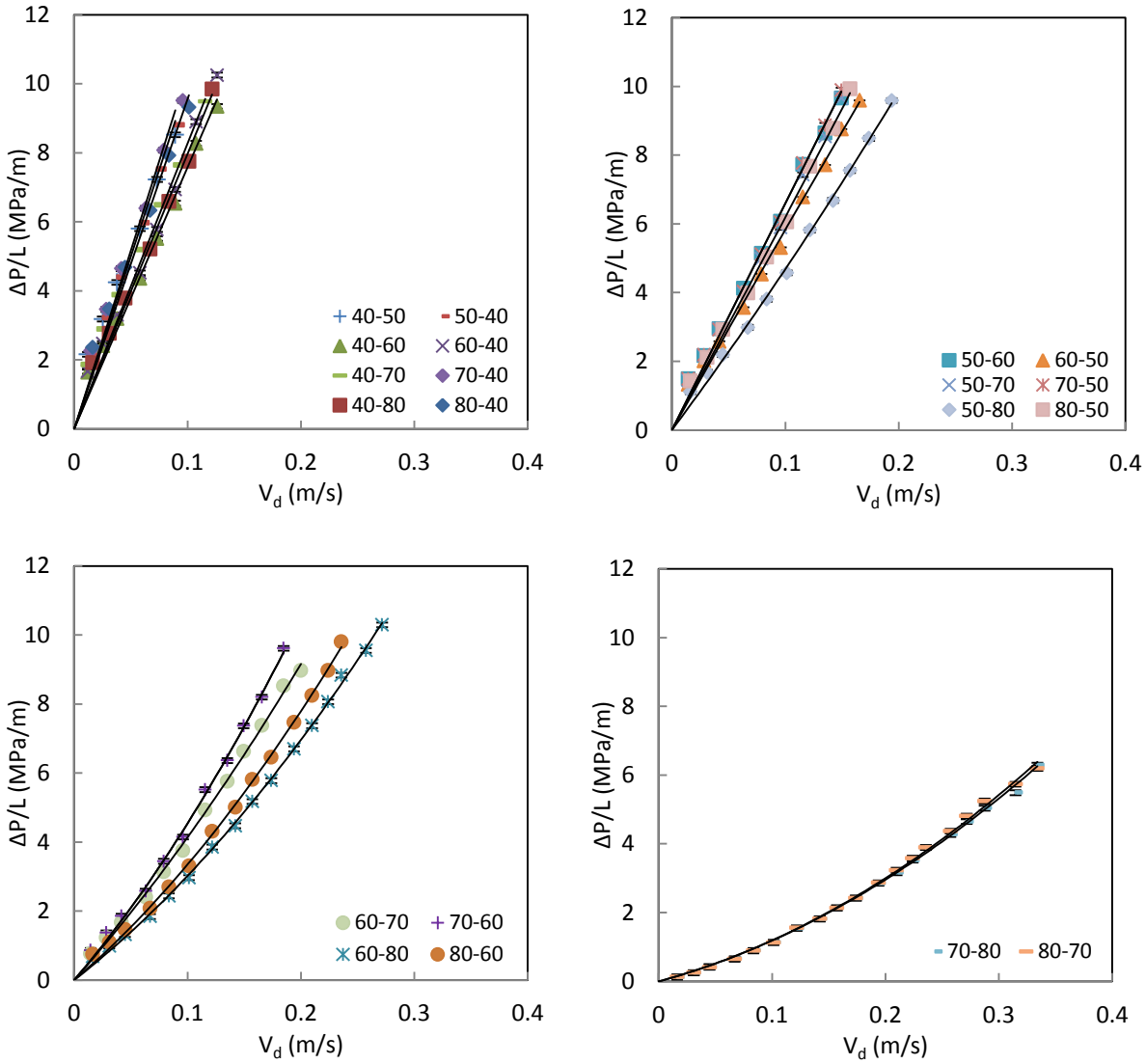

Figure 5.32: Length-normalised pressure drop versus water flow velocity graphs for segmented vertical bilayer structures.

Due to the very high pressure drop in some segmented vertical bilayer samples, only small ranges of data were gathered in these cases. In general, a higher pressure drop was observed for samples containing a low porosity layer. For the same Darcian velocity, the samples whose lower porosity was 40% showed the highest pressure drop, followed by samples with the lower porosity of 50%, then 60%, while samples whose lower porosity is 70% showed the lowest pressure drop.

5.6.2 Transition from Darcy Regime to Forchheimer Regime

Plotting $\frac{\Delta P}{LV_d}$ against V_d, as seen in Fig. 5.33, shows that the data trend line is composed of two segments of straight lines. The transition from one segment to another occurs at V_d = 0.05-0.07 m/s, similar to that found in homogeneous samples. The transition flow velocities are presented in Table 5.13.

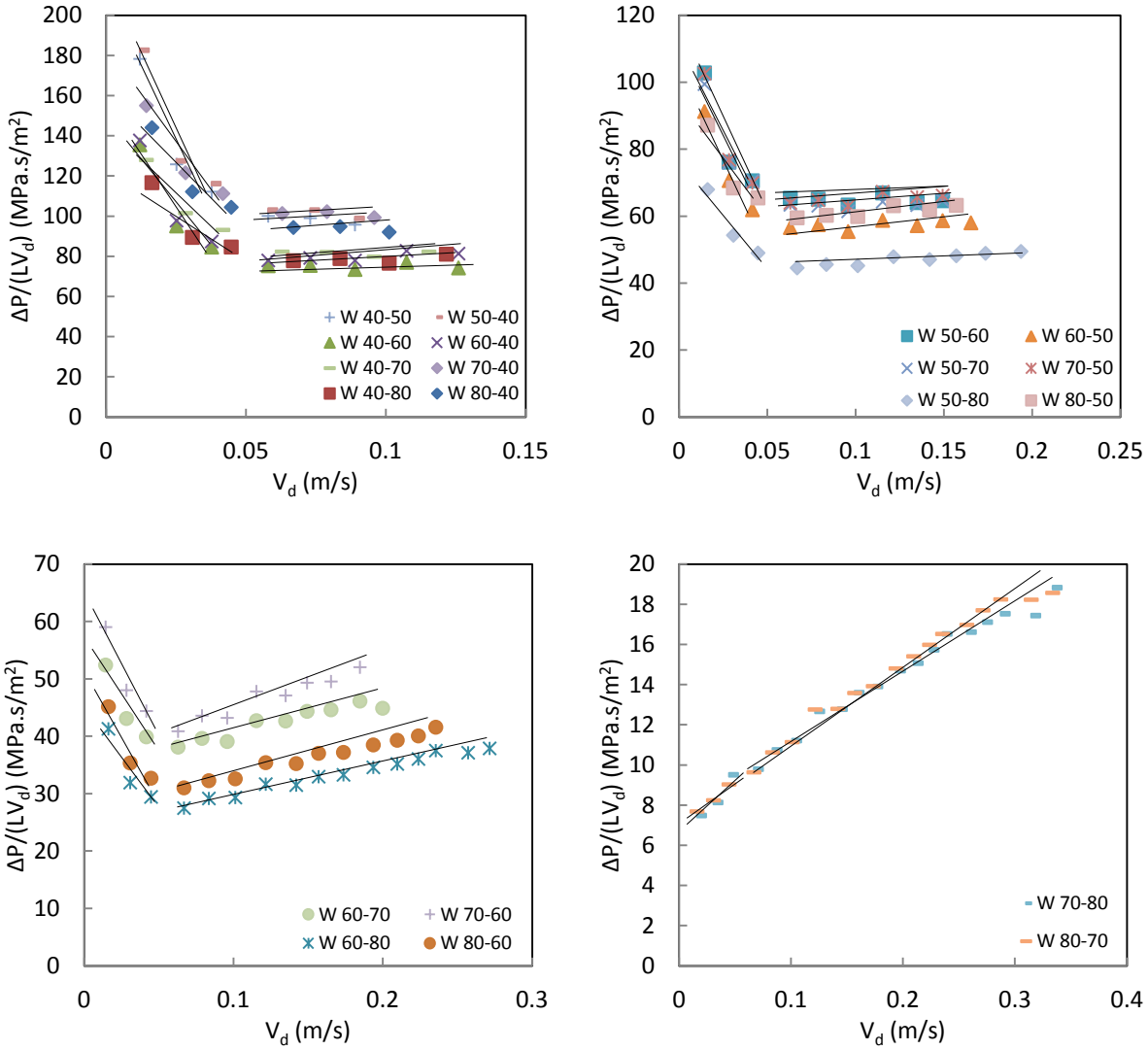

Figure 5.33: $\frac{\Delta P}{LV_d}$ *versus* V_d *graphs for samples with segmented vertical bilayer structures.*

Table 5.13: Transition flow velocity for water flow in LCS samples with segmented vertical bilayer structure.

Sample Reference	Layer 1 nominal porosity % / Layer 2 nominal porosity %	Transition flow velocity (m/s)
SVB1 A	40/50	0.058
SVB1 B	50/40	0.058
SVB2 A	40/60	0.058
SVB2 B	60/40	0.058
SVB3 A	40/70	0.063
SVB3 B	70/40	0.063
SVB4 A	40/80	0.067
SVB4 B	80/40	0.067
SVB5 A	50/60	0.063
SVB5 B	60/50	0.063
SVB6 A	50/70	0.063
SVB6 B	70/50	0.063
SVB7 A	50/80	0.067
SVB7 B	80/50	0.067
SVB8 A	60/70	0.063
SVB8 B	70/60	0.063
SVB9 A	60/80	0.067
SVB9 B	80/60	0.067
SVB10 A	70/80	0.067
SVB10 B	80/70	0.067

5.6.3 Permeability and Form Drag Coefficient

The permeability and form drag coefficients were calculated from the second segment data of the $\frac{\Delta P}{LV_d}$ against V_d graphs (Fig. 5.33), and were shown in Table 5.14 and displayed in Figs. 5.34 and 5.35. In some samples whose lower porosity is 40%, a negative *C* value was obtained and these values were ignored.

Table 5.14: Water permeability and form drag coefficient of LCS samples with segmented vertical bilayer structure (pore size: 425-710µm).

Sample Reference	Layer 1 nominal porosity % / Layer 2 nominal porosity %	Water Permeability ($x10^{-10}$ m^2)	Form Drag Coefficient ($x10^3$ m^{-1})
SVB1 A	40/50	0.092	-
SVB1 B	50/40	0.090	-
SVB2 A	40/60	0.132	-
SVB2 B	60/40	0.138	62
SVB3 A	40/70	0.120	-
SVB3 B	70/40	0.092	-
SVB4 A	40/80	0.137	44
SVB4 B	80/40	0.098	-
SVB5 A	50/60	0.153	-
SVB5 B	60/50	0.180	17
SVB6 A	50/70	0.162	16
SVB6 B	70/50	0.161	30
SVB7 A	50/80	0.238	39
SVB7 B	80/50	0.177	41
SVB8 A	60/70	0.302	57
SVB8 B	70/60	0.299	86
SVB9 A	60/80	0.433	51
SVB9 B	80/60	0.393	59
SVB10 A	70/80	1.370	32
SVB10 B	80/70	1.440	34

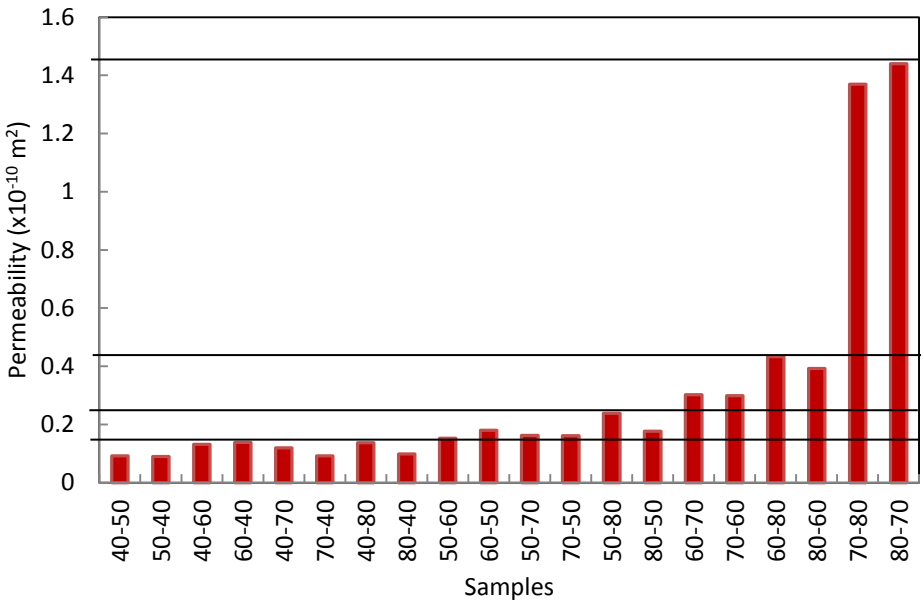

Figure 5.34: Variations in water permeability of the segmented vertical bilayer samples. The numbers in the x-axis indicate nominal porosities of the layers in the sample.

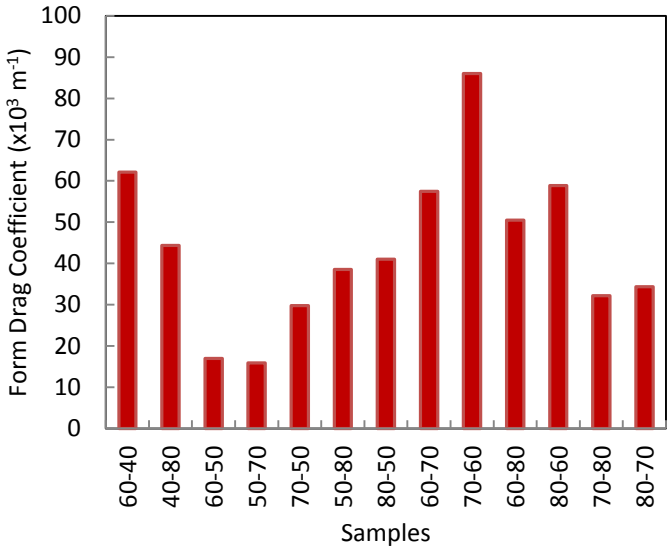

Figure 5.35: Variations in form drag coefficient of the segmented vertical bilayer samples. The numbers in the x-axis indicate nominal porosities of the layers in the sample.

Fig. 5.34 displays the variation in the water permeability of the segmented vertical bilayer samples, arranged according to the porosity of the "lower-porosity" layer. The effect of the orientation of the sample on the permeability was also displayed on Fig. 5.34. It is apparent that changing the orientation of the layers had very little effect on the permeability. The overall permeability of the sample remains the same regardless of the orientation of the layers. There is no general trend between the sample's orientation and the form drag coefficient (Fig. 5.35). For most samples whose lower porosity is 40%, the form drag coefficient was a negative value and therefore, was nonsensical. The greatest form drag coefficient was obtained for sample 70-60 while sample 50-70 generated the lowest form drag coefficient.

There are four distinct levels of permeability observed in Fig. 5.34. The lowest level of permeability represents samples whose lower porosity was 40% and the highest level

represents samples whose lower porosity was 70%. This suggests that the overall permeability of the samples was limited by the permeability of the lower porosity layer. Similar to integrated vertical bilayers, the lower-porosity layer restricts the overall permeability of the samples with segmented vertical bilayers. This is because the lower-porosity layer acts as the flow control valve that regulates the flow in the system (Section 5.5.3). For sample 70/80 or 80/70, the permeability coefficient was very high. This is due to the layers in the 70/80 sample having very high porosities and so, there are more channels for fluid flow.

The overall porosity of the whole sample no longer dictates the permeability. For example, sample 40/80 (overall porosity of 60%) has a lower permeability than sample 50/60 (overall porosity of 55%). Likewise, for samples with similar overall porosity, the permeability differs. For example, 50/80 is less permeable than 70/60 even though they have the same overall porosity.

Fig. 5.36 compares the permeability of the segmented vertical bilayers to homogeneous samples. For all samples, the permeability of the segmented vertical bilayers was higher than the homogeneous samples when compared based on the porosity of the lower-porosity layer. For example, sample 60/80 is more permeable than the homogeneous 60% porosity sample (60/60). This is due to the second layer having a higher porosity.

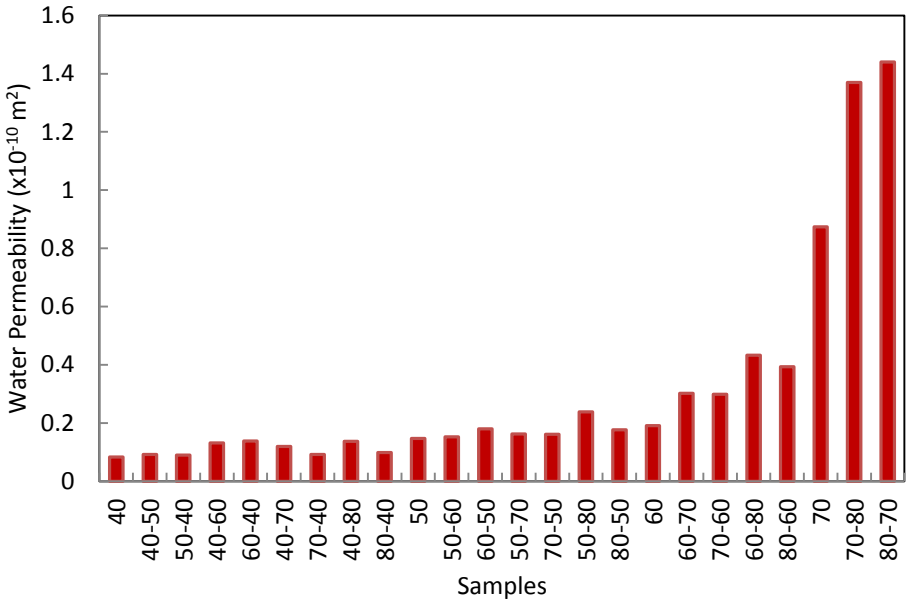

Figure 5.36: Variations in the water permeability of the integrated vertical bilayer samples in comparison to homogeneous LCS samples. The numbers in the x-axis indicate nominal porosities in the sample.

5.6.4 Comparison between Segmented and Integrated Vertical Bilayers

There was a gap (hard boundary) present in the SVB samples due to poor coupling of the layers, whereas a soft boundary was present in IVB structures since the layers were fully connected during sintering. Fig. 5.37 displays the permeabilities of the homogeneous samples, integrated vertical bilayer (IVB) samples and segmented vertical bilayers (SVB) samples for comparison. In general, for samples whose lower porosity layer is 40%, 50% or 60%, the permeabilities for IVB and SVB were similar. This suggests that the hard boundary in the SVB structures has very little effect on the overall permeability of the samples with low porosities. For samples whose lower porosity is 70%, however, the permeability of SVB samples was approximately 40% higher than that of the IVB samples.

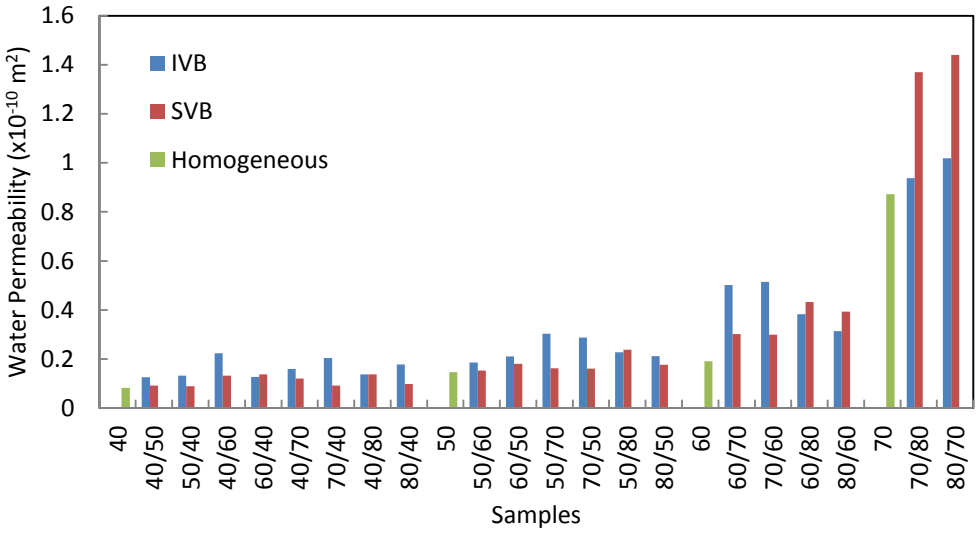

Figure 5.37: Comparison between the water permeabilities of the integrated vertical bilayer (IVB), segmented vertical bilayer (SVB) and homogeneous samples. The numbers in the x-axis indicate nominal porosities in the sample.

For both IVB and SVB structures, the overall permeability of the sample is largely limited by the lower-porosity layer. Four distinct levels were present In SVB, whereas only three distinct levels were observed in IVB. For IVB, there was no clear distinction between the permeability in samples whose lower porosity layer is 40% or 50% (Section 5.5). This difference may be because the layers in the integrated vertical bilayers are not identical since these samples were manufactured as one whole sample. The layers in the segmented vertical bilayers are identical; therefore, there is less deviation in the results, hence a clearer distinction in the permeability values observed.

The orientation of the samples has little effect on the overall permeability for both the IVB and SVB samples. This is in agreement with Medraj et al. (2007) and Baril et al. (2008).

5.6.5 Theoretical Prediction of Permeability for LCS Samples with SVB and IVB Structures

The segmented or integrated vertical bilayer structures are composed of two layers with different porosities. As a consequence, each layer has a different permeability than the other. When assembled in series (next to each other) in the sample chamber to form the IVB or SVB structure, the overall permeability of the IVB or SVB structure will depend on the permeability of each layer.

Analogous to electrical circuits, the overall permeability to fluid flow in the vertical bilayer structures K_{VB} can be expressed as:

$$\frac{1}{K_{VB}} = \frac{1}{2}\left(\frac{1}{K_l} + \frac{1}{K_h}\right) \tag{5.8}$$

where K_l and K_h are the permeabilities of the low porosity and high porosity layers in the vertical bilayer structure, respectively.

Fig. 5.38 compares the theoretical permeability using Eq. (5.8) with the actual permeability of the SVB and IVB samples. In general, there is a good agreement between the measured and calculated permeability values, especially for SVB structures. Lower porosity layers with lower permeability contribute more to the resistance to fluid flow. A larger difference between the actual and theoretical permeability for IVB samples can also be observed. Since the IVB samples were produced as whole structures, the individual layers within the structure will vary between samples.

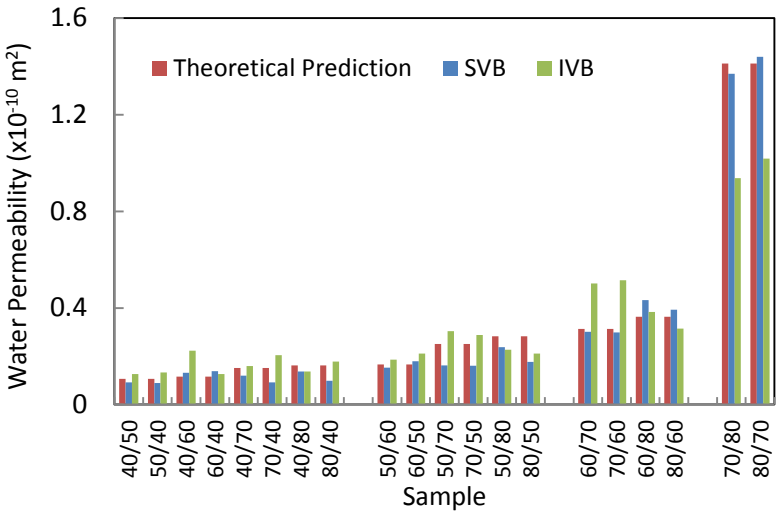

Figure 5.38: Comparison between measured and predicted permeability for LCS samples with IVB and SVB structures.

5.6.6 Comparison with Other Porous Media

There is very little attention given in the past on the study of the pressure drop or permeability of porous media with structures similar to that with IVB and SVB structures produced in this present study. The closest porous structures studied in the past similar to these vertical bilayer structures were stacked layers of porous metals with different pore size (Medraj, et al. 2007, Baril, et al. 2008, Oun and Kennedy 2015, Carpenter and da Silva 2014).

Past studies observed an increase in pressure drop of stacked multiple porous discs with similar pore size and porosity compared to single homogeneous discs of similar lengths. The reasons for the increase in pressure drop were attributed to (Medraj, et al 2007, Baril, et al. 2008, Oun and Kennedy, 2014, Zaragosa and Goodall 2012):

1) additional entrance/exit effects due to the gaps in between stacks which disturb fluid flow;
2) presence of gaps generates additional pressure drop
3) discontinuity in the structure; and
4) misalignment of pores.

These reasons do not apply in the IVB sample since the layers are fully connected such that no air gaps/hard boundaries are present. As evident in Fig. 5.36, the permeability of IVB samples was roughly in the same range as their homogeneous counterparts.

Baril et al. (2008) commented that the differences in pressure drop and permeability in stacked multiple porous discs depend on the differences in the permeability of the materials tested. In this study, the pressure drop and permeability were apparently dictated by the "lowest-porosity" layer, although the "higher-porosity" layer also contributed to the overall permeability of the sample.

Past research also found that having a less permeable layer by the fluid entrance led to the increase in pressure drop and decrease in permeability, but only at very high flow rates (10 m/s for air flow) (Baril et al. 2008). However, at low flow rates, the pressure drops remain similar regardless of the orientation of the layers (Baril et al. 2008). Furthermore, Medraj et al. (2007) observed that alternating the order of stacking did not affect the pressure drop of the whole foam, which was consistent with the findings in the present study. Medraj et al. (2007) added that as the fluid comes into contact with the vertical bilayer stacked foam, pressure is lost due to the sudden change in momentum; however, changing the orientation

of the layers would have very little effect on the pressure drop, hence, the permeability of the whole structure. In both the SVB and IVB structures, the change in fluid momentum was greatly influenced by the lower porosity layer. However, the pressure drop and permeability of the whole sample were not affected by the orientation of the layers, which is in agreement with the previous studies.

5.7 Flow in Samples with Multi-boundary Segmented Structures

From the comparative analysis of the IVB and SVB structures, it was apparent that the presence of a hard boundary between the layers in SVB had very little effect on the overall pressure drop and permeability of the samples. Since the overall permeability of both IVB and SVB samples was mainly limited by the porosity of the lower-porosity layer, the effect of boundaries may have been too small relative to the effect of the lower-porosity layer. In this section, LCS porous copper samples with segmented structures were produced to analyse the effects of hard boundaries between layers of same porosity on permeability and form drag coefficient. This will ensure that the effect of the lower-porosity layer found in SVB and IVB samples does not overshadow the hard boundary effect.

To investigate the influence of hard boundaries on the permeability and form drag coefficient, homogeneous LCS samples with 40%, 50% and 60% nominal porosities and 425-710 µm pore size, with known permeability, were cut into two sections (each section 15 mm in length). The pressure drop, water permeability and form drag coefficient of the assembled sections were analysed. The two sections were then further cut to give a total of six sections (each section approximately 5 mm in length). Again, the pressure drop, water permeability and form drag coefficient of the assembled sections were measured. Table 5.15 summarises the multi-boundary segmented structures tested.

Table 5.15: Number of sections of the segmented LCS porous copper samples (pore size: 425-710µm).

Sample Reference	Nominal Porosity (%)	Number of Sections	Number of Boundaries
SS1 A	40%	1	0
SS1 B		2	1
SS1 C		6	5
SS2 A	50%	1	0
SS2 B		2	1
SS2 C		6	5
SS3 A	60%	1	0
SS3 B		2	1
SS3 C		6	5

5.7.1 Length-normalised Pressure Drop

Fig. 5.39 plots the length-normalised pressure drop $\frac{\Delta P}{L}$ against Darcian velocity for the LCS porous copper samples with segmented structures. The samples were categorised according to the number of sections present within the sample. In general, the pressure drop for all samples increases with increasing velocity in a quadratic trend ($R^2 \geq 98\%$).

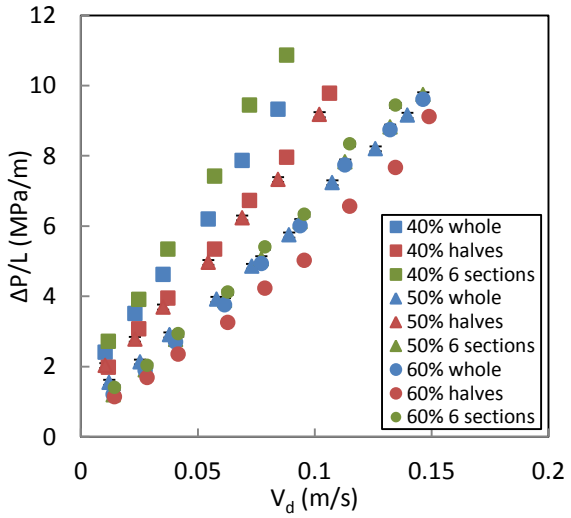

Figure 5.39: Length-normalised pressure drop versus water flow velocity graphs for segmented LCS porous samples.

For samples with 40% porosity, having six sections (or 5 cuts) showed the greatest pressure drop, followed by the whole sample and then the halved sample. For 50% porosity samples,

the greatest pressure drop was observed for halved samples, and the 6-sectioned sample and the whole sample showed very similar pressure drops, with the former having just a slightly higher pressure drop than the latter. For 60% porosity samples, the greatest pressure drop was observed for 6-sectioned sample, followed by the whole sample then the halved sample. These results show that the pressure drop is generally greater in samples with six sections. Having two sections (one gap), however, may generate higher or lower pressure drops than the whole sample. The differences between the pressure drops of samples with similar porosity and different number of sections or gaps, however, were very small.

5.7.2 Transition from Darcy Regime to Forchheimer Regime

Fig. 5.40 plots $\frac{\Delta P}{LV_d}$ against Darcian velocity and each curve is composed of two straight lines. These two straight lines intersect at a Darcian velocity 0.05-0.07 m/s. The transition flow velocities are presented in Table 5.16.

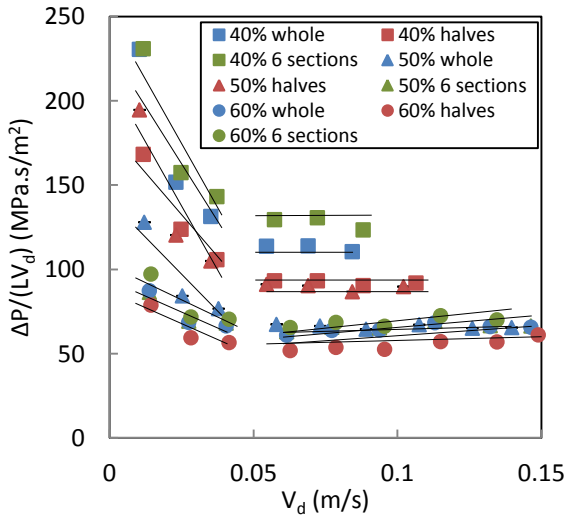

Figure 5.40: $\frac{\Delta P}{LV_d}$ versus V_d graphs for LCS samples with segmented structures.

Table 5.16: Transition flow velocities for water flow in LCS samples with multi-boundary segmented structures.

Sample Reference	Nominal Porosity (%)	Number of Sections	Transition flow velocity (m/s)
SS1 A	40%	1	0.055
SS1 B		2	0.057
SS1 C		6	0.057
SS2 A	50%	1	0.058
SS2 B		2	0.055
SS2 C		6	0.061
SS3 A	60%	1	0.062
SS3 B		2	0.063
SS3 C		6	0.063

5.7.3 Permeability and Form Drag Coefficients

The permeability and form drag coefficients are shown in Table 5.17. In the case of samples whose porosity is 40% or 50% with one or two sections, negative form drag coefficients were obtained and so these values are ignored.

Table 5.17: Water permeability and form drag coefficient of LCS samples with multi-boundary segmented structures.

Sample Reference	Nominal Porosity (%)	Number of Sections	Water Permeability ($x10^{-10}$ m^2)	Form Drag Coefficient ($x10^3$ m^{-1})
SS1 A	40%	1	0.083	-
SS1 B		2	0.105	-
SS1 C		6	0.070	-
SS2 A	50%	1	0.147	-
SS2 B		2	0.159	-
SS2 C		6	0.161	39
SS3 A	60%	1	0.192	26
SS3 B		2	0.222	99
SS3 C		6	0.163	73

Fig. 5.41 displays the variation in the water permeability of the segmented structures, arranged according to the nominal porosity and number of sections of the samples. For

segmented structures, the permeability was still mainly dependent on the sample's porosity. Samples with nominal porosity of 40% showed the lowest permeability while samples with nominal porosity of 60% showed highest permeability.

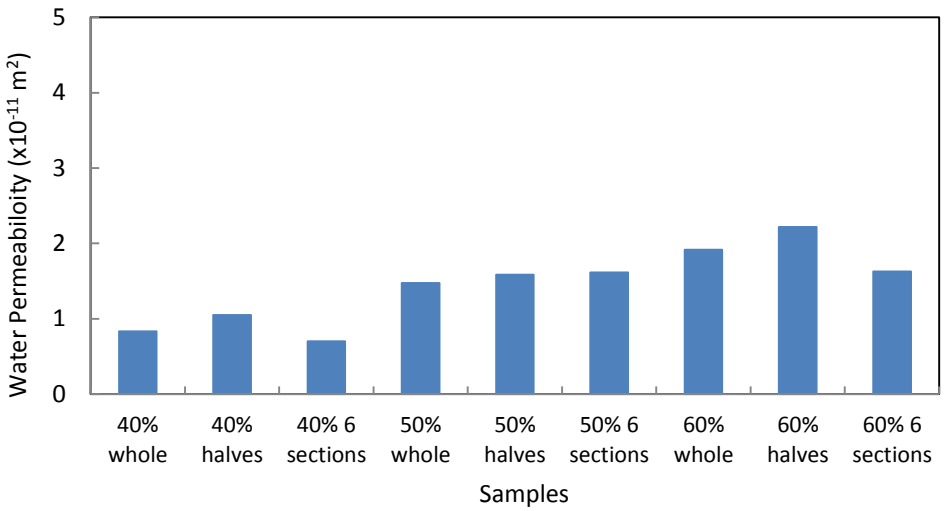

Figure 5.41: Variations in the water permeability of the segmented LCS porous Cu samples.

For each porosity group, there was no obvious relationship between the number of hard boundaries present and permeability. The permeability for the samples with a similar porosity was similar and within the uncertainty range. This suggests that the presence of hard boundaries in the LCS structures with porosities of 40%-60%, has very little effect on the permeability.

The introduction of boundaries may result in gaps which lead to additional entrance/exit effects (Baril et al. 2008). As the water flow approaches the boundaries, it changes direction, which leads to turbulence in the flow. The presence of boundaries causes the flow direction to change every time the flow leaves one layer and enters another, therefore causing more turbulence. However, the presence of boundaries has little effect on the pressure drop and therefore, the overall permeability of the sample. This suggests that the effect of boundary

is negligible, compared with other limiting factors, such as the sample's porosity or sample's structure which is already very complex.

Comparative analysis of the form drag coefficients was quite difficult since most of the coefficients resulted in negative values. This may suggest that Darcy's (linear) law may be more applicable to these samples than the Forchheimer (quadratic) law. Furthermore, there are only limited data points representing the pressure drops of these samples, making it difficult to determine the pressure drop trends and evaluate the form drag coefficient.

5.7.4 Comparison with Other Porous Media

The results showed that the number of cuts does not affect the overall permeability of the sample, which is similar to observations for SVB layers (Section 5.6). Carpenter and da Silva (2014) also observed that for aluminium foams, the number of hard boundaries did not have a significant effect on the pressure drop, because the presence of hard boundaries does not significantly disturb the already complex flow. Baril et al. (2008) reported that a slightly higher pressure drop was observed for a segmented sample only at very high flow velocities, compared to a whole sample of similar thickness. They argued that the presence of a hard boundary generated an additional pressure drop which resulted from the additional foam surface in the flow path (additional entrance and exit). However, they added that the contribution of the additional entrance/exit effect as well as the misalignment of the layers to the overall pressure drop was insignificant. Oun and Kennedy (2015) also confirmed that the hard boundaries only had a small contribution to the pressure drop.

Similar to past studies, the effects of hard boundaries in LCS porous copper samples (30 mm x 20 mm x 5 mm dimensions) on the pressure drop and permeability are insignificant for both the SVB and segmented structures. This is likely because the effects are relatively small in comparison to the effect of the sample's porosity or complex structure.

5.8 Water Flow in Samples with Directional Porosity

Porous copper samples with additional directional porosity (four tubular channels) added along the centre of the homogeneous samples, were manufactured using the LCS process. The effects of adding four tubular channels on the overall pressure drop, permeability and form drag coefficient of the samples with different nominal porosities (40% to 80%) were examined. Table 5.18 lists the nominal and actual porosities of the samples with directional porosity (DP) tested. The actual porosities were measured using the direct-volume method (Section 3.2.2).

Table 5.18: Nominal and actual porosities of LCS porous Cu samples with directional porosity (pore size: 425-710μm).

Sample Reference	Nominal Porosity (%)	Actual Porosity (%)
DP1	40%	54.4
DP2	50%	63.8
DP3	60%	67.1
DP4	70%	75.3
DP5	80%	82.3

The actual porosities of all the samples with directional porosity were higher than their nominal porosities due to the additional tubular channels. A 36% increase was seen in the 40% porosity sample. As the porosity increases however, the difference between the actual and nominal porosities decreased to 2.8% in 80% porosity sample. This is because the additional porosity effect due to the added open channels was more prominent in lower porosity samples than in higher porosity samples.

5.8.1 Length-normalised Pressure Drop

The length-normalised pressure drop is plotted against Darcian velocity for each sample as shown in Fig. 5.42. In general, the pressure drop for all samples increases with increasing

velocity in a quadratic trend (R^2>99%), similar to that observed in homogeneous samples. The highest pressure drop was observed in the 40% porosity sample, while the lowest pressure drop was observed in the 80% porosity sample.

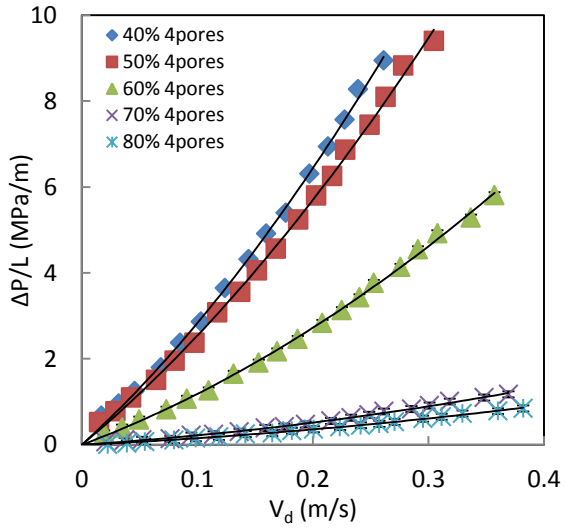

Figure 5.42: Length-normalised pressure drop versus water flow velocity for LCS porous sample with additional directional porosity.

The directional porosity within the samples can be treated as circular pipes. The effect of the directional porosity alone on the pressure drop was examined using Poiseulle's equation (White 2009):

$$\Delta P = \frac{8\mu QL}{\pi r^4} \qquad \text{(Eq. 5.9)}$$

Fig. 5.43 compares the pressure drops between the LCS porous samples with DP and the pressure drop due to DP alone, calculated using Eq. (5.9).

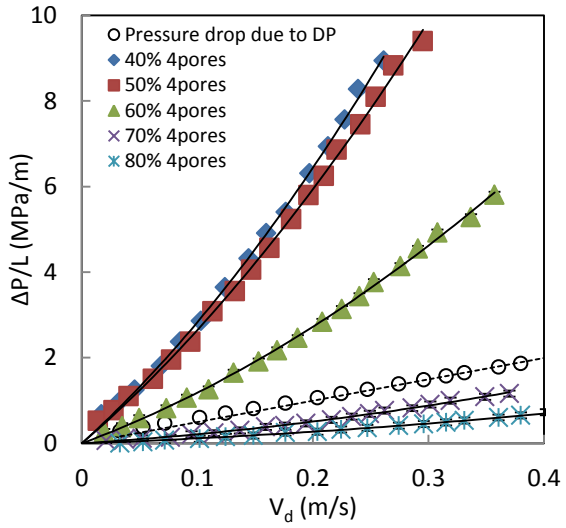

Figure 5.43: Length-normalised pressure drop versus water flow velocity for LCS porous sample with additional directional porosity in comparison to the effect of DP alone on the pressure drop.

The addition of DP provides a direct pathway for fluid flow, reducing the flow resistance, and hence decreasing the overall pressure drop of the whole sample. The contribution of DP on the overall pressure drop is lower in samples with lower porosity. A high volume of solid copper still exists in lower porosity samples, which impedes fluid flow. Whereas in higher porosity samples, the addition of DP along with the low volume fraction of solid copper leads to lower resistance to fluid flow, hence lower overall pressure drop.

5.8.2 Transition from Darcy Regime to Forchheimer Regime

By plotting $\frac{\Delta P}{LV_d}$ and V_d, as seen in Fig. 5.44, it is apparent that the data line is composed of two segments of straight lines with the transition point at a Darcian velocity of 0.06 - 0.08 m/s. The transition flow velocities for these samples are listed in Table 5.19.

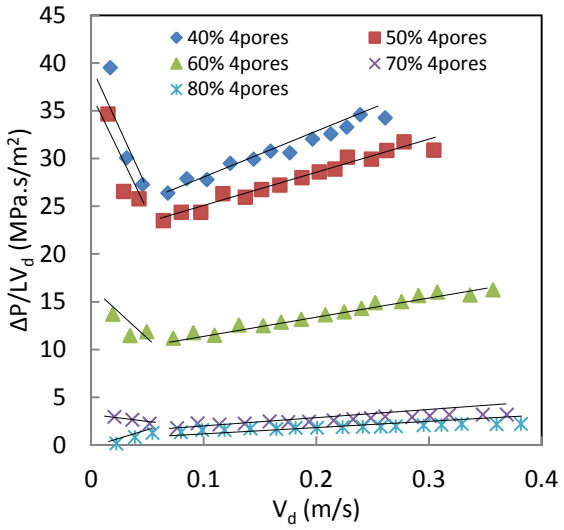

Figure 5.44: $\frac{\Delta P}{LV_d}$ *versus water flow velocity graphs for LCS samples with directional porosity.*

Table 5.19: Transition flow velocity for water flow in LCS samples with directional porosity (pore size: 425-710µm).

Sample Reference	Nominal Porosity (%)	Translation flow velocity (m/s)
DP1	40	0.068
DP2	50	0.064
DP3	60	0.073
DP4	70	0.077
DP5	80	0.080

No horizontal trend lines were present in the first segments of the data (Fig. 5.44), suggesting that the first segments were not in the linear-Darcy regime, but may represent the transition between Darcy's flow and Forchheimer's flow. The data points in the second segments are linear with increasing gradients. This suggests that the inertial effects become important at high flow velocities (V_d > 0.6 - 0.8 m/s).

5.8.3 Permeability and Form Drag Coefficient

From the second segment data of the $\frac{\Delta P}{LV_d}$ against V_d graphs (Fig. 5.43), the permeability and form drag coefficients of the samples with directional porosity were calculated. The results are shown in Table 5.20, Figs. 5.45 and 5.46.

Table 5.20: Water permeability and form drag coefficients of LCS porous copper samples with directional porosity (pore size: 425-710µm).

Sample Reference	Nominal porosity	Water Permeability ($x10^{-10}$ m^2)	Form Drag Coefficient ($x10^3$ m^{-1})
DP1	40%	0.418	41
DP2	50%	0.464	34
DP3	60%	1.021	19
DP4	70%	6.105	5
DP5	80%	8.006	3

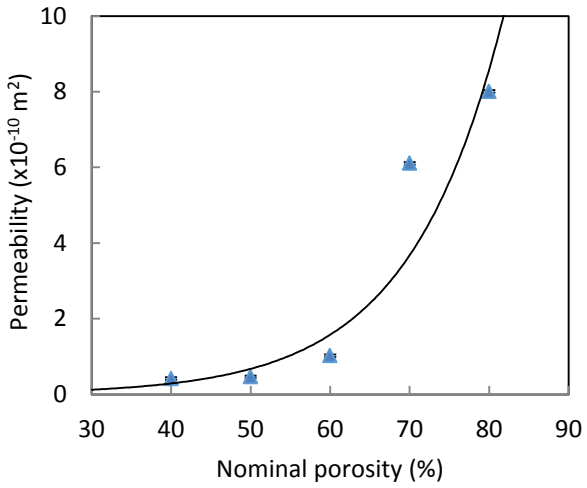

Figure 5.45: Variation in the water permeability with porosity for the LCS porous Cu samples with directional porosity.

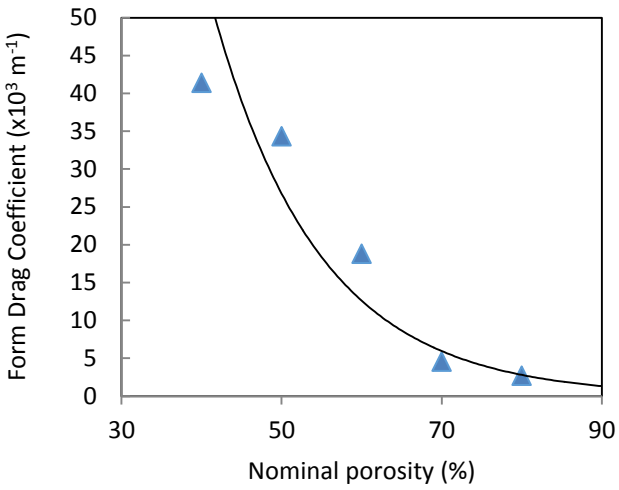

Figure 5.46: Variation in the form drag coefficient with porosity for the LCS porous Cu samples with directional porosity.

Figs. 5.45 and 5.46 show that when the porosity of the sample increased from 40% to 80%, the permeability increased while the form drag coefficient decreased. Samples with low porosity, e.g. 40%, had higher form drag coefficients than the samples with high porosity, e.g. 80%. Although the fluid flow is more concentrated in the added tubular channels parallel to the fluid flow in lower porosity samples, resistance to fluid flow remains high because there is still a high density of copper present in low porosity sample. As a consequence, a higher pressure drop and lower permeability in samples with low porosity was observed.

In higher porosity samples, a large proportion of pores are already present. The addition of four tubular channels further increased the volume of pores. As a result, permeability was much higher in samples with higher porosity (Fig. 5.45).

5.8.4 Comparison with Samples with Homogeneous Structure

LCS porous samples with directional porosity are essentially homogeneous samples with directional pores added at the centre parallel to fluid flow. Figs. 5.47 and 5.48 compare the permeabilities and form drag coefficients of homogeneous samples and samples with directional porosity.

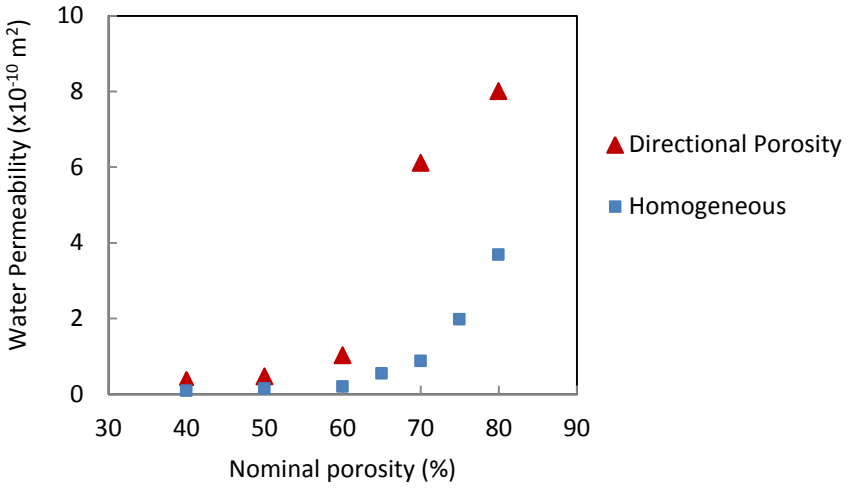

Figure 5.47: Variations in the water permeability with porosity for the LCS porous Cu samples with and without directional porosity (pore size 425-710um).

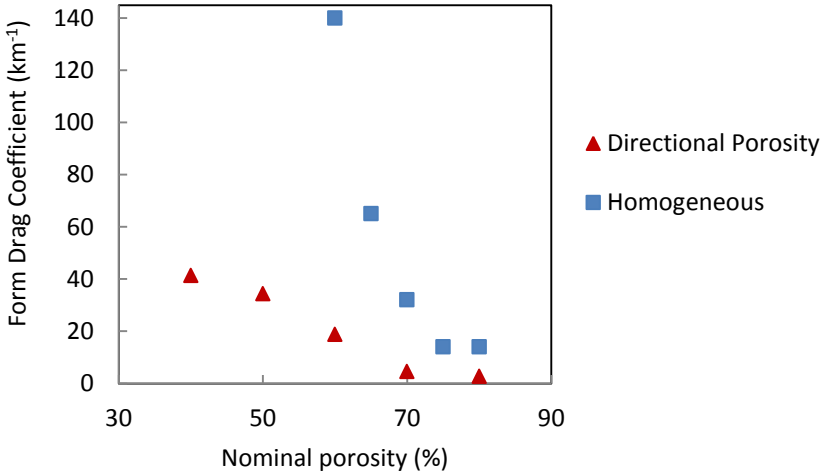

Figure 5.48: Variations in form drag coefficients with porosity for the LCS porous Cu samples with and without directional porosity (pore size: 425-710um).

For samples with directional porosity, the permeability increased with increasing nominal porosity in a trend similar to homogeneous samples, and higher than that of their homogeneous counterparts. Similarly, the form drag coefficient of samples with directional porosity decreased with increasing porosity in a similar trend to the homogenous samples, and was lower than that of their homogeneous counterparts.

The addition of directional porosity in the form of tubular channels parallel to fluid flow contributes to the overall porosity of the structure (Section 4.2.3) and provides direct fluid flow routes along the sample. As observed in horizontal bilayer structures with two layers of different porosities parallel to the water flow (Section 5.4), the majority of the water flow passes through the higher porosity layer. Similarly, for samples with directional porosity, the added channels parallel to water flow acts as a very high porosity layer where the majority of the water flow can pass through directly. There is very little resistance to fluid flow in these open channels. Therefore, a lower overall pressure drop and hence a higher permeability and lower form drag coefficient in the whole sample were observed in Figs. 5.47 and 5.48, when compared to homogeneous samples.

Similar to homogeneous samples, the porosity dictates the pressure drop, permeability and form drag coefficient of the samples with directional porosity. For DP samples with 40%, 50% and 60% nominal porosity, the tubular channels increased the overall actual porosity significantly by 36%, 28% and 12% respectively. However, the effect of this increase on the permeability was less significant. The porosity of the homogeneous part of DP samples still has a significant effect on the fluid flow because of its high volume fraction.

The additional channels in the 70% and 80% porosity samples contributed 8% and 3% more, respectively, to the overall actual porosity. However, this small increase had a significant effect on the permeability (Fig. 5.47).

5.8.5 Comparison with Micro-channels and Lotus Structures

The structure of the LCS samples with directional porosity is to some extent comparable to micro-channels or "lotus-type" copper, where fluid can flow directly along the channels. In lotus metal, the small pores are randomly positioned throughout the structure, with the pores all aligned in the same direction (Muramatsu et al. 2013). Micro-channels contain deep rectangular channels with widths of about 50 µm and depth of 300 µm (Tuckerman and Pease 1981). The pressure drop of lotus type porous copper was 2.5 times greater than that in micro-channels (Ogushi, Chiba and Nakajima 2006). In comparison, the pressure drop of the LCS porous samples with directional porosity investigated in this present study is at least 90 times greater (80% porosity LCS sample with DP) than the lotus copper sample.

This large difference between the pressure drops in lotus metal foam, micro-channels and LCS porous copper with directional porosity is due to the difference in their structures. In lotus copper and micro-channels, all the pores within the structure are aligned in the same direction and the fluid flow through these channels have very little resistance. In contrast, only four of the pores form direct channels in LCS samples with directional porosity. The remaining pores are randomly distributed and are not aligned. As a consequence, there is a much higher resistance to the flow in the random pores, leading to higher pressure drops especially at high flow velocities.

5.9 Summary

For all the porous structures studied in this chapter, the length-normalised pressure drop increased with increasing velocity in a quadratic trend, fitting well with Eq. (3.7) with a determination coefficient R^2>99%. Re-arranging Eq. (3.7) provided a linear relationship between $\frac{\Delta P}{LV_d}$ and V_d (Eq. 5.1) and allowed the determination of the transition between the Darcy regime and the Forchheimer regime. For water flow, all the structures showed a transition at the Darcian velocity in range of 0.5-0.8 m/s. For air flow, the transition occurred at Darcian velocity in range of 2.5-3 m/s.

Both the water and air permeabilities were independent of the sample's length when it is greater than 7 mm. This validates Darcy's or Forchheimer's law and shows that permeability is a structural parameter independent of the sample's length.

For homogeneous LCS structures, the permeability increased while the form drag coefficient decreased with increasing porosity and decreasing pore size. This was due to the high volume of copper walls which impede fluid flow in low porosity LCS samples, and the low pore density in samples with larger pore sizes.

LCS samples with horizontal bilayers structures had a higher permeability and a lower form drag coefficient than the homogeneous samples with the same overall porosity. This was due to the stratification of the flow through the HB structure such that the majority of the flow passed through the higher porosity layer, which dictated the overall flow in the structure.

On the other hand, for samples with vertical bilayers (IVB and SVB), the flow was limited by the lower porosity layers. In general, the permeability of vertical bilayer structures was slightly higher than their homogeneous counterparts with the same overall porosity due to the presence of the higher porosity second layer. However, the form drag coefficient of the vertical bilayers was greater than that of their homogeneous counterparts because the presence of the boundary between the two layers disrupted the flow. In the IVB and SVB structures, the orientation of the layers did not affect the permeability and form drag coefficient.

For SVB and multi-boundary segmented structures, the presence of a hard boundary between the layers had negligible effect on the permeability but affected the form drag coefficient due to increased flow turbulence. The effect of the number of hard boundaries on the permeability and form drag coefficients was not significant.

The addition of directional porosity in the form of tubular channels in LCS structures increased the permeability and decreased the form drag coefficient, in comparison to their homogeneous counterparts. This was because the directional pores provided direct channels for the fluid flow. The overall porosity still affected the permeability and form drag coefficient because the high volume of the random pores within the structure still obstructed the fluid flow.

Chapter 6 Heat Transfer Coefficient of LCS Porous Copper

This chapter presents and discusses the results obtained from the heat transfer experiments on LCS porous copper with homogeneous and non-homogeneous structures using water as the coolant. The water flow rate ranged from 0.28 L/min to 1.12 L/min. The effects of porosity, pore size and non-homogeneous structure on the heat transfer coefficient were studied.

6.1 Heat Transfer Coefficient of Homogeneous Samples

6.1.1 Heat Flux

Fig. 6.1 shows the relationship between the heat flux (J), determined using Eq. (3.8), and the (T_b-T_{in}) at different water flow rates. There is a very good linear correlation between J and (T_b-T_{in}) ($R^2 \geq 0.99$), following Newton's law of cooling. This suggests that for each water flow rate, a constant heat transfer coefficient can be determined from the gradient of the graphs in Fig. 6.1 using Eq. (3.9).

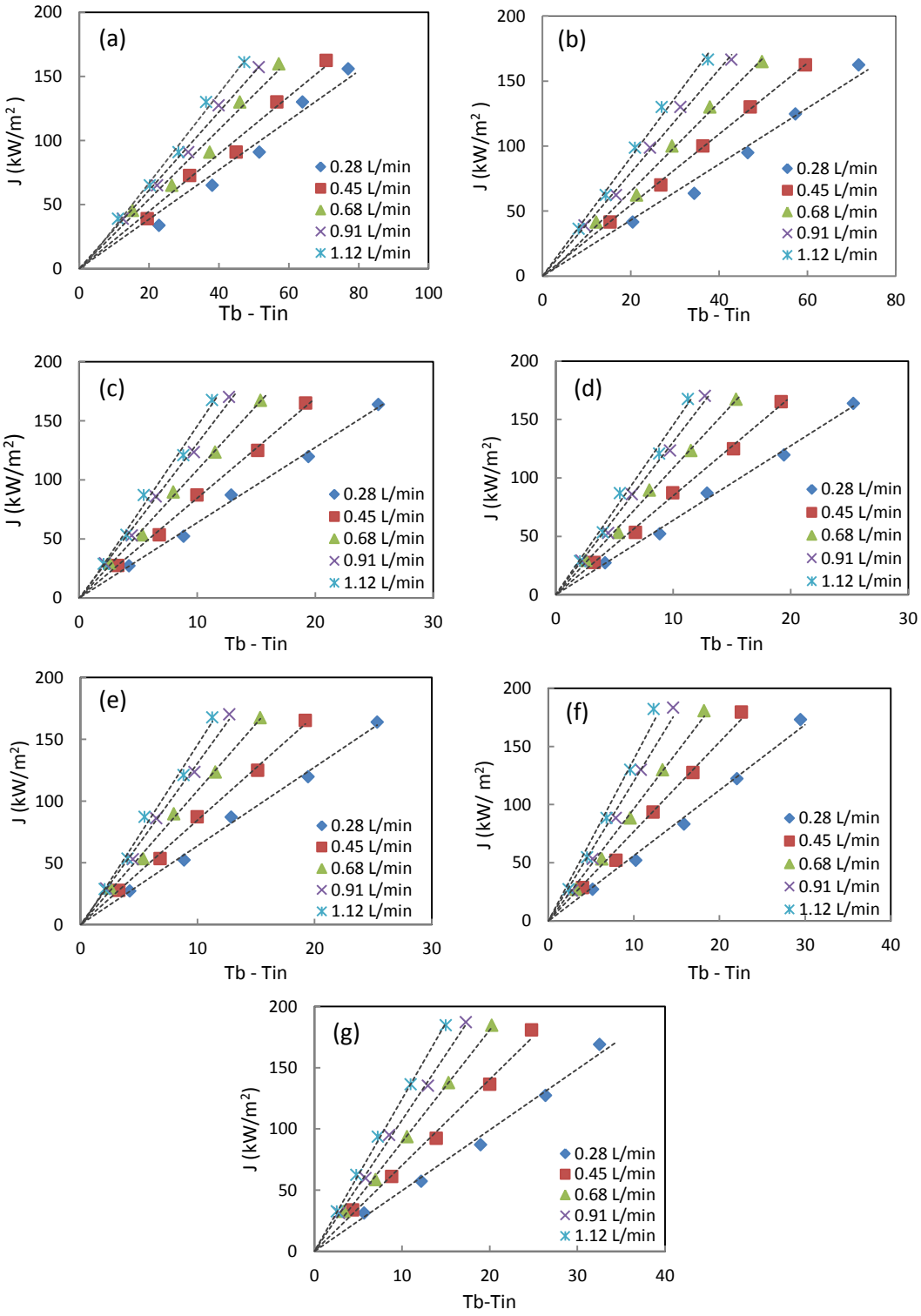

Figure 6.1: Heat flux (J) versus (T_b-T_{in}) for LCS homogeneous samples (H5-H11) with the same pore size (425-710µm) but different actual porosity: a) 45.8% b) 54.2%, c) 59.2%, d) 63.8%, e) 68.7%, f) 73.8% and g) 77%.

6.1.2 Effect of Porosity

Table 6.1 lists the heat transfer coefficients of homogeneous samples with different porosity, determined using Eq. (3.9). For comparison, the heat transfer coefficient with only water flow and no sample in the chamber (100% porosity) was measured and included.

Table 6.1: Heat transfer coefficients of homogeneous LCS samples (pore size: 425-710µm) with different porosity for a range of water flow rates.

Sample	Nominal Porosity (%)	Water Flow Rate (L/min)	Heat Transfer Coefficient (kW/(m^2.K))
H5	40	1.12	3.4
		0.91	3.1
		0.68	2.7
		0.45	2.2
		0.28	1.9
H6	50	1.12	4.6
		0.91	4.0
		0.68	3.3
		0.45	2.7
		0.28	2.1
H7	60	1.12	19.5
		0.91	16.9
		0.68	14.3
		0.45	11.2
		0.28	8.2
H8	65	1.12	18.5
		0.91	16.1
		0.68	13.1
		0.45	10.0
		0.28	7.3
H9	70	1.12	14.7
		0.91	13.0
		0.68	10.7
		0.45	8.5
		0.28	6.8
H10	75	1.12	13.9
		0.91	12.0
		0.68	10.0
		0.45	7.7
		0.28	5.7
H11	80	1.12	12.3
		0.91	10.7
		0.68	9.0
		0.45	7.0
		0.28	5.1
Only water flow (no sample)	100	1.12	3.9
		0.91	3.5
		0.68	2.7
		0.45	2.6
		0.28	2.4

Fig. 6.2 shows that the sample's porosity has a strong influence on the heat transfer coefficient. For samples with 40% and 50% porosity, the heat transfer coefficients were very small for all the water flow rates. Increasing the porosity to 60% led to a sharp rise in the heat transfer coefficient. Increasing the sample's porosity further to 80%, however, led to the gradual decline in the heat transfer coefficient. This suggests that an optimum porosity offering the maximum heat transfer coefficient for LCS homogeneous samples exists. This is approximately 60% for the pore size range of 425-710 µm.

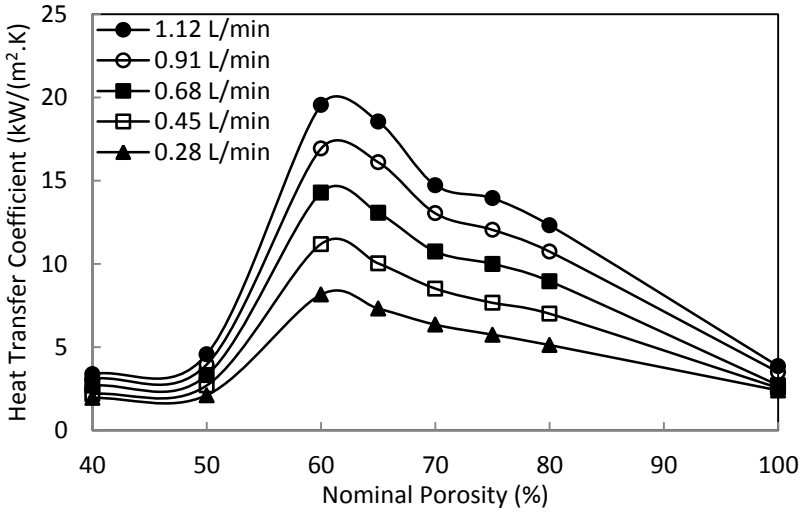

Figure 6.2: Variations in heat transfer coefficient with nominal porosity for LCS homogeneous samples (pore size: 425-710 µm).

Heat removal within the LCS porous copper-water cooling system occurs through thermal conduction and thermal convection. Fig. 6.3 schematically illustrates the temperature distribution within the water-cooled LCS porous copper. Heat from the heat source is transported to the LCS copper samples by conduction and is removed subsequently by the flowing water coolant through convection. Therefore, the overall heat transfer performance of the LCS porous copper sample is determined by the parameters affecting these

processes, i.e., the sample's thermal conductivity and the sample's permeability to the coolant.

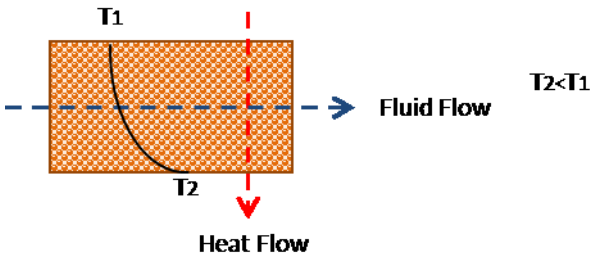

Figure 6.3: Heat transfer through the LCS homogeneous copper sample showing the temperature profile.

For samples with low porosity (e.g. 40% and 50%), there is a high volume of copper present, resulting in high thermal conductivity. However, high volume of copper also means more resistance to fluid flow, as found in Section 5.1. Samples with low porosity have very low internal passage for fluid flow and very low fluid permeability, leading to poor heat removal by the water coolant through convection. Even though low porosity samples have good thermal conductivity, the overall heat transfer performance is limited by the poor thermal convection within the structure.

On the other hand, the high porosity LCS samples (e.g. 80%) have a small volume of copper. This leads to high internal passage and high permeability for fluid, as established in Section 5.1. Heat removal by thermal convection in high porosity samples is enhanced as a consequence. However, thermal conductivity within the high porosity samples is compromised since there is a smaller volume of copper present to conduct heat. As a

consequence, the overall heat transfer performance is limited by the thermal conductivity of the porous copper matrix.

An optimum porosity of 60% was identified from Fig. 6.2, at which heat removal by thermal conduction through the copper matrix and thermal convection from the matrix to the flowing coolant is balanced. LCS samples with 60% porosity are permeable to fluid flow, with a relatively low permeability. Their form drag coefficient, however, was very high, suggesting greater turbulence in the fluid flow, especially at high water flow rates (Section 5.1). This leads to more mixing in the flow and greater access to smaller interstices within the structure. As a consequence, heat removal by heat convection is enhanced. Additionally, a relatively high volume of copper is present within the 60% porosity LCS sample. Therefore, heat removal by thermal conduction is substantial within the copper matrix.

Fig.6.4 illustrates the contribution of thermal conduction (thermal conductivity) and thermal convection (Nusselt number) to the overall heat transfer in LCS porous copper samples. Nusselt number (*Nu*) is the ratio of convection to pure conduction heat transfer, and for porous metals, it can be expressed as:

$$Nu = \frac{hD_h}{k_f} \tag{6.1}$$

where D_h is the hydraulic diameter (Incropera et al. 2007, Xiao 2013). A large Nusselt number indicates that convection is dominating the heat transfer. For LCS porous copper, the thermal conductivity (λ) was calculated using:

$$\lambda = \lambda_s(1-\phi)^{1.82s+1.81} \tag{6.2}$$

where s_r is the particle/pore size ratio(Xiao 2013).

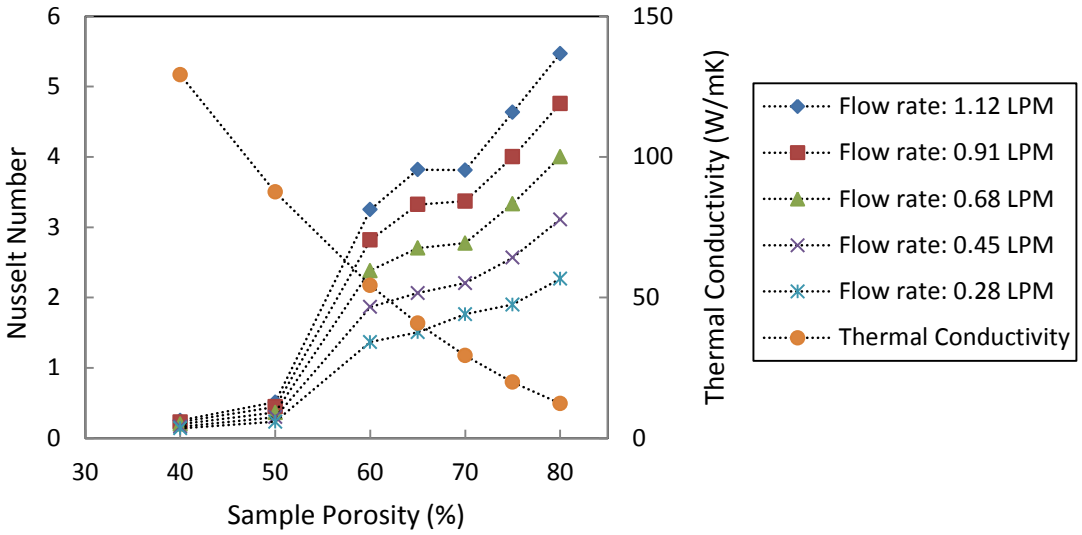

Figure 6.4 Correlation between Nusselt number, thermal conductivity and sample porosity.

From Fig 6.1, it was apparent that above the optimum porosity, thermal conduction limits the overall heat transfer. On the other hand, heat transfer by thermal convection was the limiting factor below the optimum porosity. At the optimum porosity, there is a balance between conduction and convection, maximising the heat transfer.

Moreover, placing the 40% porosity LCS sample in the sample chamber yielded a heat transfer coefficient similar to the empty channel (100% porosity) from Fig. 6.2. This is because the 40% porosity sample has a low fluid permeability so heat removal by thermal convection is greatly limited. When a 60% porosity sample was placed in the sample chamber, on the other hand, the heat transfer coefficient was approximately four times greater than that of an empty channel (100% porosity). This demonstrates that LCS porous

copper greatly improves the heat transfer performance and is suitable for thermal management applications.

6.1.3 Effect of Water Flow Rate

The water flow rate greatly affects the heat transfer performance of the LCS homogeneous samples. The heat transfer coefficient increased with increasing water flow rate for all the samples (Fig. 6.2), with the greatest variance in heat transfer coefficient observed for sample H7. This is because heat removal by convection occurs more rapidly at higher water flow rates. Additionally, at higher water flow rates, the flow is more turbulent (as discussed in Section 5.1.2). This results in increased mixing in the water flow and greater access to inter-particle pores within the porous structure. Therefore, a larger copper surface comes into contact with the coolant, enhancing the heat transfer between the two media. Hence, a better heat transfer performance was observed at high coolant flow rate.

6.1.4 Effect of Pore Size

The effect of pore size on the heat transfer coefficient of the LCS homogeneous samples was investigated by studying three samples of similar porosity but different pore sizes (H3, H9 and H18). The heat transfer coefficients for the samples at varying water flow rates are summarised in Table 6.2 and displayed in Fig. 6.5.

Table 6.2: Summary of heat transfer coefficients of homogeneous LCS samples with similar porosity (approximately 70%) but different pore size.

Sample Reference	Pore Size (µm)	Flow Rate (L/min)	Heat Transfer Coefficient (kW/(m^2.K))
H3	250-425	1.12	12.8
		0.91	11.5
		0.68	9.8
		0.45	8.2
		0.28	6.8
H9	425-710	1.12	14.7
		0.91	13.0
		0.68	10.7
		0.45	8.5
		0.28	6.8
H18	1000-1500	1.12	19.8
		0.91	17.1
		0.68	14.4
		0.45	11.4
		0.28	8.6

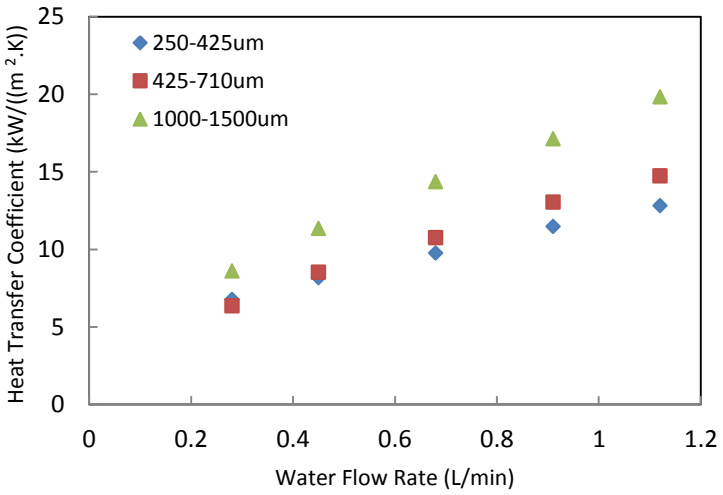

Figure 6.5: Variations in heat transfer coefficient for samples with similar porosities (approximately 70%) and different pore sizes.

Apparent from Fig. 6.5 is that the heat transfer coefficient increases with increasing pore size at any given water flow rate. The greatest heat transfer performance for all the water

flow rates studied was observed for sample H18, which has the largest pore size. On the other hand, the lowest heat transfer coefficient was observed for sample H3 which has the smallest pore size.

In samples with smaller pores, there is smaller space for a convection current, which limits heat transfer by convection. On the other hand, the samples with larger pores have enough space to accommodate convection currents. In addition, inertial effects are greater in samples with larger pores, as discussed in Section 5.1. The turbulent flow leads to greater mixing and greater access to smaller channels within the structure. This enhances heat removal by convection, and therefore, results in a higher heat transfer performance.

6.2 Heat Transfer Coefficient of Samples with Horizontal Bilayer Structure

The heat transfer coefficients of LCS porous copper samples with horizontal bilayer structures (HB1, HB3 and HB4) were measured at different water flow rates. The effect of changing the orientation of the layers on the heat transfer performance of the whole structure was also studied. Label "L/H" denotes that the low porosity layer was in contact with the heat source while "H/L" denotes that the high porosity layer was in contact with the heat source. The results are summarised in Table 6.3.

Table 6.3: Heat transfer coefficients of LCS samples with horizontal bilayer structures.

Sample Reference	Layer 1 / Layer 2 Porosity (%)	Overall Porosity (%)	Flow Rate (L/min)	Heat Transfer Coefficient ($kW/m^2.K$)	
				L/H	H/L
HB1	40/70	55	1.12	9.3	13.1
			0.91	8.6	11.5
			0.68	7.6	9.1
			0.45	6.5	6.5
			0.28	5.4	4.1
HB3	40/80	60	1.12	10.5	15.0
			0.91	9.7	13.5
			0.68	8.4	11.4
			0.45	7.1	9.0
			0.28	5.8	6.7
HB4	50/70	60	1.12	8.9	11.5
			0.91	8.0	9.8
			0.68	6.9	7.7
			0.45	5.5	5.4
			0.28	4.0	3.6

6.2.1 Effect of Layer Porosity

Fig. 6.6 compares the heat transfer coefficients of horizontal bilayer LCS samples with different porosity combinations. For samples with L/H orientation, increasing the porosity of the bottom layer (away from the heat source) while keeping the porosity of the top layer (next to the heat source) constant, e.g. 40/70 vs 40/80, led to an increase in the heat transfer coefficient. Increasing the porosity of the top layer, e.g. 40/70 vs 50/70, led to a slight decrease in the heat transfer performance.

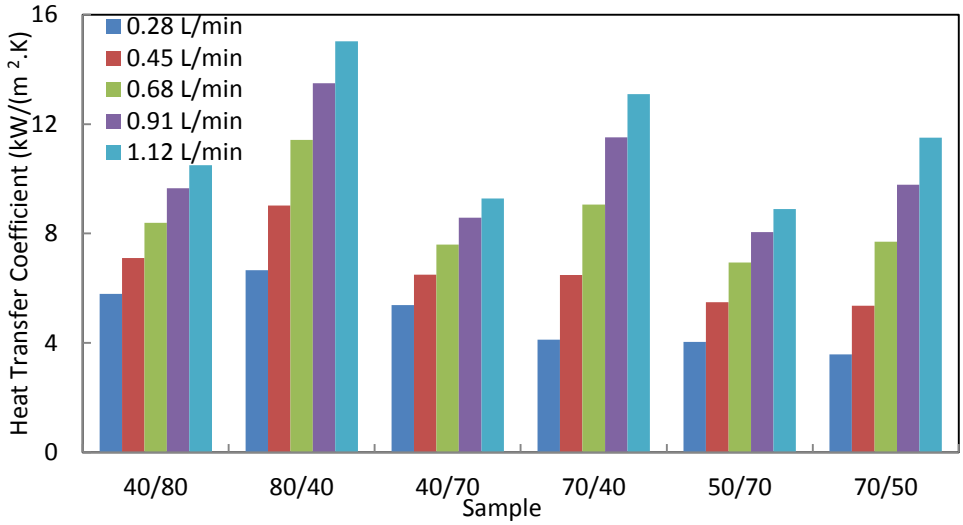

Figure 6.6: Variation in heat transfer coefficient with water flow rate for LCS samples with horizontal bilayer structure.

For samples with H/L orientation, on the other hand, increasing the porosity of the bottom layer, e.g. 70/40 vs 70/50, led to a decrease in the heat transfer coefficient. Meanwhile, increasing the porosity of the top layer, e.g. 70/40 vs 80/40, led to an increase in the heat transfer coefficient.

Comparing samples 40/70 and 40/80, a slightly higher overall porosity is present in sample 40/80, which reduces its thermal conductivity. However, the permeability is greater in sample 40/80 (Section 5.4), since its second layer is more porous than in the 40/70 sample.

The majority of the flow will pass through the high porosity 80% layer, enhancing heat removal by convection. This suggests that in this case, heat removal by convection is more efficient than conduction.

Comparing samples 40/80 and 50/70, they both have similar overall porosity of 60%, and therefore similar thermal conductivity. However, 40/80 showed better heat transfer than 50/70. This is because 40/80 had a higher permeability than 50/70 (Section 5.4) due to the more porous 80% layer, which leads to greater heat removal by convection.

Comparing samples 40/70 and 50/70, a lower porosity layer is present in sample 40/70. Since sample 40/70 is less permeable to the coolant (Section 5.4), heat removal by convection is less in sample 40/70. However, the thermal conductivity of sample 40/70 is greater than in 50/70 since more copper is present. The greater thermal conductivity of sample 40/70 outweighs its lower permeability, and as a consequence, it has a higher heat transfer coefficient than sample 50/70. In general, sample 40/80 had the highest heat transfer coefficient, followed by sample 40/70 and sample 50/70 for all water flow rates.

The above results showed the importance to strike a balance between heat removal by conduction and convection to achieve efficient heat transfer performance. The overall heat transfer performance can be manipulated by varying the contribution of heat conduction and convection through changing the structure and layer porosity.

6.2.2 Effect of Orientation

Fig. 6.6 also compares the effect of the orientation of the layers on the heat transfer performance of the LCS samples with horizontal bilayer structures. For all the samples studied, having the higher porosity layer by the heat source (H/L orientation) gave a higher heat transfer coefficient. The contribution of a layer in the LCS sample to the heat transfer decays quickly with increasing distance from the heat source (Xiao and Zhao 2013). Therefore, in horizontal bilayer structures, the layer directly in contact with the heat source plays a more important role in the overall heat transfer performance.

As discussed in Section 5.4, the fluid flow chooses preferentially the layers with higher permeability. As a consequence, the fluid flow rate is greater in the higher porosity layer, with majority of the flow passing though this layer (Ho and Webb 2006, Xiao and Zhao 2013). From Section 6.1, increasing the flow rate enhances the heat transfer rate since heat removal by convection is greater. Consequently, having the higher porosity layer directly in contact with the heat source will result in higher heat transfer performance. In general, the heat transfer coefficient was at least 30% greater when the higher porosity layer was directly in contact with the heat source.

6.2.3 Analysis by Segment Model

Xiao and Zhao (2013) developed a segment model designed for homogeneous samples, which can be used to predict the contributions of the individual layers within the HB structure on the overall heat transfer performance. The segment model states that the overall heat transfer performance (h) can be estimated using:

$$h = \sum_{i=1}^{i=\infty} w_i h_i \tag{6.2}$$

where h_i and w_i are the heat transfer coefficient and weighting factor of the ith layer. The weighting factor indicates the convective contribution of a particular layer of the sample (from $x=x_1$ to $x=x_2$) to the overall heat transfer, and is defined as:

$$w = e^{-\frac{4x_1}{t}} - e^{-\frac{4x_2}{t}} \tag{6.3}$$

where x is the distance of the layer from the heat plate and t is the overall thickness of the sample. This suggests that the layer closer to the heat plate has the highest contribution to the overall heat transfer performance of the HB structure. Fig. 6.7 schematically illustrates the temperature distribution within the HB structure.

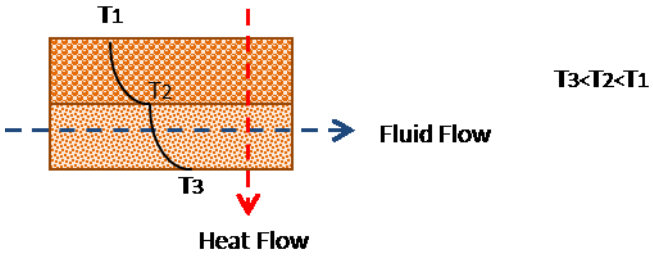

Figure 6.7: Heat transfer through the LCS horizontal bilayer structure showing the temperature profile.

Fig. 6.8 compares the measured heat transfer coefficients of the HB samples with the coefficients predicted using the segment model (t= 5 mm in this case). In general, a good correlation between the measured and predicted coefficients can be observed, especially for samples with H/L orientation. However, the measured coefficients of samples with L/H orientation are slightly higher than the predicted values. Since the segment model was designed for homogeneous samples, applying it to multi-layer samples will results in errors.

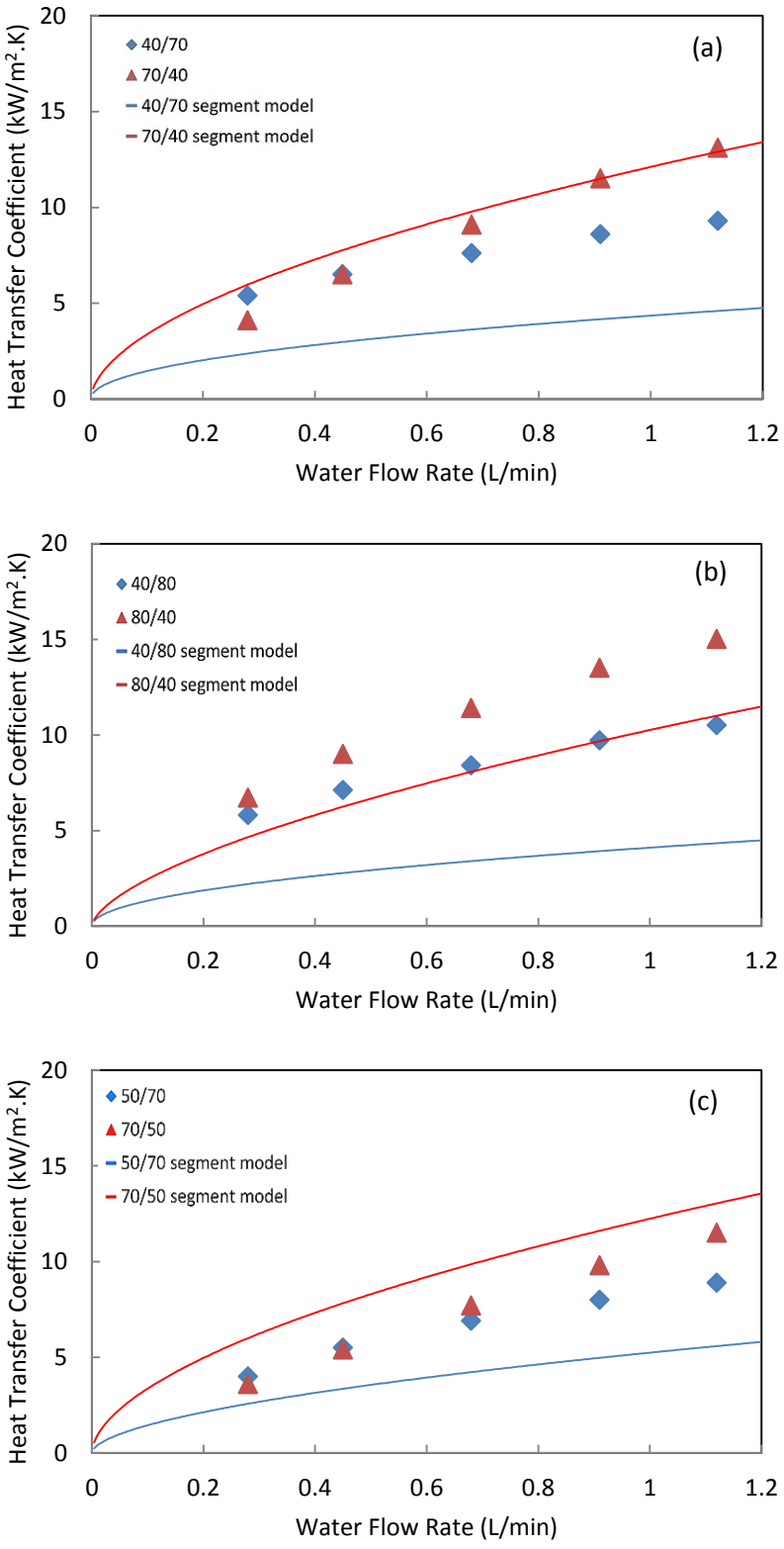

Figure 6.8: Comparison between the measured and the predicted heat transfer coefficients for the horizontal bilayer samples of H/L and L/H orientations: a) 40/70, b) 40/80 and c) 50/70.

6.2.4 Comparison with LCS Homogeneous Structure

Fig. 6.9 compares the heat transfer coefficients of the horizontal bilayer structures with LCS homogeneous structures according to the overall porosity of the structures for different water flow rates. It is apparent from Fig. 6.9 that the heat transfer coefficients of homogeneous samples are greater than the HB samples of similar overall porosity. These results are similar to that found by Xiao and Zhao (2013) and Xiao (2013).

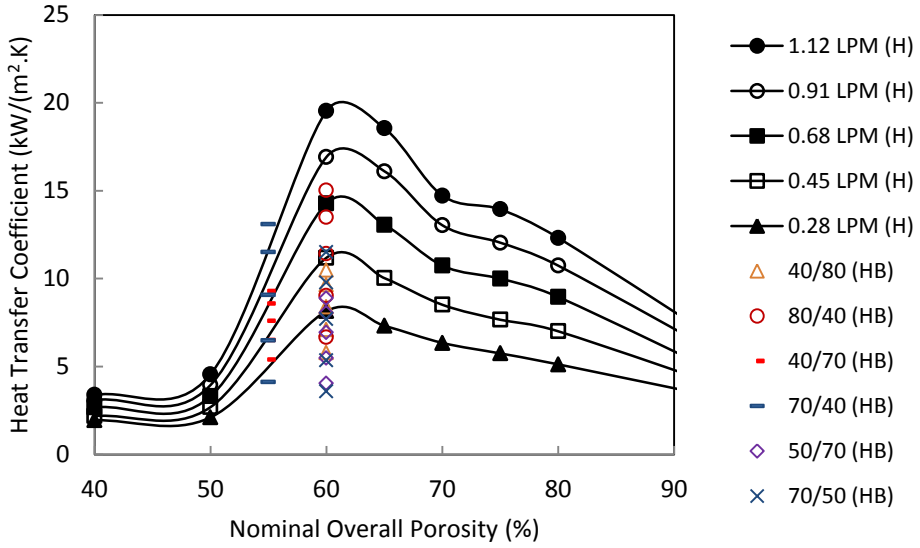

Figure 6.9: Comparison of heat transfer coefficients between LCS samples with horizontal bilayer (HB) structure and homogeneous (H) structure for different water flow rates.

Even though HB structures contain similar copper content and therefore similar thermal conductivity as their homogeneous counterparts (similar overall porosity), their permeabilities are different. According to the flow stratification model, the majority of the flow will pass through the more permeable, higher porosity layer of the horizontal bilayer structure. Therefore, the permeability of horizontal bilayer structures is greater than the homogeneous structures of a similar overall porosity (as evident in Section 5.4), which could increase the heat transfer by convection. It is likely that the porosity of the HB structures studied is further from the "optimum porosity", while the porosity of their homogeneous

counterparts is closer to the “optimum porosity”. As a consequence, the overall heat transfer performance of the HB structures is worse than their homogenous counterparts for the porosity range in this study.

6.3 Heat Transfer Coefficient of Samples with Integrated Vertical Bilayer Structure

The heat transfer coefficients of LCS porous copper samples with integrated vertical bilayer structures (IVB1-IVB10) were measured at different water flow rates. The effect of changing the orientation of the layers on the heat transfer performance of the whole structure was also investigated. Label “L/H” denotes that the first layer (layer closer to the water inlet) is the lower porosity layer, while “H/L” denotes that the first layer is the higher porosity layer. The results are summarised in Table 6.4.

Table 6.4: Heat transfer coefficients of LCS samples with integrated vertical bilayer structures.

Sample Reference	Layer 1/Layer 2 Porosity (%)	Overall Porosity (%)	Flow Rate (L/min)	Heat Transfer Coefficient ($kW/m^2.K$)	
				L/H	H/L
IVB1	40/50	45	1.12	7.6	16.0
			0.91	6.6	13.3
			0.68	5.4	11.1
			0.45	4.4	8.3
			0.28	3.6	6.8
IVB2	40/60	50	1.12	14.1	24.0
			0.91	12.3	17.7
			0.68	9.6	12.0
			0.45	7.7	8.3
			0.28	6.0	6.0
IVB3	40/70	55	1.12	17.5	24.6
			0.91	14.9	18.7
			0.68	11.9	12.7
			0.45	8.8	10.0
			0.28	6.1	7.1
IVB4	40/80	60	1.12	26.0	60.8
			0.91	20.2	43.0
			0.68	15.0	27.2
			0.45	11.0	17.6
			0.28	7.4	13.0
IVB5	50/60	55	1.12	20.8	32.7
			0.91	17.2	21.0
			0.68	11.5	15.3
			0.45	7.9	10.2
			0.28	4.7	7.0
IVB6	50/70	60	1.12	14.7	19.7
			0.91	12.6	16.1
			0.68	10.1	12.1
			0.45	7.7	9.8
			0.28	5.3	7.5
IVB7	50/80	65	1.12	17.3	21.7
			0.91	14.5	17.7
			0.68	11.6	14.7
			0.45	8.7	10.6
			0.28	6.3	7.4
IVB8	60/70	65	1.12	25.5	31.2
			0.91	23.1	25.5
			0.68	18.5	21.4
			0.45	13.9	14.7
			0.28	9.8	10.2
IVB9	60/80	70	1.12	15.3	18.1
			0.91	13.2	16.1
			0.68	10.5	13.5
			0.45	8.1	10.3
			0.28	5.7	7.1
IVB10	70/80	75	1.12	23.6	20.9
			0.91	20.1	18.8
			0.68	16.8	14.8
			0.45	13.2	12.1
			0.28	9.7	8.6

6.3.1 Effect of Porosity

Fig. 6.10 displays the heat transfer coefficients of all the IVB samples, categorised according to the overall porosity of the whole structure, for each water flow rate. There is no obvious general trend existing between the heat transfer coefficient and the overall nominal porosity for all the water flow rates. Sample 80-40 showed the greatest heat transfer coefficient while sample 40-50 showed the lowest heat transfer coefficient for the range of water flow rates studied.

Fig. 6.11 compares the heat transfer coefficients of the IVB samples categorised according to the porosity of the first layer (layer closer to the water inlet) and the porosity of the second layer (layer closer to the water outlet). Figs. 6.11 a-b, 6.11 c-d, 6.11 e-f, 6.11 g-h and 6.11 i-j show the results of all IVB samples with 40%, 50%, 60%, 70% and 80% porosity layer, respectively. The figures on the left show the effect of changing the porosity of the second layer and the figures on the right show the effect of changing the porosity of the first layer, while keeping the porosity of the other layer constant.

For samples whose first or second layer porosity is 40% (Fig. 6.11 a-b), increasing the porosity of the other layer from 50% to 80% led to an increase in the heat transfer coefficient, with sample 40-80 showing the highest heat transfer coefficient in both orientations. Meanwhile, for samples whose first or second layer porosity is 50% (Fig. 6.11 c-d), no obvious trend in heat transfer coefficient was seen when the porosity of the other layer was increased from 60% to 80%. Sample 50-60 showed the highest heat transfer coefficient in both orientations.

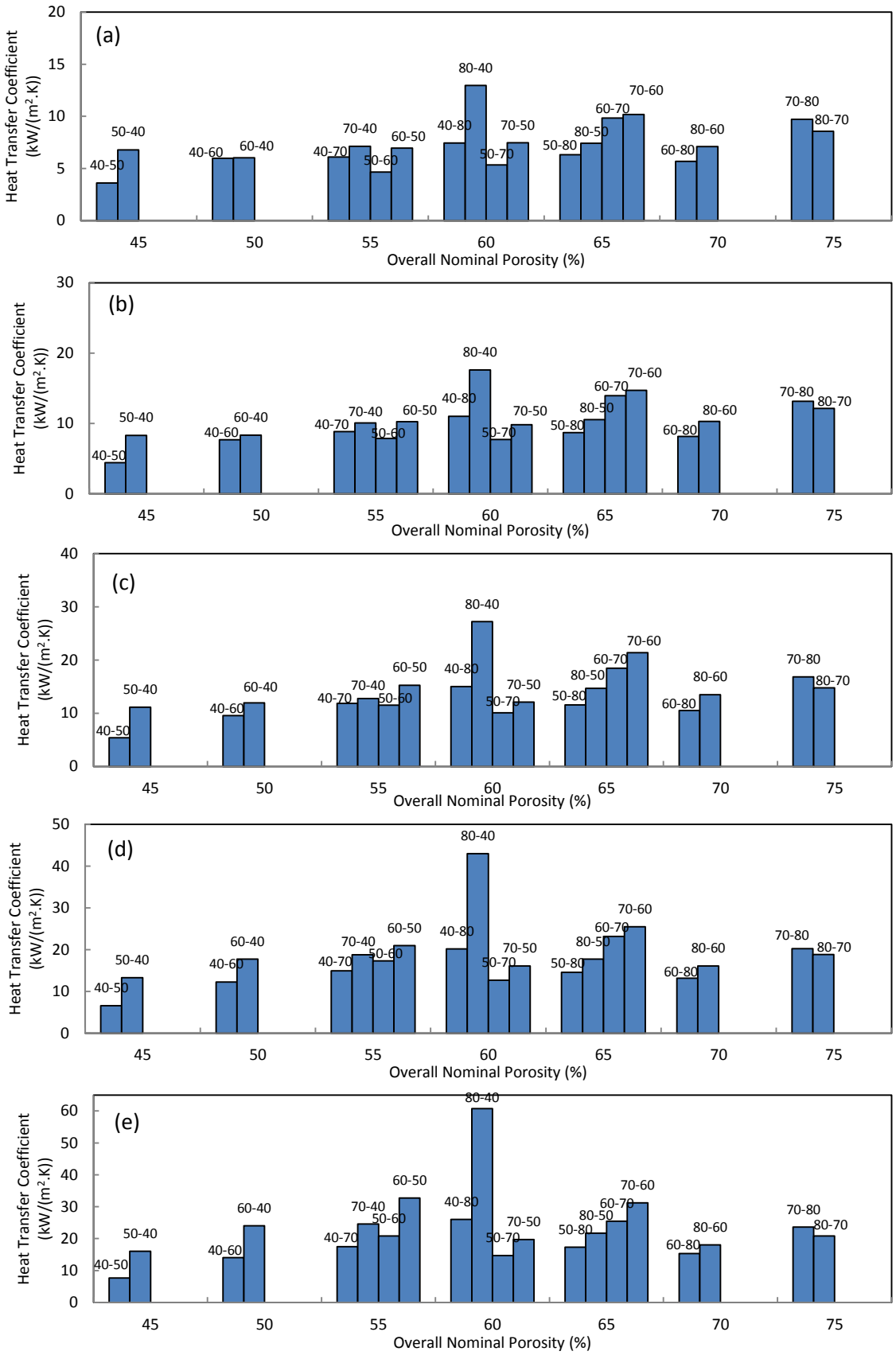

Figure 6.10: Variations in the heat transfer coefficient of LCS samples with IVB structures categorised according to the sample's overall porosity for each water flow rate: a) 0.28 L/min, b) 0.45 L/min, c) 0.68 L/min, d) 0.91 L/min and e) 1.12 L/min.

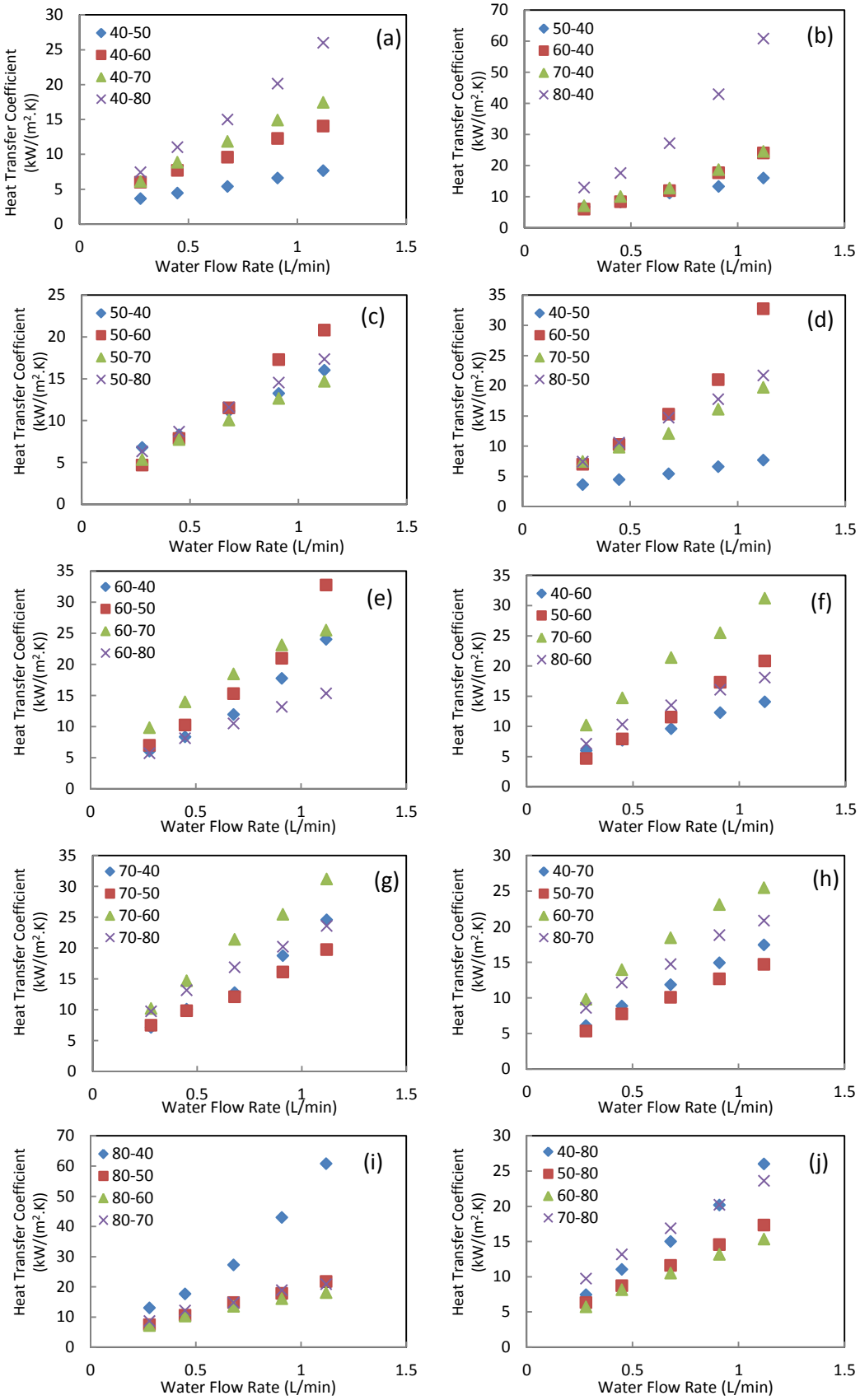

Figure 6.11: Variation in heat transfer coefficient with water flow rate for LCS samples with IVB structure categorised according to the nominal porosity of the first (left) or second (right) layer.

For samples whose first or second layer porosity is 60% (Fig. 6.11 e-f), increasing the porosity of the other layer from 40% to 50% led to an increase in the heat transfer coefficient, while increasing the porosity of the other layer from 70% to 80% showed a decrease in the heat transfer coefficient. The best heat transfer coefficient was measured for sample 60-70 at lower water flow rates and for sample 60-50 at higher water flow rates (Fig. 6.11e). Sample 70-60 showed the greatest heat transfer coefficient for all the flow rates investigated from Fig. 6.11f.

For samples whose first or second layer porosity is 70% (Fig. 6.11 g-h), no obvious trend in heat transfer coefficient was observed when the porosity of the other layer was increased from 40% to 60%. Sample 60-70 showed the highest heat transfer coefficient in both orientations.

For samples whose first or second layer porosity is 80% (Fig. 6.11 i-j), no obvious trend in heat transfer coefficient can be observed when the porosity of the other layer was increased from 40% to 70%. Sample 40-80 showed high heat transfer coefficient in both orientations (Fig. 6.11 i-j), while sample 70-80 showed high heat transfer coefficient at low water flow rates (Fig. 6.11j).

As seen from Fig. 6.11, increasing the water flow rate resulted in higher heat transfer coefficients for all the IVB samples. It appears that there is an optimum combination of layer porosity for IVB structures which gave the best heat transfer performance. Table 6.5 lists the

optimum combination of layer porosity found for each porosity category. In general, samples 40-80, 50-60 and 60-70 showed better heat transfer performance. It is worth noting that the overall porosities of these combinations are 60%, 55% and 65%, respectively.

Table 6.5: Optimum combinations of layer porosity for samples with IVB structures.

Nominal Porosity of First Layer (%)	Optimum Combination	Nominal Porosity of Second Layer (%)	Optimum Combination
40	40-80	40	80-40
50	50-60	50	60-50
60	60-70 at Q= 0.28-0.91 L/min 60-50 at Q= 1.12 L/min	60	70-60
70	70-60	70	60-70
80	80-40	80	70-80 at Q=0.28-0.68 L/min 40-80 at Q=0.91-1.12 L/min

It appears that the heat transfer coefficient is mainly determined by the overall porosity. The optimum overall porosity for the samples studied varied between 55% and 65%, which is similar to the case of homogeneous LCS samples whose optimum porosity was 60% (Section 6.1). As in homogeneous samples, when the overall porosity of the IVB sample is too low, heat removal is limited by thermal convection. When the overall porosity is too high, heat removal is limited by thermal conduction. The optimum porosity which offers the best heat transfer performance is achieved when heat removal by conduction and convection is balanced.

6.3.2 Effect of Orientation

Fig. 6.10 displays the effect of the orientation of the layers on the heat transfer performance of LCS samples with IVB structures. For most of the samples studied, apart

from samples 70-80, having the higher porosity layer by the water inlet (H/L orientation) gave a higher heat transfer coefficient. As seen from Section 5.5, changing the orientation of the layers within the IVB structure had insignificant effect on the permeability and form drag coefficient of the whole IVB structure. The variation in the heat transfer performance with sample orientation is likely due to the "soft boundary" effect between the layers.

Fig. 6.12 schematically illustrates the temperature distribution within the IVB structure. As the fluid approaches the low porosity region from the high porosity region, the fluid slows down. Therefore, the fluid dwells longer in the high porosity region and turbulence mixing occurs. This increases convective heat transfer. On the other hand, when the fluid approaches the high porosity region from the low porosity layer, the fluid has more opportunities to find alternative routes at the boundary. As a consequence, the fluid does not dwell for long within the IVB structure and less turbulence mixing occurs. This decreases heat removal by convection. For sample 70-80, however, the porosities of the layers are very high and the difference is small, so the boundary effect is negligible.

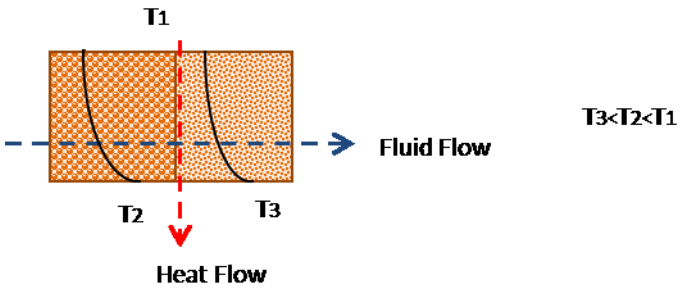

Figure 6.12: Heat transfer through the LCS integrated vertical bilayer structure showing the temperature profile.

6.3.3 Comparison with LCS Homogeneous Samples

Fig. 6.13 compares the heat transfer coefficients of IVB structures with LCS homogeneous (H) structures according to the overall porosity for different water flow rates. The heat transfer coefficients of most IVB samples (apart from 50-70, 50-80 and 60-80) are higher than their homogeneous counterparts with a similar overall porosity. This is because the porosity combination of the layers within the IVB samples maximises heat removal by conduction and convection (Section 6.3.1).

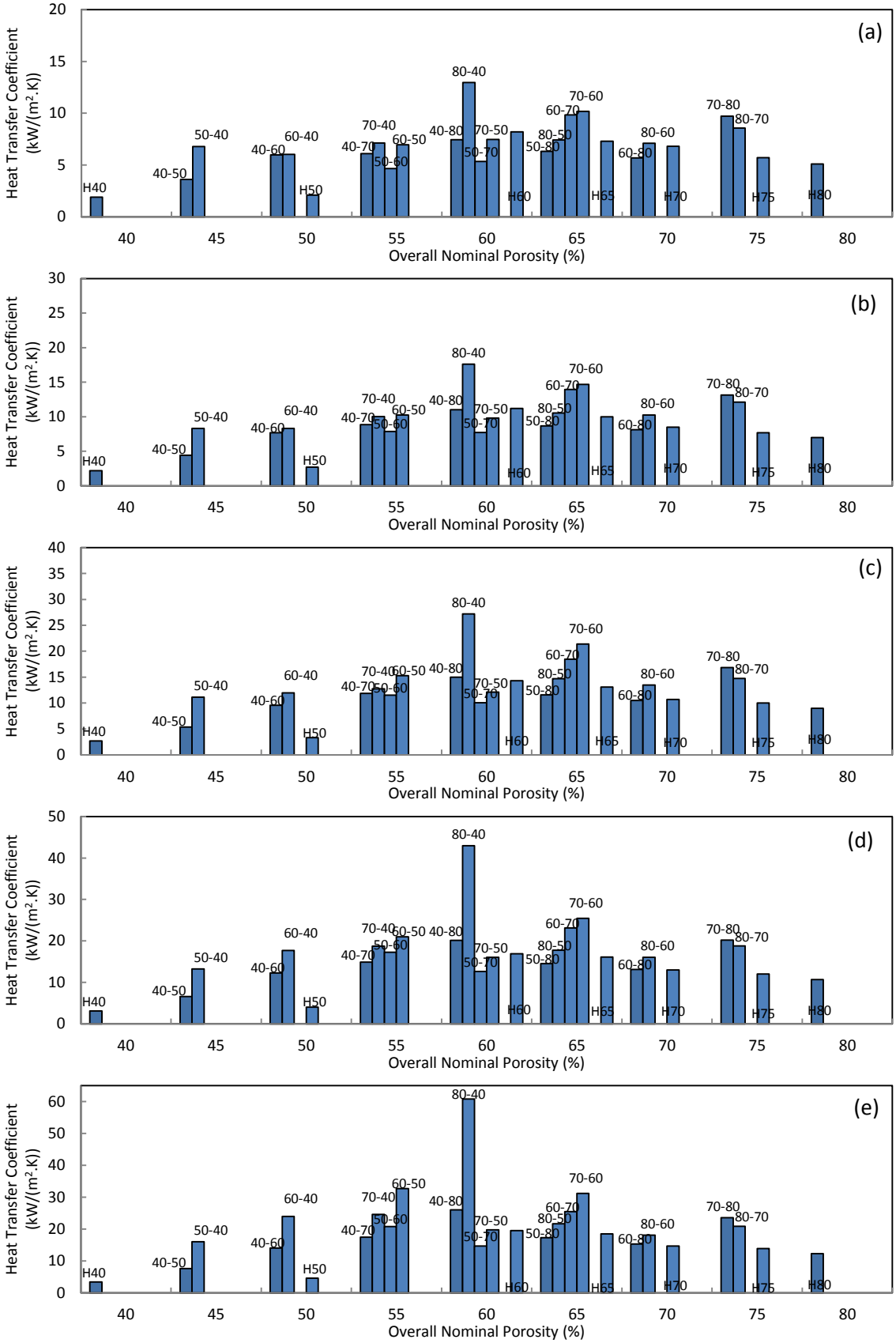

Figure 6.13: Variations in the heat transfer coefficient of LCS samples with IVB structures in comparison to homogeneous samples (H) for different water flow rates: a) 0.28 L/min, b) 0.45 L/min, c) 0.68 L/min, d) 0.91 L/min and e) 1.12 L/min.

When compared according to the lower porosity layer (e.g. 40-50 vs H40), the IVB structures have higher heat transfer coefficients than their homogeneous counterparts, except sample 60-80. This is because the second layer of the IVB structure has a higher porosity, which increases the overall porosity of the sample towards the optimum porosity (Section 6.3.1), at which heat removal by both conduction and convection is maximised. Sample 60-80, on the other hand, has a lower heat transfer coefficient than the homogeneous 60% sample. This is because the high porosity layer (80%) increases the overall porosity and pushes it away from the optimum porosity (Section 6.3.1).

6.4 Heat Transfer Coefficient of Samples with Segmented Vertical Bilayer Structure

The heat transfer coefficients of LCS porous copper samples with segmented vertical bilayer structures (SVB1-SVB10) were measured for water flow rates ranging between 0.28 L/min to 1.12 L/min. The effect of changing the orientation of the layers within the SVB structure on the overall heat transfer performance was also investigated. Label “L-H” indicates that the first layer (layer closer to the water inlet) is the lower porosity layer, while “H-L” indicates that the first layer is the higher porosity layer. The results are summarised in Table 6.6.

Table 6.6: Heat transfer coefficients of samples with segmented vertical bilayer structures.

Sample Reference	Layer 1/Layer 2 Porosity (%)	Nominal Porosity (%)	Flow Rate (L/min)	Heat Transfer Coefficient ($kW/m^2.K$)	
				L-H	H-L
SVB1	40/50	45	1.12	16.5	13.3
			0.91	13.4	11.8
			0.68	10.2	9.1
			0.45	7.4	7.2
			0.28	5.3	4.9
SVB2	40/60	50	1.12	35.7	24.3
			0.91	27.9	18.1
			0.68	19.3	13.2
			0.45	10.5	9.3
			0.28	6.5	6.1
SVB3	40/70	55	1.12	29.5	27.4
			0.91	22.0	19.9
			0.68	16.0	13.2
			0.45	11.5	9.7
			0.28	8.3	6.4
SVB4	40/80	60	1.12	101.7	44.3
			0.91	74.6	38.8
			0.68	42.6	28.8
			0.45	25.6	21.5
			0.28	15.1	13.2
SVB5	50/60	55	1.12	23.3	20.9
			0.91	18.9	17.4
			0.68	14.4	12.8
			0.45	10.2	8.6
			0.28	6.6	6.3
SVB6	50/70	60	1.12	25.7	20.4
			0.91	19.3	17.3
			0.68	13.9	13.6
			0.45	10.4	10.2
			0.28	7.6	6.9
SVB7	50/80	65	1.12	64.1	32.4
			0.91	44.7	26.4
			0.68	28.6	17.5
			0.45	19.6	12.3
			0.28	12.9	8.7
SVB8	60/70	65	1.12	34.3	25.6
			0.91	27.8	20.5
			0.68	22.7	15.2
			0.45	14.7	10.5
			0.28	9.5	7.2
SVB9	60/80	70	1.12	57.3	51.9
			0.91	44.6	40.7
			0.68	26.4	26.0
			0.45	17.0	16.8
			0.28	11.3	9.1
SVB10	70/80	75	1.12	43.8	42.6
			0.91	37.9	35.2
			0.68	26.6	26.0
			0.45	19.9	17.9
			0.28	13.9	11.9

6.4.1 Effect of Porosity

Fig. 6.14 displays the heat transfer coefficients of all the SVB samples categorised according to the overall nominal porosity for each water flow rate. There is no obvious general trend between the heat transfer coefficient and the overall porosity for all the water flow rates. Sample 40-80 showed the greatest heat transfer coefficient while sample 40-50 showed the lowest heat transfer coefficient for the range of water flow rates studied.

Fig. 6.15 compares the heat transfer coefficients of the SVB samples categorised according to the porosity of the first layer (layer closest to the water inlet) or the porosity of the second layer (layer closest to the water outlet). Figs. 6.15 a-b, 6.15 c-d, 6.15 e-f, 6.15 g-h and 6.15 i-j show the results of all SVB samples with 40%, 50%, 60% 70% and 80% porosity layer, respectively. The figures on the left show the effect of changing the porosity of the second layer and the figures on the right show the effect of changing the porosity of the first layer, while holding the porosity of the other layer constant. No general trend in the heat transfer coefficient can be observed when the porosity of one of the layers was increased.

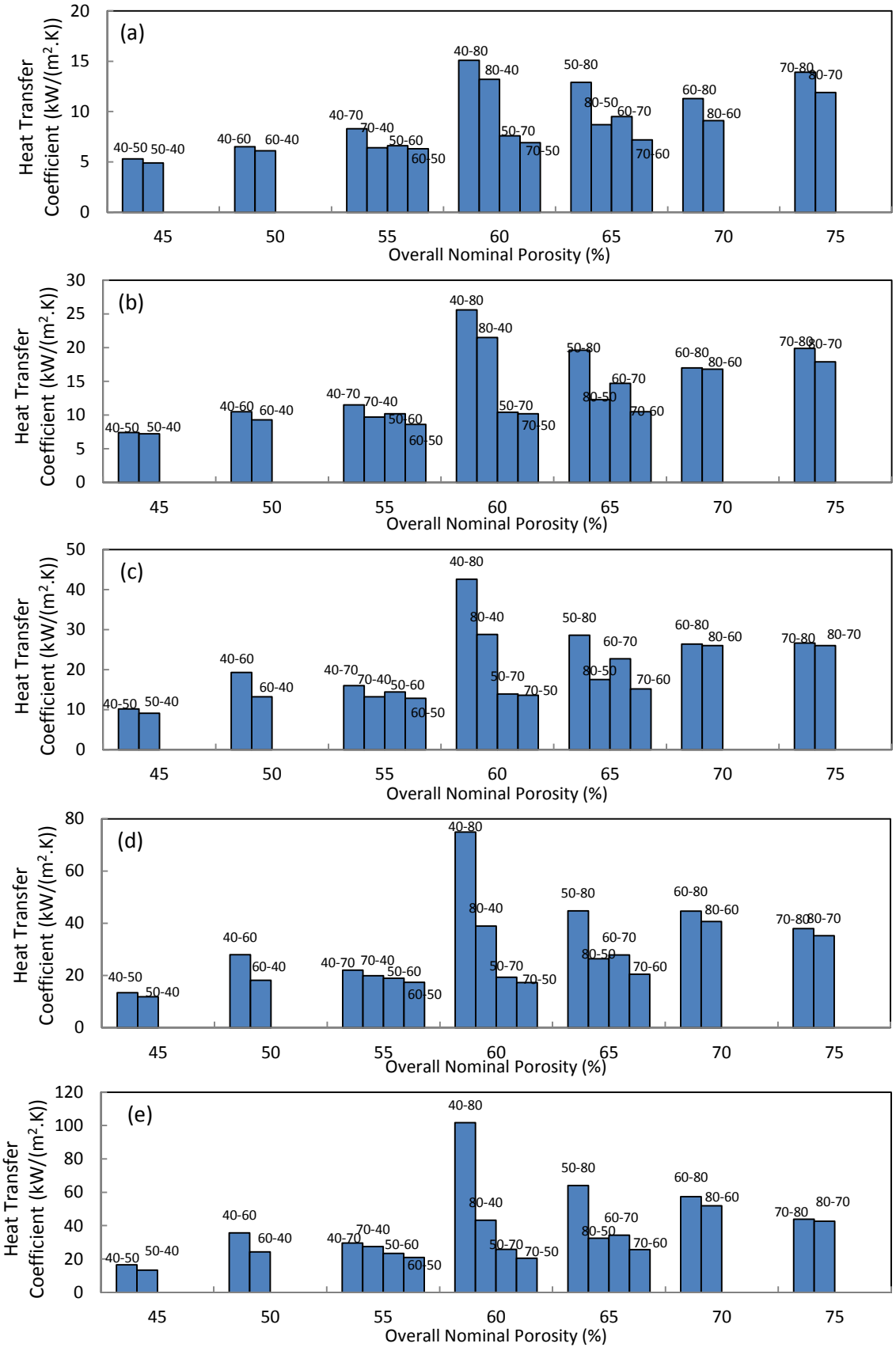

Figure 6.14: Variations in the heat transfer coefficient of LCS samples with SVB structures arranged according to the structure's overall nominal porosity for each water flow rate: a) 0.28 L/min, b) 0.45 L/min, c) 0.68 L/min, d) 0.91 L/min and e) 1.12 L/min.

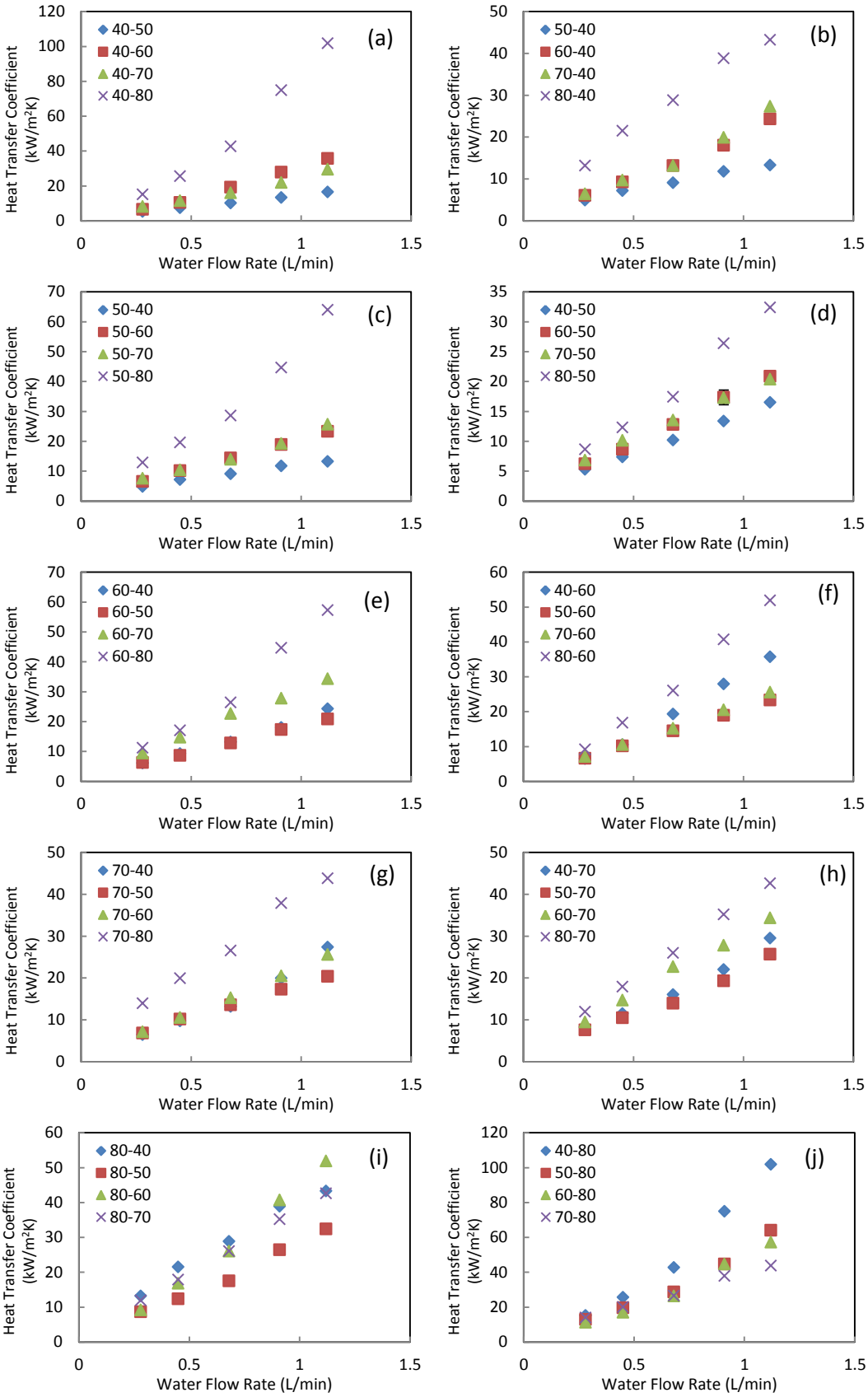

Figure 6.15: Variation in heat transfer coefficient with water flow rate for LCS samples with SVB structure categorised according to the nominal porosity of the first (left) or second (right) layer.

Similar to that observed in IVB structures, there seems to be an optimum combination of layer porosity for SVB structures at which the maximum heat transfer coefficient is displayed for each porosity category. Table 6.7 lists the optimum combination of layer porosity for each category. In general, introducing the high porosity layer (80%) resulted in the greatest heat transfer coefficient. It is also worth noting that the overall porosity of these optimum porosity combinations varied from 60% to 75%, which is slightly different from that found in the homogeneous and IVB structures (60% optimum overall porosity). This difference could be due to the presence of hard boundaries or gaps in the SVB structures.

Table 6.7: Optimum combination of layer porosity for samples with SVB structures.

Nominal Porosity of First Layer (%)	Optimum Combination	Nominal Porosity of Second Layer (%)	Optimum Combination
40	40-80	40	80-40
50	50-80	50	80-50
60	60-80	60	80-60
70	70-80	70	80-70
80	80-40 at Q= 0.28-0.68 L/min 80-60 at Q= 0.91-1.12 L/min	80	40-80

6.4.2 Effect of Orientation

Figs. 6.14 and 6.15 display the effect of the layer orientation on the heat transfer performance of LCS samples with SVB structures. For all the SVB samples studied in this section, having the lower porosity layer by the water inlet (L-H orientation) gave a higher heat transfer coefficient than having the higher porosity layer by the water inlet (H-L orientation).

Fig. 6.16 schematically illustrates the temperature distribution within the SVB structure. Since SVB structures were produced from two halved homogeneous layers, a “hard

boundary" exists between the layers. A gap may exist due to poor coupling, which acts as a large pore between the layers. The fluid in the first layer dwells in the boundary region when it approaches the second layer. The fluid entering the second layer is therefore pre-heated. To compensate the reduced temperature gradient, the second layer needs to have an increased surface area (Carpenter and da Silva 2014). The high porosity layer by the water outlet served this function and therefore, gave a better heat transfer performance.

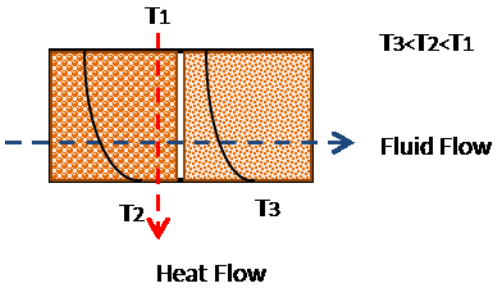

Figure 6.16: Heat transfer through the LCS segmented vertical bilayer structure showing the temperature profile.

6.4.3 Comparison with Other LCS Porous Structures

6.4.3.1 Comparison with Homogeneous Samples

Fig. 6.17 compares the heat transfer coefficients of LCS SVB structures with LCS homogeneous structures (H) according to the overall porosity of the structures for different water flow rates. In general, the heat transfer coefficients of SVB samples were higher than their homogeneous counterparts of similar overall porosity. This is because the combination of the layers within the SVB samples maximises heat removal by conduction and convection (Section 6.4.1). In addition, the presence of a gap (due to poor coupling) between the SVB layers can act as a large pore where fluid can dwell. Heat transfer by convection in the

vertical direction at the interface (gap) can therefore occur, which enhances the overall heat transfer performance of the SVB structure.

Comparative analysis according to the lower porosity layer (e.g. 40-50 vs H40) shows that the SVB structures have higher heat transfer coefficients than their homogeneous counterparts, especially at high water flow rates, because the higher porosity layer increases heat removal by convection (as discussed in Section 6.4.1). The difference in the heat transfer coefficients between the SVB and homogeneous structures becomes greater at higher water flow rates due to intensified convection.

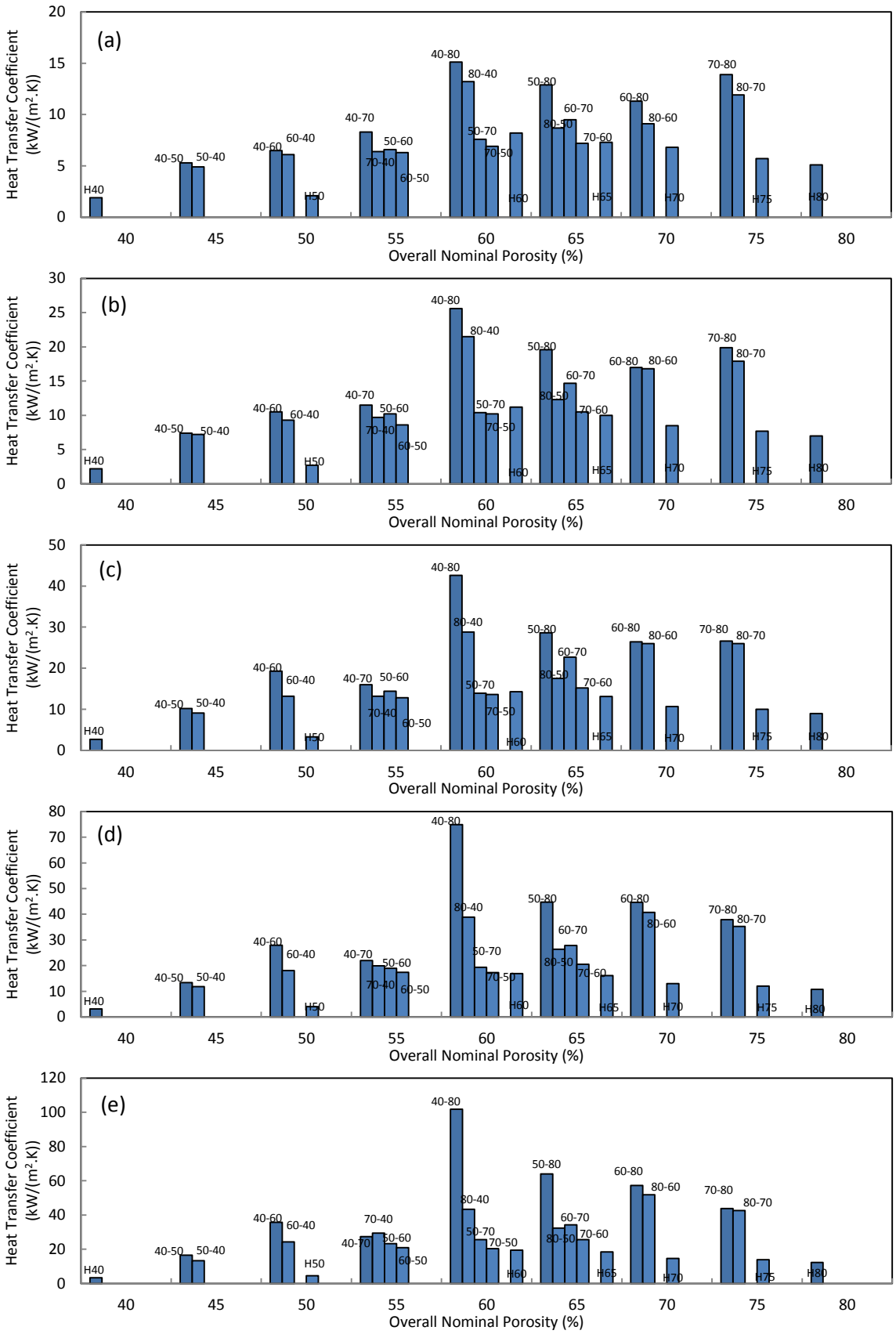

Figure 6.17: Variations in the heat transfer coefficient of LCS samples with SVB structures in comparison to homogeneous (H) samples for each water flow rate: a) 0.28 L/min, b) 0.45 L/min, c) 0.68 L/min, d) 0.91 L/min and e) 1.12 L/min.

6.4.3.2 Comparison with Integrated Vertical Bilayer Structures

Fig. 6.18 compares the heat transfer coefficients of SVB structures with IVB structures according to the nominal overall porosity of the structures for different water flow rates. For samples with L-H orientation, the SVB structures have greater heat transfer coefficients than their IVB counterparts for the range of water flow rates studied. For samples with H-L orientation, however, the same trend was not observed. Some IVB samples showed greater heat transfer performance than their SVB counterparts.

The biggest difference between the IVB and SVB structures is the presence of a hard boundary or gap between the layers in SVB structures. As shown in Section 5.6, the permeability of the whole SVB structure was insensitive to the presence of the hard boundary or gap. However, it seems that the effect of the boundary or gap on the heat transfer is significant, especially for SVB samples containing 80% porosity layer.

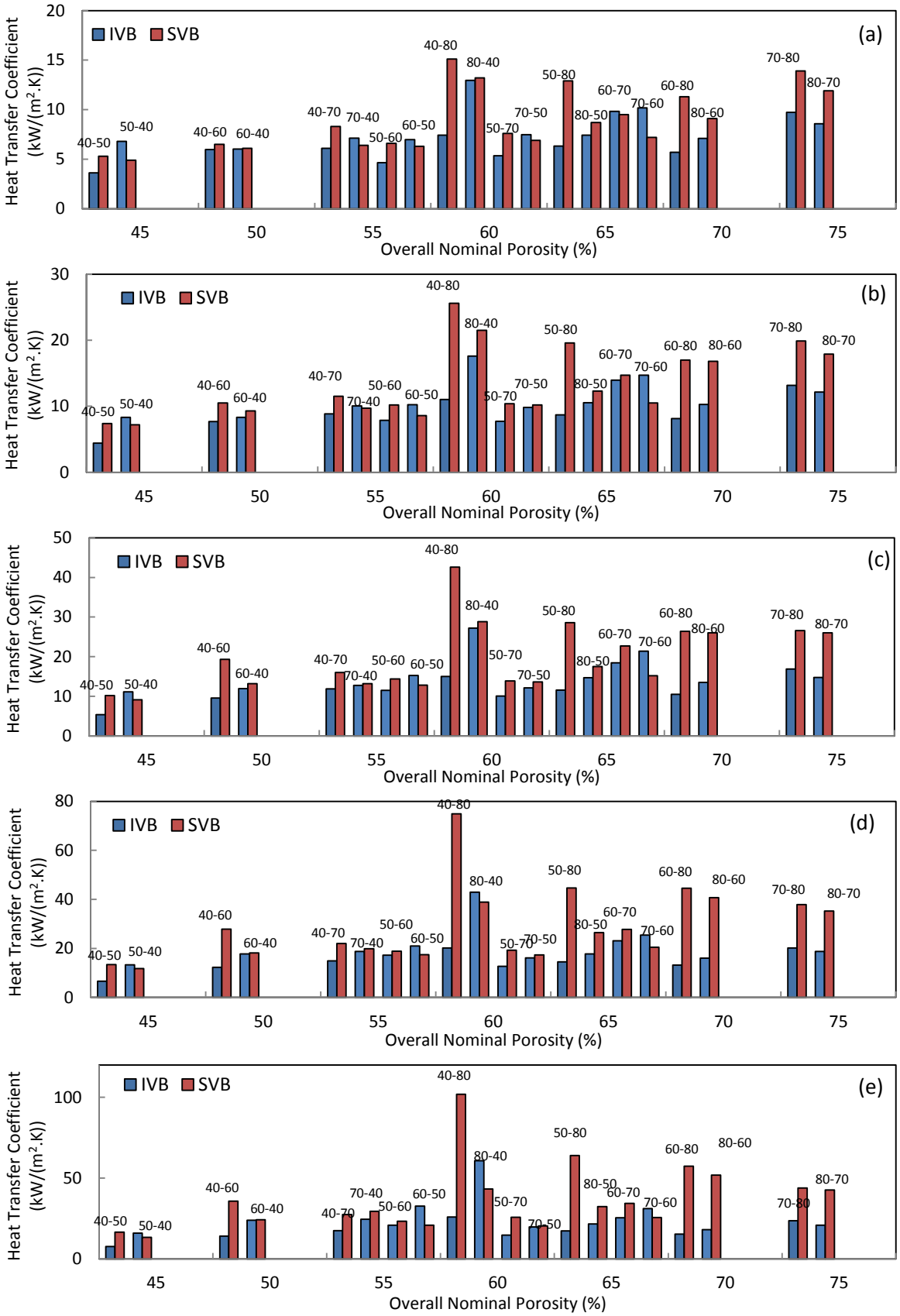

Figure 6.18: Comparison of the heat transfer coefficient of SVB structures with IVB structures for each water flow rate: a) 0.28 L/min, b) 0.45 L/min, c) 0.68 L/min, d) 0.91 L/min and e) 1.12 L/min.

The existence of a hard boundary or gap can enhance the heat transfer. Firstly, the gap increases the opportunity of the fluid to find alternative routes as the fluid enters the second layer. The warmed fluid can leave the sample quickly, optimising heat transfer. Secondly, the fluid can reside in the gap and enhance heat transfer by convection in the vertical direction. In the L-H orientation of the SVB structures, the high porosity second layer has a high surface area for heat transfer which compensates the reduced temperature gradient. The sum of these effects led to the large increase in the heat transfer coefficient of SVB structures with L-H orientation, in comparison to the H-L orientation and IVB structures.

The effect of the hard boundary on the heat transfer performance of the vertical bilayer samples was more prominent with layer orientation. In IVB structures, the H-L orientation gave a higher heat transfer performance. In SVB structures on the other hand, the L-H orientation performed better. For most samples (except samples 40-80, 50-80, 60-80 and 70-80), the heat transfer coefficients of IVB structures and SVB structures with H-L orientation were very similar, especially at higher water flow rates. This suggests that the effect of hard boundary in SVB structures may be very little when the layers are in the H-L orientation. This could be due to the more prominent effect of the lower porosity layer on the overall fluid flow when placed by the water outlet (Section 5.6), overshadowing the "hard boundary/gap effect". On the other hand, in an L-H orientation, the hard boundary follows the low porosity layer, so the effect of the hard boundary becomes more noticeable in SVB structures with L-H orientation.

6.5 Heat Transfer Coefficient of Samples with Multi-boundary Segmented Structures

The heat transfer coefficients of LCS porous copper with multi-boundary segmented structures (SS1-SS3), with all sections having the same porosity, were measured for water flow rates ranging from 0.28 L/min to 1.12 L/min. Only segmented structures (SS) with 40%, 50% and 60% nominal porosities were studied because the structural integrity becomes poor at very high porosities. The heat transfer results of these samples are summarised in Table 6.8.

Table 6.8: Heat transfer coefficients of LCS samples with multi-boundary segmented structures.

Sample Reference	Nominal Porosity (%)	Number of Sections	Flow Rate (L/min)	Heat Transfer Coefficient ($kW/m^2.K$)
SS1 A	40	1	1.12	3.4
			0.91	3.1
			0.68	2.7
			0.45	2.2
			0.28	1.9
SS1 B		2	1.12	13.0
			0.91	11.0
			0.68	9.0
			0.45	6.7
			0.28	4.8
SS1 C		6	1.12	41.9
			0.91	30.4
			0.68	23.7
			0.45	16.9
			0.28	10.9
SS2 A	50	1	1.12	4.6
			0.91	4.0
			0.68	3.3
			0.45	2.7
			0.28	2.1
SS2 B		2	1.12	16.6
			0.91	12.9
			0.68	9.9
			0.45	7.4
			0.28	5.2
SS2 C		6	1.12	56.2
			0.91	43.5
			0.68	28.1
			0.45	18.7
			0.28	11.0
SS3 A	60	1	1.12	19.5
			0.91	16.9
			0.68	14.3
			0.45	11.2
			0.28	8.2
SS3 B		2	1.12	26.4
			0.91	20.2
			0.68	14.8
			0.45	11.5
			0.28	8.3
SS3 C		6	1.12	64.7
			0.91	45.0
			0.68	30.9
			0.45	19.1
			0.28	10.9

Fig. 6.19 displays the heat transfer coefficients of the LCS porous copper samples with segmented structures (SS) categorised according to the number of sections present within the structure for each water flow rate. Fig. 6.20 plots the variation in heat transfer coefficients with water flow rate categorised according to the sample's nominal porosity.

Fig. 6.19 shows that increasing the porosity of the samples from 40% to 60% led to increase in the heat transfer coefficient for all water flow rates. Figs. 6.19 and 6.20 show that the heat transfer coefficient increased with increasing number of sections, which is more noticeable at higher water flow rates.

As the layers within the segmented structures have the same porosity, the increase in the heat transfer coefficient is mainly due to the increased number of hard boundaries (or gaps due to poor coupling). This suggests that the number of hard boundaries in the segmented structures has a significant influence on the overall heat transfer performance of the whole structure.

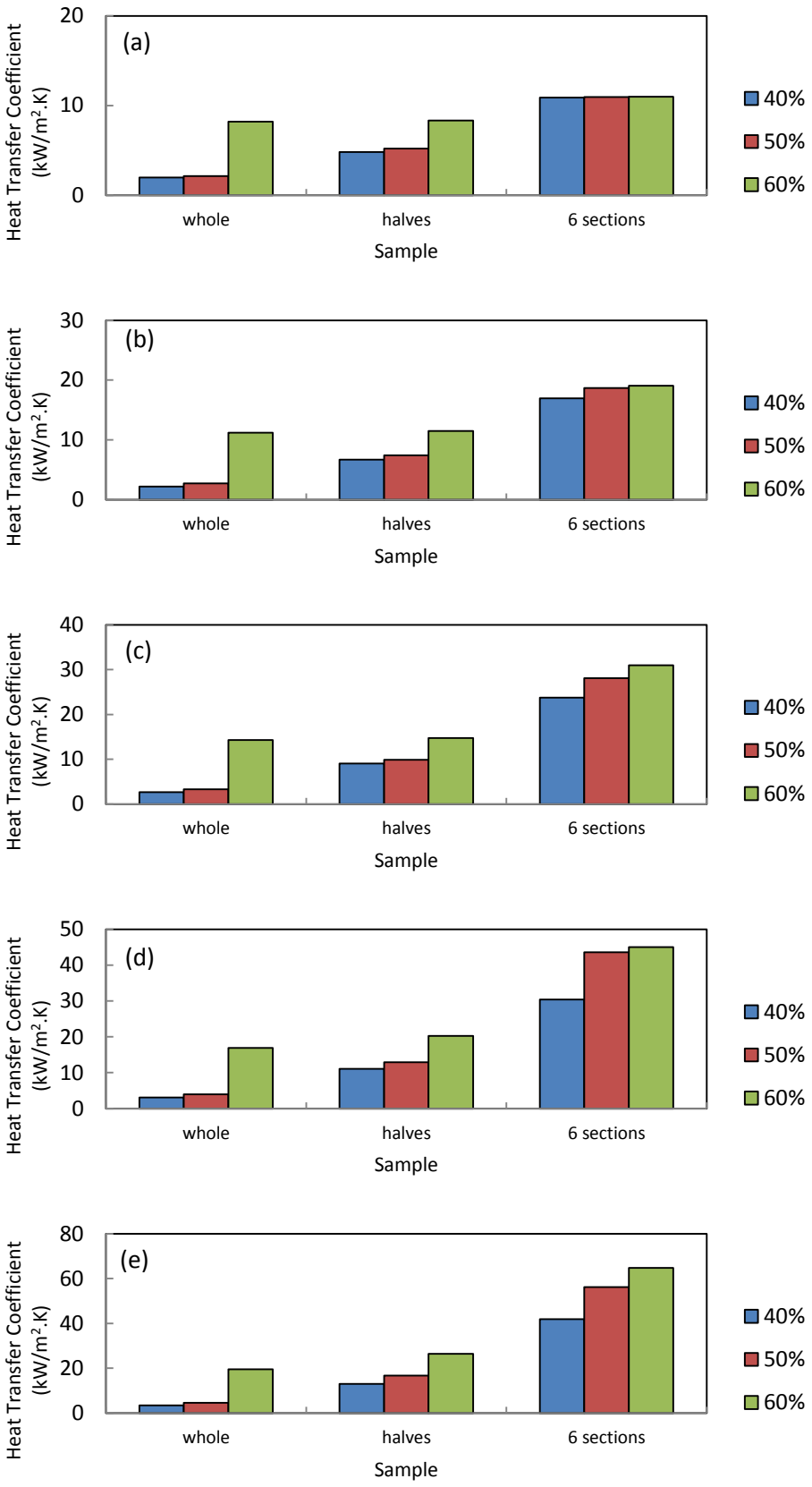

Figure 6.19: Variations in the heat transfer coefficient of LCS samples with SS structures arranged according to the number of sections present within the structure for each water flow rate: a) 0.28 L/min, b) 0.45 L/min, c) 0.68 L/min, d) 0.91 L/min and e) 1.12 L/min.

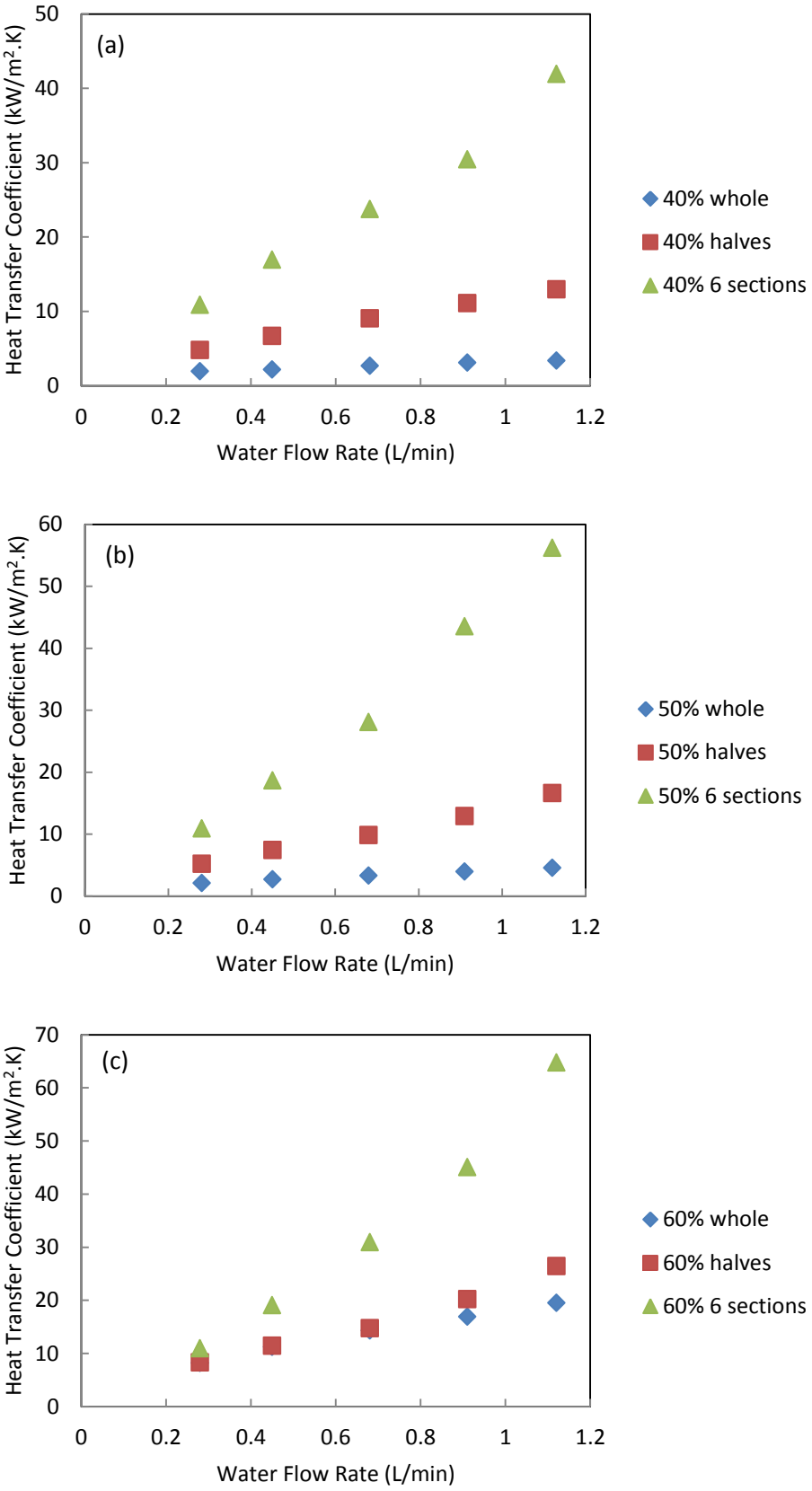

Figure 6.20: Variation in heat transfer coefficient with water flow rate for LCS segmented structures with different nominal porosities: a) 40%, b) 50% and c) 60%.

Fig. 6.21 schematically illustrates the temperature distribution within the SS structure. As discussed in Section 6.4, the gaps/hard boundaries between the layers act as a large pore where the fluid can reside and therefore, contribute to heat transfer by convection in the vertical direction. This contribution to the heat transfer is enhanced with increased number of gaps. Moreover, at high water flow rates, the convection effects in the hard boundary region are further enhanced, leading to more pronounced contribution to heat removal.

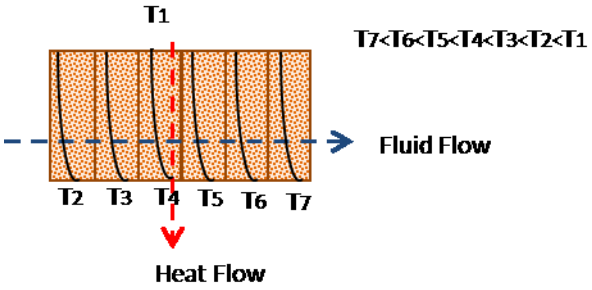

Figure 6.21: Heat transfer through the LCS multi-boundary segmented structure showing the temperature profile.

6.5.1 Comparison with Segmented Vertical Bilayer Structures

Fig. 6.22 compares the heat transfer coefficients of SVB samples with SS halved samples. In general, the heat transfer coefficients of SS samples with two sections are similar to their SVB counterparts.

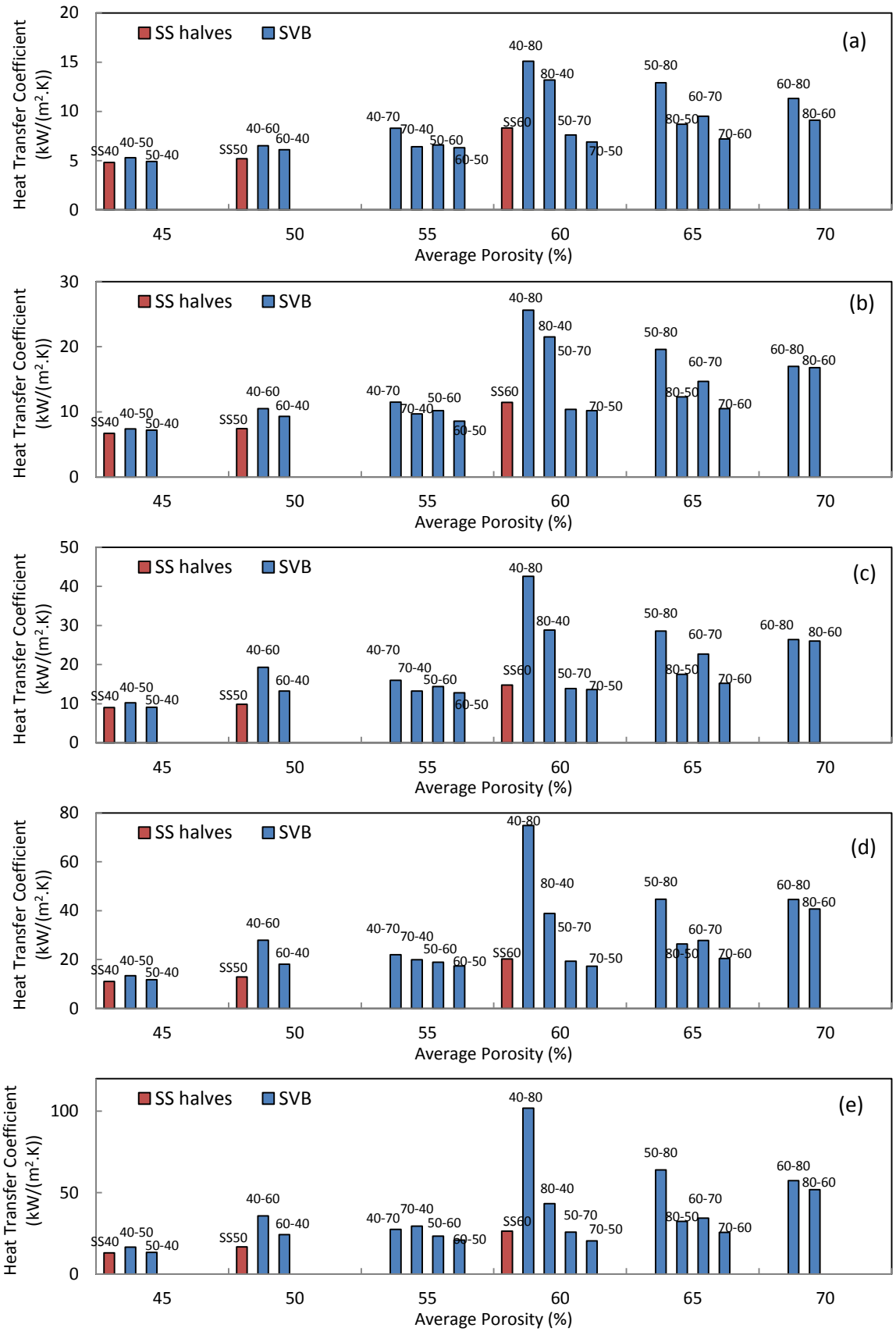

Figure 6.22: Comparison between the heat transfer coefficients of LCS segmented structures (halves) with SVB structures for each water flow rate: a) 0.28 L/min, b) 0.45 L/min, c) 0.68 L/min, d) 0.91 L/min and e) 1.12 L/min.

6.5.2 Comparison with Results in Literature

Very little attention has been given so far on the study of the heat transfer performance of porous media with structures containing soft or hard boundaries similar to that in SS, SVB and IVB structures. Only very few studies are currently available in the literature, amongst which were those conducted by Zaragoza and Goodall (2013) and Carpenter and da Silva (2014).

Zaragoza and Goodall (2013) found that the presence of gaps or hard boundaries decreased the heat transfer performance of segmented samples when compared to their integrated structure counterparts (soft boundary), using air as coolant. On the other hand, Carpenter and da Silva (2014) found that increasing the number of hard boundaries or gaps did not affect the heat transfer performance of segmented porous structures, using air as the coolant. These contradict the results presented in the current section.

The fluid used in the previous studies was air, whereas in this present study, water was used as the coolant. The fluid flow properties (form drag particularly) are more sensitive to water flow than air flow in LCS porous samples, as evident in Section 5.2. This means that even though the permeability coefficient of the LCS sample is a constant regardless of the fluid used, the form drag in the fluid flow is still influenced by the type of fluid. The form drag coefficients were higher in water flow than in air flow for LCS homogeneous samples (Section 5.2) and as a consequence, turbulence mixing is greater with water flow. Turbulence mixing enhances heat removal by convection, hence, for segmented LCS porous

structures, a higher heat transfer performance was achieved in comparison to their homogeneous counterparts.

Zaragoza and Goodall (2013) also reported that for segmented bilayer structures with hard boundaries, placing the more permeable layer by the air inlet and the less permeable layer by the air outlet led to greater heat transfer coefficient. Similarly, Carpenter and da Silva (2014) also reported the same trend in heat transfer with layer orientation for stacked bilayer samples containing hard boundaries. This contradicts the results for SVB structures in this study, wherein having the more permeable layer by the water outlet resulted in better heat transfer performance. This disagreement could be due to the differences in the structure of these porous media (Section 5.1.5) such that the effects of the hard boundary along with the already complex structure of the LCS samples are more prominent than the effect of the layer orientation in SVB structures.

On the other hand, placing the higher porosity layer (more permeable) by the water inlet gave a higher heat transfer coefficient for IVB structures (soft boundary) in this study (Section 6.3.2). This is in agreement to that reported by Zaragoza and Goodall (2013) for integrated porous bilayer samples with soft boundaries.

6.6 Heat Transfer Coefficient of Samples with Directional Porosity

The heat transfer coefficients of LCS porous copper samples with directional porosity (DP1-DP5) were measured for water flow rates ranging from 0.28 L/min to 1.12 L/min. The effect of adding four tubular channels on the overall heat transfer coefficient of the LCS samples with different nominal porosities were investigated. The heat transfer coefficients are summarised in Table 6.9 and displayed in Fig. 6.23.

Table 6.9: Heat transfer coefficients of LCS samples with directional porosity.

Sample Reference	Nominal Porosity (%)	Actual Porosity (%)	Flow Rate (L/min)	Heat Transfer Coefficient ($kW/m^2.K$)
DP1	40	54.4	1.12	26.6
			0.91	19.6
			0.68	15.3
			0.45	10.8
			0.28	7.7
DP2	50	63.8	1.12	36.7
			0.91	28.1
			0.68	19.6
			0.45	13.9
			0.28	8.2
DP3	60	67.1	1.12	66.7
			0.91	52.5
			0.68	42.7
			0.45	26.5
			0.28	17.0
DP4	70	75.3	1.12	38.6
			0.91	32.8
			0.68	27.2
			0.45	18.7
			0.28	13.0
DP5	80	82.3	1.12	36.7
			0.91	31.6
			0.68	24.4
			0.45	17.8
			0.28	12.6

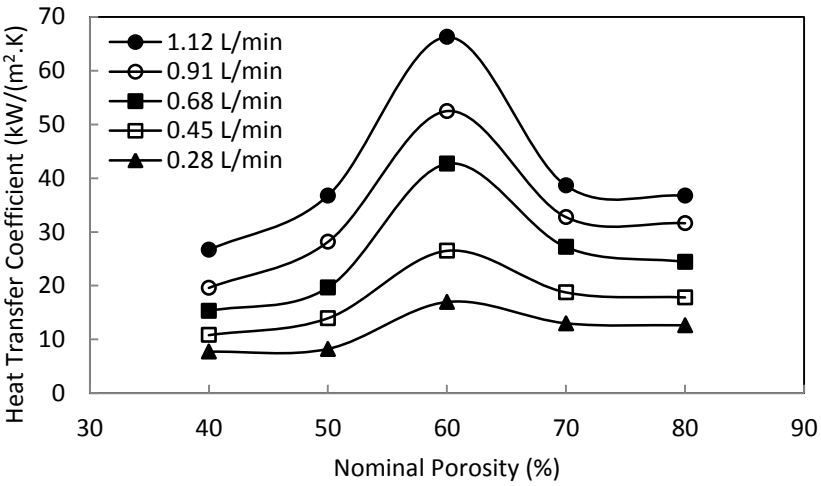

Figure 6.23: Variations in heat transfer coefficients with nominal porosity of LCS porous copper samples with directional porosity.

The heat transfer coefficient of the LCS samples with directional porosity (DP) increases with increasing water flow rate because more water is available to remove heat from the porous sample. Also apparent from Fig. 6.23 is the existence of an optimum porosity of 60% for heat transfer performance.

As discussed in Section 6.1.2, the sample's permeability to the coolant and thermal conductivity are the parameters which highly influence the overall heat transfer performance of the porous LCS samples. Fig. 6.24 schematically illustrates the temperature distribution within the LCS porous copper samples with directional porosity. For DP samples with low porosity, the thermal conductivity may be high due to the high volume of copper present; however, the heat transfer performance is limited by its relatively low permeability. Similarly, for DP samples with very high porosity, heat removal by convection may be high due to its high permeability, but heat transfer is limited by thermal conduction

since less copper is available within the sample to remove heat. Therefore, to achieve the maximum heat transfer performance, heat removal by conduction and convection within the sample must be balanced, which occurs at the point of optimum porosity.

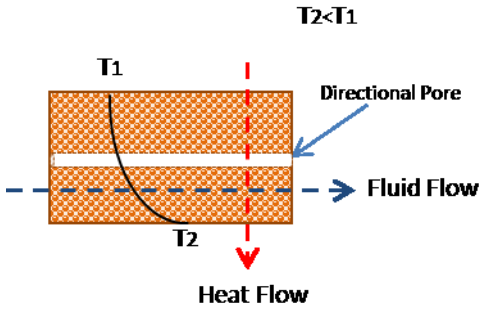

Figure 6.24: Heat transfer through the LCS porous copper sample with directional porosity showing the temperature profile.

6.6.1 Effect of Directional Porosity

Fig. 6.25 compares the heat transfer performance of LCS homogeneous copper with LCS samples with DP according to their nominal porosity. The heat transfer of LCS samples with DP is much greater than their homogeneous counterparts, especially at very high water flow rates. For low porosity samples (40%-50%), the heat transfer coefficient was improved by up to eight times when DP was introduced within the LCS structure. For higher porosity samples, a three-fold increase in the heat transfer performance was evident when DP was added to the LCS structure.

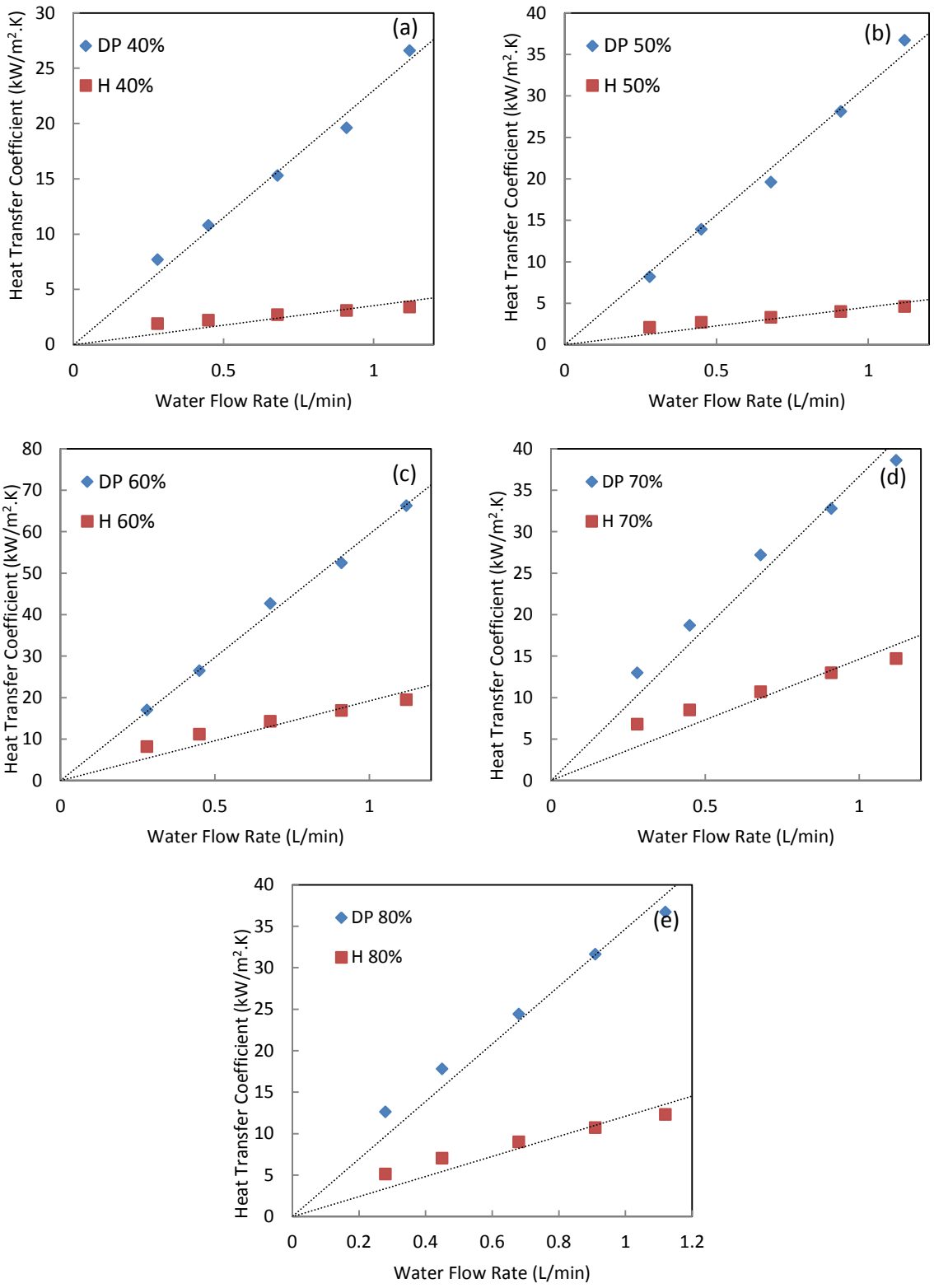

Figure 6.25: Comparison between the heat transfer coefficients of LCS homogeneous samples (H) and LCS samples with directional porosity (DP) of similar nominal porosity: a) 40%, b) 50%, c) 60%, d) 70% and e) 80%.

Fig. 6.26 shows that the trend in heat transfer coefficient as a function of nominal porosity is very similar to that found in LCS homogeneous samples. An optimum porosity of 60% was noticeable in both cases.

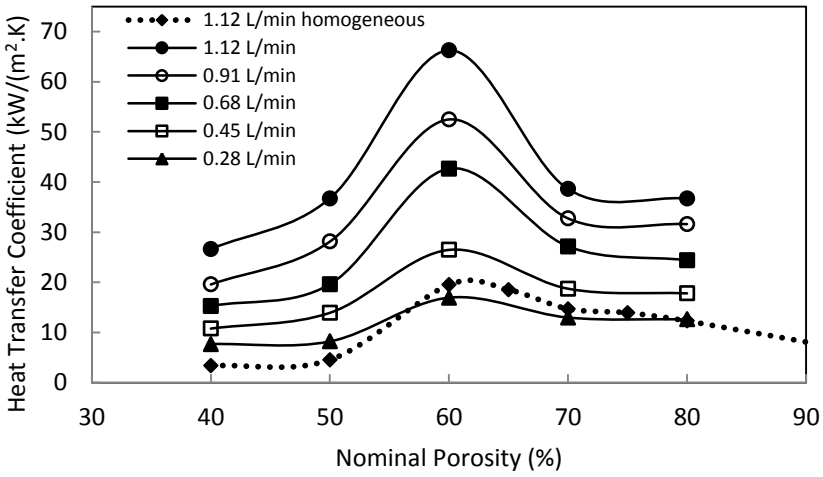

Figure 6.26: Comparison between the heat transfer coefficients of LCS homogenous samples and LCS samples with directional porosity categorised according to the nominal porosity.

Fig. 6.27 compares the heat transfer performance of LCS homogeneous samples (1.12 L/min water flow rate) with LCS samples with DP according to their actual porosity with tubular channels included. The optimum actual porosity for both structures are very similar. The trend in the heat transfer coefficient varied a little, especially at the lower actual porosity region. Nevertheless, for the same flow rate, the heat transfer coefficient of all the LCS samples with DP was greater than their homogeneous counterparts.

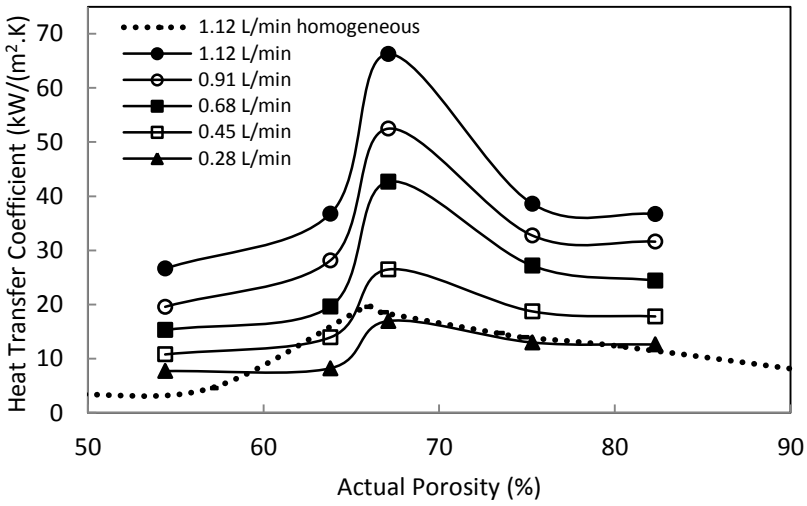

Figure 6.27: Comparison between the heat transfer coefficients of LCS homogenous samples and LCS samples with directional porosity categorised according to the actual porosity.

It is obvious from the results that the heat transfer performance of porous LCS copper was greatly improved when four tubular channels were introduced at the centre of the structure along the flow path. As shown in Section 5.8, the addition of the direct channels led to the increase in the permeability of the structure, and therefore higher heat removal by convection.

The direct tubular channels are only located at the centre of the structure and makes up a small fraction of the whole structure. The majority of the structure is still a homogenous structure. Similar to homogeneous structures, the heat transfer performance is still affected by the sample's porosity. Hence, an optimum porosity where heat transfer by thermal conduction and convection is maximised exists in LCS samples with directional porosity.

The advantage of utilising LCS samples with directional porosity is that for the same pumping power and water flow rate, a higher heat transfer performance than homogenous structures can be achieved, as evident in Figs. 6.26 and 6.27. This was because the addition of the direct tubular channels lowered the sample's overall resistance to the fluid flow with

very little reduction in the fraction of copper. Hence, the heat transfer was improved by increased permeability without compromising the sample's thermal conductivity.

6.6.2 Comparison with Other Porous Media

Currently, there is no report in the literature on the heat transfer performance of porous media with a similar structure to LCS samples with directional porosity. The porous structure currently available that offers directional porosity is lotus-type porous metal.

Muramatsu et al. (2013) reported that the heat transfer performance of lotus-type porous copper fins was higher than aluminium foam of 92% porosity using air as the coolant. A maximum heat transfer of 1.5 W/K per fin surface area was reported. Ogushi et al. (2006) and Chiba et al. (2011) reported that lotus-type porous copper heat sinks (ϕ = 39%, pore = 0.3 mm, fin thickness = 3 mm, fin gap = 5.5 mm, total width = 30 mm, total length = 20 mm, total height = 9 mm) have a heat transfer coefficient of 80 kW/m^2.K at a water flow velocity of 0.2 m/s, which was 1.7 times greater than micro-channels and 6.5 times greater than conventional fins of similar overall dimensions (Chiba et al. 2011).

In the present study, a maximum heat transfer coefficient of 66 kW/m^2.K was measured for LCS samples with directional porosity (sample DP3 at a water flow velocity of 0.2 m/s). This is close to the heat transfer performance reported by Chiba et al. (2011) and Ogushi et al. (2006). The performance of the LCS porous copper with DP could be better, considering that the LCS samples in this current study is only half as thick as the lotus-type porous copper heat sinks used in their study. However, due to the very different porous structure, comparative analysis between these two types of porous copper is difficult.

6.7 Summary

For all the structures studied in this chapter, the heat transfer performance increased with water flow rate since more water was available to remove heat. There also exists an "optimum porosity" for each structure, at which heat transfer by convection and conduction was balanced and therefore, the overall heat transfer was maximised.

For homogenous samples, an optimum porosity of 60% was found. The heat transfer coefficient was approximately four times greater than that of an empty channel (100% porosity). This demonstrates the suitability of LCS porous copper in thermal management applications.

For HB samples, the optimum heat transfer performance was influenced by the layer closest to the heat source. Having the higher porosity layer directly in contact with the heat source resulted in higher heat transfer performance. This was because more water can flow through the region close to the heat source. In general, the heat transfer performance of HB samples was inferior to their homogeneous counterparts. It is likely that the porosity of the HB structures studied was further from the "optimum porosity", while the porosity of their homogeneous counterparts was closer the "optimum porosity".

For IVB structures, optimum combinations of layer porosity were evident for each porosity category. The optimum porosity combination is equivalent to an overall porosity in the range of 55% to 65%, which is similar to that found in homogeneous samples (60%). In

addition, the H/L orientation gave a higher heat transfer coefficient than the L/H orientation. In the H/L orientation, the fluid slows down as it approaches the low porosity region from the high porosity region. Therefore, the fluid dwells longer in the high porosity region and turbulence mixing occurs, increasing the convective heat transfer. In general, when compared according to the lower porosity layer (e.g. 40-50 vs H40), the IVB structures have higher heat transfer coefficients than their homogeneous counterparts. This was because the second layer of the IVB structure has a higher porosity, increasing the overall porosity of the sample towards the optimum porosity.

Optimum combinations of layer porosity were also evident for each porosity category in SVB structures. However, the optimum porosity combination in SVB structures was due to the presence of the high porosity 80% layer allied with the presence of a hard boundary (or gap due to poor coupling) between the layers. The existence of a hard boundary enhances the heat transfer by increasing the opportunity of the fluid 1) to find alternative routes as the fluid enters the second layer, and 2) to reside in the gap and contribute to heat transfer by convection in the vertical direction. For all the SVB samples studied in this section, having the L-H orientation gave a higher heat transfer coefficient than the H-L orientation. In the L-H orientation of the SVB structures, the high porosity second layer has a high surface area for heat transfer which compensates the reduced temperature gradient. This, along with the "hard boundary effect", led to the greater heat transfer coefficient of SVB structures with L-H orientation, in comparison to the H-L orientation and their IVB and homogeneous counterparts.

For the multi-boundary segmented structures, it was obvious that the existence of hard boundaries within the LCS structure greatly improved the heat transfer performance, due to enhanced heat removal by convection. As a consequence, increasing the number of gaps present within the sample led to very high heat transfer coefficients in comparison to their homogeneous counterparts.

Similar to homogenous samples, an optimum nominal porosity of 60% was observed for samples with DP. However, much higher heat transfer coefficients were measured for LCS samples with DP. The direct tubular channels increased the permeability of the structure to the coolant flow hence, increasing heat removal by convection. For low porosity samples (40%-50%), an eight-fold increase in the heat transfer performance was evident when DP was added to the LCS porous structure, in comparison to their homogeneous counterpart. For higher porosity samples, the heat transfer coefficient was improved by up to three times when DP was introduced within the LCS porous structure.

Chapter 7 Conclusions and Future Work

7.1 Conclusions

Porous copper samples with different pore structures were manufactured using the LCS process. The copper powder (base metal) particle size ranged between 50-150 µm, while the potassium carbonate (pore former) particle size ranged between 250-1500 µm. The samples were categorised to four different pore size ranges: 250-425 µm, 425-710 µm, 710-1000 µm and 1000-1500 µm. Six different structures: homogeneous (H), horizontal bilayer (HB), integrated vertical bilayer (IVB), segmented vertical bilayer (SVB), multi-boundary segmented structures (SS) and structures with directional porosity (DP), were manufactured. Their structural, fluid flow and heat transfer properties were investigated. Table 7.1 summarises the main characteristics of each structure, and its effect on the overall permeability and heat transfer performance.

Table 7.1: Effects of the structure on the fluid flow and heat transfer.

Structure	Description	Effect on Permeability	Effect on Heat Transfer
Homogeneous	Uniform distribution of porosity throughout the sample	Permeability increased with increasing porosity since there is less copper walls impeding fluid flow	Optimum porosity of 60% was observed, offering four times greater heat transfer than an empty channel (100% porosity)
Horizontal Bilayer	Two integrated layers with different porosities parallel to fluid flow	Majority of the flow passed through the high porosity region	Placing the higher porosity layer next to the heater led to higher heat transfer since more water can flow though the region closer to the heat source
Integrated Vertical Bilayer	Two integrated layers with different porosities perpendicular to fluid flow	Permeability was limited by the lower porosity layer	The H-L orientation gave higher heat transfer since the fluid can dwell longer in the high porosity region, allowing turbulence mixing.
Segmented Vertical Bilayer	Two segmented layers with different porosities perpendicular to fluid flow	Permeability was limited by the lower porosity layer and the presence of a hard boundary had negligible effect on the overall permeability.	The L-H orientation performed better since heat removal by convection was enhanced by both the high porosity second layer and the presence of a hard boundary
Multi-boundary Segmented Structure	Segmented layers with the same porosity	The increasing number of hard boundaries (gaps) had negligible effect on the overall permeability.	Increasing the number of hard boundaries enhanced heat transfer by convection in the vertical direction.
Directional Porosity	Homogeneous structure with the addition of four directional pores parallel to fluid flow	Directional pores increased the sample's permeability to fluid flow, in comparison to homogeneous samples.	The directional pores increased the heat transfer by convection.

7.1.1 Structural Properties of LCS Porous Copper

The topography, macrostructure and microstructure of the LCS porous copper were analysed using optical microscope and SEM. The as-produced samples were of similar size as the mould used during the compaction and kept their shape during sintering. The pore morphology closely resembled that of the potassium carbonate powder, proving the capability of the LCS process in producing porous samples with controlled pore size and pore shape. Necking between the copper particles was also observed, which ensured good mechanical strength of the porous metal matrix. The smaller cavities/voids between the

copper particles (inter-particle pores) allowed the interconnection of the larger pores produced by the space-holder (potassium carbonate). The presence of these voids increased the sample's overall porosity. As a consequence, the actual porosities measured by the direct-volume and Archimedes methods were greater than the nominal porosities for all the homogeneous samples.

7.1.2 Fluid Flow in LCS Porous Copper

The permeability of the LCS porous copper was measured using a purpose-built apparatus. The pressure drop increased with increasing fluid flow velocity, fitting well with Forchheimer's equation. Both air and water permeabilities were found to be independent of the sample's length.

For homogeneous structures, the permeability increased and the form drag coefficient decreased with increasing porosity and decreasing pore size. The flow was stratified in the HB structures such that the majority of the flow passed through the higher porosity layer, leading to higher permeabilities than their homogeneous counterparts. For both IVB and SVB structures, the permeability was largely limited by the lower porosity layer and the presence of the boundary between the layers led to higher form drag coefficients. For both SVB and SS samples, the presence of the hard boundaries had negligible effect on the overall permeability. The addition of open tubular channels or directional porosity (DP) in homogeneous structures led to much greater permeability and lower form drag coefficients.

7.1.3 Heat Transfer Coefficient of LCS Porous Copper

The heat transfer performance of the LCS porous copper samples was characterised by the heat transfer coefficient measured using a purpose-built apparatus. With increasing water flow rate, the heat transfer coefficient increased for all the structures studied. An optimum porosity was observed for all the structures, where heat transfer by convection and conduction is balanced, maximising the overall heat transfer.

For homogeneous structures, an optimum porosity of 60% was observed (425-710 µm pore size), which offered four times greater heat transfer than an empty channel (100% porosity). For HB samples, having the higher porosity layer next to the heater resulted in higher heat transfer performance since more water can flow though the region closer to the heat source. The heat transfer performance of HB structures was lower than their homogeneous counterparts with the same overall porosity. For IVB structures, the optimum porosity combinations fell within the overall porosity range of 55% - 65%. The H/L orientation gave a higher heat transfer coefficient than the L/H orientation. This was because the fluid dwells longer in the high porosity region and turbulence mixing occurs, increasing the convective heat transfer. For SVB structures, the presence of the 80% layer allied with the hard boundary led to better heat transfer performance. The L-H orientation offered better heat transfer because the high porosity second layer has a higher surface area for heat transfer, which compensates the reduced temperature gradient. The existence of a gap at the hard boundary can enhance the heat transfer by convection in the vertical direction. In general, the vertical bilayer structures (IVB and SVB) have higher heat transfer coefficients than their homogeneous counterparts because increased flow turbulence and mixing at the boundary

enhanced the heat transfer by convection. Multi-boundary segmented structures had higher heat transfer coefficients than the homogeneous structures, and increasing the number of hard boundaries increased the overall heat transfer performance. The addition of open tubular channels in homogeneous structures (DP) led to a three- to eight-fold increase in the heat transfer performance in comparison to their homogeneous counterparts. The direct tubular channels increased the permeability of the structure to the coolant flow and hence, increased heat removal by convection.

The results of this study showed that the structural, fluid flow and heat transfer properties of the LCS porous copper can be altered by developing tailored, non-homogeneous structures. Apart from the HB structures, the non-homogeneous structures studied in this work offered a better heat transfer performance than their homogeneous counterparts.

7.2 Future Work

The LCS process is a versatile process which allows the development of porous metals with controlled structural parameters (i.e. porosity, pore size and pore shape). This study only focused on spherical pores and the effect of varying the pore size was only investigated for homogeneous LCS structures. The effect of varying the pore shape on the fluid flow and heat transfer performance of the LCS porous copper can be investigated in the future. For non-homogeneous samples, the effect of changing the pore size of the layers on the overall fluid flow and heat transfer performance can also be studied.

Theoretical modelling of the fluid flow and heat transfer performance of the LCS porous copper with homogeneous and tailored structures would also be beneficial. This would allow increased understanding of the fluid dynamics and heat transfer mechanisms by conduction and convection within the complex LCS porous structure. Heat transfer performance predictions for other structures not considered in this study would also be feasible, allowing rapid development of LCS porous structures with excellent thermal exchange properties.

The process parameters for the production of the non-homogeneous LCS structures can be optimised further to produce higher quality samples. In particular, for the LCS copper with directional porosity, the design of the directional pores (i.e. diameter, orientation and shape) can be optimised to further enhance the heat transfer performance.

In addition, the heat transfer performance of the existing porous metals in literature can be investigated using the same experimental set-up. This would allow more accurate evaluation of the results and better comparative analysis.

References

Alkan, H. 2009. Percolation model for dilatancy-induced permeability of the excavation damaged zone in rock salt. *International Journal of Rock Mechanics and Mining Sciences,* 46**,** 716-724.

Ashby, M. & Gibson, L. 1998. *Cellular Solids Technology,* Oxford, Pergamon Press.

Ashby, M. F., Evans, A. G., Fleck, N. A., Gibson, L. J., Hutchinson, J. W. & Wadley, H. N. G. 2000. *Metal Foams: A Design Guide,* Burlington, Butterworth-Heinemann.

Babcsan, N., Leitimeier, D. & Banhart, J. B. 2005. Metal foams - high temperature colloids - Part I. Ex situ analysis of metal foams. *Colloids and Surfaces a-Physicochemical and Engineering Aspects,* 261**,** 123-130.

Babcsán, N., Mészáros, I. & Hegman, N. 2003. Thermal and electrical conductivity measurements on aluminum foams. *Materialwissenschaft und Werkstofftechnik,* 34**,** 391-394.

Banhart, J. 2001. Manufacture, characterisation and application of cellular metals and metal foams. *Progress in Materials Science,* 46**,** 559.

Banhart, J., Ashby, M. & Fleck, N. 1999. *Metal foams and porous metal structures,* Germany, MIT Publishing, Breman.

Baril, E., Mostafid, A., Lefebvre, L. P. & Medraj, M. 2008. Experimental demonstration of entrance/exit effects on the permeability measurements of porous materials. *Advanced Engineering Materials,* 10**,** 889-894.

Bayles, G. A., Klinzing, G. E. & Chiang, S. H. 1989. Fractal mathematics applied to flow in porous systems. *Particle & Particle Systems Characterization,* 6**,** 168-175.

Bejan, A. 2004. Designed porous media: maximal heat transfer density at decreasing length scales. *International Journal of Heat and Mass Transfer,* 47**,** 3073-3083.

Bethke, C. M. 1985. A numerical-model of compaction-driven groundwater-flow and heat-transfer and its application to the paleohydrology of intracratonic sedimentary basins. *Journal of Geophysical Research-Solid Earth and Planets,* 90**,** 6817-6828.

Bhattacharya, A., Calmidi, V. V. & Mahajan, R. L. 2002. Thermophysical properties of high porosity metal foams. *International Journal of Heat and Mass Transfer,* 45**,** 1017-1031.

Blick, E. F. & Civan, F. 1988. Porous-media momentum equation for highly accelerated flow. *SPE Reservoir Engineering,* 3**,** 1048-1052.

Bonnet, J. P., Topin, F. & Tadrist, L. 2008. Flow laws in metal foams: compressibility and pore size effects. *Transport in Porous Media,* 73**,** 233-254.

Boomsma, K. & Poulikakos, D. 2001a. The effects of compression and pore size variations on the liquid flow characteristics in metal foams. *Journal of Fluids Engineering,* 124**,** 263-272.

Boomsma, K. & Poulikakos, D. 2001b. On the effective thermal conductivity of a three-dimensionally structured fluid-saturated metal foam. *International Journal of Heat and Mass Transfer,* 44**,** 827-836.

Boomsma, K., Poulikakos, D. & Zwick, F. 2003. Metal foams as compact high performance heat exchangers. *Mechanics of Materials,* 35**,** 1161-1176.

Bourantas, G. C., Skouras, E. D., Loukopoulos, V. C. & Burganos, V. N. 2014. Heat transfer and natural convection of nanofluids in porous media. *European Journal of Mechanics B-Fluids,* 43**,** 45-56.

Bram, M., Stiller, C., Buchkremer, H. P., Stover, D. & Baur, H. 2000. High-porosity titanium, stainless steel, and superalloy parts. *Advanced Engineering Materials,* 2**,** 196-199.

Calmidi, V. V. & Mahajan, R. L. 1999. The effective thermal conductivity of high porosity fibrous metal foams. *Journal of Heat Transfer-Transactions of the Asme,* 121**,** 466-471.

Carman, P. C. 1956. *Flow of gases in porous media*, UK, Butterworth's London.

Carpenter, K. P. & Da Silva, A. K. 2014. A combined hydro-thermal characterization of high-porosity metal foam test sections with discrete pore-size gradients. *International Journal of Heat and Mass Transfer,* 77**,** 770-776.

Chiba, H., Ogushi, T. & Nakajima, H. 2011. Development of heat sinks for air cooling and water cooling using lotus-type porous metals ASME/JSME 2011 8th Thermal Engineering Joint Conference, March 13–17, 2011 Honolulu, Hawaii, USA. T10142-T10142-9.

Cornell, D. & Katz, D. L. 1953. Flow of gases through consolidated porous media. *Industrial and Engineering Chemistry,* 45**,** 2145-2152.

Costa, A. 2006. Permeability-porosity relationship: A re-examination of the Kozeny-Carman equation based on a fractal pore-space geometry assumption. *Geophysical Research Letters,* 33.

Dai, Z., Nawaz, K., Park, Y. G., Bock, J. & Jacobi, A. M. 2010. Correcting and extending the Boomsma-Poulikakos effective thermal conductivity model for three-dimensional, fluid-saturated metal foams. *International Communications in Heat and Mass Transfer,* 37**,** 575-580.

Darcy, H. 1856. *Les fontaines publiques de la ville de dijon,* Paris, Dalmont.

Davis, P. A., Olague, N. E. & Goodrich, M. T. 1992. Application of a validation strategy to Darcy's experiment. *Advances in Water Resources,* 15**,** 175-180.

Despois, J. F. & Mortensen, A. 2005. Permeability of open-pore microcellular materials. *Acta Materialia,* 53**,** 1381-1388.

Diao, K. K., Xiao, Z. & Zhao, Y. Y. 2015. Specific surface areas of porous Cu manufactured by Lost Carbonate Sintering: Measurements by quantitative stereology and cyclic voltammetry. *Materials Chemistry and Physics,* 162**,** 571-579.

Dienes, J. K. 1983. Permeability, percolation and statistical crack mechanics. Proceedings of the 23rd Symposium on Rock Mechanics, American Institute of Mining, Mettalurgy & Petroleum Engineers, New York, USA, 86.

Ding, X. R., Lu, L. S., Chen, C., He, Z. S. & Ou, D. S. 2011. Heat transfer enhancement by using four kinds of porous structures in a heat exchanger. *Advances in Mechanical Engineering, Pts 1-3,* 52-54**,** 1632-1637.

Du, M., Zhang, H. W., Li, Y. X., Liu, Y., Chen, X. & He, Y. 2015. Fabrication and wettability of monolithic bimodal porous Cu with Gasar macro-pores and dealloying nano-pores. *Applied Surface Science,* 353**,** 804-810.

Du Plessis, J. P. & Masliyah, J. 1988. Mathematical modelling of flow through consolidated isotropic porous media. *Transport in Porous Media,* 3**,** 145-161.

Dukhan, N. 2013. *Metal foams : fundamentals and applications*, Lancaster, PA : DEStech Publications, Inc., 2013.

Dukhan, N. & Ali, M. 2012. Strong wall and transverse size effects on pressure drop of flow through open-cell metal foam. *International Journal of Thermal Sciences,* 57**,** 85-91.

Dukhan, N., Bagci, O. & Ozdemir, M. 2014. Metal foam hydrodynamics: flow regimes from pre-Darcy to turbulent. *International Journal of Heat and Mass Transfer,* 77**,** 114-123.

Dukhan, N. & Patel, P. 2008. Equivalent particle diameter and length scale for pressure drop in porous metals. *Experimental Thermal and Fluid Science,* 32**,** 1059-1067.

Eisenmann, M. 1998. *ASM Handbook,* USA ASM International.

Ejlali, A., Ejlali, A., Hooman, K. & Gurgenci, H. 2009. Application of high porosity metal foams as air-cooled heat exchangers to high heat load removal systems. *International Communications in Heat and Mass Transfer,* 36**,** 674-679.

Ergun, S. 1952. Fluid flow through packed columns. *Chemical Engineering Progress,* 48**,** 89-94.

Farkas, T., Zhong, G. M. & Guiochon, G. 1999. Validity of Darcy's law at low flow-rates in liquid chromatography. *Journal of Chromatography A,* 849**,** 35-43.

Faulkner, D. R. & Rutter, E. H. 2000. Comparisons of water and argon permeability in natural clay-bearing fault gouge under high pressure at 20 degrees C. *Journal of Geophysical Research-Solid Earth,* 105**,** 16415-16426.

Fujibayashi, S., Neo, M., Kim, H. M., Kokubo, T. & Nakamura, T. 2004. Osteoinduction of porous bioactive titanium metal. *Biomaterials,* 25**,** 443-50.

Furbish, D. J. 1997. *Fluid physics in geology: An introduction to fluid motions on Earth's surface and within its crust*, Oxford University Press Oxford.

Garboczi, E. J. 1990. Permeability, diffusivity, and microstructural parameters: a critical review. *Cement and Concrete Research,* 20**,** 591-601.

Geertsma, J. 1974. Estimating the coefficient of inertial resistance in fluid flow through porous media. *Society of Petroleum Engineers Journal,* 14**,** 445-450.

Ghabezloo, S., Sulem, J. & Saint-Marc, J. 2009. Evaluation of a permeability-porosity relationship in a low-permeability creeping material using a single transient test. *International Journal of Rock Mechanics and Mining Sciences,* 46**,** 761-768.

Ghosh, I. 2009. How good is open-cell metal foam as heat transfer surface? *Journal of Heat Transfer,* 131**,** 101004.

Gibson, A. G. 1992. Modification of Darcy's law to model mould interface effects in composites processing. *Composites Manufacturing,* 3**,** 113-118.

Gladysz, G. M. & Chawla, K. K. 2015. *Voids in materials: from unavoidable defects to designed cellular materials,* Netherlands, Elsevier.

Hakamada, M., Kuromura, T., Chino, Y., Yamada, Y., Chen, Y. Q., Kusuda, H. & Mabuchi, M. 2007. Monotonic and cyclic compressive properties of porous aluminum fabricated by spacer method. *Materials Science and Engineering a-Structural Materials Properties Microstructure and Processing,* 459**,** 286-293.

Harte, A. M., Fleck, N. A. & Ashby, M. F. 1999. Fatigue failure of an open cell and a closed cell aluminium alloy foam. *Acta Materialia,* 47**,** 2511-2524.

Hassanizadeh, S. M. & Gray, W. 1987. High velocity flow in porous media. *Transport in Porous Media,* 2**,** 521-531.

Ho, C. K. & Webb, S. W. 2006. *Gas transport in porous media,* Netherlands, Springer.

Hunt, M. L. & Tien, C. L. 1988. Effects of thermal dispersion on forced convection in fibrous media. *International Journal of Heat and Mass Transfer,* 31**,** 301-309.

Hutter, C., Buchi, D., Zuber, V. & Von Rohr, P. R. 2011. Heat transfer in metal foams and designed porous media. *Chemical Engineering Science,* 66**,** 3806-3814.

Hwang, J. J., Hwang, G. J., Yeh, R. H. & Chao, C. H. 2001. Measurement of interstitial convective heat transfer and frictional drag for flow across metal foams. *Journal of Heat Transfer,* 124**,** 120-129.

Incropera F, Dewitt D, Bergman T & A, L. 2007. *Introduction to heat transfer,* USA, John Wiley & Sons.

Jin, I., Kenny, L. D. & Sang, H. 1990. PCT Patent WO 91/03578.

Jones, S. C. 2013. A rapid accurate unsteady-state Klinkenberg permeameter. *Society of Petroleum Engineers Journal,* 12**,** 383-397.

Kaviany, M. 1995. *Principles of heat transfer in porous media,* New York, Springer.

Kececioglu, I. & Jiang, Y. X. 1994. Flow through porous-media of packed spheres saturated with water. *Journal of Fluids Engineering-Transactions of the ASME,* 116**,** 164-170.

Kenny, L. D. & Thomas, M. 1994. PCT Patent WO 94/09931.

Khayargoli, P., Loya, V., Lefebvre, L. P. & Medraj, M. The impact of microstructure on the permeability of metal foams. CSME forum, 2004. 220-228.

Kim, S. Y., Paek, J. W. & Kang, B. H. 2000. Flow and heat transfer correlations for porous fin in a plate-fin heat exchanger. *Journal of Heat Transfer-Transactions of the ASME,* 122**,** 572-578.

Klinkenberg, L. J. 1941. The permeability of porous media to liquids and gases. Drilling and production practice. *American Petroleum Institute*.

Li, D. & Engler, T. W. 2001. Literature review on correlations of the non-Darcy coefficient. *Society of Petroleum Engineers*.

Li, J., Yang, Q. M. & Zhitornirsky, I. 2008. Nickel foam-based manganese dioxide-carbon nanotube composite electrodes for electrochemical supercapacitors. *Journal of Power Sources,* 185**,** 1569-1574.

Li, P., Petrinic, N., Siviour, C. R., Froud, R. & Reed, J. M. 2009. Strain rate dependent compressive properties of glass microballoon epoxy syntactic foams. *Materials Science and Engineering a-Structural Materials Properties Microstructure and Processing,* 515**,** 19-25.

Liu, J. F., Wu, W. T., Chiu, W. C. & Hsieh, W. H. 2006. Measurement and correlation of friction characteristic of flow through foam matrixes. *Experimental Thermal and Fluid Science,* 30**,** 329-336.

Liu, P. S. 2010. A new method for calculating the specific surface area of porous metal foams. *Philosophical Magazine Letters,* 90**,** 447-453.

Liu, P. S. & Chen, G. F. 2014. Chapter 1 - General introduction to porous materials. *Porous Materials.* Boston: Butterworth-Heinemann.

Liu, X., Civan, F. & Evans, R. D. 1995. Correlation of the non-Darcy flow coefficient. *Journal of Canadian Petroleum Technology,* 34**,** 50-54.

Lloyd, D. J., Mcleod, A. D., Morris, P. L. & Jin, I. 1991. PCT Patent WO 91/19823.

Lu, M. & Zhao, Y. Y. 2010. Mechanical properties of LCS porous steel: Comparison between the dissolution and decomposition routes'. Supplemental Proceedings of TMS 2010 Annual Meeting & Exhibition, USA, 137-142.

Lu, M., Zhao, Y. Y., Seiffert, G. & Hopkins, C. 2009. Acoustic absorption characteristics of an porous steel. Materials Research Society Symposium Proceedings, 207-212.

Lu, T. J. 1999. Heat transfer efficiency of metal honeycombs. *International Journal of Heat and Mass Transfer,* 42**,** 2031-2040.

Ma, J. 2015. Review of permeability evolution model for fractured porous media. *Journal of Rock Mechanics and Geotechnical Engineering,* 7**,** 351-357.

Ma, X., Peyton, A. J. & Zhao, Y. Y. 2006. Eddy current measurements of electrical conductivity and magnetic permeability of porous metals. *Ndt & E International,* 39**,** 562-568.

Madani, B., Topin, F., Rigollet, F. & Tadrist, L. 2007. Flow laws in metallic foams: Experimental determination of inertial and viscous contributions. *Journal of Porous Media,* 10**,** 51-70.

Mahdi, R. A., Mohammed, H. A., Munisamy, K. M. & Saeid, N. H. 2015. Review of convection heat transfer and fluid flow in porous media with nanofluid. *Renewable and Sustainable Energy Reviews,* 41**,** 715-734.

Mancin, S., Zilio, C., Diani, A. & Rossetto, L. 2012. Experimental air heat transfer and pressure drop through copper foams. *Experimental Thermal and Fluid Science,* 36**,** 224-232.

Mao, S. L., Love, N., Leanos, A. & Rodriguez-Melo, G. 2014. Correlation studies of hydrodynamics and heat transfer in metal foam heat exchangers. *Applied Thermal Engineering,* 71**,** 104-118.

Matyka, M. & Koza, Z. 2012. How to calculate tortuosity easily? *AIP Conference Proceedings,* 1453**,** 17-22.

Medraj, M., Baril, E., Loya, V. & Lefebvre, L. P. 2007. The effect of microstructure on the permeability of metallic foams. *Journal of Materials Science,* 42**,** 4372-4383.

Moreira, E. A., Innocentini, M. D. M. & Coury, J. R. 2004. Permeability of ceramic foams to compressible and incompressible flow. *Journal of the European Ceramic Society,* 24**,** 3209-3218.

Morris, J. P., Lomov, I. N. & Glenn, L. A. 2003. A constitutive model for stress-induced permeability and porosity evolution of Berea sandstone. *Journal of Geophysical Research-Solid Earth,* 108.

Muramatsu, K., Ide, T., Nakajima, H. & Eaton, J. K. 2013. Heat transfer and pressure drop of lotus-type porous metals. *Journal of Heat Transfer-Transactions of the ASME,* 135**,** 072601.

Nelson, P. H. 1994. Permeability-porosity relationships in sedimentary rocks. *Log Analyst,* 35**,** 38-62.

Nield, D. & Bejan, A. 2013. *Convection in Porous Media.* Springer, New York.

Ogushi, T., Chiba, H. & Nakajima, H. 2006. Development of lotus-type porous copper heat sink. *Materials Transactions,* 47**,** 2240-2247.

Oun, H. & Kennedy, A. 2015. Tailoring the pressure-drop in multi-layered open-cell porous inconel structures. *Journal of Porous Materials,* 22**,** 1627-1633.

Paek, J. W., Kang, B. H., Kim, S. Y. & Hyun, J. M. 2000. Effective thermal conductivity and permeability of aluminum foam materials. *International Journal of Thermophysics,* 21**,** 453-464.

Pal, L., Joyce, M. K. & Fleming, P. D. 2006. A simple method for calculation of the permeability coefficient of porous media. *Tappi Journal,* 5**,** 10-16.

Parvanian, A. M. & Panjepour, M. 2013. Mechanical behavior improvement of open-pore copper foams synthesized through space holder technique. *Materials & Design,* 49**,** 834-841.

Preziosi, L. & Farina, A. 2002. On Darcy's law for growing porous media. *International Journal of Non-Linear Mechanics,* 37**,** 485-491.

Richardson, J. T., Peng, Y. & Remue, D. 2000. Properties of ceramic foam catalyst supports: pressure drop. *Applied Catalysis a-General,* 204**,** 19-32.

Rodriguez, E., Giacomelli, F. & Vazquez, A. 2004. Permeability-porosity relationship in RTM for different fiberglass and natural reinforcements. *Journal of Composite Materials,* 38**,** 259-268.

Sahimi, M. 1996. Linear and nonlinear, scalar and vector transport processes in heterogeneous media: Fractals, percolation, and scaling laws. *Chemical Engineering Journal,* 64**,** 21-44.

Seyf, H. R. & Layeghi, M. 2010. Numerical analysis of convective heat transfer from an elliptic pin fin heat sink with and without metal foam insert. *Journal of Heat Transfer-Transactions of the ASME,* 132**,** 071401-071401.

Shapovalov, V. I. 1998. Porous and cellular materials for structural applications. *In:* D.S. Schwartz, D. S. S., A.G. Evans, H.N.G. Wadley (ed.) *MRS Symp. Proc.,* 521, 281.

Sharafat, S., Ghoniem, N., Sawan, M., Ying, A. & Williams, B. 2006. Breeder foam: an innovative low porosity solid breeder material. *Fusion Engineering and Design,* 81**,** 455-460.

Sun, Z. F., Tang, X. W. & Cheng, G. C. 2013. Numerical simulation for tortuosity of porous media. *Microporous and Mesoporous Materials,* 173**,** 37-42.

Tamayol, A. & Hooman, K. 2011. Thermal assessment of forced convection through metal foam heat exchangers. *Journal of Heat Transfer,* 133**,** 111801.

Tanikawa, W. & Shimamoto, T. 2006. Klinkenberg effect for gas permeability and its comparison to water permeability for porous sedimentary rocks. *Hydrology & Earth System Sciences Discussions,* 3**,** 1315-1338.

Tao, X. F., Zhang, L. P. & Zhao, Y. Y. 2007. Mechanical response of porous copper manufactured by lost carbonate sintering process. *Thermec 2006, Pts 1-5,* 539-543**,** 1863-1867.

Thauvin, F. & Mohanty, K. K. 1998. Network modeling of non-Darcy flow through porous media. *Transport in Porous Media,* 31**,** 19-37.

Thewsey, D. J. & Zhao, Y. Y. 2008. Thermal conductivity of porous copper manufactured by the lost carbonate sintering process. *Physica Status Solidi a-Applications and Materials Science,* 205**,** 1126-1131.

Tiab, D. & Donaldson, E. C. 2012. Chapter 7 - Applications of Darcy's Law. *In:* Tiab, D. & Donaldson, E. C. (eds.) *Petrophysics (Third Edition).* Boston: Gulf Professional Publishing.

Tuckerman, D. B. & Pease, R. F. W. 1981. High-performance heat sinking for VLSI. *Electron Device Letters,* 2**,** 126.

Walsh, J. B. & Brace, W. F. 1984. The effect of pressure on porosity and the transport properties of rock. *Journal of Geophysical Research: Solid Earth,* 89**,** 9425-9431.

White, F. 2009. *Fluid Mechanics 7th Ed.,* New York, USA, McGraw-Hill.

Wright, D. 1968. Non-linear Flow Through Granular Media. *Journal of the Hydraulics Division,* 94**,** 851-872.

Xiao, Z. 2013. *Heat transfer, fluid transport and mechanical properties of porous copper manufactured by Lost Carbonate Sintering.* Ph.D., University of Liverpool.

Xiao, Z. & Zhao, Y. Y. 2013. Heat transfer coefficient of porous copper with homogeneous and hybrid structures in active cooling. *Journal of Materials Research,* 28**,** 2545-2553.

Xiao, Z. & Zhao, Y. Y. 2014. Thermal properties of porous copper manufactured by lost carbonate sintering. *Materials Science Forum.*, 783-786, 1603-1608.

Yang, Y. L. & Aplin, A. C. 2010. A permeability-porosity relationship for mudstones. *Marine and Petroleum Geology,* 27**,** 1692-1697.

Zaragoza, G. & Goodall, R. 2013. Metal foams with graded pore size for heat transfer applications. *Advanced Engineering Materials,* 15**,** 123-128.

Zeng, Z. W. & Grigg, R. 2006. A criterion for non-Darcy flow in porous media. *Transport in Porous Media,* 63**,** 57-69.

Zhang, H. Y., Pinjala, D., Joshi, Y. K., Wong, T. N., Toh, K. C. & Iyer, M. K. 2005. Fluid flow and heat transfer in liquid cooled foam heat sinks for electronic packages. *IEEE Transactions on Components and Packaging Technologies,* 28**,** 272-280.

Zhang, L. P., Mullen, D., Lynn, K. & Zhao, Y. Y. 2009. Heat transfer performance of porous copper fabricated by Lost Carbonate Sintering Process. *MRS Online Proceedings Library,* 1188**,** 213-218.

Zhang, L. P. & Zhao, Y. Y. 2008. Fabrication of high melting-point porous metals by lost carbonate sintering process via decomposition route. Proceedings of the Institution of Mechanical Engineers, *Part B: Journal of Engineering Manufacture*, 267-271.

Zhao, C. Y. 2012. Review on thermal transport in high porosity cellular metal foams with open cells. *International Journal of Heat and Mass Transfer,* 55**,** 3618-3632.

Zhao, C. Y., Kim, T., Lu, T. J. & Hodson, H. P. 2004a. The temperature dependence of effective thermal conductivity of open-celled steel alloy foams. *Materials Science and Engineering: A,* 367**,** 123-131.

Zhao, C. Y., Lu, T. J., Hodson, H. P. & Jackson, J. D. 2004b. Thermal transport in high porosity cellular metal foams. *Journal of Thermophysics and Heat Transfer,* 18**,** 309-317.

Zhao, Y. Y., Fung, T., Zhang, L. P. & Zhang, F. L. 2005. Lost carbonate sintering process for manufacturing metal foams. *Scripta Materialia,* 52**,** 295-298.

Zhong, W., Li, X., Liu, F. H., Tao, G. L., Lu, B. & Kagawa, T. 2014. Measurement and correlation of pressure drop characteristics for air flow through sintered metal porous media. *Transport in Porous Media,* 101**,** 53-67.

Zhu, W. L. & Wong, T. F. 1997. The transition from brittle faulting to cataclastic flow: Permeability evolution. *Journal of Geophysical Research-Solid Earth,* 102**,** 3027-3041.